Summer 2018

Solid Oxide Electrochemical Cells for High Temperature Hydrogen Production: Theory, Fabrication and Characterization

Can Zhou
Old Dominion University

SOLID OXIDE ELECTROCHEMICAL CELLS FOR HIGH TEMPERATURE HYDROGEN PRODUCTION: THEORY, FABRICATION AND CHARACTERIZATION

by

Can Zhou
B.S. June 2012, Nanjing University of Aerospace and Astronautics
M.E. June 2014, Nanjing University of Aerospace and Astronautics

A Dissertation Submitted to the Faculty of
Old Dominion University in Partial Fulfillment of the
Requirements for the Degree of

DOCTOR OF PHILOSOPHY

MECHANICAL ENGINEERING

OLD DOMINION UNIVERSITY
July 2018

Approved by:

Xiaoyu Zhang (Director)

Shizhi Qian (Member)

Alvin Holder (Member)

Dipankar Ghosh (Member)

ABSTRACT

SOLID OXIDE ELECTROCHEMICAL CELLS FOR HIGH TEMPERATURE HYDROGEN PRODUCTION: THEORY, FABRICATION AND CHARACTERIZATION

Can Zhou
Old Dominion University, 2018
Director: Dr. Xiaoyu Zhang

In this dissertation, the concept of water splitting using solid oxide photoelectrochemical cells (SOPCs) at high temperature was introduced and experimentally investigated. High temperature photoelectrochemical water splitting physically broadens the selection of potential applicable semiconductor materials and enables more visible sunlight absorption. This newly conceived concept provides a unique pathway for solar hydrogen production, as compared to conventional photoelectrochemical cells (PECs) that use wide band gap semiconductors in aqueous environments. The theoretical framework of SOPC was elaborated, followed by the experimental investigation to search for appropriate high temperature materials. Selected high temperature Schottky and p-n junction diodes, which were expected to be applicable to the photocatalytic/oxygen electrodes of SOPCs, were fabricated and evaluated. Their rectifying characteristics were characterized at elevated temperatures. Among those diodes, only LSM/TiO_2 demonstrated acceptable rectifying properties up to 450 °C, indicating that such configuration may be applicable to the proposed SOPC.

The further investigation was carried out on fabrication of the electrodes of SOPC and solid oxide fuel cell (SOFC) using fused deposition modeling (FDM), a technique of 3D printing. The goal was to directly print out ceramic substrates and eventually make porous electrodes. Ceramic filaments that consist of ceramic electrode materials and thermoplastics were fabricated

in house. After experimenting many thermoplastics, Nylon 12 was identified as an ideal thermoplastic polymer to make composite ceramic filaments. The printouts were sintered in the furnace to burn out all the organics, leaving behind porous electrodes made of pure ceramics. The 3D printed cathodes on half SOFCs were evaluated and demonstrated comparable performance to conventional SOFCs using dip-coating method. Therefore, FDM provides a viable and low cost means to fabricate the porous electrodes of SOPC/SOFC.

This thesis is dedicated to the proposition
that the harder you work, the luckier you get.

ACKNOWLEDGMENTS

First, I would like to express my sincere gratitude to my advisor Prof. Zhang, for the four years support of my Ph.D study and related research, for his patience, motivation and immense knowledge. I have always been grateful for the precious opportunity he offered me to study abroad. Besides, his guidance helped me in all the time of living life and job references. I could not have imagined having a better advisor and mentor for my Ph.D study.

Then, I would like to thank the committee members: Prof. Qian, Prof. Holder and Prof. Ghosh, not only for their insightful comments and encouragement, but also for the hard questions which incented me to widen my research from various perspectives.

My sincere thanks also go to the Applied Research Center (ARC) of William & Mary, which gave me the access to the laboratory and research facilities to characterize my samples. It's impossible to conduct my research without their support. They provided me a training opportunity of SEM and EDX and such experience greatly helped me to get the job offer.

I would like to thank my fellow labmates: Lanju, Elias, Tim, Yashar and Grace, for the inspiring discussions and writing papers during the last four years. It's a great honor and a lot of fun to work together with them.

Last but not least, many thanks go to my family: my parents and brother. Thanks for supporting me in all the time. Whenever I have a problem, they are the first that I want to ask for help and advice. It is they that raise me up to more than I can be.

NOMENCLATURE

hv	Photon
e^-	Electron
p^+	Hole
ΔG	The change of Gibbs free energy, kJ/mol
ΔH	The change of enthalpy, kJ/mol
ΔS	Entropy change, kJ/(mol·K)
N_e	The number of reacted electrons
$N_p^{absorbed}$	The number of absorbed photons
$N_p^{incident}$	The number of incident photons
E_{H2}	The energy of photogenerated hydrogen
$E_s^{incident}$	The energy of incident solar energy
$E_g(T)$	The semiconductor bandgap, eV
$E_g(0)$	The bandgap at absolute temperature of 0 K, eV
T	Absolute temperature, K
E	Nernst potential, V
E_0	Standard cell potential, V
R	Ideal gas constant, 8.314 J/(mol·K)
F	Faraday constant, 96485.3329, C/mol
P	Partial pressure, Pa
$\Delta\dot{N}_{H_2}$	Molar hydrogen generation rate
N_C	The number of unit cell in the stacks
Φ_M	Work function of metal, eV
Φ_S	Work function of semiconductor, eV
Φ_{MS}	Schottky barrier height, eV
E_C	Energy of conduction band

E_V	Energy of valance band
E_F	Energy of Fermi level
χ	Semiconductor electron affinity
A^*	Effective Richardson constant
q	Electron charge
I_s	Saturation current, A
k	Boltzmann constant, 1.38064852×10^{-23} J/K
n	Non-ideal factor
V_{bi}	Build-in potential, V
N_A	Concentrations of acceptors
N_D	Concentrations of donors
n_i	Carrier concentration in the neutral region
D_p,D_n	The diffusivities of the holes and electrons respectively
p_{n0}	The hole concentration in the neutral region of n-type semiconductors
n_{p0}	The electron concentration in the neutral region of p-type semiconductors
L_p, L_n	The depletion lengths of p-type and n-type semiconductors respectively
I_{diff}	Diffusion current
I_{rec}	Recombination current
τ_g, τ_p	The generation lifetime and p-type carrier lifetime respectively
W	The width of space charge region
ε	The dielectric permittivity
N	The dielectric constant
a_{H+}	The activity of H^+
η_{PEC}	Efficiency limit for a PEC device made of a single junction diode
j_{op}	Maximum exchange current density
E_{rxn}	Nernst potential of water electrolysis
f_{FE}	Faradaic efficiency, which ideally is unit
P_{in}	Incident solar power

V	Volume, cm^3
W	Weight, g
ρ	Density, g/cm^3
ϕ	Initial porosity before sintering

TABLE OF CONTENTS

Page

LIST OF TABLES 10

LIST OF FIGURES 11

Chapter

I. INTRODUCTION 18
1.1 Photoelectrochemical cells 20
1.1.1 Fundamental mechanism of photoelectrochemical system 22
1.1.2 Main process of photoelectrochemical system 25
1.1.3 Photocatalytic activity of photoelectrochemical system 27
1.1.4 Photoelectrochemical process driven by UV light 28
1.1.5 Two-step photoelectrochemical system driven by visible light 30
1.1.6 Tandem photoelectrochemical system driven by visible light 34
1.1.7 Hybrid photoelectrochemical system driven by visible light 38
1.1.8 Summary and prospects 40
1.2 Solid-state photoelectrochemical cells 41
1.2.1 Proton-exchange-membrane based PEM system 43
1.2.2 The MIEC based PEC system 44
1.2.3 Integrated-PV/EC PEC system 47
1.2.4 Summary and prospects 48
1.3 Solid oxide electrolysis cells 50
1.3.1 History 51
1.3.2 Operating principles 54
1.3.3 Thermodynamics 56
1.3.4 Configurations and Materials 59
1.3.5 Manufacturing 66
1.3.6 Hydrogen and Oxygen Production via SOEC 70
1.3.7 SOEC Degradation 73

1.3.8 Summary and prospects 76

II. WATER SPLITTING USING HIGH TEMPERATURE SOLID OXIDE PHOTOELECTROCHEMICAL CELL AND VISIBLE LIGHT: SEARCHING FOR THE APPROPRIATE SEMICONDUCTOR MATERIALS 78

2.1 Background 79

2.2 Theoretical framework 81

2.2.1 Thermodynamics 81

2.2.2 Schottky Barriers 82

2.2.3 p-n junction 86

2.2.4 Constrains and challenges 92

2.3 SOPC configuration 94

2.4 Experimental 96

2.4.1 Electrolysis cell materials 96

2.4.2 PV cell materials 96

2.4.3 Experiments 99

2.5 Results and discussion 102

2.6 Summary 107

III. FABRICATION OF SOLID OXIDE ELECTRODES USING 3D PRINTING 108

3.1 Background 108

3.2 Experimental 114

3.2.1 3D printer and extruder 114

3.2.2 Searching for appropriate thermoplastics 117

3.2.3 Mixing 119

3.2.4 Extrusion 121

3.2.5 Printing 123

3.2.6 Sintering 125

3.2.7 SOFC button cell preparation 127

3.2.8 Experimental setup for SOFC characterization 130

3.2.9 SEM inspection 132

3.3 Results and discussion 134

3.3.1 Dip-coating LSM cathode 134

3.3.2 SOFC button cell with 3D printed LSM cathode 139
3.3.3 SOFC button cell with 3D printed LSCF cathode 157
3.3.4 Cathode surface characterization 168
3.4 Summary 176
IV. CONCLUSIONS AND FUTURE RESEARCH 178
4.1 Conclusions 178
4.2 Future research 179
4.2.1 OCV characterization of SOPC with light irradiation at high temperature 180
4.2.2 Oxygen pump test of SOPC with light irradiation at high temperature 181
4.2.3 Steam electrolysis of SOPC with light irradiation at high temperature 182

REFERENCES 183

APPENDICES 212

VITA 215

LIST OF TABLES

Table 1. Material and manufacturing summary of SOEC electrolyte, fuel electrode and oxygen electrode. 76

Table 2. Selected p-n junction diodes for further evaluation of their rectifying properties at high temperature (partially adapted from [182]) 97

Table 3. Physical and chemical properties of common thermoplastic materials for 3D printing [228, 229]. 118

Table 4. Ingredients of polymer-ceramic composite for filament fabrication. 120

Table 5. Summary of the SOFC button cell characterization. 176

Table 6. Summary of long-term degradation of SOEC in stack level. 212

LIST OF FIGURES

Figure 1. Hydrogen production pathways published by DOE [1]. 20

Figure 2. Schematic diagram of photoelectrochemical devices [2]. 22

Figure 3. Fundamental mechanism of photoelectrochemical reaction [3]. 23

Figure 4. Semiconductors for PECs. The bandgap positions are relative to the redox potential of water [4]. 24

Figure 5. Schematic diagram of the photoelectrochemical process, including I. Photon absorption, II. Photon excitation, III. Charge separation, IV. Charge transfer, and V. Charge recombination [3]. 25

Figure 6. Schematic redox energy diagram of PEC using two-step systems [15]. 31

Figure 7. Schematic diagram of PEC systems: (a) n-type photoanode, (b) p-type photocathode, and (c) tandem system [11]. 35

Figure 8. Electron-flow fundamentals of tandem PEC system [11]. 36

Figure 9. Illustrative diagram of the electron transfer in CdS/(Pt-TiO_2) hybrid photocatalytic system [42]. 39

Figure 10. Schematic diagram of proton-exchange-membrane based process [56]. 44

Figure 11. Schematic diagram of solid oxide photoelectrochemical cells used as the light-charged oxygen battery [51-54]. 45

Figure 12. Schematic diagram of MIEC based solid-state PEC system designed by Ye *[51]*, I. Charge separation, II. Electron transfer, III. Holes migration, IV. Water splitting, V. Oxygen ion transfer, VI. Oxygen generation [51, 52]. 47

Figure 13. Schematic diagram of PV/EC integrated solid-state PEC system [53, 55]. 48

Figure 14. The renewable hydrogen production and electricity/hydrogen cogeneration infrastructure system proposed by national renewable energy laboratory (NREL) [65]. 51

Figure 15. Operation principles of SOFC and SOEC [84]. 55

Figure 16. Thermodynamics water electrolysis from 273K to 1000K [87]. 57

Figure 17. Nernst potential for H_2O splitting at atmosphere pressure as temperature increases.. 59

Figure 18. Exploded view of a 10-cell stack from Cermatec [93]. 61

Figure 19. Exploded view of a 5-cell stack from MSRI [93]. 63

Figure 20. Schematic diagram of tubular SOECs with a continuous electrolyte [114]. 63

Figure 21. Schematic diagram of several possible configurations for tubular stacks with discontinuous electrolytes [114]. 64

Figure 22. Schematic drawing of the fabricated electrolyzer cell [115]. 65

Figure 23. The design of a 2-cell bielectrode-supported stack [117]. 66

Figure 24. The hydrogen production rate of SOE stacks as a function of time. 70

Figure 25. Durability test of a 20-cell stack operated at high current density [151]. 72

Figure 26. A simplified exploded view of a single-repeating unit (SRU) and a few of the possible degradation mechanisms [152]. 75

Figure 27. Schematic energy diagram of Schottky barriers for different types of semiconductors and metals: a. $\Phi_M > \Phi_S$, n-type; b. $\Phi_M > \Phi_S$, p-type; c. $\Phi_M < \Phi_S$, n-type; d. $\Phi_M < \Phi_S$, p-type [170]. 84

Figure 28. Schematic diagram of p-n junction in thermal equilibrium with zero-bias voltage applied [173]. 87

Figure 29. Schematic diagram of p-n junction under various conditions. a. thermal equilibrium condition, b. forward bias condition, c. reverse bias condition [170]. 89

Figure 30. Schematic diagram of band energy of heterojunction. a. before contact, b. thermal equilibrium [170]. 92

Figure 31. Schematic diagram of hydrogen or syngas (H_2+CO) production using a SOPC, which integrates a PV cell and an electrolysis cell [179]. 95

Figure 32. Band alignment of candidate n- and p-type oxide semiconductors suitable to form p-n junction diodes (adapted from [3, 175, 191, 192]). 99

Figure 33. SEM images showing the (a) cross-section and (b) surface of the Ti/TiO2 pellets prepared by thermal oxidation [179]..... 101

Figure 34. Rectifying characteristics of TiO_2 based diodes from room temperature to 500 °C. (a), (b), (c) and (d) show the Ag/TiO_2, LSM/TiO_2, LSC/TiO_2 and LSCF/TiO_2 diodes respectively [179]. 104

Figure 35. Knee voltages of Ag/TiO_2, LSM/TiO_2, LSC/TiO_2 and LSCF/TiO_2 diodes as a function of temperature compared to thresholds of steam electrolysis [179]. 106

Figure 36. FDM devices: a. 3D printer; b. extruder..... 115

Figure 37. Schematic diagram of FDM process. 116

Figure 38. Heating system design of filament extruder: a. before design, b. after design..... 117

Figure 39. Thermoplastic-ceramic composite mixing: a. ABS-Al_2O_3; b. Aquazol-Al_2O_3; c. PVA-Al_2O_3; d. PVA-LSM; e. PA12-LSM; f. PA12-LSM-YSZ. 121

Figure 40. Extruded thermoplastic-ceramic filaments based on the ingredients in table 4. a. ABS-Al_2O_3; b. Aquazol-Al_2O_3; c. PVA- Al_2O_3; d. PVA-LSM; e. PA12 based composites including PA12-LSM-YSZ and PA12-LSCF-YSZ; f. flexibility of PA12 based composite filaments..... 123

Figure 41. 3D printing objects using the composite filaments: a. Aquazol-Al_2O_3; b. PVA- Al_2O_3; c. PVA-LSM; d. PA12-LSM; e. SOFC cathodes including PA12-LSM-YSZ and PA12-LSCF-YSZ. 125

Figure 42. The 3D printed composite samples after sintering: a. PVA-Al_2O_3; b. PVA-LSM; c. PA12-LSM. 126

Figure 43. Bonding 3D printed cathode on the electrode: a. before melting; b. after melting; c. after sintering; d. during sintering. 128

Figure 44. SOFC button cell preparation: a. pressing and sintering; b. dip-coating; c. electrical collector on the cathode; d. electrical collector on the anode. 130

Figure 45. Experimental setup for SOFC characterization: a. ceramic tube assembly; b. hydrogen inlet/outlet and voltage/current detection; c. temperature control by furnace; d. gas control and data acquisition. 132

Figure 46. Inspection equipment: a. sputter coater; b. sputtering process; c. SEM; d. optical microscope. 134

Figure 47. Characterization of SOFC button cell #1 with dip-coating LSM cathode (0.5 cm^2 active area). 136

Figure 48. Post-inspection of SOFC button cells: a. cracking problems; b. applying ceramic paste to avoid cracking. 137

Figure 49. Characterization of SOFC button cell #2 with dip-coating LSM cathode (0.5 cm^2 active area). 138

Figure 50. Voltage scan of SOFC button cell #2 with dip-coating LSM cathode (0.5 cm^2 active area) at 750 °C. 139

Figure 51. Characterization of SOFC button cell #3 with 3D printed LSM cathode (0.5 cm^2 active area). 140

Figure 52. Characterization of SOFC button cell #4 with 3D printed LSM cathode (1 cm^2 active area) at H_2 flow rate of 100 sccm. 141

Figure 53. Voltage scan of SOFC button cell #4 with 3D printed LSM cathode (1 cm^2 active area). 142

Figure 54. Characterization of SOFC button cell #5 with 3D printed LSM cathode (0.5 cm^2 active area). 143

Figure 55. V-I characterization of SOFC button cell #5 for two cycles at 750 °C and 100 sccm of H_2. 145

Figure 56. Voltage scan of SOFC button cell #5 with 3D printed cathode (0.5 cm^2 active area) at 750 °C and the hydrogen flow rate of 50, 100, 200 sccm respectively. 146

Figure 57. Characterization of SOFC button cell #6 with 3D printed LSM cathode (0.5 cm^2 active area). 148

Figure 58. Voltage scan of SOFC button cell #6 with 3D printed LSM cathode (0.5 cm^2 active area) at 750 °C and H_2 flow rate of 50 sccm, 100 sccm and 200 sccm respectively. 149

Figure 59. Voltage scan of SOFC button cell #6 with 3D printed LSM cathode (0.5 cm^2 active area) at 800 °C and H_2 flow rate of 50 sccm, 100 sccm and 200 sccm respectively. 150

Figure 60. Voltage scan of SOFC button cell #6 with 3D printed LSM cathode (0.5 cm^2 active area) at 700 °C and H_2 flow rate of 50 sccm, 100 sccm and 200 sccm respectively. 151

Figure 61. Voltage scan of SOFC button cell #6 with 3D printed LSM cathode (0.5 cm^2 active area) at 100 sccm of H_2 and temperature of 700 °C, 750 °C and 800 °C respectively. 152

Figure 62. Characterization of SOFC button cell #7 with 3D printed LSM cathode (1 cm^2 active area)..... 153

Figure 63. Voltage scan of SOFC button cell #7 with 3D printed LSM cathode (1 cm^2 active area) at 750 °C and H_2 flow rate of 50 sccm, 100 sccm and 200 sccm respectively. 154

Figure 64. Voltage scan of SOFC button cell #7 with 3D printed LSM cathode (1 cm^2 active area) at 800 °C and H_2 flow rate of 50 sccm, 100 sccm and 200 sccm respectively 155

Figure 65. Voltage scan of SOFC button cell #7 with 3D printed LSM cathode (1 cm^2 active area) at 700 °C and H_2 flow rate of 50 sccm, 100 sccm and 200 sccm respectively. 156

Figure 66. Voltage scan of SOFC button cell #7 with 3D printed LSM cathode (1 cm^2 active area) at 100 sccm of H_2 and temperature of 700 °C, 750 °C and 800 °C respectively. 157

Figure 67. Characterization of SOFC button cell #8 with 3D printed LSCF cathode (1 cm^2 active area)..... 158

Figure 68. Voltage scan of SOFC button cell #8 with 3D printed LSCF cathode (1 cm^2 active area) at 750 °C and H_2 flow rate of 50 sccm, 100 sccm and 200 sccm respectively. 159

Figure 69. Voltage scan of SOFC button cell #8 with 3D printed LSCF cathode (1 cm^2 active area) at 800 °C and H_2 flow rate of 50 sccm, 100 sccm and 200 sccm respectively 160

Figure 70. Voltage scan of SOFC button cell #8 with 3D printed LSCF cathode (1 cm^2 active area) at 700 °C and H_2 flow rate of 50 sccm, 100 sccm and 200 sccm respectively. 161

Figure 71. Voltage scan of SOFC button cell #8 with 3D printed LSCF cathode (1 cm^2 active area) at 100 sccm of H_2 and temperature of 700 °C, 750 °C and 800 °C respectively. 162

Figure 72. Characterization of SOFC button cell #9 with 3D printed LSCF cathode (1 cm^2 active area)..... 163

Figure 73. Voltage scan of SOFC button cell #9 with 3D printed LSCF cathode (1 cm^2 active area) at 750 °C and H_2 flow rate of 50 sccm, 100 sccm and 200 sccm respectively. 164

Figure 74. Voltage scan of SOFC button cell #9 with 3D printed LSCF cathode (1 cm^2 active area) at 800 °C and H_2 flow rate of 50 sccm, 100 sccm and 200 sccm respectively. 165

Figure 75. Voltage scan of SOFC button cell #9 with 3D printed LSCF cathode (1 cm^2 active area) at 700 °C and H_2 flow rate of 50 sccm, 100 sccm and 200 sccm respectively. 166

Figure 76. Voltage scan of SOFC button cell #9 with 3D printed LSCF cathode (1 cm^2 active area) at 100 sccm of H_2 and temperature of 700 °C, 750 °C and 800 °C respectively. 167

Figure 77. SEM surface characterization of dip-coating LSM cathode with scale bar of a. 100 µm; b. 10 µm; c. 5 µm; d. 1 µm. 169

Figure 78. SEM surface characterization of Ag collector (a) and 3D printed LSM cathode with scale bar of b. 8 µm; c. 3 µm and d. 1 µm. 171

Figure 79. SEM surface characterization of 3D printed LSCF cathode with scale bar of a. 10 µm; b. 5 µm and c. 1 µm. 173

Figure 80. Surface characterization of 3D printed LSCF cathodes using optical microscopy: a. 2D surface and b. 3D surface. 175

Figure 81. OCV characterization of SOPC with light irradiation at high temperature. 180

Figure 82. Oxygen pump test of SOPC with light irradiation at high temperature. 181

Figure 83. Steam electrolysis of SOPC with light irradiation at high temperature. 182

CHAPTER 1

INTRODUCTION

Hydrogen is considered as one of the most promising energy carriers for vehicles and various other applications. Compared to traditional fossil fuels, hydrogen has its salient advantages. First, hydrogen production is not dependent on non-renewable natural resources since it can be generated from water. Second, unlike oil and natural gas, the availability of hydrogen does not depend on geographical, political, and other factors. Last but not least, using hydrogen is environmentally friendly with zero-emissions of greenhouse gas (GHG) and other air pollutants. Therefore, many countries, led by Japan, Germany and United States, are focusing on the research and development (R&D) of technologies of hydrogen production. Currently, most hydrogen is produced from natural gas reforming that could emit GHG into the air and potentially cause global warming. Aimed at more economical and environmental hydrogen production in the future, the Department of Energy (DOE) has supported a variety of technologies such as the thermal process, electrolytic process, photolytic process and biochemical process. In the thermal process, hydrogen is released by using the energy contained in the resources such as natural gas, coal or biomass. Water can also be used as the feedstock to produce hydrogen through thermochemical process when the heat is combined with closed chemical cycles. Techniques of thermal process includes the natural gas reforming, renewable liquid fuel reforming, coal gasification, biomass gasification, and high-temperature water splitting. In the electrolytic process, water is decomposed into hydrogen and oxygen by external electricity. When the electrolysis is coupled with renewable energy, such as wind, solar and nuclear sources, the whole process is sustainable with zero carbon emission that would be the greatest pathway for large-scale hydrogen production. In the photolytic process, the water

molecules are separated directly into hydrogen and oxygen by light energy. The carriers could be either algae through photosynthesis or semiconductor through photoelectrochemical (PEC) reaction. In the biochemical process, the organic biomass is converted into hydrogen by biochemical or microbial methods. Typically, the biochemical process includes the fermentation and microbial electrolysis cells. To facilitate the commercial development of hydrogen production with a target cost of less than $4/kg, the DOE has scheduled a roadmap of various techniques from near to long terms considering the hydrogen production scale as shown in Figure 1. Near-term development is limited to the natural gas reforming that is not sustainable, and mid-term development mainly focuses on thermal process techniques at distribute and semi-central production. In a long-term perspective, hydrogen production via solar energy and high-temperature electrolysis are the most promising techniques for the semi-central and central production facilities.

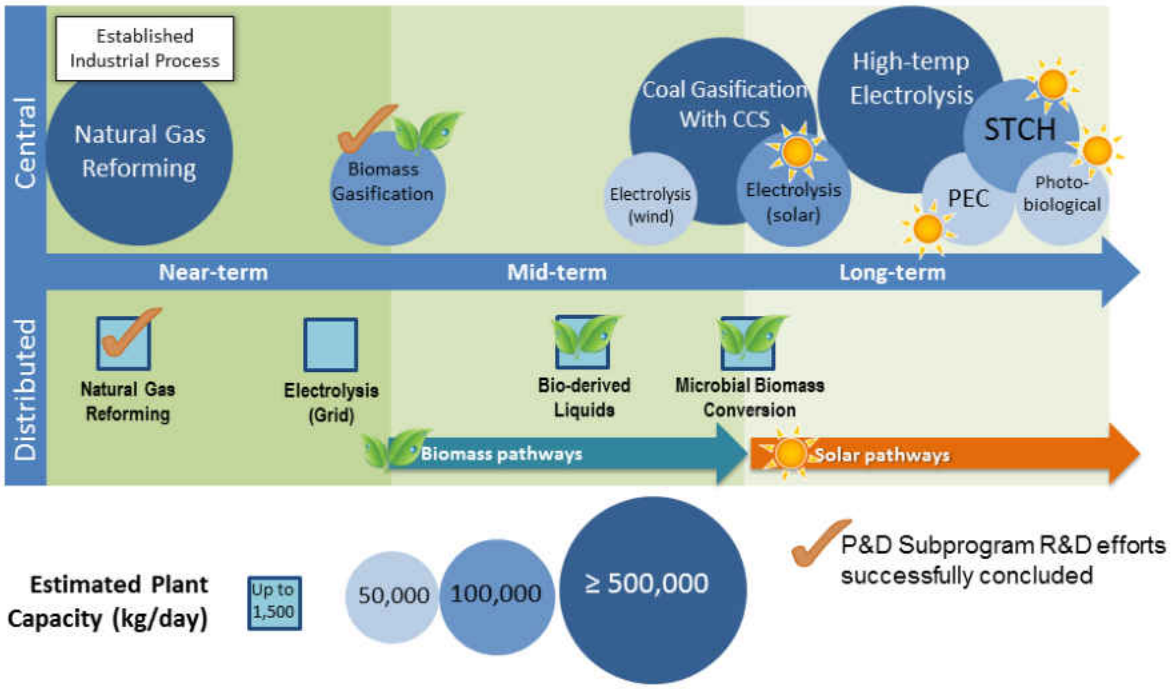

Figure 1. Hydrogen production pathways published by DOE [1].

In this dissertation, a novel concept of solar hydrogen production using solid oxide photoelectrochemical cell (SOPC) is introduced. The SOPC we proposed includes two key components, the photovoltaic (PV) cell and high temperature electrolysis cell (SOEC). Therefore, two parts of review will be presented in this dissertation for PEC and SOEC, respectively. Both parts of review focus on literature survey, fundamentals, and operation principles.

1.1 Photoelectrochemical cells

As shown in Figure 1, the PEC pathway is a long-term technique for hydrogen production for semi-central facilities. Basically, the solar energy is converted directly to chemical energy in forms of hydrogen and oxygen via the photoelectrochemical process. The semiconductor materials used in the PEC devices are similar to those used in the PV cells. In photovoltaic devices, the key component is the p-n junction that integrates the p-type and n-type

doped semiconductors. At the junction interface, the excess of electrons from the n-type semiconductor tend to diffuse into the p region that will leave the positive holes in the n region. Likewise, the excess of holes in the p-type doped semiconductors tend to diffuse into n region leaving negative electrons in the p region. The immigration of electrons and holes results in a space charge region where the internal electric field is created. When the space charge region is irradiated by light energy that is larger than the semiconductor bandgap, the excited-state electrons will jump over the bandgap into the conduction band leaving the holes in the valence band. Due to the internal electric field, the electrons and holes then will move to opposite directions leading to electric current if an external load is connected. The photovoltaic process is also applicable to Schottky junction where the metals serve as p-type semiconductors with combination of n-type semiconductors. Unlike the PV cell that integrates the semiconductor electrodes together, the PEC cell has separated electrodes that are both immersed into the electrolyte as shown in Figure 2. The separated electrodes are connected through an external conductive wire that is used for electron transfer. After solar irradiation the surface of n-type semiconductor, oxygen evolution is observed at the photoanode while hydrogen bubbles are generated at the Pt photochathode.

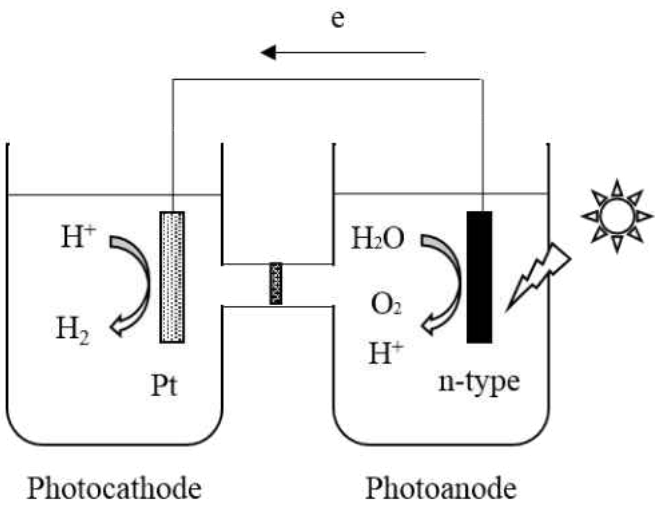

Figure 2. Schematic diagram of photoelectrochemical devices [2].

1.1.1 Fundamental mechanism of photoelectrochemical system

The fundamental principles of the photoelectrolysis process are shown in Figure 3. Typically, as a semiconductor photocatalyst, the photoanode semiconductor could absorb solar irradiation during the photoelectrochemical reaction. At the stage of semiconductor's "photo-excited" state, the electrons in the valance band of TiO_2 are excited to the conduction band while extra holes are left at valance band. This photocatalytic process creates the electron-hole pairs. After some inevitable recombination of such pairs, the electrons are then transferred to the photocathode through external circuit for hydrogen production. The left holes at TiO_2 electrode are responsible for oxygen evolution due to its oxidation capability of water molecules. The photoelectrochemical reactions happening on both electrodes could be described as follows:

$$\text{n-type} + 2\,h\nu \rightarrow 2\,e^- + 2\,p^+ \quad 1)$$

$$2\ p^{+} + H_2O \rightarrow \tfrac{1}{2}\ O_2 + 2\ H^{+} \qquad \text{at photoanode} \qquad (2)$$

$$2\ e^{-} + 2\ H^{+} \rightarrow H_2 \qquad \text{at photocathode} \qquad (3)$$

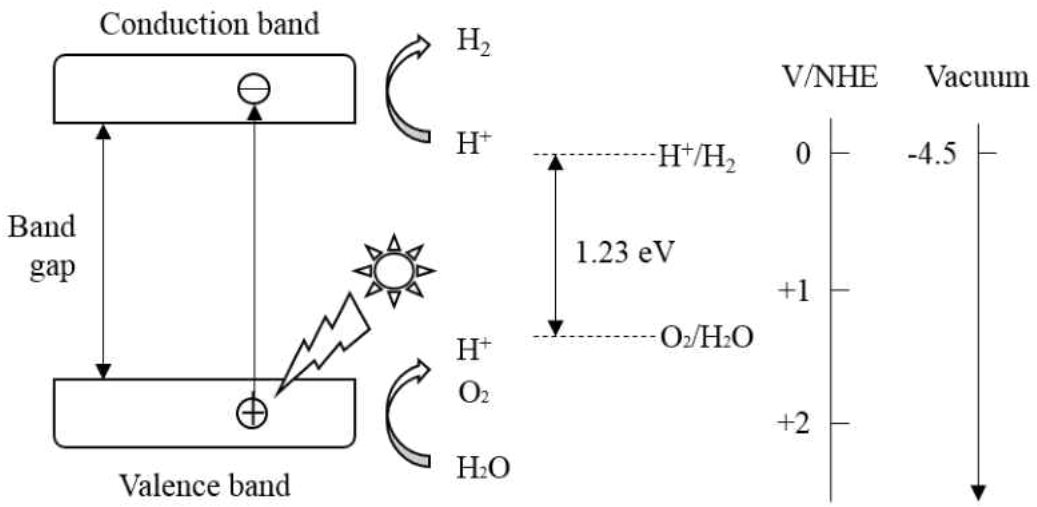

Figure 3. Fundamental mechanism of photoelectrochemical reaction [3].

The theoretically thermodynamic threshold for water splitting is 1.23 V at standard conditions according to the change of Gibbs free energy, as shown in equation 4.

$$H_2O \rightarrow \tfrac{1}{2}\ O_2 + H_2; \quad \Delta G = +237\ \text{kJ/mol} \qquad (4)$$

Such energy threshold corresponds to a wavelength of approximate 1000 nm. Note that the visible light with spectrum of more than 400 nm corresponds to the bandgap energy of less than 3.1 eV. To guarantee the photoexcited reduction and oxidation of water molecules, the bandgap of photocatalytic semiconductor must straddle the redox potentials for water splitting. Specifically, the energy level of conduction band should be more negative than the reduction

potential of H^+/H_2 while the energy level of valance band has to be more positive than the oxidation potential of O_2/H_2O. Figure 4 shows the bandgap structures of some typical semiconductors compared with redox potential of water splitting. Besides TiO_2, many photocatalytic materials, such as $BaTiO_3$, ZnO, SiC, CdSe, CdS etc., have the potential to be applied in the PECs. However, the photocatalytic generation of hydrogen from water splitting is dependent not only the bandgap structure of semiconductor, but also other factors such as overpotentials, separation and recombination of electron-hole pairs, mobility, and lifetime of electrons/holes [3]. Therefore, the photoelectrode materials and semiconductor substrate determine the system performance.

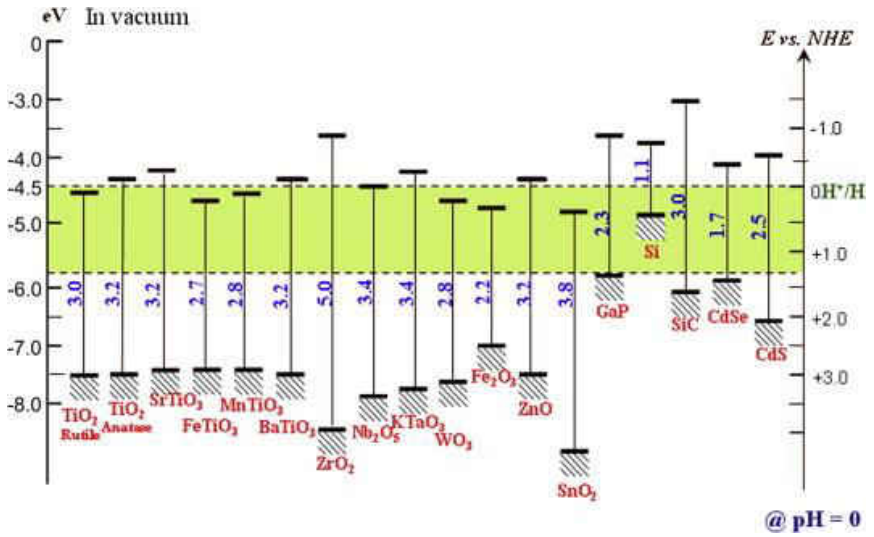

Figure 4. Semiconductors for PECs. The bandgap positions are relative to the redox potential of water [4].

1.1.2 Main process of photoelectrochemical system

The schematics of photocatalytic water splitting is illustrated Figure 5. The processes include photon absorption, photon excitation, charge separation, charge transfer, and charge recombination. The hydrogen generation efficiency of PEC system is significantly dependent on these processes. Among them, the charge recombination is considered as the deactivation process and it is the only process that consumes the photoexcited electrons. Therefore, possible steps should be taken to avoid charge recombination. Meanwhile, the other activation processes should be facilitated to maximize the PEC system efficiency.

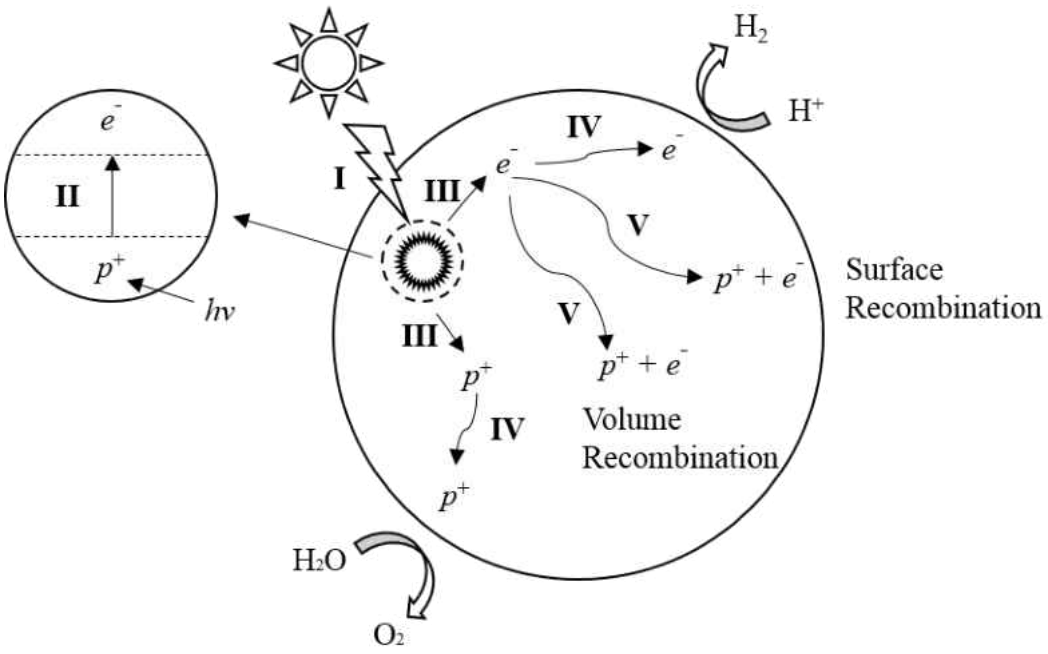

Figure 5. Schematic diagram of the photoelectrochemical process, including I. Photon absorption, II. Photon excitation, III. Charge separation, IV. Charge transfer, and V. Charge recombination [3].

As mentioned above, with light irradiation, the processes of photon absorption, photon excitation and charge separation take place in the semiconductor photocatalysts. Thus, small bandgap semiconductor materials are preferred to absorb the photons as much as possible. However, the utilization of those photocatalysts with too narrow bandgap is not suggested due to the excess waste of light energy. In addition, the light reflection and scattering by the semiconductors should be minimized. Furthermore, the photocatalysts should have a strong junction, i.e. internal electric field, which is effective in generating and separating charges.

Once the photogenerated charges are created, charge transfer (IV) and charge recombination (V) are the two important competitive processes that could significantly affect the hydrogen production efficiency. The charge recombination includes the volume recombination and the surface recombination. Both deactivation processes will consume the photogenerated charges by emitting light or releasing heat energy. On the other hand, charge transfer is an activation process due to the charges on the photocatalyst surface for hydrogen and oxygen production. Therefore, it is fundamentally important to facilitate the charge transfer and suppress the charge recombination. Effective approaches consist of designing internal electric field of junction and developing high photoconductive photocatalysts.

When the hydrogen and oxygen evolve at the photocatalyst surface, it is possible for the reaction of these two gas molecules and this chemical process is known as surface back reaction (SBR). The SBR has a negative influence in the PEC systems, since the amount of photogenerated hydrogen will be decreased. Typically, there are two main ways of avoiding SBR effectively. The first approach is to add redox mediators in the electrolyte. The electron donors or acceptors of the sacrificial reagents can supply an external force to drive the PEC reaction and suppress the combination of product molecules. The other way is to create separation sites for

water reduction and oxidation. For example, Pt and Au are the most common materials used to be deposited on the photocatalyst surface. Due to the excellent electron conductivity, the Pt or Au can supply an ideal reaction site for hydrogen generation.

Considering all the processes that can significantly affect the PEC efficiency, there are two key factors for developing suitable semiconductor photocatalysts driven by visible light. First, the bandgap should be in the range from 1.23 eV to 3eV with corresponding to the spectrum wavelength from 400 nm to 1000 nm. This range can enable the photocatalysts to harvest the solar energy as much as possible without losing the capability of splitting water. Second, both deactivation processes of the charge recombination and SBR should be depressed. The effective approaches include design of internal-build electric field, addition of sacrificial reagents into electrolyte and creation of active reaction sites.

1.1.3 Photocatalytic activity of photoelectrochemical system

Photocatalytic activity is an important indicator for evaluating the hydrogen production efficiency of PEC system. It can be calculated directly by measuring the amount of hydrogen evolution or indirectly by converting gas generation to effective electron transfer within a certain testing duration. There are many research groups of PEC systems and their experiments are usually conducted using different setup configurations, i.e. inner irradiation and top irradiation, and light sources, i.e. Xe lamp and Hg lamp. Different experimental results may be achieved despite of using same catalysts. Therefore, it is necessary to normalize the testing data and get approximate correlations between these experimental results. The units of photogenerated hydrogen production rate are denoted as μmol/h or μmol/h/$g_{catalyst}$. These units are universal and can be used to compare different photocatalysts under different experimental conditions.

In addition, the quantum yield, including overall and apparent quantum yields, has been widely used to evaluate the photocatalytic efficiency of PEC systems. The overall quantum yield (OQY) and apparent quantum yield (APY) are defined by equations 5 and 6 respectively.

$$OQY = N_e/N_p^{absorbed} \times 100\% \quad (5)$$

$$APY = N_e/N_p^{incident} \times 100\% \quad (6)$$

Where, the N_e is the number of reacted electrons, $N_p^{absorbed}$ and $N_p^{incident}$ denote the number of absorbed and incident photons, respectively.

Apparently, the OQY is lower than the APY due to the fact that the semiconductor photocatalysts cannot absorb all the incident photons to generate charges. Besides, the solar to hydrogen (STH) efficiency is another common indicator that has been frequently reported in the literature review, and it is defined by equation 7.

$$STH = E_{H2}/E_s^{incident} \times 100\% \quad (7)$$

Where, E_{H2} and $E_s^{incident}$ denote the energy of photogenerated hydrogen and incident solar energy, respectively.

1.1.4 Photoelectrochemical process driven by UV light

The photoelectrochemical cell was first demonstrated in Fujishima and Honda's pioneering work using an n-type TiO_2 electrode [2]. Afterwards, hydrogen production via photocatalytic splitting water has been considered as one of the most promising technologies to solve the world energy crisis [5]. Over the past four decades, considerable research has been

conducted on the R&D of semiconductor photocatalysts working in the ultraviolet (UV) light region [6-10]. Takahashi *et al*. applied a polymerized complex (PC) technique to prepare a highly active photocatalyst, $K_2La_2Ti_3O_{10}$, at various conditions and the highest activity was obtained when the sample was calcined at 1173 K for 2 h [9]. $Sr_2Ta_2O_7$ and $Sr_2Nb_2O_7$ with layered perovskite structure both exhibited photocatalytic activities under UV irradiation. When NiO was loaded as a cocatalyst with pretreatment, the $Sr_2Ta_2O_7$ photocatalyst showed a quantum yield of 12% at 270 nm [7]. Kato *et al*. also confirmed the importance of NiO-loaded cocatalyst, and the quantum yield of NiO/$NaTaO_3$:La photocatalyst was 56% at 270 nm [6]. $La_2Ti_2O_7$ with layered perovskite structure was synthesized by Kim *et al*. via PC method. The quantum yield of $La_2Ti_2O_7$ photocatalyst could be as high as 27% [8]. Maeda *et al*. prepared a non-oxide photocatalyst, β-Ge_3N_4, for photocatalytic water splitting. Loaded by RuO_2, β-Ge_3N_4 behaved the highest activity in 1 M H_2SO_4 under UV irradiation (λ<200 nm).

Even though these impressive results can be achieved by developing new materials, the overall solar-to-hydrogen (STH) efficiency is limited due to the fact that the UV spectrum only takes a minority part (just over 8%) of the whole solar spectrum. So far, one of the most challenging problems is how to harvest more visible light using the semiconductor photocatalysts. Generally, strategies to utilize visible light include creating two-step photoexcitation systems, innovating new photocatalysts via band engineering, developing novel cocatalysts, fabricating efficient photoelectrodes and constructing tandem-type PEC systems [11]. Therefore, during the recent years, the mainstream research has been focused on the development of novel semiconductor photocatalysts and advanced cell configurations and a few excellent reviews have been published [3, 11-14].

1.1.5 Two-step photoelectrochemical system driven by visible light

As shown in Figure 6, the two-step photoexcitation process is considered as an effective design to harvest visible light, and it is also known as the Z-scheme [15-17]. The PEC process is decomposed into two stages: SI and SII for hydrogen production and oxygen production respectively. The reversible redox mediators, i.e. IO_3^-/I^-, are added into the electrolyte to realize the photocatalytic water splitting under visible light. In the stage SI for hydrogen evolution, the energy of visible photons is large enough to excite the electrons jumping over the narrow bandgap. The excited electrons will then reduce the water molecules into hydrogen while the holes left at the valance band will oxidize the Red mediator into Ox mediator, i.e. $I^- \rightarrow IO_3^-$. Likewise, in the stage SII for oxygen production the photoexcited electrons in the conduction band will be oxidized by the Ox mediator in the electrolyte while the left holes will oxidize the water molecules to produce oxygen. The PEC reactions for both stages are shown in the following equations:

$$2\ H^+ + Red \rightarrow H_2 + Ox \qquad \text{for SI stage} \qquad (5)$$

$$H_2O + Ox \rightarrow \tfrac{1}{2}\ O_2 + 2\ H^+ + Red \qquad \text{for SII stage} \qquad (6)$$

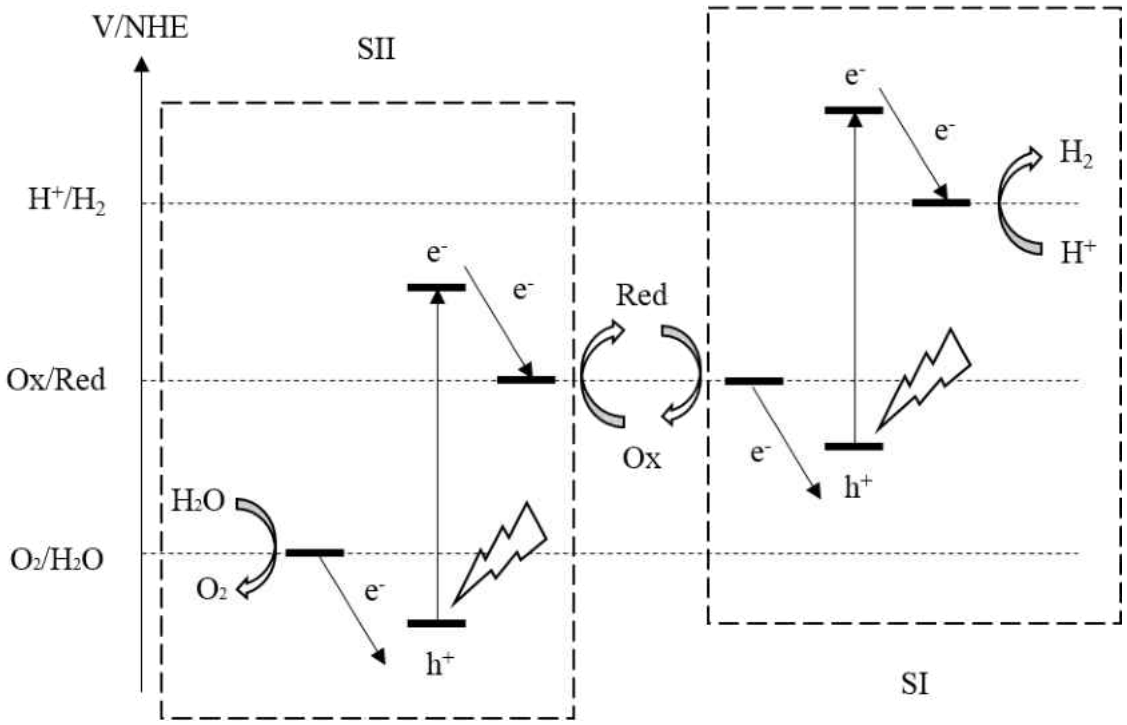

Figure 6. Schematic redox energy diagram of PEC using two-step systems [15].

Compared with one-step systems, the two-step systems reduce the energy requirements for water electrolysis and allow the photoelectrodes to harvest more visible light efficiently. Therefore, more semiconductor materials that are not applicable for one-step systems could be potentially used in Z-scheme systems. For example the band structure of WO_3 doesn't straddle the redox potentials of water electrolysis according to Figure 4 so that it cannot be used directly in one-step systems. However, the valance band of WO_3 falls below the redox potential of O_2/H_2O and the photoexcited holes are able to oxidize the water molecules into oxygen. Meanwhile, if the reversible redox mediators can be reduced by the photoexcited electrons from the conduction band, WO_3 will be suitable for the photoanode materials in Z-scheme systems. Similar material candidates that can utilize the visible light are TiO_2 (rutile), $FeTiO_3$, $MnTiO_3$, Fe_2O_3 and SnO_2 as shown in Figure 4. Another advantage of the two-step system is that

hydrogen and oxygen can be produced separately by adding a gas filter. The filter only allows the transportation of redox mediators in the electrolyte and blocks the recombination of gas products. It is impossible for the one-step system of PEC to collect different gases independently when the hydrogen and oxygen are simultaneously photogenerated on the surface of semiconductor particles.

The two-stage PEC system was first proposed by Bard in 1978 [18]. The creative design is innovated by the biological photosynthesis that carries out the water oxidation and the CO_2 reduction. After that, the mainstream research effort has been focused on the developing new photoelectrode materials and reversible redox mediators. Sayama *et al*. developed the RuO_2-WO_3 photocatalysts that were suspended in H_2SO_4 solution with redox mediators of Fe^{3+}/Fe^{2+}. When irradiated by visible light at less than 460 nm, the WO_3 particles could oxidize the water molecules into oxygen and reduce Fe^{3+} into Fe^{2+}. Meanwhile, hydrogen gas was evolved and the Fe^{2+} was oxidized back to Fe^{3+} at the surface of RuO_2 catalyst with UV irradiation at less than 280 nm [19]. Bamwenda *et al*. obtained higher initial oxygen production rates but lower long term yields using WO_3 photocatalysts when the $Fe_2(SO_4)_3$ was replaced by $Fe(NO_3)_3$ or $FeCl_3$ as a source of electrons acceptors [20]. The aqueous suspension of TiO_2 and Ag_2O was proved to have the ability of PEC process with pH adjustment of NaOH [21]. With visible light of less than 630 nm, Ag_2O was reduced into Ag when the oxygen is produced at pH<7.4. If the pH was increased up to 12.3-12.6, the Ag was oxidized back to Ag_2O with the photogenerated hydrogen. Tennakone *et al*. found with UV light irradiation, the CuCl suspension in dilute HCl could be oxidized to $CuCl_2$ when producing photogenerated hydrogen. The $CuCl_2$ can be reduced back to CuCl by photocatalysts, i.e. $SrTiO_3$, TiO_2 and WO_3, with oxygen evolution [22]. TiO_2 was also found to enable photogeneration of hydrogen when ground with MnO_2 in an alkaline solution.

TiO_2 suspension with MnO_4^{2-}, on the other hand, was observed to produce hydrogen when irradiated by a 90 W medium pressure mercury lamp [23]. When loaded by Pt, TiO_2 suspension with I_3^- could reduce the water molecules into hydrogen under visible light. The PEC reaction wouldn't proceed until the I_3^- concentration reached a certain level to overcome the back reaction. The highest reaction rate was obtained at pH of 2.4 [24, 25]. Br^- could also be used as the electron donor for the hydrogen production on the surface of Pt loaded TiO_2 [26]. For the other PEC stage, pure TiO_2 particles could act as the photocatalyst to oxide water molecules into oxygen with visible light if the Fe^{3+} was used as the electron acceptor [26-28]. Abe *et al.* successfully demonstrated the PEC water splitting with visible light irradiation ($\lambda > 420$ nm) using Z-scheme systems. Pt-$SrTiO_3$:Cr/Ta and Pt-WO_3 are used as the photocatalysts for hydrogen and oxygen evolutions respectively with the reversible redox mediators of IO_3^-/I^- [15-17]. Trari and co-workers successfully synthesized a series of photocatalysts for hydrogen production driven by visible light irradiation. These semiconductor combinations consisted of p-$CuMnO_2$/n-Cu_2O [29], p-$CuCrO_2$/n-Cu_2O [30], p-$CuAlO_2$/n-TiO_2 [31], p-$CuFeO_2$/n-SnO_2 [32], p-$ZnFeO_4$/n-$SrTiO_3$ [33]. The corresponding redox mediators included S^{2-}/S_n^{2-}, SO_3^{2-}/SO_4^{2-}, $SO_3^{2-}/S_2O_6^{2-}$ [29-33]. Jang and his Korean research group also found p-$AgGaS_2$/n-CdS [34] and p-$AgGaS_2$/n-TiO_2 [35] showed high photocatalytic activity for hydrogen evolution under visible light (λ>420nm). The hole scavengers used in the experiments were Na_2S, Na_2SO_3 [34, 35].

As mentioned above, most researchers focused only on the half PEC reactions, i.e. either hydrogen or oxygen evolution. This results from the fact that the two-stage reactions have different favorable pH and redox concentrations. For example, the hydrogen evolves more readily with lower pH and higher concentration of reduction mediators. On the other hand, oxygen generation prefers to higher pH and higher concentration of oxidation mediators. Even

though the hydrogen favorable conditions can facilitate the hydrogen production rate, it will suppress the oxygen evolution. Besides, in the most cases of Z-scheme system, the backward reactions can potentially proceed. For example, due to the redox potential difference as shown in Figure 6, the photoexcited electrons in the SI stage are more likely to reduce the oxidation mediators instead of water molecules into hydrogen. Meanwhile, the photoexcited holes in the SII stage tend to be reduced by reduction mediators instead of water molecules for oxygen evolution. Therefore, it's much more difficult to achieve the hydrogen and oxygen production simultaneously for the two-stage PEC systems. Furthermore, due to the two stages of PEC reactions, the Z-scheme systems require much more photons to split water molecules. This is also considered as a disadvantage compared with simple one-step photoexcitation systems. To realize the two-stage PEC systems, a high selectivity for forward reactions is necessary for future research and development.

1.1.6 Tandem photoelectrochemical system driven by visible light

Another effective design to harvest visible light is to use the tandem PEC system. As shown in Figure 7 (a) and (b), traditional PEC configurations include either n-type photoanode system or p-type photocathode system. The fundamentals of former configuration have been explained. In the latter configuration, the p-type semiconductor serves as the photocatalyst. With light irradiation, excess of holes are excited into the valance band leaving the electrons in the conduction band. The water molecules are then reduced into hydrogen by the electrons on the material surface while the oxygen is generated by the oxidation of water on the counter electrode. In both configurations of n-type photoanode and p-type photocathode, a short wavelength of light source, i.e. UV, is necessary to supply enough excitation energy for the majority carriers. Besides, an external bias between the photoelectrodes is usually applied due to insufficient

photogenerated potential. However, in terms of the system energy consumption and efficiency, required extra electrical energy is undesirable. Thus, innovated by the heterogeneous photocatalytic systems, the tandem PEC configuration is proposed as shown in Figure 7(c). The tandem system consists of an n-type photoanode and an appropriate p-type photocathode. The two electrodes have sufficient high band level and eligible for hydrogen and oxygen production respectively when irradiated by visible light. Other tandem PEC system that includes a semiconductor photoelectrode and a solar cell to supply bias potential will not be discussed here.

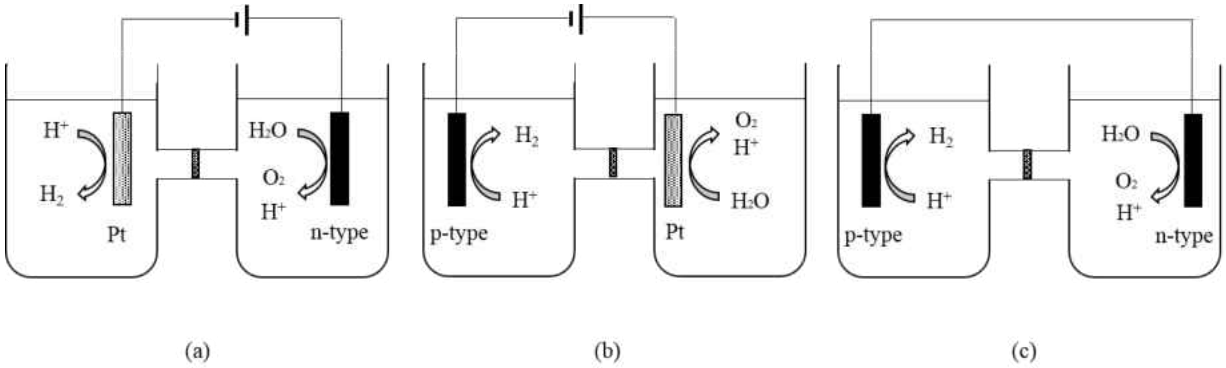

Figure 7. Schematic diagram of PEC systems: (a) n-type photoanode, (b) p-type photocathode, and (c) tandem system [11].

The tandem PEC system is based on two photosystems that are connected in a series as shown in Figure 8. The n-type semiconductor serves as the photoanode to absorb the irradiated photons and then create photoexcitation electrons and holes in conduction band and valance band respectively. The holes will oxidize the water molecules into oxygen as equation (2). The conduction-band electrons are fed into the valance band of p-type photosystem to combine with the holes that has been photoexcited. Hydrogen is generated due to the reduction ability of electrons at the surface of p-type photocathode. The whole process is close analogy to the Z-scheme system of two-stage PEC. There are three material criteria for the photoelectrode

selection. First, the bandgap of photoanode should straddle over the redox potential of O_2/H_2O to enable the oxidation of water molecules. Similarly, the bandgap of photocathode needs straddle over the redox potential of H^+/H_2 to enable the photogenerated hydrogen. Last, the energy level of n-type conduction band should be higher than that of p-type valance band, so that photoexcited electrons in the p-type can be compensated by those fed from n-type conduction band. The overall PEC process can be driven by visible light if appropriate n-type and p-type semiconductors are selected as the photoelectrodes.

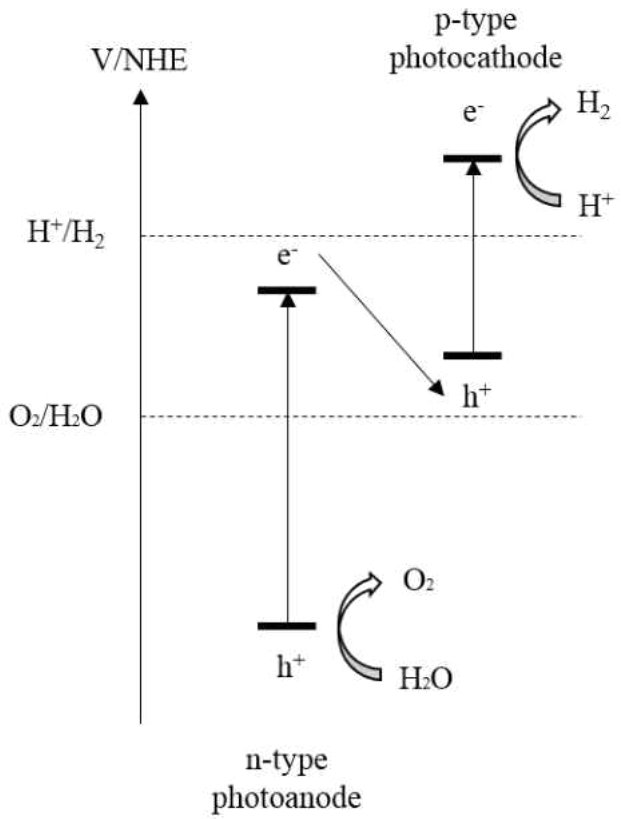

Figure 8. Electron-flow fundamentals of tandem PEC system [11].

The most challenging problem for developing tandem PEC systems is to find new materials and semiconductor combinations with high STH efficiency. Nozik constructed a p-GaP/n-TiO_2 tandem PEC diode that was much more efficient than single p-GaP or n-TiO_2

devices for water splitting [36]. Because the tandem heterojunction could significantly suppress the recombination of photoexcited hole-electron pairs and thus facilitate the charge separation during the PEC process. Hu *et al*. developed a p-Cu_2O/n-WO_3 tandem system by coupling the electrodeposited Cu_2O powders with WO_3 in suspensions. It was found that the crystalline texture played a very important role in hydrogen production rate of tandem systems and the p-Cu_2O with [1 1 1] orientation could be a promising photocatalyst for photogenerated hydrogen [37]. Kim *et al*. fabricated a bulk heterojunction structure promoted by Pt and RuO_2, the photocatalytic configuration was RuO_2/n-$MgFe_2O_4$/p-$CaFe_2O_4$/Pt. With visible light irradiation (λ>420nm), the PEC devices achieved a quantum yield of 10.1% for hydrogen evolution [38]. p-$CaFe_2O_4$/n-$PbBi_2Nb_{1.9}W_{0.1}O_9$ was proved as a photocatalytic nanodiode with high efficiency. Experimental results showed a quantum yield of oxygen evolution of 38% with visible light irradiation [39]. Low-cost photocatalysts, i.e. WO_3 [40] or Fe_2O_3 [41], could also serve as the top electrode of tandem PEC system with combination of nanocrystalline TiO_2. The top electrodes were responsible for the absorbing the blue part of solar spectrum while the TiO_2 electrode could capture the green and red parts.

Compared to the two-stage photocatalytic system, the tandem PEC system doesn't require the addition of redox mediators into the electrolyte. Thus, the backward reactions of Z-scheme system can be avoided and the system complexity decreases. Besides, the photocatalyst semiconductors can be fabricated into electrodes instead of powder suspension, which is more convenient for gas collection. However, to satisfy the three material criteria as mentioned above, there are more requirements of the manufacturing of the semiconductor photocatalysts. It is very necessary to develop new catalytic materials for tandem PEC system.

1.1.7 Hybrid photoelectrochemical system driven by visible light

In addition to the Z-scheme systems of two-stage and tandem PEC, the hybrid catalytic system has been shown as another way of improving the PEC efficiency. The system includes a variety of combinations of p-type, n-type semiconductors and metals with different fabrication configurations. Generally, the heterojunction structure of semiconductor combinations can effectively separate the photogenerated electro-hole pairs and suppress the recombination process. The catalytic metals, i.e. Pt and Au, are loaded onto the surface of heterojunction that can extremely enhance the photocatalytic activity. Therefore, the overall hydrogen production efficiency is significantly dependent on the catalytic materials and configurations.

The CdS is a well-known photocatalyst driven by visible light. However, this semiconductor material is unstable and photocorrosive because of self-oxidation by the photogenerated holes in the valance band. Therefore, it's necessary for CdS to be embedded in various inert matrices, i.e. TiO_2, ZnO etc. Figure 9 illustrates the PEC mechanism of CdS/(Pt-TiO_2) hybrid photocatalytic system. The Pt was first photodeposited on the TiO_2 particles which was followed by the deposition of CdS [42]. With visible light irradiation, the photoexcited electron in CdS will jump over the bandgap (2.5 eV) to the conduction band. Due to the energy level difference of conduction bands between two semiconductors, the electrons tend to transfer to the conduction band of TiO_2 and avoid to be recombined with the valance band holes. The electrons continue moving to the Pt catalyst where the hydrogen evolves by reducing the water molecules. On the other hand, the holes left at the valance band of CdS are responsible for oxidizing the water molecules into oxygen.

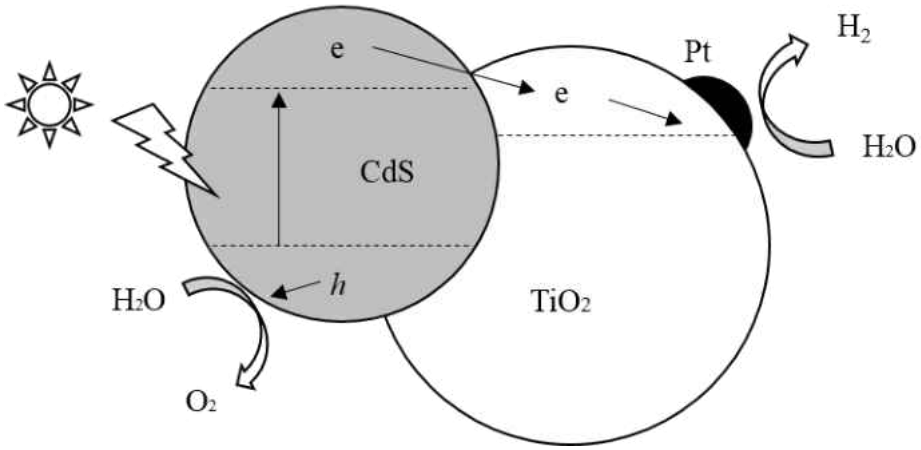

Figure 9. Illustrative diagram of the electron transfer in CdS/(Pt-TiO_2) hybrid photocatalytic system [42].

As mentioned above, the performance of the hybrid catalytic system is determined by the material combinations and system configurations. The visible-light driven hydrogen production rate of CdS/(Pt-TiO_2) system ranged 6~9×10^{-3} mol/(h·g), that was higher by a factor of 3~30 than other configurations, i.e. Pt-(CdS/TiO_2), at the same testing conditions [42]. Since the semiconductor combination of the hybrid catalytic system has been proven as an effective way of separating photogenerated carriers, many other different combinations of PEC systems have been developed. Silva and co-workers developed a series of hybrid photocatalytic systems based on CdS, including cubic-phase CdS (c-CdS) and hexagonal CdS (hex-CdS). After comparing the hydrogen production rate of different combinations under visible light, the photocatalytic activity of CdS based systems were found to be c-CdS/Pt/hex-CdS > Pt/c-CdS/hex-CdS > Pt/hex-CdS > hex-CdS > c-CdS/hex-CdS > quantum-sized c-CdS. It was concluded that the potential gradient formations at the material interface were necessary to achieve the efficient charge separation and transfer [43]. Tada *et al*. constructed the anisotropic CdS-Au-TiO_2 heterojunction with all three components spatially fixed. The system shoed an impressive photocatalytic activity that far

exceeded either single or two-component system. This was explained by the two-step excitation of TiO_2 and CdS that could drive the vectorial electron transfer [44]. Wang *et al*. synthesized a novel composite PEC system, Zn-doped Lu_2O_3/Ga_2O_3, for stoichiometric water splitting with UV irradiation. The composite semiconductor was proved to be a promising approach for high efficient catalyst due to the ability of charge separation [45]. Similarly, Pd- $TiO_{2-x}N_x$-WO_3 showed a good performance for photogenerated hydrogen production with the S^{2-}/SO_3^{2-} as the redox mediators [46]. Other hybrid photocatalytic systems that has been approved successfully includes Cr-doped $Ba_2In_2O_5/In_2O_3$ [47], MWNT-TiO_2 [48] etc.

Compared to Z-scheme systems of two-stage and tandem PEC, the hybrid photocatalytic system can achieve higher hydrogen or oxygen production rate, thus increasing the STH efficiency. In addition, the backward reactions in the two-stage systems can be avoided since the redox mediators are not necessary for the hybrid PEC system. However, fabrication complexity may increase due to the additional deposition of active-site materials for hydrogen evolution.

1.1.8 Summary and prospects

The photoelectrochemical has been proven as a promising technique for the hydrogen production in a long-term pathway. Currently, the highest apparent quantum yield of PEC system, to our best knowledge, was reported to be 75% with the light wavelength ranging 350 to 500 nm [49]. The 3D organic/inorganic material was used as the photoelectrode based on CdS-IO (inverse opal) networks and Nafion polymers. However, the overall STH efficiency has been still quite low with consideration of the whole spectrum. The best experimental results are reported from a $BiVO_4$-perovskite tandem PEC system with STH efficiency of 6.2% [50]. This is still far from the STH efficiency target for practical application (15%). Therefore, it is necessary to develop the cost-effective and high efficient photocatalyst for PEC systems under visible light.

For the visible-light-driven photocatalysts, the bandgap needs fall into the energy range between 1.6 eV and 3.0 eV in addition to straddling the redox potentials of hydrogen and oxygen. Thus, bandgap engineering, i.e. ion doping, semiconductor sensitization and solid solution, can be applied to modify the band structure and make it suitable for visible-light-active systems. Other factors such as chemical composition, electronic properties, crystallinity, surface state and morphology, can determine the band structure and need to be further investigated in great details. Besides, adding the redox mediators into the electrolyte is another effective way of increasing the STH efficiency. Traditional sacrificial reagents include I^-/IO_3^-, S^{2-}/S_n^{2-}, SO_3^{2-}/SO_4^{2-}, $SO_3^{2-}/S_2O_6^{2-}$, Fe^{3+}/Fe^{2+} etc. These electron donors/acceptors tend to participate into the half-reactions and make the hydrogen and oxygen generation separately. This can prohibit the undesirable charge recombination and facilitate the production rate. However, the concentration of sacrificial reagents should be precisely controlled according to different PEC systems to avoid backward reactions. Furthermore, noble metals, i.e. Pt and Au, can be deposited on the photocatalysts and used as the active site for hydrogen evolution. The application of metal catalysts is beneficial for photogenerated electron transfer and can effectively suppress the backward reaction of hydrogen and oxygen molecules. Nevertheless, the noble materials are too expensive and not economic for practical application despite of high catalytic efficiency. Alternative catalysts, such as non-noble metals and derived metal-based compounds, need to be developed as the substitutes for Pt or Au.

1.2 Solid-state photoelectrochemical cells

For a traditional photoelectrochemical system, liquid electrolyte is necessary to supply the electrochemical environment for redox reactions and ion transportation. The PEC process is significantly dependent on the aqueous electrolyte conditions such as the pH and concentrations

of sacrificial reagents. However, it is not easy to find the appropriate liquid electrolyte for a specific photocatalyst with consideration of the material properties, redox potential, Fermi energy alignment etc. To overcome those problems, solid-state PEC systems have recently attracted a lot of research interest [51-56]. All the components, including electrolyte, of the innovative systems are solid materials. The concept of solid-state photoelectrochemical water splitting was independently proposed by Zhang [57] and Ye *et al*. [51] in 2013, though with different cell configurations. In Zhang's original concept, a solid oxide photoelectrochemical cell (SOPC) was proposed, which integrated a solid oxide electrolysis cell (SOEC) and a photovoltaic (PV) cell. However, only a small output voltage (around 100 mV) was achieved using TiO_2/Pt Schottky diode based cells in the preliminary research [57]. Based on a heterojunction between a light absorber and a mixed ionic and electronic conducting (MIEC) oxide, the integrated high temperature PECs proposed by Ye *et al.* absorb both thermal and photon energy from concentrated solar light. Specifically, the light absorber semiconductor is able to separate electron-hole pairs, while the MIEC oxide conducts the excited electrons and oxygen ions at a temperature range from 400 °C to 700 °C [51, 52]. The feasibility of high temperature photoelectrochemical water splitting was first experimentally demonstrated by Brunauer *et al.* recently, using a solid oxide photoelectrochemical cell (namely SOPEC) [53, 55]. An open circuit voltage (V_{oc}) of 920 mV was achieved using a $LaSrCrO_3/SrTiO_3$ p-n junction diode at 400 °C under ultraviolet (UV) light. Then an electrochemically oxygen pump driven by UV light was demonstrated using the SOPECs [55]. The same group reported that cells with configurations of $SrTiO_3$/YSZ and TiO_2/YSZ were able to store oxygen upon UV light from 360 °C to 460 °C. Their further experiments showed that oxygen vacancies in $SrTiO_3$ or TiO_2 were filled during UV illumination, leading to a battery-type voltage of 30-70 mV at 460 °C [53,

54]. To date, both the theoretical and experimental research on high temperature photoelectrochemical water splitting is extremely limited, since it is a newly conceived concept.

The solid-state PEC systems that have been developed so far can be divided into three categories, the system based on proton-exchange-membrane (PEM), the mixed ionic and electronic conductor (MIEC), and integrated PV/EC (electrolysis cell).

1.2.1 Proton-exchange-membrane based PEM system

Xu *et al.* replaced the traditional aqueous electrolyte with a proton conducting hydrated Nafion polymer membrane and fabricated the sandwiched configuration of PEM system as shown in Figure 10 [56]. The system consisted of Pt/C-based cathode, Nafion electrolyte, and photoanode that was made by either thermally prepared TiO_2 film on Ti foil (T-TiO_2) or highly ordered TiO_2 nanotubes (TNT) with different lengths. The working principles are similar to those of traditional PEC systems as described in section 1.1.1. The difference is that only photoanode is immersed in the liquid, either pure water or Na_2SO_4 solution. The short-circuit photocurrent of PEC cell was characterized under the UV-rich light with the intensity of 4 mW/cm^2. The PEC system with TNT electrode exhibited a better performance with 230 μA/cm^2 and 400 μA/cm^2 at pure water and Na_2SO_4 (aq), respectively. Due to the high ionic conductivity of the salt solution, the APY of solid-state PEM system can reach as high as 33%. Further study needs to be focused on the utilization of visible-light-driven photoanode, improvement of solid electrolyte and hydrogen production in the cathode chamber.

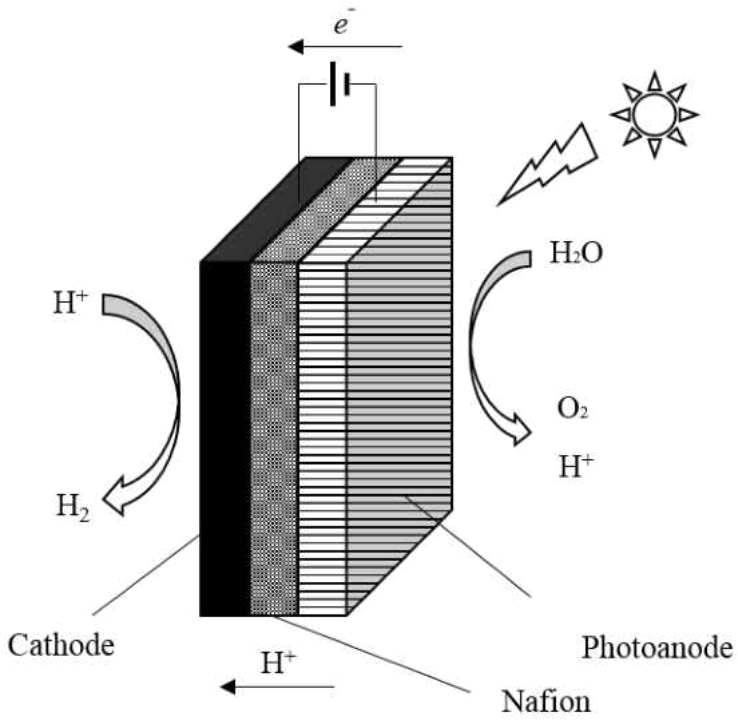

Figure 10. Schematic diagram of proton-exchange-membrane based process [56].

1.2.2 The MIEC based PEC system

Recently, MIEC based solid-state PEC systems have been developed independently by both J. Fleig's [53, 54] and C. Chueh's [51, 52] research groups. This is innovated by the fact that solid electrolyte, typically YSZ, has been successfully used in solid oxide fuel cells (SOFC) or electrolysis cells (SOEC) at high temperature. The solid oxide photoelectrochemical cells (SOPEC) of J. Fleig's research group is shown in Figure 11. The solid electrolyte, YSZ, was pulsed-laser deposited on the MIEC substrate, $SrTiO_3$ or TiO_2. The porous Pt counter electrode was then applied on the YSZ surface via paste brush. The metal grid was deposited on the MIEC electrode as the current collector. The whole system was operated at temperature of 360-460 °C. With UV irradiation, the SOPEC cell exhibited a build-up battery voltage of more than 300 mV. After turning off the light source, the electric potential decayed slowly. This is caused by two

mechanisms of UV-induced oxygen incorporation into the MIEC, the electrochemical process and photovoltaic process. Generally, when the UV is turned on, the majority of existing oxygen vacancies of MIEC tend to be filled leading to the charge state of SOPEC. On the other hand, after UV off, the oxygen ions tend to be released from MIEC leading to the discharge currents. Thus, the SOPEC cell based on the MIEC can be considered as the light-charged oxygen battery, which is similar to the electrical charging of Lithium-ion battery by intercalating Li into carbon.

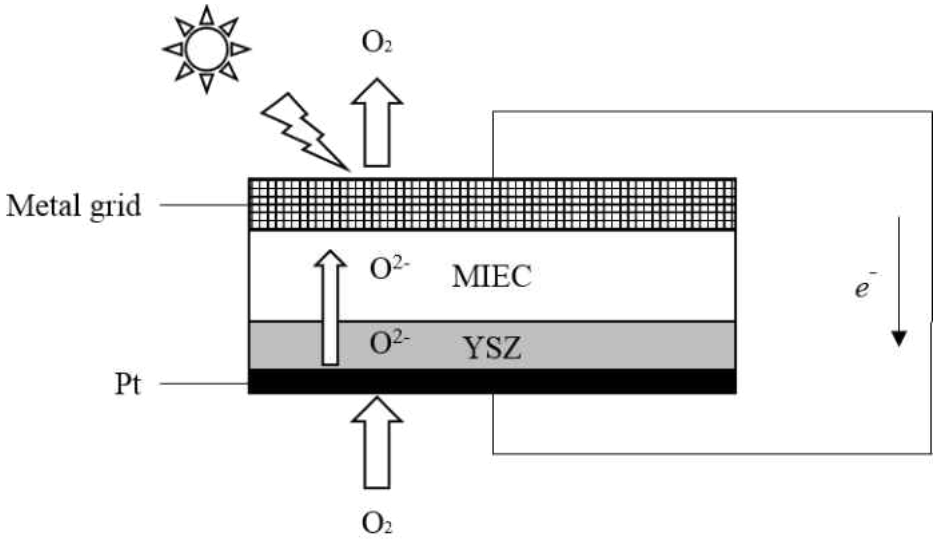

Figure 11. Schematic diagram of solid oxide photoelectrochemical cells used as the light-charged oxygen battery [51-54].

Another configuration of MIEC based PEC system was developed by C. Chueh and his co-workers [51, 52] as shown in Figure 12. The MIEC should have a sufficiently large bandgap (>3eV) to allow most light spectrum to be utilized by light absorber. Many ceria-based and ferrite-based materials can meet such requirement. The lighter absorber should have the bandgap ranging from 2.0 eV to 3.0 eV and maintain stable performance at elevated temperature. Fe_2O_3, $SrTiO_3$, and TiO_2 could be potential material candidates. Similar to the SOEC materials, YSZ

and LSCF can be used to fabricate electrolyte and anodes, respectively, because these materials can exhibit excellent performance at high temperature. The whole system is projected to work between 400 °C to 700 °C. With illumination of visible light, 97% of the whole spectrum will pass through the MIEC due to the large bandgap. Incident photons with higher energy than the bandgap of light absorber can excite the electrons into the conduction band leaving the holes at the valance band (step I in Figure 12). The photoexcited electrons with extra energy can thermalize and heat up the absorber rapidly. Despite the energy barrier at the absorber/MIEC interface, the fully thermalized conduction-band electrons can be thermionically emitted into MIEC conduction band (step II). Meanwhile, the valance-band holes tend to migrate to anode due to diffusion (step III). The water molecules are reduced by the emitted electrons to produce hydrogen and oxygen ions at the MIEC surface (step IV). The oxygen ions then diffuse through the solid electrolyte at high temperature to combine with the migrated holes at the anode (step V). Eventually, the oxygen gas can be evolved at the anode surface due to the oxidization ability of the photoexcited holes (step VI). Compared to the conventional PEC cells, the proposed MIEC heterojunction integrates the charge excitation, separation, emission, transportation, and gas generation into a single device that remarkably decreases the system complexity. A temperature-dependent photoelectrode model was developed to simulate the MIEC based PEC system [51]. It was concluded that an efficiency of 17% and 11% can be achieved at 450 °C and 600 °C respectively from the devices with the absorber bandgap of 2.0 eV and uphill band offset of 0.3 eV.

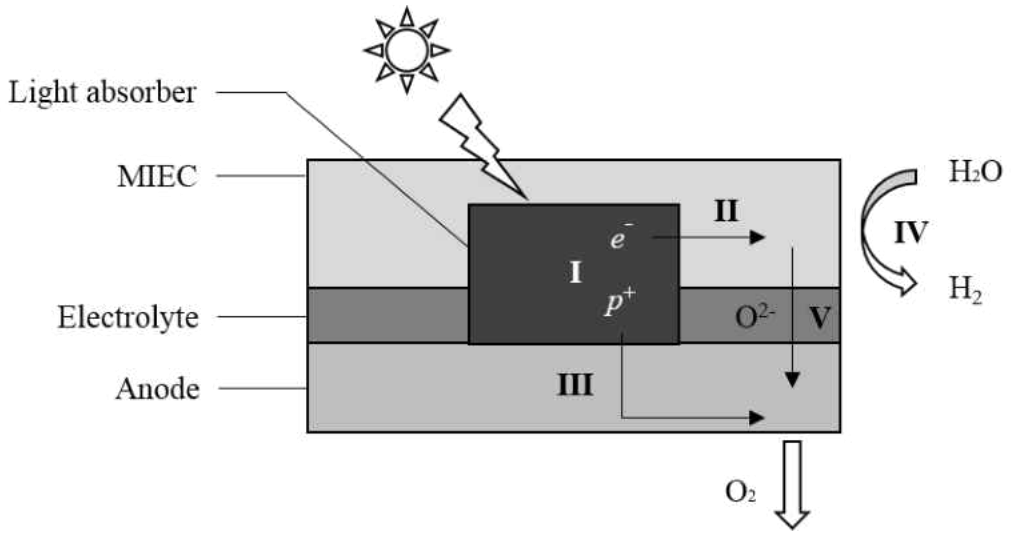

Figure 12. Schematic diagram of MIEC based solid-state PEC system designed by Ye *[51]*, I. Charge separation, II. Electron transfer, III. Holes migration, IV. Water splitting, V. Oxygen ion transfer, VI. Oxygen generation [51, 52].

1.2.3 Integrated-PV/EC PEC system

Instead of simply combing the PV and EC cells, the two subsystems can be integrated into a single device, named SOPEC [53, 55], as shown in Figure 13. In the configuration, the PV part is based on the LSCr/$SrTiO_3$ heterojunction and the design of EC part is symmetric with two porous LSF electrodes and TZP electrolyte. The PV part has a shared bottom electrode that acts as the top electrode of EC part. Thus, the electric energy produced from the PV cell can be directly used by the EC cell for water electrolysis. This solid-state PEC cell is operated between 400 °C and 500 °C under 365 nm UV light. The PV part exhibited an open circuit voltage (OCV) of 920 mV at 400 °C. Even though this electric potential is not enough for water electrolysis of EC part, it can act as a driving force to pump the oxygen from low partial pressure (EC side) to

high partial pressure (PV side). The experimental results demonstrate the feasibility of light-driven chemical storage by the SOPEC.

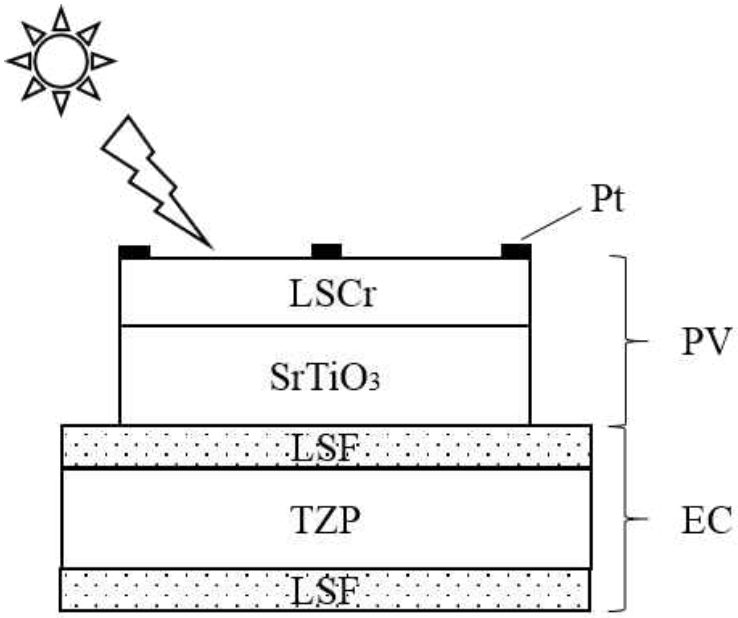

Figure 13. Schematic diagram of PV/EC integrated solid-state PEC system [53, 55].

1.2.4 Summary and prospects

Compared to conventional PEC systems, the solid-state PEC systems have a huge potential to achieve the high STH efficiency. These new PEC configurations have several advantages over the traditional PEC systems. First, the system complexity will decrease because the solid-state PEC process is generally a one-step approach so that the Z-scheme systems and sacrificial reagents become unnecessary. Second, the backward reaction can be avoided. The hydrogen and oxygen are evolved on the separate electrodes instead of the particle surface. Thus, it is beneficial for collecting the gases while suppressing the recombination process. Last but not

least, the solid-state PEC systems can be operated at elevated temperature. This will bring even more benefits such as more absorption of visible light, low requirement of photovoltaic potential, reduced threshold of water electrolysis, faster kinetics and application of cost-effective catalysts. However, since the solid-state PEC is a new technique that was proposed only 5 years ago, there hasn't been any report that can successfully demonstrate the photogenerated hydrogen. To achieve the goal of STH via solid-state PEC devices, scientific research should focus on the following areas. First, the material candidates should maintain the electrochemical properties and stability at elevated temperature. It means that the selected semiconductor material has a high melting point and cannot be further oxidized. Second, the configuration design needs to be improved. The selected p-type and n-type semiconductors are able to form a strong p-n junction and maintain an acceptable performance at elevated temperature. Currently, the most effective configuration of solid-state PEC systems is the integrated PV/EC with an OCV of 0.92 V at 400 °C and this is still not enough for water electrolysis. Third, the bandgap theory of semiconductors at high temperature is necessary. The bandgap of selected semiconductors usually narrows with increasing temperature. Several studies have been performed to quantify the effect of temperature on the band gap energy of TiO_2 [58-64] based on the following correlation:

$$E_g(T) = E_g(0) - \frac{\alpha T^2}{T + \beta} \quad 8)$$

Where, $E_g(0)$ is the bandgap at absolute temperature of 0 K, T denotes the temperature (K), α and β are constants independent on the temperature change. It was predicted that the bandgap of TiO_2 will narrow down to 1.7-2.3 eV as temperature rises to 1000 K [58-64]. However, the energy levels of the conduction band and valance band still remain unclear.

Furthermore, similar studies or experiments need to be conducted on other semiconductor candidates, such as $SrTiO_3$, Fe_2O_3 etc.

1.3 Solid oxide electrolysis cells

As shown in Figure 1, the high-temperature electrolysis pathway is a long-term technique for hydrogen production for central facilities. The process can be realized by using SOECs. Reversibly, the hydrogen product can generate electricity with combination of air through SOFCs, which is exactly the same device as SOECs. Figure 14 depicts the future energy infrastructure with various scenarios for producing renewable hydrogen and electricity. The hydrogen energy system plays a very important part as a conversion energy carrier. Specifically, the excess of renewable energy can be converted into hydrogen as the energy storage by the electrolyzer. Similar to the gasoline, the hydrogen then is compressed in the tanks and transported to the places where there is a need, i.e. synthesizing natural gas and ammonia. Besides, with hydrogen as the feedstock, fuel cells can act as the power plants that are integrated into the electric grid when there is a peak demand.

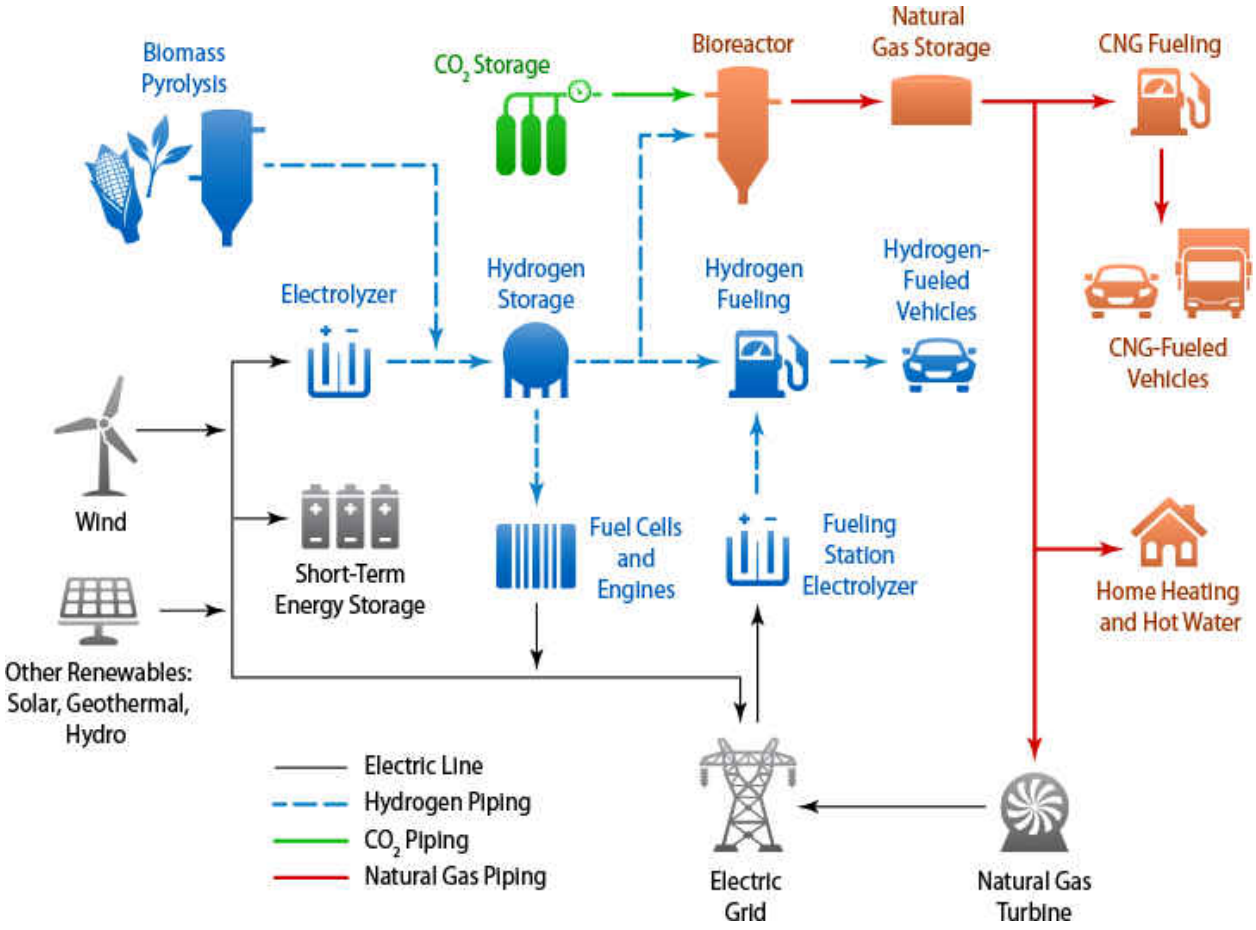

Figure 14. The renewable hydrogen production and electricity/hydrogen cogeneration infrastructure system proposed by national renewable energy laboratory (NREL) [65].

1.3.1 History

Water electrolysis for production of hydrogen and oxygen is the reverse chemical process of the hydrogen fuel cell. The word "electrolysis" was introduced by Faraday in 19th century, and the English scientist provided a mathematical explanation of his two laws of electrolysis in 1834. It was not until the 'HotElly' project in 1980s that SOEC attracted worldwide interest. After theoretical and experimental analysis, Doenitz *et al*. reported that the thermal efficiency of electrolysis at elevated temperature can be as high as 40-50% [66]. The German researchers first tested a single SOEC using tubular configuration and a typical current density of 0.4 A/cm^2 was

achieved when the cell was operated at 900 °C with an applied voltage of 1.3 V. Subsequently, a 10-cell tubular stack was assembled using modular electrolysis units to investigate the feasibility of high production rate of H_2 [67]. Furthermore, a concept of 3.5 kW prototype plant was demonstrated at the end of the German project [68]. After that, the worldwide R&D of solid-oxide focused on solid oxide fuel cells (SOFCs), and research on innovative materials, thermodynamic modeling, degradation issues etc. has increased remarkably in recent two decades. Recently, the global energy and environment crisis have revoked the R&D of SOECs due to the potential of hydrogen economy. Many research groups and companies all over the world have been focusing on efficiently producing hydrogen, oxygen as well as syngas in a large scale using SOECs. In the Idaho National Laboratory (INL), SOEC research scope included fundamental mechanism, small-scale experiments, CFD simulation, system modeling, and technology demonstration. Under the DOE Nuclear Hydrogen Initiative (NHI), the scale of test activities ranged from button cell (1.5 W) to multiple-stack module (12 kW) from 2003 to 2009 [69]. During FY09, DOE selected High-Temperature Electrolysis (HTE) as the primary technology of nuclear hydrogen production and from FY10 to FY12, HTE research was funded under the Next Generation Nuclear Plant (NGNP) in INL. In European Institute for Energy Research (EIFER), many long duration experiments of SOECs including single cells and assembled stacks have been conducted since 2004 under the European project Hi2H2. With current densities of 0.4-1 A/cm^2, the lifetime of these tests ranged from 1000 to 9000 hours and finally a lifetime of more than 20000 h was estimated for the single cells with active area of 45 cm^2 [70]. Researchers in Technical University of Denmark (DTU) Energy have been working on the performance and durability of SOECs in the past decade. The improvements consisted of the increase of anode performance, purification of inlet streams, upgrade of processing route and

optimization of fuel electrode structure. As a result, the degradation rate and area specific resistance have been decreased from 40%/kh to 0.4%/kh and from 0.44 Ωcm^2 to 0.15 Ωcm^2 respectively at -0.5 A/cm^2 and 750 °C [71]. Aimed at increasing the performance, durability and reliability as well as reducing the cost, the French researchers in Alternative Energies and Atomic Energy Commission (CEA) designed low-weight SOEC stacks with 3 to 25 cells. Based on the 25-cell stack, H_2 fuel production of 1.2 Nm^3/h was achieved 700 °C with an overall electrical consumption of 3.9 kWh/Nm^3 [72]. In China, the R&D of HTE technology started from 2005 in Institute of Nuclear and New Energy Technology (INET) of Tsinghua University. SOECs technology was selected as one of the approaches in high temperature gas-cooled reactor (HTGR) project that was aimed at efficiently utilizing the nuclear process heat in the future. Currently, H_2 production of 274 L/h in the lab scale has been achieved and coupling such key technology with HTR-10 in the pilot scale is underway [73]. Besides, Chinese researchers in Ningbo Institute of Material Technology and Engineering (NIMTE) have achieved H_2 production rate of 360 NL/h using a 30-cell SOE stack operated at 750 °C under a current density of -0.5 A/cm^2 with 4.06%/kh degradation rate [74]. To reach the DOE target of 78% water electrolysis efficiency based on low heating value (LHV) before 2020, Versa Power System have been developing SOECs technology which is capable of operating at ultra-high current density of more than 3 A/cm^2 with an upper voltage limit of 1.6 V. By increasing the fuel electrode porosity, a performance of over -6 A/cm^2 was delivered in a single SOEC at 78% efficiency (LHV) and a degradation rate of 1.8%/kh was demonstrated with the current density of -3 A/cm^2. Moreover, the current density of -3 A/cm^2 was achieved for a 20-cell stack at operation voltage of 1.493 V with 83.9% water electrolysis efficiency (LHV). NASA scientists have designed a CES plant using combination of SOECs and Sabatier Reactor for human

exploration of Mars. With inlet CO_2 from Mars atmosphere (95% CO_2) combined with steam and H_2, the plant could produce pure O_2 for human life support as well as CH_4 for Earth-return propellant [75, 76]. By replacing the metal interconnect with Ca-doped $LaCrO_3$ ceramic, the power density of SOECs increased significantly from 0.5 to 4.1 kW/L, leading to a remarkable reduce of transportation cost for Mars exploration [77]. In addition, significant progress has been achieved on SOECs in the rest of the world such as Italy, Switzerland, Korea, Japan, etc. [78-81].

1.3.2 Operating principles

The electrochemical reactions at SOECs are inverse to those at SOFCs as shown in Figure 15. Due to the opposite cell polarizations, the roles of cathode and anode are interchanged. Specifically, for steam electrolysis, the water vapor is reduced to hydrogen at cathode, while the other product, oxygen ions, is transferred through the electrolyte and then oxidized to oxygen molecules at anode. The reactions at fuel electrode (cathode) and oxygen electrode (anode) are as follows:

$$H_2O + 2\,e^- \rightarrow O^{2-} + H_2 \qquad \text{cathode} \tag{9}$$

$$O^{2-} \rightarrow \tfrac{1}{2}\,O^2 + 2\,e^- \qquad \text{anode} \tag{10}$$

$$H_2O \rightarrow \tfrac{1}{2}\,O^2 + H_2 \qquad \text{overall} \tag{11}$$

The SOECs is also eligible for operating co-electrolysis. Compared to the water electrolysis, the half reaction of co-electrolysis at cathode is different while the other at anode side remains the same.

$$CO_2 + 2\,e^- \rightarrow O^{2-} + CO \qquad \text{cathode} \qquad (12)$$

$$O^{2-} \rightarrow \tfrac{1}{2}\,O^2 + 2\,e^- \qquad \text{anode} \qquad (13)$$

$$CO_2 \rightarrow \tfrac{1}{2}\,O^2 + CO \qquad \text{overall} \qquad (14)$$

Besides, when the feedstock is the mixture of steam and CO_2, syngas (CO/H_2) will be generated at fuel electrode, that is defined as "co-electrolysis". The CO/H_2 mixture can be further used to produce liquid fuel through the Fischer-Tropsch process [82]. During co-electrolysis, the steam electrolysis is the principal reaction due to the fact that there was almost no difference of area-specific resistance for co-electrolysis versus steam electrolysis [83]. Part of H_2 from steam electrolysis is used to reduce CO_2 via the reverse water-gas shift (RWGS) reaction [84]:

$$H_2 + CO_2 \leftrightarrow H_2O + CO \qquad (15)$$

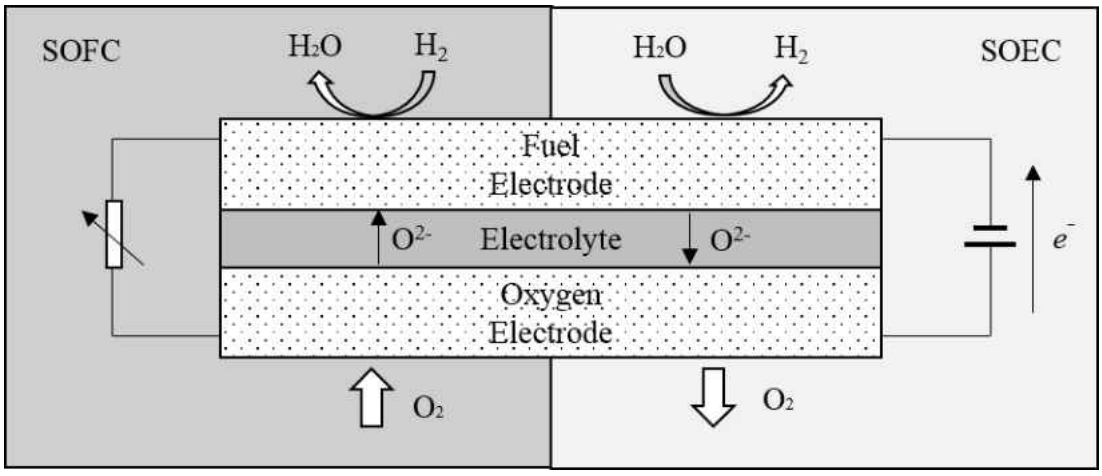

Figure 15. Operation principles of SOFC and SOEC [84].

1.3.3 Thermodynamics

Due to different working temperatures, there are two main types of electrolysis technology, the low temperature electrolysis (LTE) and high temperature electrolysis (HTE). The alkaline electrolyzers and proton-exchange membrane (PEM) electrolyzers are the most widely used LTE systems and these devices are reported to achieve an energy efficiency as high as 75% [85]. Even though the LTE is a mature technology, the high electric energy consumption is still a major problem. Basically, the Nernst potential for water electrolysis is 1.23 V at standard conditions. But the practically applied voltage is required to be 1.6~1.8 V with consideration of overpotentials. This can degrade the competitiveness of the LTE technique. On the other hand, the HTE shows a great potential for splitting water due to the highly endothermic process at elevated temperatures. Specifically, the electrical power demand is reduced with increasing temperature. Because the joule heat can compensate a portion of total required energy for water electrolysis. In addition, the overpotential of electrodes can be effectively suppressed leading to less power loss in the SOECs. The HTE process consumes electrical energy as well as thermal energy. The minimum electric energy required for electrolysis is equal to the change of Gibbs free energy (ΔG):

$$\Delta G = \Delta H - T\Delta S \quad (16)$$

where ΔH is the change of enthalpy and indicate the total energy requirement. T and ΔS denote operation temperature and entropy change respectively.

In terms of thermodynamics, the increase in the thermal energy requirement is more noticeable than that of total energy demand as temperature increases. Therefore, the required electrical energy decreases with temperature increasing as shown in Figure 16. When the heat

energy is obtained from other renewable sources such as solar, wind, nuclear etc., the HTE has a distinct advantage over LTE due to its lower electrical input and thus higher efficiency. Besides, several restraining factors for LTE, e.g. kinetics, activation and ohmic overpotentials decrease significantly with rising temperature [86].

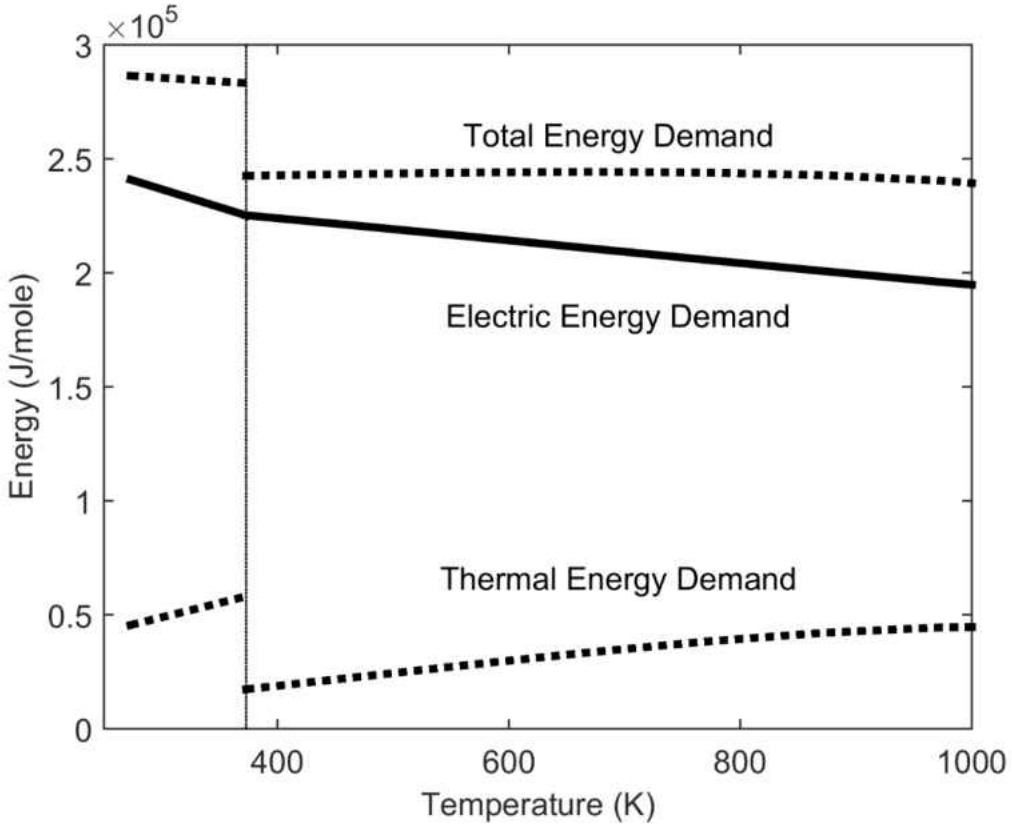

Figure 16. Thermodynamics water electrolysis from 273K to 1000K [87].

The thermal energy can be obtained from Joule heat that is converted from electrical energy when the current passes through the cell. Thus, at a certain applied voltage, the cell can run in the electrolysis model with maintaining high temperature. Such thermoneutral potential is defined as:

$$E = \frac{\Delta H}{nF} \quad 17)$$

where n is the electron number involved in the electrochemical reactions, and F is the Faraday constant. If the applied voltage is lower than the thermoneutral potential, the electrical energy supply is less than the total energy consumption. Therefore, the SOEC works in endothermic model and extra thermal energy compensation is required to maintain the operation temperature. On the other hand, if the applied voltage is higher than the thermoneutral potential, SOEC operates in exothermic model and the electrical energy can drive the electrolysis without extra energy supply. Even though the electrical efficiency cannot reach 100%, high current density will be achieved leading to high H_2 production.

Besides temperature and thermal energy supply, reactant concentrations have remarkable effect on electrical voltage in HTE as well as shown in Figure 17. Taking steam electrolysis as an example, water vapor is usually mixed with hydrogen as inlet reactants to avoid the oxidation and degradation of cathode. Therefore, the minimum electrical energy requirement of mixture is lower than that of steam at atmosphere pressure. This can be described by Nernst potential [88] as follows:

$$E = E_0 - \frac{RT}{2F} \ln \frac{P_{H_2O}}{P_{H_2} P_{O_2}^{1/2}} \quad 18)$$

where E_0 is the standard cell potential; R is the ideal gas constant; T is the operating temperature; F is Faraday constant; and P_{H_2O} , P_{H_2}, and P_{O_2} represent the partial pressure of H_2O, H_2, and O_2, respectively. At standard conditions, the Nernst potential is 1.23 V for water splitting. As shown in Figure 17, at elevated temperatures, Nernst potential significantly decreases. It can be further reduced using higher steam content. Furthermore, activation overpotentials are very small at high

temperature. A practical V_{OC} value of 0.85-0.95 V (based on various steam contents) is commonly observed in high temperature electrolysis [87, 89, 90].

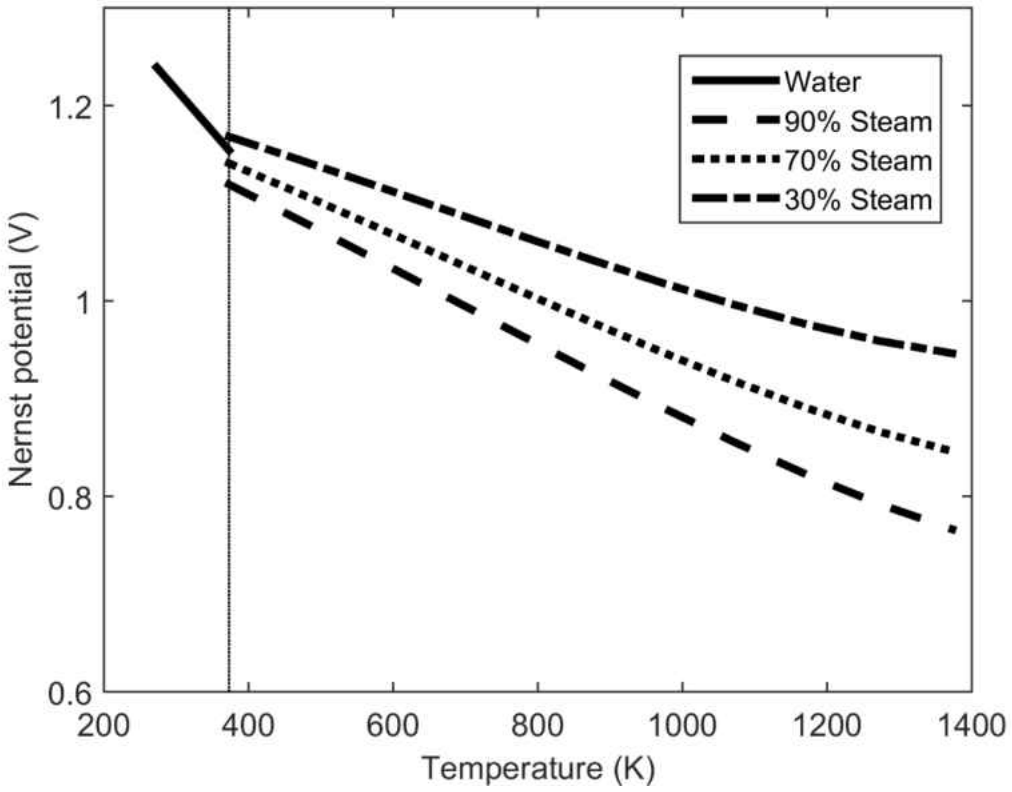

Figure 17. Nernst potential for H_2O splitting at atmosphere pressure as temperature increases.

1.3.4 Configurations and Materials

A number of SOE cell/stacks have been developed and tested since the German 'HotElly' project in 1980s. Among all the cell/stacks, planar and tubular designs are the most focused in the stack level. Initially, tubular configuration was more popular due to its sealing advantages even though the fabrication cost of tubular designs is much higher than that of planar designs. Besides, tubular cell unit could be much easier to be connected in series with respect to electrical

current and gas flow [91]. Afterwards, with R&D of sealing materials and designs, planar configuration became dominant because of its shorter current collection paths and higher volumetric density. Furthermore, all ceramic SOE stacks were innovated by NASA for Mars exploration since it could reduce the stack weight and volume significantly thus resulting in higher power density. The three stack designs mentioned above will be discussed in detail in the following sections.

According to the supported components of SOECs, there are four types of cell designs, namely: anode-supported, electrolyte-supported, cathode-supported, and externally supported configurations [92]. Electrolyte-supported and electrode-supported configurations are the most common designs. Generally, electrolyte-supported SOEC stacks have much higher area specific resistance (ASR) due to thicker electrolytes. Therefore, higher energy input is required to compensate the ohmic loss. However, the experimental results showed that electrolyte-supported SOEC stacks had higher possibility to survive during the long-term degradation test because electrode-supported SOEC stacks were more sensitive to thermal cycles and unintentional redox events [93].

1.3.4.1 Electrolyte-supported cells

Scandia-stabilized zirconia (ScSZ) and 3 mole% yttria-stabilized zirconia (3YSZ) exhibit high ionic conductivity at elevated temperature and they are the most common electrolyte materials in electrolyte-supported SOECs [83, 94]. Figure 18 shows the planar stack fabricated by Ceramatec, Inc., of Salt Lake City, UT. The thickness of ScSZ electrolyte was approximately 140 um. The graded air-sweep electrode consisted of a manganite/zirconia inner layer (13 um), a manganite middle layer (18 um) and a cobaltite outer bond layer. The steam/hydrogen electrode was graded as well and were made of an inner layer of nickel cermet (13 um) and an outer layer

of pure nickel (10 um) [69]. A variety of experimental investigations about ScSZ-supported SOE stacks have been conducted at INL. The testing stack level ranged from multi-cell stacks (10-cell, 25-cell) to multi-stack systems (720-cell) [69, 83, 93, 95-99]. Besides, a 5-cell 3YSZ-supported SOE stack was fabricated by Energy research Center of Netherland (ECN). The 3YSZ electrolyte was made through tape casting with thickness of 90 um. Both electrodes were screen-printed and the oxygen electrode was made of strontium-doped lanthanum ferrite/cobaltite (LSCF). The hydrogen/steam electrode consisted of three layers, namely Nickel and ceria-gadolinia (CGO) with thickness of 40 um [94].

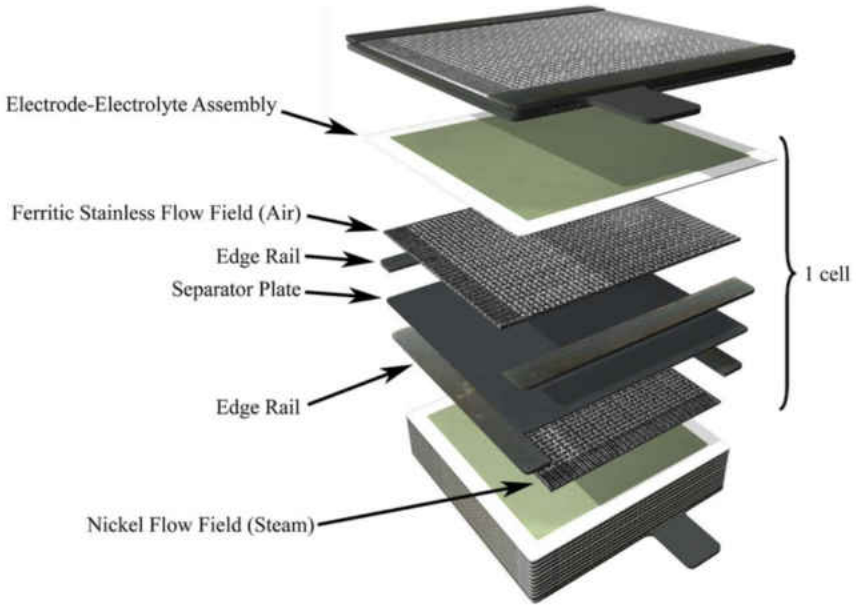

Figure 18. Exploded view of a 10-cell stack from Cermatec [93].

1.3.4.2 Electrode-supported cells

Nickel (Ni) is extremely popular in cathode materials of SOECs due to its electrical conductivity, mechanical strength and catalytic property. As a supported component, the cathode

thickness ranged from 300 um to 700 um in the stack level [73, 86, 100]. However, the different thermal expansion coefficients between cathode and electrolyte could cause electrolyte cracking during fabrication and operation. Therefore, mixture of Ni and electrolyte were usually recommended for cathode materials to reduce the mismatch of thermal expansion coefficients. For example, Ni-YSZ and Ni-CeO_2 were cathode materials in terms of YSZ and ScSZ electrolytes, respectively [80, 93]. Figure 19 shows a 5-cell SOE stack fabricated by Materials and Systems Research Inc. (MSRI). The supported steam/hydrogen electrode was made of Ni-YSZ and the corresponding electrolyte and oxygen electrode were YSZ and LSCF, respectively [93]. Besides, other oxygen electrode materials, such as LSC [101-103], LSM [70, 100, 104], LSCF [105], LSCF-GDC [73, 74], LSM-YSZ [78, 106-108], CGO|LSC-CGO|LSC [109], LSCF-CGO [79, 110, 111], YDC-LSCF [112, 113] and LSC-GDC [80], were reported to be suitable for cathode-supported SOE stacks as well.

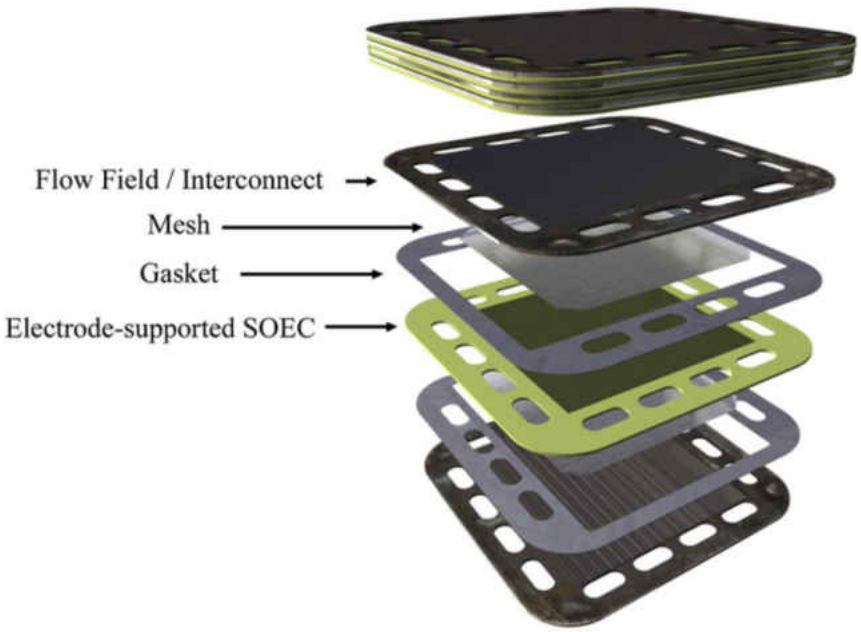

Figure 19. Exploded view of a 5-cell stack from MSRI [93].

1.3.4.3 Tubular cells

Tubular configurations were extremely common during the initial development of SOE stacks. Generally, there were two common designs as shown in Figure 20 and Figure 21 [114]. In the first design, the electrolyte was continuous and thus can provide a convenient structural element. However, the principal problem is to series-connect the anode and cathode through electrolyte without introducing leaks. In the second design, electrolyte was discontinuous and the anodes and cathodes were connected directly. With the development of sealing materials and technology, the discontinuous design was more popular because there was no concern about the mismatch of thermal expansion for connection wires and electrolytes.

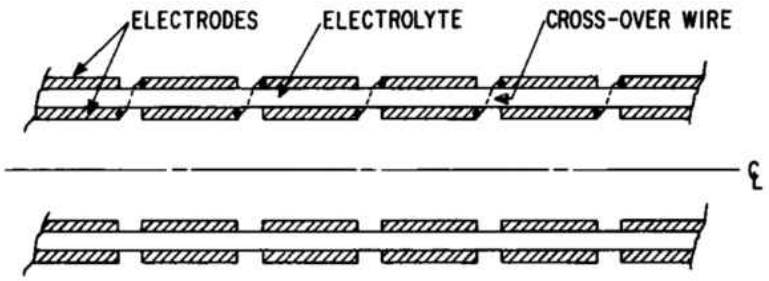

Figure 20. Schematic diagram of tubular SOECs with a continuous electrolyte [114].

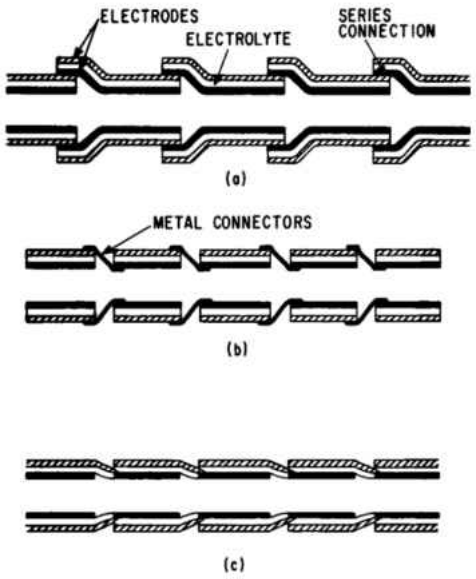

Figure 21. Schematic diagram of several possible configurations for tubular stacks with discontinuous electrolytes [114].

Figure 22 shows the tubular electrolyzer stacks from the German 'HotElly' project in 1980s [115]. The unit cells with inner diameter of 13 mm were connected in series and used Pt foils as interconnectors. The electrolyte was made of ZrO_2 + 8 mol% Y_2O_3 ceramic with thickness of 1.5 mm and had a high O^{2-} conductivity of 0.1 S/cm at 1000 °C. Both anode and cathode were made of porous Pt with porosity of less 3%. Besides, other inner cathode materials such as Ni-YSZ [81, 116] and outer anode materials such as $LaCoO_3$ [116], LSM [116] and LSC [81] were reported in tubular SOE stacks.

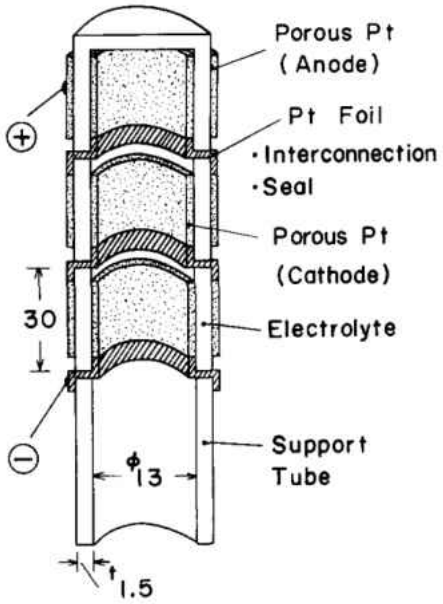

Figure 22. Schematic drawing of the fabricated electrolyzer cell [115].

1.3.4.4 All ceramic SOEC stacks

As shown in Figure 23, NASA Glen Research Center (GRC) has developed a novel design of SOE stack for sample return missions and human exploration of Mars [77, 117]. The metal interconnects and frames accounted for 70% of the stack mass in traditional SOE stacks. These were replaced by a thin, Ca-doped $LaCrO_3$ (LCC) layer with a thickness of 30-60 μm in state-of-the-art planar stack from GRC. Therefore, this all ceramic SOE stacks had the potential to improve the power density by 3 to 4 times [117]. The unit cell was symmetrical structurally and named bielectrode-supported cell (BSC). The thin YSZ electrolyte layer was supported by identical, porous YSZ electrodes on both sides through a freeze-casting technique. The porous electrodes were graded from smallest pores (1-5 um) at electrode/electrolyte interface to 80-100 um pores as air and fuel channels. The fuel and air pathways were perpendicular to each other

without interference in BSC stack. Besides, the seals were made of YSZ as well to match the CTE with LCC interconnect.

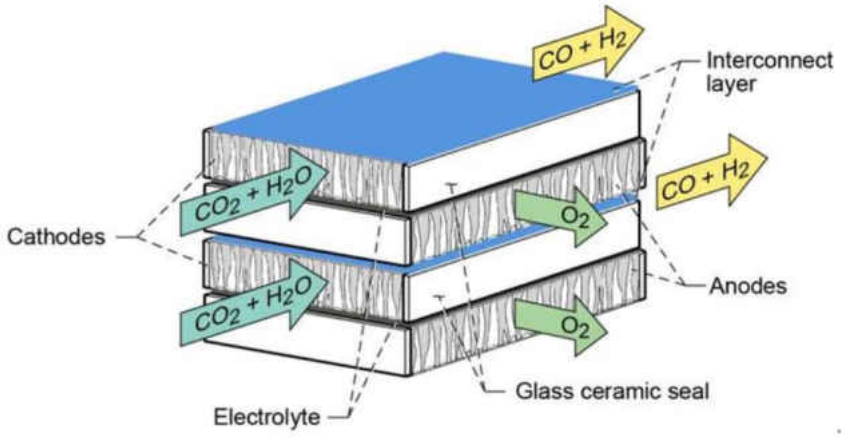

Figure 23. The design of a 2-cell bielectrode-supported stack [117].

1.3.5 Manufacturing

1.3.5.1 Electrolyte manufacturing

The electrolyte layer has to be dense with high ionic conductivity, zero gas penetration and negligible electric conductivity. To improve the ionic conductivity, the small particle size of electrolyte powders is preferred. It has been reported that the ionic conductivity of YSZ particle with 300 nm is 95% higher than that with 2.15 um [118]. The tape casting and lamination is the most widely used fabrication technique [119-121]. First, a three-layer YSZ wafer is prepared by laminating the ceramic tapes. The central layer is a dense wafer sandwiched by two porous electrode layers. Note that, the central wafer only includes YSZ and organic binders while the other electrode wafers contains sacrificial pore formers, i.e. graphite or polyethylene. Then, the multi-layer disc synthesized by tape casting is sintered around 1500 °C leading to a dense YSZ

electrolyte and two porous electrodes. Besides, vacuum system coating is considered as another effective method of fabricating dense electrolyte layer. The coating techniques include magnetron sputtering [122], plasma spraying [123], slip casting [124], physical vapor deposition [125], etc. Depending on various methods and electrolyte materials, the sintering temperature ranges from 1100 °C to 1600 °C. Pressing has also been reported as a successful manufacturing technique of electrolyte [125-131]. The electrolyte powder is typically pressed under pressure from 140 MPa to 200 MPa before sintering. On the other hand, the electrolyte powder can be mixed with organic binder in the ball milling and screen-printed on the electrodes [132]. The organic binder (terpineol based) is removed when the sintering temperature is above 800 °C.

1.3.5.2 Fuel electrode manufacturing

To transport the ions and electrons during the H_2O/H_2 redox reactions, the fuel electrode must have a high ionic and electric conductivity. It is usually made of metal-ceramic mixture (Ni-YSZ), where the metal and ceramic materials are responsible for conducting electrons and ions respectively. The metal-ceramic mixture can also avoid delamination issues due to the mismatch of thermal expansion coefficients between electrodes and electrolytes. The overall conductivity of fuel electrode materials is required to be 1 S/cm with consideration of various cell designs and path lengths of current collection [133, 134]. Another important parameter of fuel electrode is porosity. The electrode with high porosity can supply sufficient area for electrochemical reactions. However, the electrical conductivity decreases with an increase of electrode porosity because high porosity leads to the discontinuous conductor materials, thus increasing the ohmic resistance. The suggested porosity for SOFC ranges from 35% to 40% [135]. Higher porosity of 50% is required for SOEC mode due to different gas transport

mechanisms. For instance, H_2O has a remarkable influence in Knudsen diffusion, so that the diffusion is affected more significantly in electrolysis mode [136].

Nickel (Ni) is the most commonly used metal material in the mixture due to its high conductivity and catalytic property. The ceramic part is dependent on the electrolyte materials including YSZ, GDC, ScSZ, etc. Generally, these materials are either wet or dry and mixed in a ball mill. Compared to the dry milling, the wet milling can develop a more uniform structure by coating YSZ particles on Ni surface, leading to a higher conductivity [137]. The powder forming techniques of fuel electrode include dip coating [119, 121, 138, 139], pressing [132, 137, 140-142], screen-printing [126, 128, 129, 143, 144], air plasma spraying [123], spray painting [145], etc. The last two methods are applied for depositing thin layer with thickness of less than 70 μm. Thus, they are limited to manufacturing electrolyte-support SOFC/SOEC. Except for air plasma spraying, all the fabrication techniques require the ceramic suspension as the preparation. The casting devices, such as doctor blade, stencil and immersion holder, are necessary as well. The porous electrode structure can be created by adding the pore formers into the suspension before sintering. The electrode porosity is controlled by the concentration of pore formers. Normally, there are two main categories of pore former materials, including organic formers and inorganic formers. The utilization of organic formers can achieve higher porosity but lower electrical conductivity than that of inorganic formers [140, 146]. The sintering temperature of electrode ranges from 800 °C to 1200 °C and it is usually lower than that of electrolyte.

1.3.5.3 Oxygen electrode manufacturing

Similar to the fuel electrode, the oxygen electrode must have a high electrical conductivity, high ionic conductivity and high catalytic activity for oxygen reduction. Besides, the materials should be compatible with electrolyte at high temperature. LSM is the most widely

used materials of oxygen electrode due to its electro-catalytic conductivity. The thermal expansion coefficient of LSM is close to that of YSZ electrolyte and this can avoid delamination issues during SOFC/SOEC operation. However, the oxygen reduction only takes place in a small area at the electrolyte/electrode interface, so the poor ionic conductivity limits the performance of SOFC/SOEC based on LSM. To solve such a problem, a composite electrode of LSM and YSZ is usually employed to improve the ionic conductivity [145]. Other composite electrodes have been reported as well, such as LSF-YSZ [119, 120], LSC-YSZ [120], BSCF-SDC [147], SSC-BCZY [126], LSCF-GDC [148], etc.

The oxide powders of oxygen electrode are generally synthesized though calcination at high temperature. For example, the nitrates of $La(NO_3)_3 \cdot 6H_2O$, $Sr(NO_3)_2$, $Fe(NO_3)_3 \cdot 9H_2O$ are dissolved in the acid solution of NH_4NO_3. The LSF powders can be achieved after calcination at 900 °C [119]. They are later mixed with YSZ powders in the ball mill at a specific ratio. The porous formers are usually necessary to generate porosity in the electrodes. Furthermore, the pore formers can reduce the shrinkage rate of electrode layers during sintering or operation, thus avoiding delamination between layers and cracking issues. The graphite is the most common pore formers for the electrodes and porosity can be adjusted by mixing electrode materials at different ratios. The processing techniques are similar to those of fuel electrodes such as dip coating [119-121, 125], screen-printing [130, 132, 149, 150], spray-painting [145], plasma-spraying [123], etc. They are selected according to different shapes and component sizes.

1.3.6 Hydrogen and Oxygen Production via SOEC

1.3.6.1 Hydrogen production

Except for electricity price, the capacity of H_2 production was the most significant parameter influencing the hydrogen production cost. When the H2 production capacities were between 50 and 900 Nm3/h, the hydrogen production cost would vary between 2.45 €/kg and 3.45 €/kg with electricity price of 50 €/MWe and SOEC lifetime of 40,000 hours [70]. Figure 24 summarizes the H_2 production rate in stack level as a function of publication year of experimental results. Note that, the hydrogen production rate could be estimated based on downstream dewpoint measurements. Besides, the molar hydrogen generation rate can be predicted independently by the applied the current through the equation as follows:

$$\Delta \dot{N}_{H_2} = \frac{I}{2F} N_c \tag{19}$$

where N_C is the number of unit cell in the stacks, and F is Faraday constant.

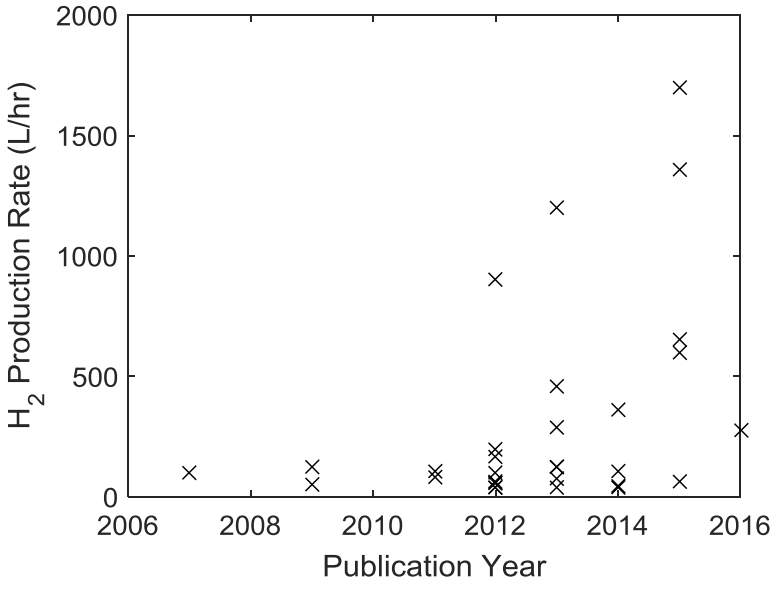

Figure 24. The hydrogen production rate of SOE stacks as a function of time.

Currently, the most impressive hydrogen production rate is 1.7 Nm^3/h from a 25-cell stack at CEA in 2015 [103]. The cathode-supported SOE stack consisted of Ni-YSZ hydrogen electrode, 8% molar YSZ electrolyte, LSC oxygen electrode and CGO diffusion barrier layer. With a feedstock of 90% steam, the SOE stack was operated at 800 °C. A current density of 1.6 A/cm2 was obtained with the applied voltage below 1.3 V. For the long-term durability test, the best performance for hydrogen production is 1.38 Nm^3/h determined from the supplied current using Faraday's law [86]. Besides, a hydrogen production rate of 1.2 Nm3/h was achieved for the 15 kW ILS test facility at INL [69]. Note that the 720-cell multi-stack was reported to produce hydrogen at a peak value of 5.7 Nm3/h based on the measured current.

To reach the DOE target of 78% electrolysis efficiency based on low heating value (LHV) by 2020, the Versa Power System (VPS) focuses on developing SOE cell/stack with ultra-high electrolysis current density and efficiency. Over 20 types of RSOFC cells have been innovated in the project that funded by DOE and VPS. One type of cells, RSOFC-7, was successfully operated with current density up to 4 A/cm2 at an upper potential limit of 1.6 V. Besides, in the long-term durability test, RSOFC-7 demonstrated a degradation rate of only 1.8%/kh at current density of 3 A/cm^2 after 1200 hours' operation. Furthermore, VPS assembled a SOE stack using 20 RSOFC-7 unit cells with active area of 22.3 cm^2. With fuel inlet of 78% H_2O and steam utilization of 50%, the stack was capable of operation at 800 °C with current density of 3.004 A/cm^2 corresponding to 83.9% electrolysis efficiency (LHV). The stack was then operated over 1000 hours for durability test at 2 A/cm^2 corresponding to hydrogen production of 333 L/h. No apparent voltage degradation for average cell was observed as shown in Figure 25. VPS are

currently preparing for production of Compact SOFC Architecture (CSA) stack that will be deployed later in 2017 for hydrogen production of 2.775 Nm^3/h.

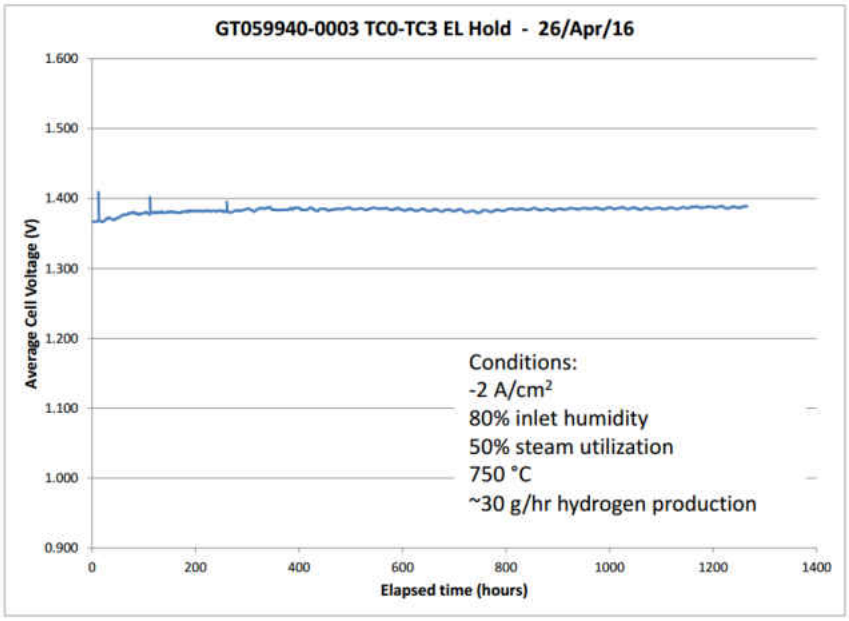

Figure 25. Durability test of a 20-cell stack operated at high current density [151].

1.3.6.2 Syngas production from high temperature co-electrolysis

The research on large-scale production of syngas using SOE stacks is limited. To our best knowledge, the best experimental performance for co-electrolysis is obtained from a 10-cell stack with syngas production rate of 286 Nl/h [110, 111]. The stack was fabricated by Topsoe Fuel Cell and assembled with 10 electrode-supported cells with an active area of 9.6×9.6 cm2. All the cells consist of Ni-YSZ hydrogen electrode, YSZ electrolyte and LSCF-CGO or LSM-YSZ oxygen electrode. The feedstock were a mixture of 45% CO2, 45% steam and 10% H2 with a flow rate of 540 L/h and pure oxygen with a flow rate of 60 L/h for both electrode sides. The durability test was operated at 800 °C for 1000 hours with a current density of 0.75 A/cm2. The impressive results with low degradation demonstrated the feasibility of long-term co-electrolysis.

Besides, co-electrolysis using SOE stacks has been conducted and remarkable results have been achieved in INL [83, 97], Italy [78] and Switzerland [79].

1.3.6.3 Oxygen production for space missions

As shown in Figure 23, a 3-cell stack with cell area of 4 cm^2 was developed in NASA GRC [117]. Including the interlayers, the mass of stack was only 36 g. The SOE stack was operated at 850 °C with a mixture of H_2 (200 sccm), steam (100 sccm) and CO_2 (395 sccm) for anode side and sweep air (1000 sccm) for cathode side. However, a low current density (<0.1 A/cm2) was measured corresponding to oxygen production of 0.25 L/h. The severely current limited problem resulted from excessive reaction between the Ca-doped $LaCrO_3$ interconnect and the YSZ electrode scaffold layer. Recently, Pt-GDC was chosen as cathode material due to the expected oxidation tolerance and catalytic activity for CO_2 reduction of Pt [117]. With steam to H2 ratio of 1:1, the advanced single cell was tested at 850 °C using DC voltage sweep method. A current density up to 0.57 A/cm2 was achieved corresponding to an oxygen production of 1.77 L/h. Besides, the durability experiments of two Pt-GDC single cells were conducted in steam electrolysis mode. Both tests were operated under constant current densities of 0.2 A/cm2. It was reported that cell #1 showed 3% degradation over 600 hours of operation while cell #2 saw <1% degradation over 1200 hours of operation. The impressive results demonstrated the promising application for Pt-GDC as a cathode material.

1.3.7 SOEC Degradation

Due to inherent complexity and interrelation between different components, multiple degradation mechanisms may potentially exist in SOE cell especially in stack level. Figure 26 summarizes various degradation issues that are well-known in a single-repeating unit (SRU) of SOE stack [152]. Besides, excellent reviews presenting common degradation problems and

solutions for SOECs have already been finished by other researchers [95, 152-155]. Furthermore, the long-term duration test with degradation rate in stack level has been summarized in Table 6 from appendices.

The contacting issues of interconnect are unique in stack level. Because of contacting directly with endplates, the top cells and bottom cells in a stack usually exhibit abnormal behaviors when the ohmic losses happen at endplate contacts. In a 25-cell stack operated in electrolysis mode over 9000 hours, the top cell (SRU 1) was observed to degrade the most with a rate of 3.0%/kh compared to an average of 2.3%/kh. On the other hand, the bottom cell showed the best performance with degradation rate of only 1.77%/kh. The main reason was the degradation of endplate contact that increased the operation temperature and improved the durability behavior of bottom cell [156]. The same problems were also reported in short stacks [79, 93, 94, 109, 110]. Besides, the SOE stack may suffer from unexpected disturbance, such as condensation in H_2 recycle loop [69], water pump failure [156], power supply failure [156], gas flow change [112], inlet gas impurities [112] etc. These interference factors from the management system could suspend the stable operation of SOE stack. Despite restoring to normal operation conditions, the degradation of stack performance is irreversible.

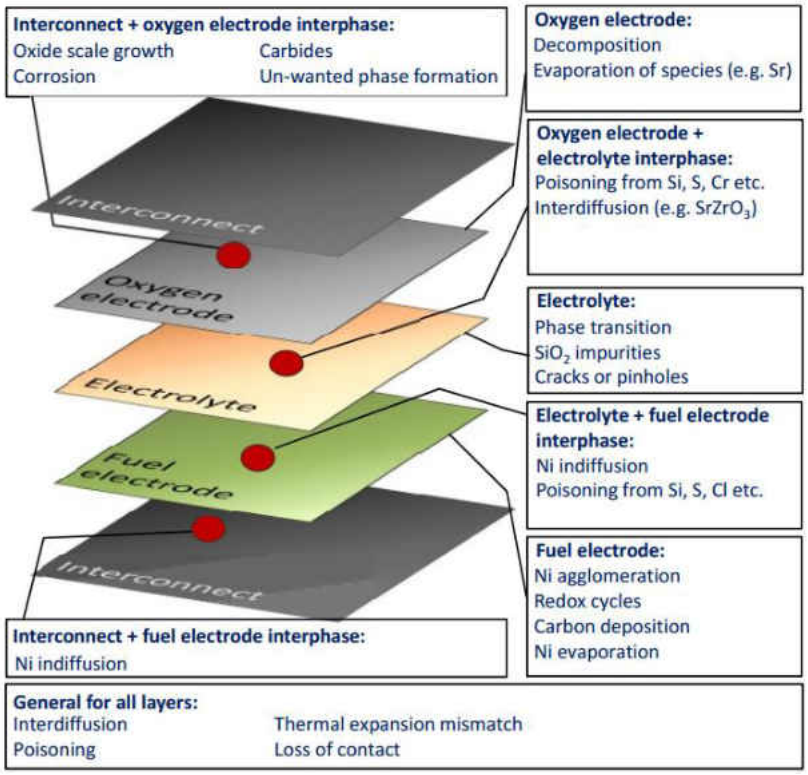

Figure 26. A simplified exploded view of a single-repeating unit (SRU) and a few of the possible degradation mechanisms [152].

To solve the contact issues, coating of interconnects has been proved as an effective method. Zhang et al. pre-treated the stainless steel based interconnects with spinel coatings before a durability test of a 10-cell SOE stack [93]. Operating the stack at either high or low current density, the average degradation rate was much lower compared to the previous SOE stack tests. The significant improvement was attributed to the novel coatings that successfully inhibited the steam oxidation and Cr contamination. Besides, surface treatment of top cell could effectively decrease the stack ASR since the top cell is directly connected with current collector plate and easily suffer from Cr poisoning.

1.3.8 Summary and prospects

The solid oxide fuel/electrolysis cells have been presented as a promising technique for large-scale hydrogen production. The materials and manufacturing of electrolyte, fuel electrode, and oxygen electrode have been reviewed and they are summarized in Table 1.

Table 1. Material and manufacturing summary of SOEC electrolyte, fuel electrode and oxygen electrode.

Components	Electrolyte	Fuel electrode	Oxygen electrode
Materials	YSZ [142] GDC [128] SDC [125] CBC [127] BCZY [126] ScSZ [148] LSGM [157]	Ni-YSZ [125] Ni-CeO_2-ZrO_2 [130] LSCM-YSZ-Pd|CYZ [119] CeO_2 [121] Cu-YSZ [129] Ni-GDC [149] Ni-BCZY [126] Ni-ScSZ [148]	LSM [125] LSC [125] LCM [130] LSCF [123] LSF-YSZ [120] LSC-YSZ [120] LSM-YSZ [120] LSF-YSZ [119] BSCF-SDC [147]
Manufacturing	Tape Casting & lamination [119] Dip coating [142], Pressing [128] Slurry coating [148] Reactive Magnetron Sputtering [122] Screen-printing [132] Slip Casting [125] Vacuum Plasma Spraying [123] Vacuum Slip Casting [124] Physical Vapor Deposition [125]	Tape Casting & Spray painting [145] Tape Casting & Dip Coating [119] Screen-printing [129] Pressing [118] Air Plasma Spraying [123] Dip coating [121]	Dip Coating [125] Screen-printing [130] Spray-painting [120] Plasma Spraying [123]

Due to its huge potential, the development of SOE cell/stack is essential on several directions in the future. First, high current density (> 2A/cm^2) is required for the stack in durability tests since it corresponds to high electrolysis efficiency of hydrogen. Currently, most

experiments are conducted at a current density of less than 1A/cm^2 that is not sufficient for future commercial applications. Therefore, the R&D of new SOEC materials is necessary to maintain the high current density with acceptable degradation during long-term operation. Second, the stability of RSOFC needs to be guaranteed during alternate SOFC and SOEC operation. Because of the different electrochemical reactions and atmosphere at electrodes, the degradation issues of RSOFC are of a greater concern for commercialization. Novel materials and new processing techniques are required to improve the cell/stack performance. Third, it's necessary for high temperature electrolysis to use SOE stacks coupled with renewable energy such as solar, wind, nuclear, etc., because the total process is sustainable and environmentally friendly with zero-carbon emission. Worldwide research activities have been focusing on producing large-scale hydrogen with nuclear power supply and this technology could be a remarkable contributor towards future hydrogen economy.

CHAPTER 2

WATER SPLITTING USING HIGH TEMPERATURE SOLID OXIDE PHOTOELECTROCHEMICAL CELL AND VISIBLE LIGHT: SEARCHING FOR THE APPROPRIATE SEMICONDUCTOR MATERIALS

In this chapter, the concept of using solid oxide photoelectrochemical cells (SOPCs) to split water at high temperature using visible sunlight was experimentally investigated, in order to search for the appropriate semiconductor materials. High temperature photoelectrochemical water splitting physically broadens the selection of potential applicable semiconductor materials and enables more visible sunlight absorption. This newly conceived concept provides a unique pathway for solar hydrogen production, compared to conventional photoelectrochemical cells that require aqueous environments, though experimental validation is needed. The main focus of this study was on the fabrication and evaluation of high temperature diodes suitable for use as the photocatalytic/oxygen electrodes of SOPCs. The rectifying characteristics of TiO_2 based diodes, including Ag/TiO_2, LSM/TiO_2, LSC/TiO_2, and LSCF/TiO_2, etc., were investigated at elevated temperatures. Among those diodes, only LSM/TiO_2 demonstrated acceptable rectifying properties up to 450 °C, indicating that such configuration may be applicable to the proposed SOPC. The results also excluded Schottky diodes from the candidates due to their rapidly degrading rectifying behaviors at elevated temperatures. Candidate semiconductors for the photovoltaic (PV) part of the cell and electrolytes for the electrolysis part were also identified and summarized in this paper for future investigations.

2.1 Background

Photocatalytic water splitting provides a renewable pathway for hydrogen production with minimum environmental impact. As a long term goal of producing hydrogen economically, the Department of Energy (DOE) of the United States has outlined several solar-to-hydrogen pathways, including solar thermochemical, photoelectrochemical, electrolysis (solar), and photobiological [158]. Among those technologies, direct water splitting using photoelectrochemical cells (PECs) and sunlight has received enormous scientific interest in recent decades, following the pioneering research by Fujishima and Honda in 1972 [2].

In order to harvest more visible sunlight and increase energy conversion efficiencies, most research on PECs has been focused on materials development and cell configurations [3, 11]. The fundamental problem is that the visible spectrum and the thermodynamic threshold for water splitting (Nernst potential for electrolysis) basically constrain the range of the semiconductor materials (photocatalysts) suitable for PECs. While most investigations focused on the former factor, few paid attention to the latter. In fact, most PECs reported were operated in aqueous environments such that, naturally, the latter factor was excluded from consideration. More specifically, an ideal PEC must have a band gap large enough (>1.23 eV at standard conditions) to support water splitting, but small enough to include most of the visible spectrum. However, at low temperature (<100 °C), significant activation overpotentials result in a minimum practical voltage of 1.6-1.7 V for splitting water [159, 160]. In addition, to include sensitivity over most of the visible spectrum, the semiconductor band gap should not be much larger than 2.2 eV. Furthermore, the semiconductor band edges must straddle the H_2O redox potentials and the material must be stable in an aqueous electrolyte solution over a range of pH

values. Simultaneous satisfaction of all these requirements has proven difficult with a single semiconductor material.

The concept of high temperature photoelectrochemical water splitting was independently proposed by us [57] and Ye *et al*. [51] in 2013, though with different cell configurations. In our original concept, a solid oxide photoelectrochemical cell (SOPC) was proposed, which integrates a solid oxide electrolysis cell (SOEC) and a photovoltaic (PV) cell. However, only a small output voltage (around 100 mV) was achieved using TiO_2/Pt Schottky diode based cells in the preliminary research [57]. Based on a heterojunction between a light absorber and a mixed ionic and electronic conducting (MIEC) oxide, the integrated high temperature PECs proposed by Ye *et al.* absorb both thermal and photon energy from concentrated solar light. Specifically, the light absorber semiconductor is able to separate electron-hole pairs, while the MIEC oxide conducts the excited electrons and oxygen ions at a temperature range from 400 °C to 700 °C [51, 52]. The feasibility of high temperature photoelectrochemical water splitting was first experimentally demonstrated by Brunauer *et al.* recently, using a solid oxide photoelectrochemical cell (namely SOPEC) [53, 55]. An open circuit voltage (V_{oc}) of 920 mV was achieved using a $LaSrCrO_3$/$SrTiO_3$ p-n junction diode at 400 °C under ultraviolet (UV) light. Then an electrochemically oxygen pump driven by UV light was demonstrated using the SOPECs [55]. The same group reported that cells with configurations of $SrTiO_3$/YSZ and TiO_2/YSZ were able to store oxygen upon UV light from 360 °C to 460 °C. Their further experiments showed that oxygen vacancies in $SrTiO_3$ or TiO_2 were filled during UV illumination, leading to a battery-type voltage of 30-70 mV at 460 °C [53, 54]. To date, both the theoretical and experimental research on high temperature photoelectrochemical water splitting are extremely limited, since it is a newly conceived concept.

In this chapter, the theoretical framework of SOPC was elaborated with highlighted advantages compared to conventional PECs. The present experimental investigation focused on searching for the appropriate high temperature semiconductor materials for SOPCs. As an initial screening process, the rectifying properties of several semiconductor diodes at elevated temperatures (up to 500 °C) were characterized. Specifically four types of diodes were investigated, including a Schottky diode (i.e. Ag/TiO_2), and three p-n junction diodes (i.e. LSM/TiO_2, LSC/TiO_2, and LSCF/TiO_2). This chapter provides an overview of this newly conceived concept and potential pathways for the future research.

2.2 Theoretical framework

2.2.1 Thermodynamics

Photoelectrochemically splitting water at high temperature has two main theoretical advantages. First, the thermodynamic threshold is significantly reduced at elevated temperatures. The ideal minimum potential for water splitting at atmosphere pressure, or Nernst potential, is given by equation (18) [88]. At standard conditions, the Nernst potential is 1.23 V for water splitting. Practically however, a minimum voltage of 1.6-1.7 V is needed for splitting water due to high activation energies [159-161]. As shown in Figure 17, at elevated temperatures, the Nernst potential significantly decreases. It can be further reduced using high steam content. Furthermore, activation overpotentials are very small at high temperature. A practical open circuit voltage (V_{OC}) of 0.85-0.95 V (based on various steam contents) are commonly observed in high temperature steam electrolysis cells [87, 89, 90].

Therefore, the minimum band gap requirement of a semiconductor for splitting H_2O is practically reduced to ~ 1.4 eV at high temperature, compared to practically 2.2 eV at standard conditions. This reduced band gap allows for a drastically different choice of semiconductors to

be made, while still using single junction solar cell. Therefore no triple junction amorphous silicon or wide band gap material is needed as is the case at room temperature.

Second, band gap narrowing enables more visible sunlight absorption. The band gap of a semiconductor determines a threshold of the light frequency required for exciting electrons from the valence band to the conduction band. Only light with frequencies higher than the threshold is able to excite electrons out. Therefore, by narrowing the band gap the threshold will decrease, enabling the semiconductor to absorb longer wavelength light (i.e. more visible light).

The band gap values of most semiconductors decrease as temperature rises, with near linear behavior at higher temperatures [162-166]. For instance, the band gap of anatase TiO_2 is ~3.2 eV at room temperature, which corresponds to a threshold of 387 nm near the ultraviolet spectrum. That means in order to excite electrons out of TiO_2, an ultra violet light source is needed. Several studies have been performed to quantify the effect of temperature on the band gap energy of TiO_2 [58-62, 64, 167] based on the following correlation:

$$E_g(T) = E_g(0) - \frac{\alpha T^2}{T + \beta} \tag{20}$$

Where, $E_g(0)$ is the band gap at temperature of absolute zero. α and β are both constants determined by experiments. Based on this correlation, the band gap of TiO_2 will narrow down to 1.7-2.3 eV as temperature rises to 1000 K [58-62, 64, 167]. That energy level falls right in the visible spectrum.

2.2.2 Schottky Barriers

The metal-semiconductor contact is known as the Schottky Barrier that usually exhibits the rectifying behavior. Such electrical behavior is significantly dependent on the barrier height, Φ_{MS}, and it can be predicted by the surface state model for a simplified case. The surface state

model is valid when the surface-state density of the semiconductor is large enough, i.e. > 10^{14} cm^{-2}. Therefore, the barrier height, Φ_{MS}, is independent on the metal part [168, 169]. For the n-type semiconductors, the barrier height can be expressed by equation 21.

$$\Phi_{MS}^{n} \approx 2/3 \cdot E_g^{n} \tag{21}$$

Where E_g^{n} denotes the n-type semiconductor bandgap. For p-type semiconductors, the barrier height can be expresses by equation 22.

$$\Phi_{MS}^{p} \approx 1/3 \cdot E_g^{p} \tag{22}$$

Where E_g^{p} denotes the bandgap of p-type semiconductors. According to the surface state model, the barrier height is only dependent on the bandgap of semiconductors when the working temperature of Schottky diode changes. This has been confirmed by Crowell [169] using the Au/n-Si Schottky diode.

For the general case, the barrier height results from the work function difference of metals and semiconductor. If the work function of the metal is larger than that of the semiconductor, the electrons will flow across the interface from the semiconductor to the metal. To equalize the Fermi levels, the band tends to bend upward leaving a depletion region in the semiconductor as shown in the Figure 27a. The space charge is then due to the donor ions when the conduction electrons are completely depleted. If the space charge is assumed to be distributed uniformly, the electric field will increase linearly along with the distance starting from the depletion region. Therefore, the electrostatic potential will increase quadratically leading to the potential barrier that is known as the Schottky barrier.

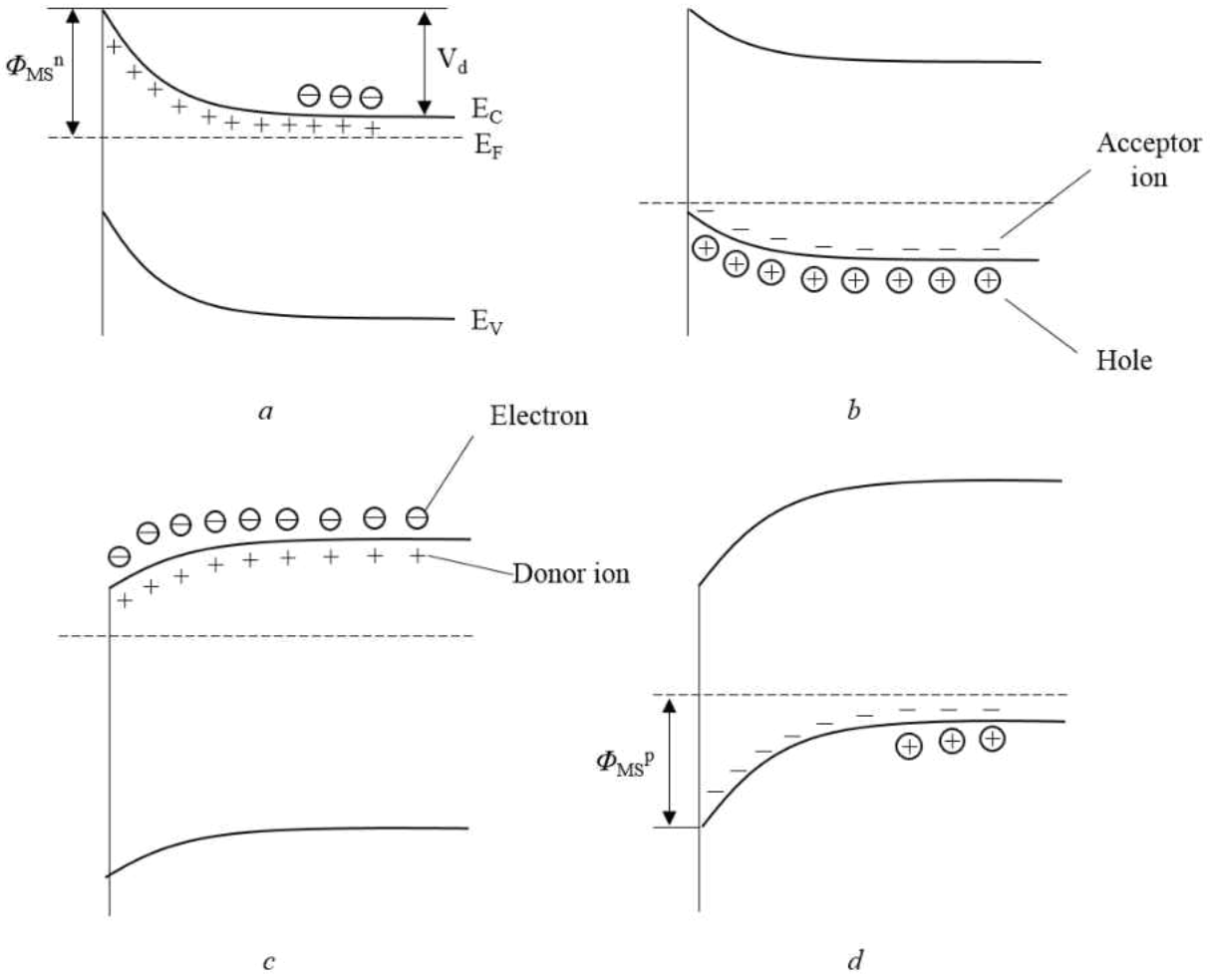

Figure 27. Schematic energy diagram of Schottky barriers for different types of semiconductors and metals: a. $\Phi_M > \Phi_S$, n-type; b. $\Phi_M > \Phi_S$, p-type; c. $\Phi_M < \Phi_S$, n-type; d. $\Phi_M < \Phi_S$, p-type [170].

The diffusion potential indicates the amount that the bands bend. It can be expressed as the difference in work functions of the metal and semiconductor,

$$V_d = \Phi_M - \Phi_S \tag{23}$$

As mentioned above, the diffusion potential is positive and the band will bend upward if the work function of metal is larger. For the n-type semiconductor, this will result in a Schottky barrier height as shown in Figure 27a.

$$\Phi_{MS}^{n} = V_d + (E_C - E_F)$$
$$= \Phi_M - \chi \quad (24)$$

Where E_C and E_F denote the energy of conduction band and Fermi level respectively. χ is the semiconductor electron affinity that is the energy required to remove the electron from the bottom of the conduction band to the vacuum level.

$$\chi = \Phi_S - (E_C - E_F) \quad (25)$$

For the p-type semiconductors, there is not hole motion despite of bending bands as shown in Figure 27b. Thus, the rectifying behavior cannot be observed due to the 'ohmic' contact.

On the other hand, the bands tend to bend downward when the work function of metal is lower than that of the semiconductor. For the p-type semiconductor, the bending bands result from the electron diffusion from the metal to the semiconductor as shown in Figure 27d. The electrostatic field is attributed to the acceptor ions in the space charge region. If the acceptor ions are assumed to be uniformly distributed, the electrostatic strength and potential vary linearly and quadratically respectively with distance from the edge of the depletion region. The Schottky barrier height can be expressed by the equation 24.

$$\Phi_{MS}^{p} = V_d + (E_F - E_V)$$
$$= E_g - (\Phi_M - \chi) \quad (26)$$

For the n-type semiconductor, the electrons will not diffuse despite of bending bands leading to the ohmic contact as shown in Figure 27c.

The rectifying behavior of Schottky diode can be expressed by equation 27 [171],

$$I = A^* T^2 e^{-\Phi_{MS}/kT}\left[e^{qV/kT} - 1\right] \quad (27)$$

where A^* is the effective Richardson constant, k is the Boltzmann constant, q is the electron charge, and T denotes the operation temperature. It has been found that when $V \geq 3kT/q$, the relation between lnI and V is linear. The saturation current I_s can be estimated by the intercept of such straight line at V=0, and defined as

$$I_s = A^* T^2 e^{-\Phi_{MS}/kT} \tag{28}$$

Apparently, I_s/T^2 decreases linearly with the increase of $1/T$ if the I_s is determined by the equation 28. Thus, the Schottky barrier can be calculated through the intercept of such linear line. However, this is only applicable when Φ_{MS} is constant and independent on the working temperature.

The equation 27 was then modified by Atalla *et al*. as shown in equation 29 [172]

$$I = I_s\left(e^{qV/nkT} - 1\right) \tag{29}$$

where n is a constant that is larger than 1. It can be adjusted to fit the curves for those non-ideal Schottky barriers. However, Padovani *et al*. investigated the Au/GaAs Schottky barrier and found the non-ideal factor is dependent on the temperature,

$$n = 1 + T_0/T \tag{30}$$

where, T_0 was found to be 50 ± 5 ° K for Au/GaAs Schottky barrier.

2.2.3 p-n junction

When the p-type and n-type semiconductors are joined together, the carrier diffusion happens due to the concentration gradients at the junction. Specifically, the holes from the p-type side tend to diffuse into n-type side. Meanwhile, the electrons from the n-type side diffuse into p-type side. As the process of carrier diffusion continues, some negative acceptor ions are left at the p-side near the junction. Similarity, some positive donor ions are left uncompensated at the n-

side near the junction as shown in Figure 28. Therefore, the negative charges accumulate at the p-side while the positive charges forms at the n-side. This space charge region will create an internal electric field with direction from n-side to p-side. The electric field can cause the hold drift from right to left and electron drift in the opposite direction. Apparently, the direction of the drift current is different from the diffusion current.

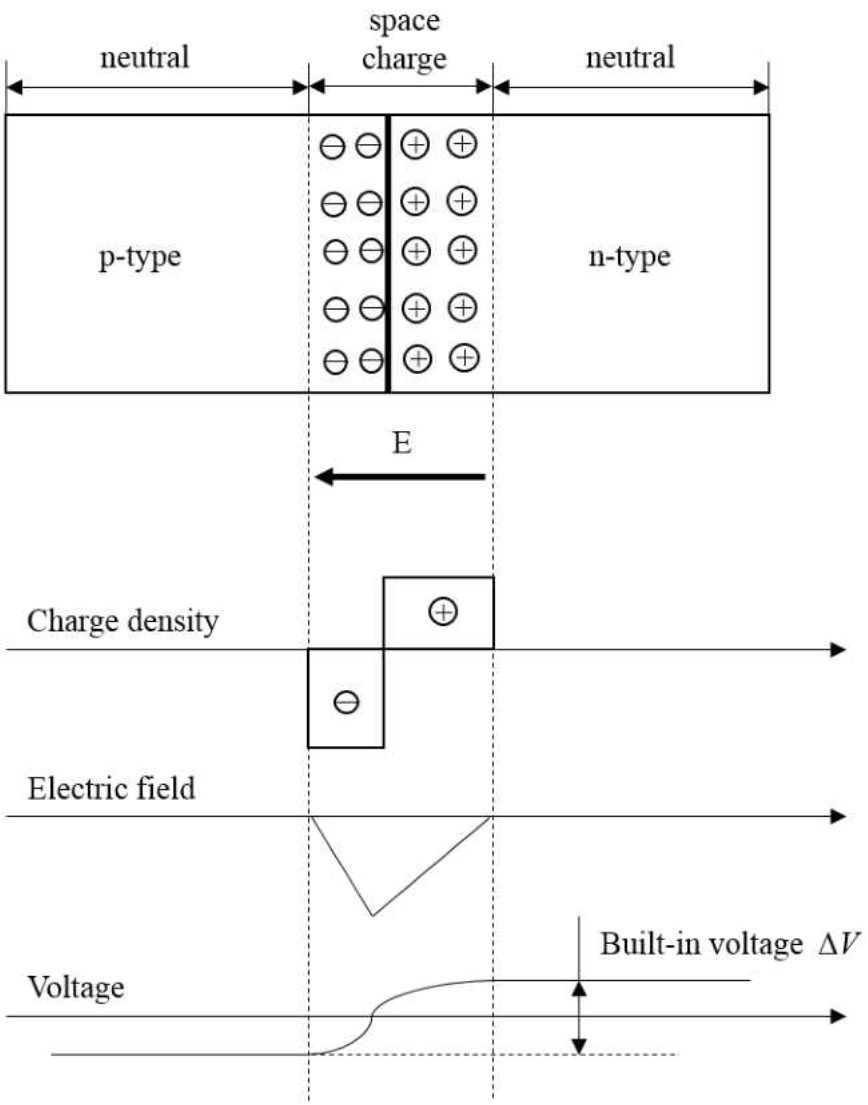

Figure 28. Schematic diagram of p-n junction in thermal equilibrium with zero-bias voltage applied [173].

At thermal equilibrium, these diffusion current and drift current are identical at a given temperature. Due to the internal electric field, the total electrostatic potential difference at the space charge region at steady-state condition can be calculated as the build-in potential.

$$V_{bi} = \frac{kT}{q}\ln\left(\frac{N_A N_D}{n_i^2}\right) \tag{31}$$

where N_A and N_D are the concentrations of acceptors and donors respectively in the depletion region, and n_i is the carrier concentration in the neutral region.

If a forward biased voltage is applied on the p-n junction as shown in Figure 29b, the total electrostatic potential across the junction will decrease to V_{bi}-V_F, leading to a narrower depletion region. Thus, more electrons have enough energy to overcome the smaller energy barrier and diffuse from the n-side to p-side. Similarly, more holes will diffuse over the shrinking energy barrier from p-side to n-side. This process is named as the minority carrier injections. On the other hand, if a reverse biased voltage is applied, the total electrostatic potential across the junction will increase to V_{bi}+V_R, resulting in a wider space charge region. It is more difficult for minority carriers to diffuse over the energy barrier and this can remarkably reduce the diffusion currents. The drift current is mainly dependent on the concentrations of minority carriers. Therefore, the barrier change due to either forward or reverse bias has negligible effect on the drift current. The drift current and diffusion current coexist in the space charge region whenever the p-n junction is in steady state conditions.

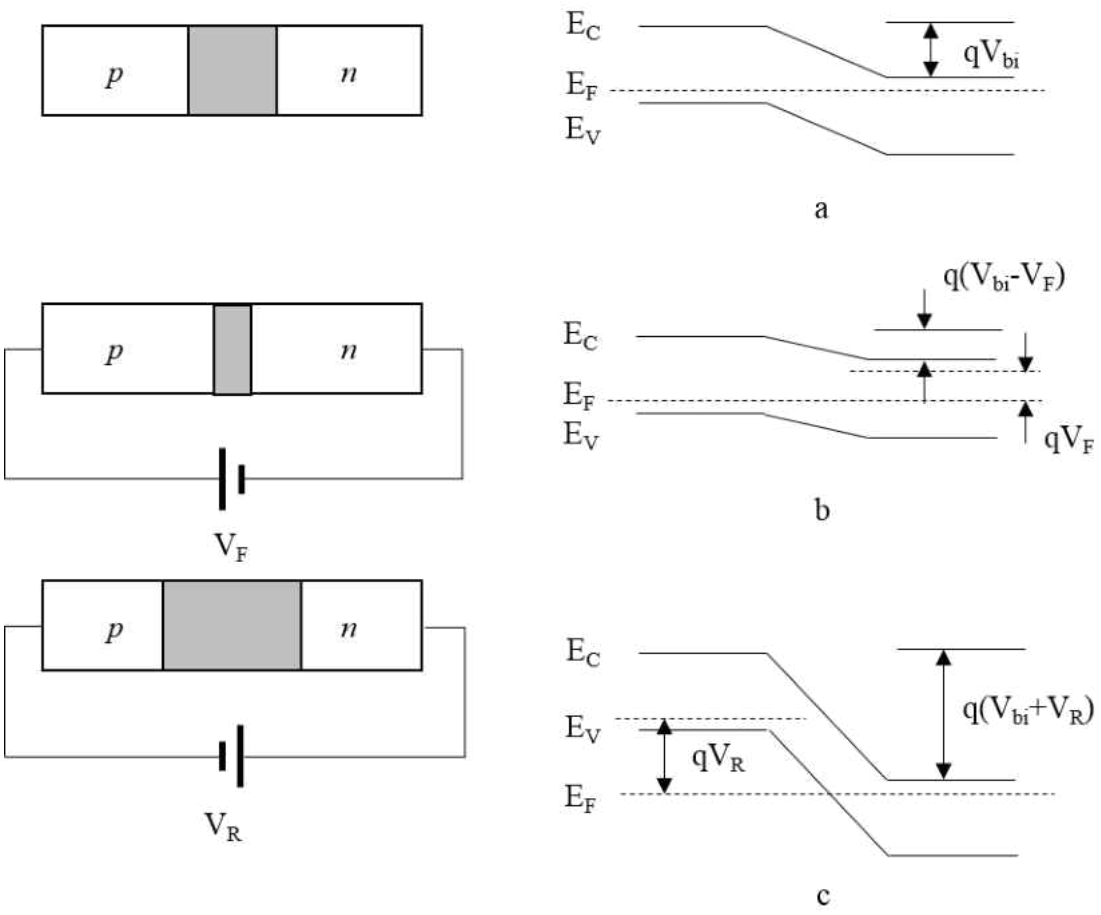

Figure 29. Schematic diagram of p-n junction under various conditions. a. thermal equilibrium condition, b. forward bias condition, c. reverse bias condition [170].

The p-n junction exhibits rectifying behaviors based on the following assumptions. First, the build-in potential and applied voltage are supported by a diploe layer with abrupt boundaries, and it is assumed to be neutral for the outside of the semiconductor boundaries. Second, Boltzmann statistics is effective. Third, the injected minority carrier densities are smaller than the majority carrier densities. Fourth, there is no generation-combination that exists inside the space charge region, and the currents of electrons and holes are constant throughout the depletion region. For an ideal case, the current-voltage characteristics of p-n junction can be described by Shockley equation [174].

$$I = I_s(e^{qV/kT} - 1) \tag{32}$$

$$I_s = \frac{qD_p p_{n0}}{L_p} + \frac{qD_n n_{p0}}{L_n} \tag{33}$$

where D_p and D_n are the diffusivities of the holes and electrons respectively. p_{n0} is the hole concentration in the neutral region of n-type semiconductors, while n_{p0} is the electron concentration in the neutral region of p-type semiconductors. L_p and L_n denote the depletion lengths of p-type and n-type semiconductors respectively.

The operation temperature has a significant influence in the device performance. Both diffusion and recombination-generation currents depend strongly on the temperature. For the forward-bias case, the ratio of diffusion current to the recombination current can be expressed by the following equation.

$$\frac{I_{diff}}{I_{rec}} \approx \exp(\frac{E_g + qV}{2kT}) \tag{34}$$

The ratio is determined by temperature and the bandgap of semiconductor. Generally, the recombination current dominates when the device is applied by a small forward voltage at room temperature. The diffusion current will become dominant when a higher forward voltage is applied. At a given forward bias, the diffusion current will increase more rapidly than the recombination current as the temperature increases.

For the one-side p^+-n junction, the diffusion current dominates. The dependence of the saturation current on the temperature can be estimated by the following equation.

$$I_s \approx \exp(\frac{E_g}{kT}) \tag{35}$$

Therefore, the bandgap of semiconductor can be obtained from the slope of I_s versus 1/T.

For the p^+-n junction in the reverse biased condition, the ratio of the diffusion current to the generation current is given as,

$$\frac{I_{diff}}{I_{rec}} \approx \frac{n_i}{N_D}\frac{L_p}{W}\frac{\tau_g}{\tau_p} \tag{35}$$

where τ_g and τ_p are the generation lifetime and p-type carrier lifetime respectively. W is the width of space charge region. Similar to the forward-bias case, the diffusion current will eventually dominate as the operation temperature increases.

The heterojunction can be formed when two different semiconductors are joined together as shown in Figure 30. The two semiconductors are supposed to have different work function and band structure, including bandgap, conduction band, valance band and Fermi level. The Figure 30b shows the thermal equilibrium state of the heterojunction. It is assumed that the heterojunction is ideal without traps or generation-recombination centers at the interface. Besides, the two semiconductors have closely matched lattice constants. The total built-in potential can be expressed by the following equations.

$$V_{bi} = V_{b1} + V_{b2} \tag{35}$$

$$V_{b1} = \frac{\varepsilon_2 N_2 (V_{bi} - V)}{\varepsilon_1 N_1 + \varepsilon_2 N_2} \tag{36a}$$

$$V_{b2} = \frac{\varepsilon_1 N_1 (V_{bi} - V)}{\varepsilon_1 N_1 + \varepsilon_2 N_2} \tag{36b}$$

where, ε is the dielectric permittivity, and N denotes the dielectric constant.

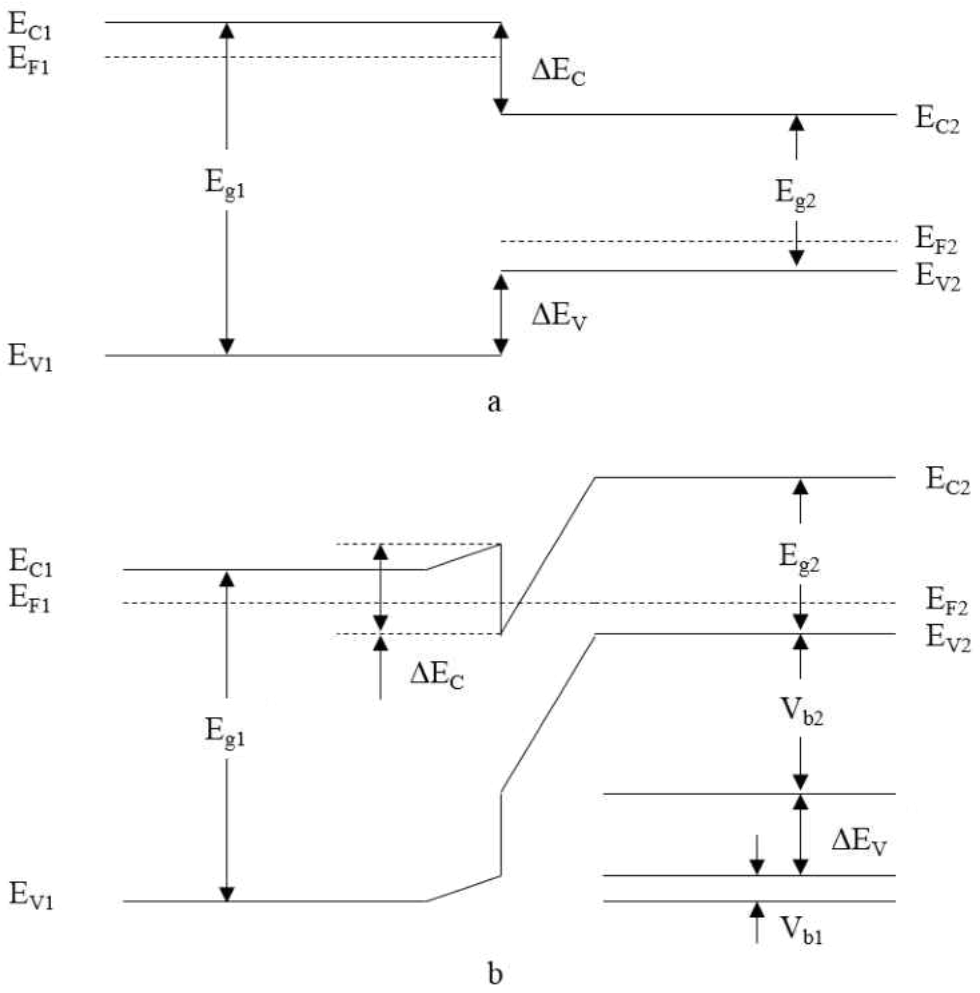

Figure 30. Schematic diagram of band energy of heterojunction. a. before contact, b. thermal equilibrium [170].

2.2.4 Constrains and challenges

High temperature photoelectrochemical water splitting faces several constraints and challenges. The most needed theoretical research is to establish the quantitative criteria for suitable semiconductors; that is to identify the band edge alignments of various semiconductors with regard to absolute H_2O redox potentials at high temperature, similar to the Figure 4 diagram shown in [175]. However, at high temperature many parameters (i.e. absolute position of the

hydrogen electrode, bandgap, absolute positions of the valence band edge and the conduction band edge) are unknown/unclear and therefore in need of both experimental and theoretical investigations. First, the water electrolysis redox potential changes with temperature, resulting in multiple diagrams needed for different temperatures. Also the absolute position of the hydrogen electrode will shift with increasing temperature and various hydrogen gas partial pressures, based on the Nernst equation below

$$E = \frac{RT}{F} ln \frac{a_{H^+}}{\sqrt{p_{H_2}/p_0}} \tag{37}$$

where a_{H+} is the activity of H^+ which depends on temperature as well; p_{H2} and p_0 are the partial pressure of hydrogen gas and the standard pressure, respectively. Second, the bandgap energy reduces with increasing temperature, but research on the impact of high temperatures on semiconductors is extremely limited. The correlation expressed in Eq. 21 is rather empirical, such that the experimental research on high temperature for various semiconductors are critical. Third, the shifts of absolute positions of the valence band edge and the conduction band edge with increasing high temperature are unknown. At low temperature, they were derived from the electronegativity,[175] but electronegativity itself is also dependent on temperature. Another major constraint of high temperature photoelectrochemical water splitting is its energy conversion efficiency at elevated temperatures. The efficiency limit for a PEC device made of a single junction diode can be expressed as [176],

$$\eta_{PEC} = \frac{j_{op} E_{rxn} f_{FE}}{P_{in}} \tag{38}$$

where j_{op} is the maximum exchange current density; E_{rxn} is the Nernst potential of water electrolysis; f_{FE} is the faradaic efficiency, which ideally is unit; P_{in} is the incident solar power.

The maximum efficiency occurs when the electrolysis voltage is very close to the Nernst potential and the current density peaks.

At higher temperatures E_{rxn} decreases, as shown in Eq. 18, which contributes to a reduction of the efficiency limit. The variation of another ruling factor j_{op} however, remains undetermined because there are two competing changes. As temperature increases, the absorber efficiency decreases due to radiation loss, whereas the carrier transport and kinetics become more activated [177]. Commonly the theoretical efficiency limit of a single junction PEC or solar cell decreases as temperature increases [177, 178]. In some rare cases, large bandgap semiconductors may shift to their peak efficiency at higher temperature due to bandgap shrinkage. Note that Eq. 21 does not include the terms of overpotentials, which could significantly impact the practical efficiency. At higher temperatures however, overpotentials become trivial, which makes the practical efficiency very close to the theoretical prediction. Nevertheless, the solar-to-hydrogen efficiency of high temperature photoelectrochemical water splitting needs further investigations to provide insights into the factors that influence the SOPC performance and to improve its efficiency.

2.3 SOPC configuration

Figure 31 shows a schematic diagram of an SOPC for hydrogen and syngas (H_2+CO) production, based on the outcomes of the experimental investigations. A SOPC integrates a photovoltaic (PV) cell and an electrolysis cell. The PV cell consists of a p-n junction diode that converts sunlight into electron-hole pairs and creates an electrolysis voltage. The materials used for both n-type and p-type semiconductors are metal oxides that are electrochemically stable in strong oxidizing environment and high temperature. The electrolysis cell is similar to a common SOEC [87], which consists of a hydrogen cathode, an oxygen ion conducting electrolyte, and an

oxygen anode. For a complete circuit, the excited electrons are conducted through an external circuit to the cathode, where they combine with protons to generate H_2. Oxygen ions (O^{2-}) migrate through the ion-conducting electrolyte to the anode, where they combine with positive holes to produce O_2 gas.

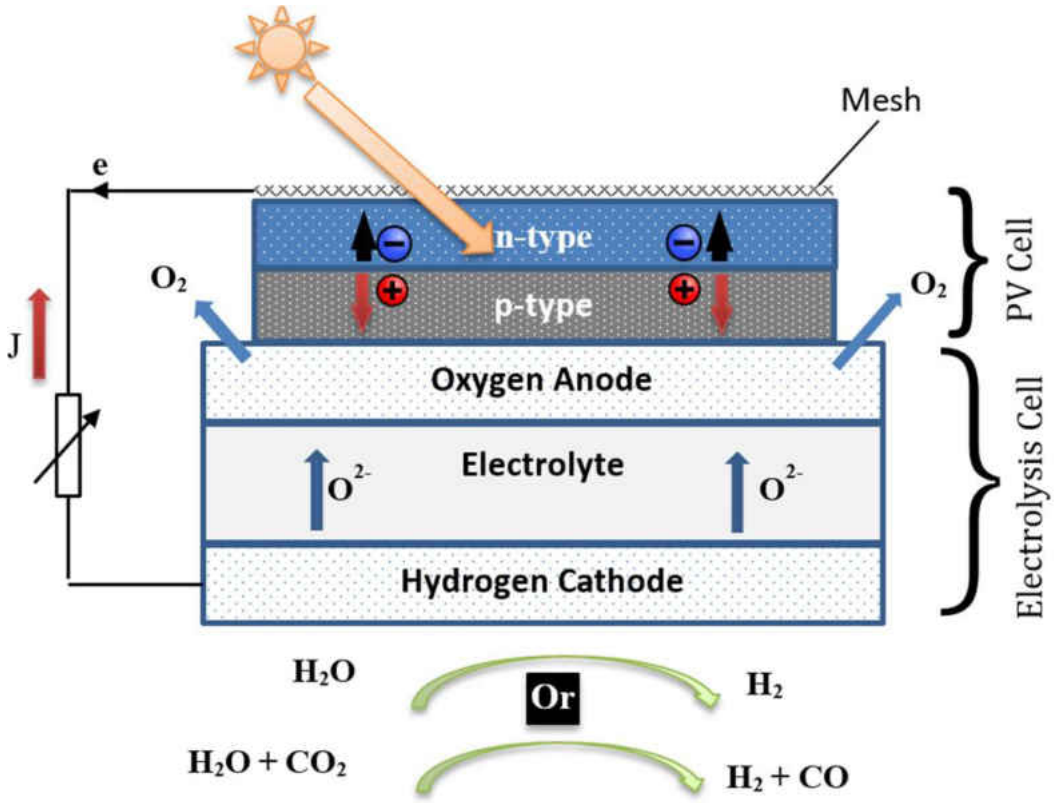

Figure 31. Schematic diagram of hydrogen or syngas (H_2+CO) production using a SOPC, which integrates a PV cell and an electrolysis cell [179].

Note that although theoretically possible, the research results in the following section indicate that Schottky diodes could easily lose their PV characteristics at elevated temperatures,

such that they may not be suitable for application in SOPCs. In addition, noble metals used in the Schottky diodes make them less attractive for further research due to cost considerations.

In addition to the capability of splitting H_2O, this SOPC can also be used to produce syngas (H_2+CO), if the feedstock consists of a steam and CO_2 mixture, as shown in Figure 31. Syngas can further be used to synthesize liquid fuel using the Fischer–Tropsch process [180]. Syngas production is a unique capability of the SOPC, which conventional PECs cannot achieve.

2.4 Experimental

2.4.1 Electrolysis cell materials

The high temperature electrolyte materials for the SOPCs are similar to the ceramic electrolytes used in SOECs. Materials such as yttria-stabilized zirconia (YSZ), scandia-stabilized zirconia (ScSZ), and gadolinia doped ceria (GDC) are widely used as the electrolytes in SOECs [87]. Those ceramic electrolytes operate over a temperature range from 400°C to 900°C [55]. The high ionic conductivity of those materials at high temperature makes those oxides ideal for SOPCs. Platinum (Pt) can be used as the hydrogen electrode for research purposes, due to its electrochemical stability and excellent catalytic activity at high temperature. Practically, nickel (Ni) can be used as the hydrogen electrode due to its low cost and relatively high catalytic activity at high temperature [181]. The oxygen electrode is made of perovskite oxides that have both high electronic conductivity and catalytic activity for oxygen reduction. Common oxygen electrode materials used in SOECs [87] include, Lanthanum Strontium Manganite (LSM), Lanthanum Strontium Cobaltite (LSC), and Lanthanum Strontium Cobalt Ferrite (LSCF).

2.4.2 PV cell materials

The most critical component in a SOPC is the photocatalytic diode formed by semiconductors. The following selection criteria of semiconductors are proposed as the guideline

for selecting suitable semiconductors. First, the selected semiconductor is electrochemically stable at high temperature (400-800 °C), which means the material has a high melting point and cannot be further oxidized. Many metal oxide semiconductors fall in this category. Second, selected p-type and n-type semiconductors are able to form a p-n junction and maintain an acceptable performance at elevated temperatures. That means the PV cell needs to work at above 400 °C and provide enough electrolysis voltage in the meantime.

Following the criteria above, Table 2 lists some metal oxide based p-n junction diodes that have been reported to demonstrate good rectifying behaviors at room temperature. Note that those semiconductors were handpicked from many candidates from a review article [182] because they demonstrated large knee voltages (V_{knee} >1 V). The knee voltage correlates the V_{OC} of a PV cell under solar irradiation. Therefore, it is expected that the photo-generated voltages achieved by those selected diodes will overcome the Nernst potentials of water splitting at high temperature. Once the rectifying behaviors at high temperature are proved to be acceptable, they can be integrated into the SOPC for evaluation. Table 2 also includes some high temperature p-n junction diodes that were either reported in the literature or are from the present research.

Table 2. Selected p-n junction diodes for further evaluation of their rectifying properties at high temperature (partially adapted from [182]) .

Semiconductors		**Rectifying Properties**		**Ref.**
n-type	p-type	V_{knee}	*Temp.*	
ZnO	$SrCu_2O_2$	1-3 V	room	[183, 184]
ZnO	$ZnRh_2O_4$	2 V	room	[185]
ZnO	NiO	1 V	room	[186, 187]
GIZO	$ZnCo_2O_4$	2.5 V	room	[188, 189]
$SrTiO_3$	$LaSrCrO_3$	-	room to 500°C	[190]
TiO_2	$LaSrMnO_3$	0.74-4.29 V	room to 500°C	This study

TiO_2	$LaSrCoO_3$	0.18-2.75 V	room to 500°C	This study
TiO_2	$LaSrCoFeO_3$	0.49-3.67 V	room to 500°C	This study

Figure 32 shows an even broader range of candidate semiconductors that might be able to form acceptable p-n junctions at high temperature. The band alignments of selected n- and p-type oxide semiconductors imply the research direction of the proposed SOPC in the future. As mentioned previously, Brunauer *et al.* fabricated SOPCs using $SrTiO_3$/$LaSrCrO_3$ based diodes and demonstrated a fully functional photoelectrochemical oxygen pump [190]. Their work first experimentally proved that the concept of p-n junction based SOPC is feasible.

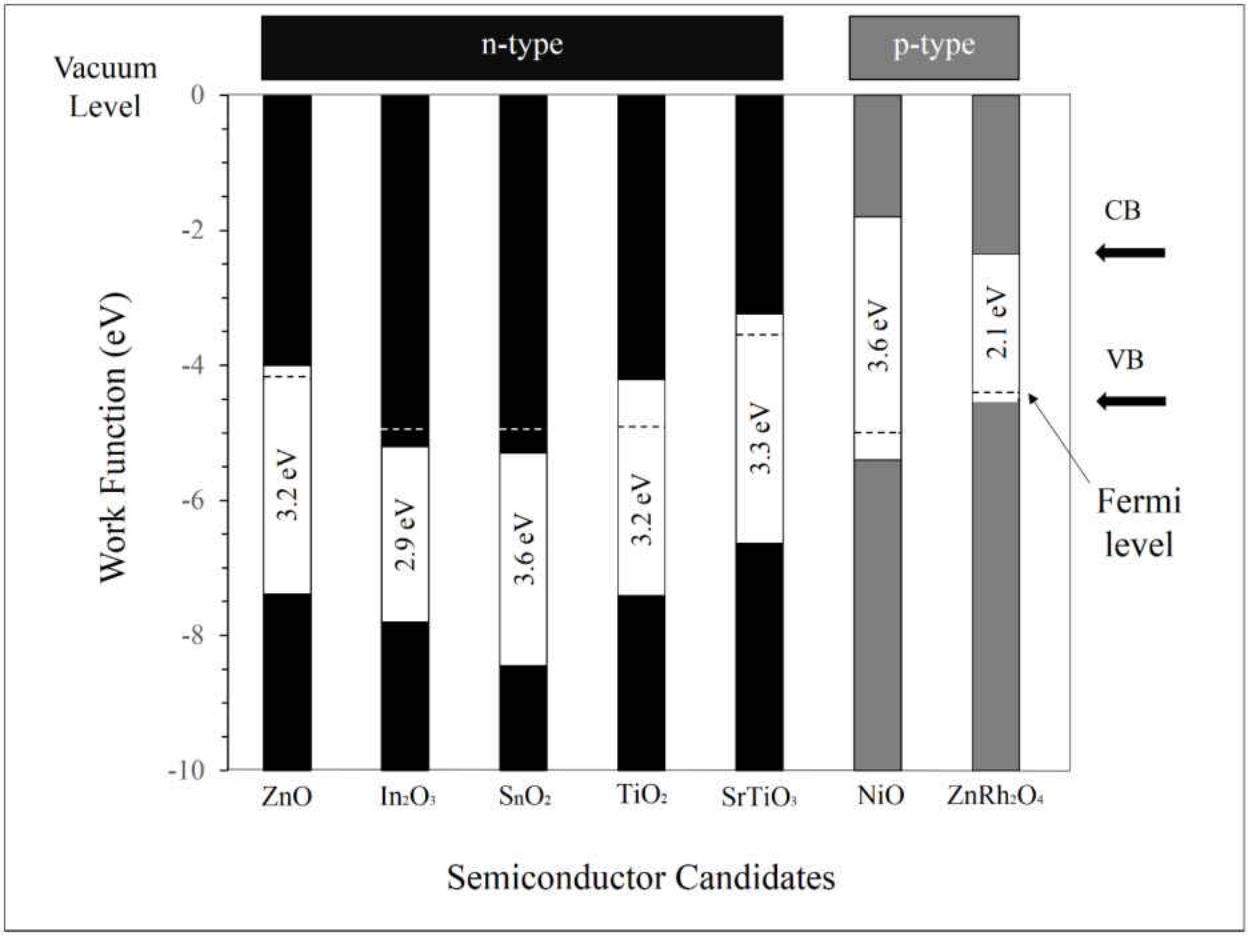

Figure 32. Band alignment of candidate n- and p-type oxide semiconductors suitable to form p-n junction diodes (adapted from [3, 175, 191, 192]).

In the present research, LSM, LSC, LSCF and NiO were selected as p-type semiconductors and expected to form p-n junctions with n-type TiO_2, ZnO and Fe_2O_3. Those materials were selected due to their p-type conductivity previously reported [193, 194].

2.4.3 Experiments

The investigation to date has therefore been focused on characterizing the rectifying behaviors of various diodes at elevated temperatures. The TiO_2 based diodes were fabricated

using direct oxidation. Titanium (Ti) pellets with dimensions of 1.5×1.5×0.1 cm^3 were initially oxidized in a muffle furnace (GSL-1100X, MIT Co.) at 700 °C for 10 hours to obtain a thin layer of TiO_2. The thickness of the oxide layer was approximately 2 μm, measured by a field emission scanning electron microscopy (Hitachi S-4700 FE-SEM) as shown in Figure 33. One side of each pellet was then polished to remove TiO_2 layer for current collection.

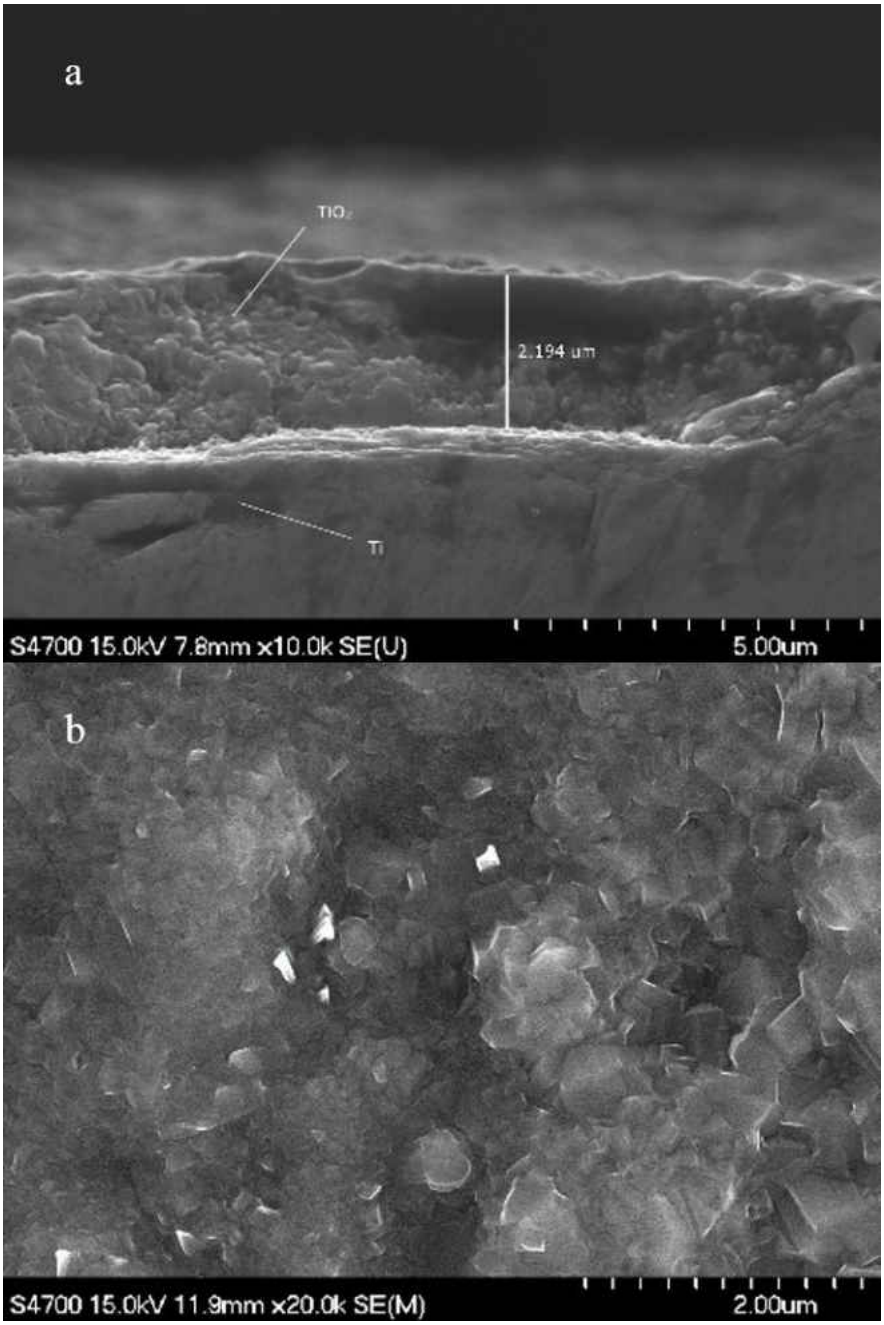

Figure 33. SEM images showing the (a) cross-section and (b) surface of the Ti/TiO2 pellets prepared by thermal oxidation [179].

To fabricate an Ag/TiO_2 Schottky diode, electron beam physical vapor deposition (EBPVD) (PVD 75, KJLC) was used to deposit an Ag layer above the TiO_2 surface. Ag slugs

(Fisher Scientific, 99.99% purity) were used as the sintering targets. A mask was adopted during deposition to ensure that silver was deposited only onto a circular area of 0.25 cm^2. Prior to deposition, the e-beam chamber was pumped down to 1.5×10^{-4} Pa to minimize the impact of residual gases. The Ag layer was deposited at 8 kV with an emission current of 66 mA. The thickness of the Ag layer was measured as 560 nm with an average deposition rate of 1.71 Å/s.

To fabricate p-n junction diodes, LSM, LSC and LSCF powders (Fuelcellmaterials, USA) were first mixed respectively with α-terpineol (Fisher Scientific) and ethanol (100%, Fisher Scientific) with a weight ratio of 1:0.5:10. The prepared slurries were then deposited onto TiO_2 layers using a spin coater (VTC-100, MTI Co.). The coating process included three cycles, each of which was performed at 3000 rpm for 40 seconds. Finally the prepared pellets were sintered at 700 °C to obtain a dense layer.

The rectifying properties of TiO_2 based diodes were characterized by I-V measurements using a Keithley 2400 SourceMeter. The scanning voltage was set symmetrically with a maximum current of 10 mA. Silver wires were attached on both sides of the diodes for current collection. The cells were tested in the center of a tubular furnace (GSL-1100X, MTI Co.) with temperatures ranging from room temperature to 500 °C.

2.5 Results and discussion

Based on the aforementioned criteria, suitable diodes for implementation in SOPCs should demonstrate acceptable rectifying behaviors at temperatures >400 °C, in accordance with the minimum operating temperature of electrolyte materials. In this study, Schottky diodes (Ag/TiO_2) and p-n junction diodes (LSM/TiO_2, LSC/TiO_2, and $LSCF/TiO_2$), were evaluated systematically from room temperature to 500 °C.

The representative rectifying behaviors of TiO_2 based diodes are shown in Figure 34. In all the cases shown in Figure 34, temperature significantly affected the rectifying properties, which diminished as the temperature increased. As a combination of the generation current (I_{gen}) and the reverse diffusion current (I_{diff}), the saturation current of TiO_2 based diodes became remarkable once the temperature surpassed 400 °C. Specifically, the generation current was caused by thermal generation of electron-hole pairs within the depletion region of diodes and the diffusion current resulted from minority carriers diffusing across the depletion region. Both I_{gen} and I_{diff} are proportional to $\exp(-E_g/xkT)$ where $x = 1$ for I_{diff} and $x = 2$ for I_{gen}. At elevated temperature, I_{gen} was dominant at forward bias making the diode junctions nearly ohmic contact while I_{diff} was more noticeable at reverse bias leading to a higher leakage current of TiO_2 based diodes.

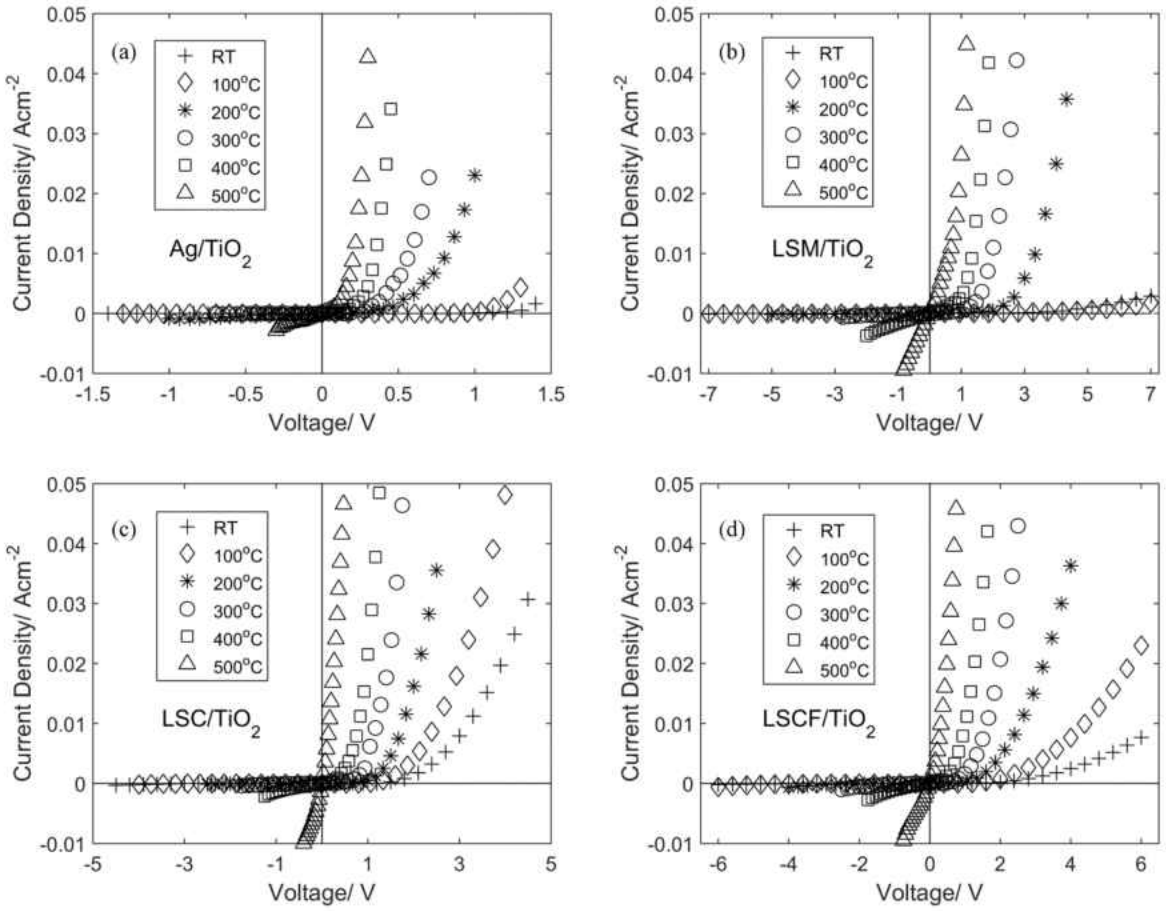

Figure 34. Rectifying characteristics of TiO_2 based diodes from room temperature to 500 °C. (a), (b), (c) and (d) show the Ag/TiO_2, LSM/TiO_2, LSC/TiO_2 and $LSCF/TiO_2$ diodes respectively [179].

The knee voltage (V_{knee}) is a performance indicator of diodes at elevated temperatures. Beyond such knee points in the *I-V* curves, the current *I* starts increasing rapidly with an increase of voltage *V*. In this paper, the knee voltages were obtained from the intersection point of voltage axis and tangent line of rectifying curves in the saturation zone. The knee voltage corresponds to an open circuit voltage that a diode works as a PV cell at various temperatures. A suitable diode for the SOPC must demonstrate a knee voltage that is larger than the Nernst potential for

electrolysis at a given temperature. As shown in Figure 34a, V_{knee} of Ag/TiO_2 based Schottky diode decreased significantly from 1.26 V at room temperature to 0.22 V at 500 °C, way below the Nernst potentials for electrolysis at those temperatures. Consequently Ag/TiO_2 diodes are not suitable for the SOPC at high temperature. The results also agree with the low photo-response voltages of TiO_2 based Schottky diodes reported by Fleig *et al* [53] and us [57]. The investigation was shifted to p-type semiconductors such as LSM, LSC and LSCF, which might form stable and strong junctions with n-type TiO_2 at high temperature.

Compared to the Schottky diodes, all the p-n junction diodes, including LSM/TiO_2, LSC/TiO_2, and LSCF/TiO_2, exhibited larger knee voltages at elevated temperatures, as shown in Figure 34 b-d. Among all the p-n junction diodes, LSM/TiO_2 performed best by demonstrating the largest knee voltages, while LSC/TiO_2 performed worst. The low performance of LSC was due to its relative high electronic conductivity, which was reported to be more than 1500 S/cm even below 500 °C [194], leading to lower knee voltages of LSC/TiO_2. The electronic conductive property of LSC could be suppressed by adding element Fe into the compound. Less than 150 S/cm was reported in LSCF below 500 °C [194], resulting in better rectifying properties of LSCF/TiO_2 than LSC/TiO_2. In fact, recent research indicated that LSCF and LSM act as p-type semiconductors up to certain temperatures [193, 194]. Therefore, a stronger junction could be formed if these p-type materials were coated onto n-type TiO_2 surface, resulting in higher knee voltages of these two diodes.

Figure 35 summarizes the knee voltages of TiO_2 based diodes from room temperature to 500 °C obtained from curve fitting in Figure 34. In all TiO_2 based diodes, V_{knee} decreased linearly as temperature rose. The reduction rates of V_{knee} were calculated as -2.3 mV/°C, -8.5 mV/°C, -5.3 mV/°C and -7.3 mV/°C for Ag/TiO_2, LSM/TiO_2, LSC/TiO_2, and LSCF/ TiO_2

respectively. To obtain an appropriate diode for used in the SOPC, one must obtain a V_{OC} that is larger than the Nernst potential for steam electrolysis. However, most TiO_2 based diodes except LSM/TiO_2 in this present research failed to satisfy this requirement and are therefore not appropriate for use in SOPCs. As a comparison, the estimated knee voltages of LSM/TiO_2 diodes were 1.26 V, 1.03 V and 0.74 V compared with the electrolysis (90% steam inlet) thresholds of 0.98 V, 0.96 V and 0.94 V at 400 °C, 450 °C and 500 °C respectively.

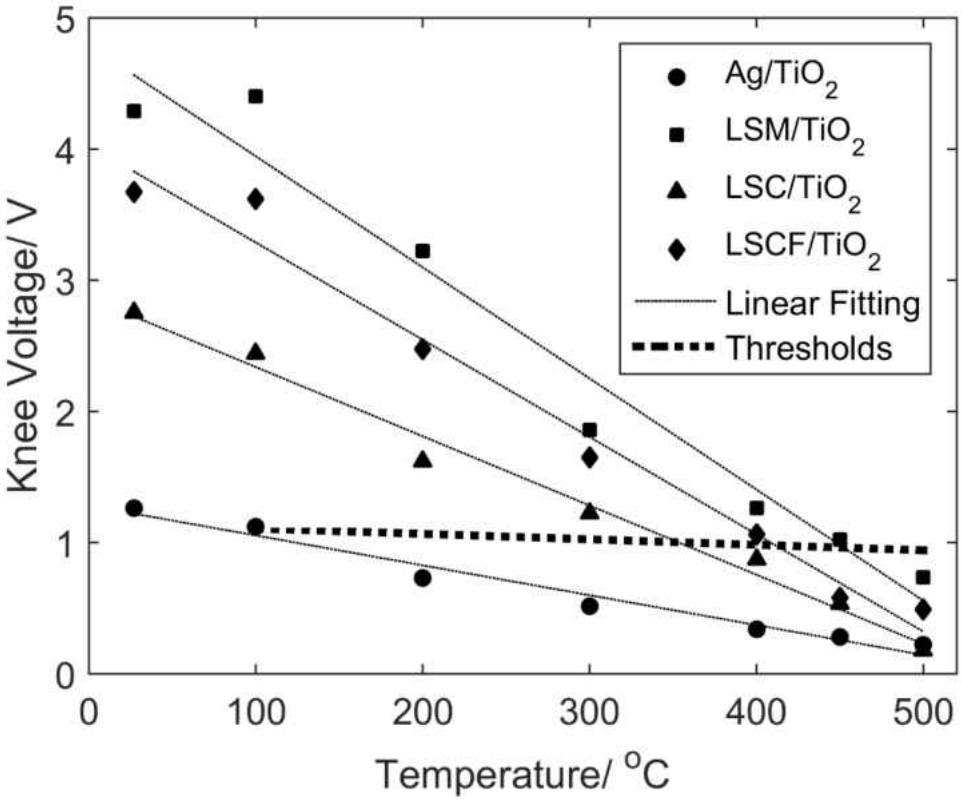

Figure 35. Knee voltages of Ag/TiO_2, LSM/TiO_2, LSC/TiO_2 and $LSCF/TiO_2$ diodes as a function of temperature compared to thresholds of steam electrolysis [179].

As a result of the present research, LSM/TiO_2 became the only candidate for the SOPC, which is limited to operate at below 450°C. Some common electrolyte materials, such as YSZ

and ScSZ, are excluded in this case due to their higher operating temperature (above 700 °C) [195, 196]. Thus, to ensure considerable ionic conductivity the appropriate electrolyte material is limited to ceria based ceramics, such as GDC, which is commonly used for intermediate temperature SOFCs above 400 °C [197]. In addition, Samaria-doped ceria (SDC) [198] and $Ba(Zr_{0.1}Ce_{0.7}Y_{0.2})O_{3-\delta}$ (BZCY7) [199] electrolytes were also reported to maintain high ionic conductivities at 400 - 700 °C and 450 - 600 °C, respectively. As a practical material for hydrogen electrodes, Ni could still maintain its high catalytic property and low resistance at low temperature if mixed with those electrolyte materials. Nevertheless, more candidate p-n junction diodes need to be evaluated at high temperatures.

2.6 Summary

In this chapter, the concept of solar water splitting using SOPCs was elaborated. The concept provides a totally different pathway for solar water splitting than the conventional low temperature PEC. Experimental investigation was carried out to search for appropriate semiconductor diodes to be used for SOPCs at high temperature. The rectifying properties of both Schottky diodes and p-n diodes, including Ag/TiO_2, LSM/TiO_2, LSC/TiO_2, and $LSCF/TiO_2$, were evaluated from room temperature to 500 °C. The knee voltages extracted from the rectifying curves and the corresponding Nernst potentials for electrolysis at elevated temperatures were used to determine whether a diode is suitable for use in SOPCs and worth further research. The results showed that only LSM/TiO_2 was suitable for the application in SOPC. Further research will focus on the integration of the LSM/TiO_2 diode and electrolysis cells to demonstrate water splitting at high temperature using light. In addition, other semiconductors materials, such as those listed in Table 2 and Figure 32, need to be explored for potential use in SOPCs.

CHAPTER 3

FABRICATION OF SOLID OXIDE ELECTRODES USING 3D PRINTING

In this chapter, 3D printing was applied as an addictive manufacturing technology to fabricate porous electrodes of SOFC/SOPC. Compared to the traditional fabrication techniques such as tape casting, sputtering and screen printing etc., the innovative approach can print the objectives from nanoscale to macroscale, thus having a great potential to accurately control the device geometry, such as dimension, morphology, and structure. Furthermore, 3D printing provides a cost-effective method of controlling the thickness and porosity of SOFC/SOPC electrodes. This study focuses on the fabrication of the electrodes of SOFC/SOPC, using homemade composite filaments and a regular 3D printer. The composite filaments of thermoplastic and ceramic materials were preheated and extruded under the specific temperature. The electrodes were then 3D printed using the fused deposition modeling method. The porous ceramic structure was obtained by sintering the green cells in kiln at high temperature. Fully assembled SOFCs were fabricated in house using commercial half cells and 3D printed cathodes. The cell performance was characterized in the fuel cell mode between 700 and 800 °C, to compare with the performance of cells that were fabricated via conventional dip-coating method.

3.1 Background

3D printing (aka. additive manufacturing) technology usually makes 3D solid objects by fabricating materials layer upon layer. It is generally controlled by modeling software of computer-aided design (CAD), such as AutoCAD, SolidWorks, and Fusion 360, etc. This allows the additive process to lay down successive layers of materials in different shapes and structures. The additive manufacturing process has been grouped by ASTM International and categorized

into seven types [200]: (1) Binder jetting, which deposits liquid bonding to join powder materials; (2) Directed energy deposition, which fuses materials by thermal energy before deposition; (3) Material extrusion, which dispenses material though a nozzle or orifice; (4) Material jetting, which deposits droplets of build material; (5) Powder bed fusion, which fuses regions of a powder bed by thermal energy; (6) Sheet lamination, which bonds material sheets to form an object; (7) Vat photopolymerization, which cures liquid photopolymer by light-activated polymerization. As a comparison, conventional manufacturing that applies cutting and drilling to remove additional materials, which wastes a lot of materials. Currently, 3D printing has been used in many applications during the product life cycle, from prototyping to post-production customization. More interestingly, the estimated market of additive manufacturing will be ranging from $230 billion to $550 billion by 2025 [201].

As mentioned in chapter 1, the components of solid oxide cells are made of ceramics. Specifically, both electrodes require porous structure, for flow distribution and electrochemical reactions on the triple phase boundaries (TPBs). The oxygen ion conductive electrolyte however, must be dense and thin to prevent the gas crossover and minimum Ohmic resistance. The SOFC performance is strongly dependent on the material compositions, thickness, and porosity. Besides, the components has to be mechanically and electrochemically stable at high temperature [202]. For example, the electrolyte need to be sintered around 1500 °C to produce gas-tight layer. The configurations of SOFC stacks are much more complicated with consideration of interconnects, joints, sealing and assembly. It was reported that more than one hundred procedures are required to manufacture SOFC stacks using traditional fabrication methods [203]. Such a huge number of steps make the manufacturing a very complicated task with low efficiency. Furthermore, the application of various fabrication techniques has a remarkable effect on the SOFC performance

and durability. Therefore, it is very difficult for the traditional manufacturing to achieve highly desirable custom-designed products with cost-effective method.

Regarding SOFC technology, the 3D printing approaches to simultaneously control the microstructures, such as TPB, porosity and thickness. Compared to traditional SOFC fabrication methods, the proposed 3D ceramic printing offers several advantages. First, 3D printing has excellent material flexibility and structure controllability. A wide range of feedstock, such as liquid, powder, and filament, can be used by various printers for different applications. Special microstructure, i.e. gas flow channels and porous electrode, can be fabricated precisely by 3D printing via digital CAD design. Second, 3D printing can precisely control the thickness of components. Due to the additive process layer by layer, the total thickness is determined by the unit layer height times the number of layers. For the fused deposition modeling, the former is controlled by the nozzle size and printing speed that are pre-set in the modeling software. For a generally commercial product, the layer height is approximately 200 μm and that allows electrode thickness to be well controlled. Third, 3D printing is considered as the cost-effective and environmentally friendly technique. During the fabrication, the materials are printed directly on the platforms on demand. Such simple one-step process can minimize the material wastage and the energy consumption.

Inkjet printing is the most commonly used 3D printing technique. It is a droplet-based material deposition process and able to fabricate complex configurations with high accuracy. Currently, Inkjet printing has been developed as a non-contact and direct deposition technique for various applications including medical, biology, and electrochemical [204]. Among them, extensive research has been focused on the development of SOFC components. Sukeshini and Cummins applied ink-jet printing to fabricate the NiO-YSZ anode interlayer and YSZ electrolyte

on a tape-cast anode-support cell before sintering at 1400 °C. The thickness of the electrolyte was measured by scanning electron microscopy (SEM) ranging from 6 µm to 12 µm. The ink-jet printed cell exhibited an open circuit voltage (OCV) of 0.95-1.06 V and a maximum power density (MPD) of 0.175 W/cm^2 [205]. Then the author used similar process to fabricate the cell electrolyte with thickness ranging from 10 µm to 12 µm. A better performance with stable OCV of 1.1 V at 800 °C and MPD of 500 mW/cm^2 at 850 °C was achieved [206]. The anode support SOFC was also fabricated with inkjet-print YSZ electrolyte, NiO-YSZ anode interlayer, LSM-YSZ cathode. Similar with the performance of conventional hand-paste slurry SOFC, the cell produced a stable OCV of 1.1 V and a MPD of 430-460 mW/cm^2 at 850°C [207]. Sukeshini also used aerosol jet printing to fabricate the LSM and GDC-LSCF cathode layers. The GDC-LSCF cathode exhibited a better performance than the LSM cathode did. It was found that the cathode current collection layer, layer thickness, solids loading and sintering temperature have a strong impact on the cell performance with a MPD ranging from 200 to 460 mW/cm^2 [208]. Tomov and his co-workers employed inkjet printing to fabricate dense YSZ electrolyte layer on the NiO-YSZ anode support SOFC. The desired electrolyte with thickness of 6 µm was achieved by moderate overlapping of nozzle opening and droplet as well as multiple coatings. With the feedstock of humidified hydrogen and ambient air, the cell could demonstrated a MPD of 170 mW/cm^2 at 800°C [209]. Similarly, the researchers employed inkjet printing to deposit NiO-GDC anode layer and GDC electrolyte layer and achieved uniform coatings with thickness below 15 µm by optimizing the printing procedure [210]. Li *et al*. used thermal inkjet printing to fabricate the thin electrolyte layer of YSZ and buffering layer of $Sm_{0.2}Ce_{0.8}O_{1.9}$ (SDC) for SOFCs. The thickness of YSZ membrane was approximately 1.5 µm and the cell delivered a MPD of 860 mW/cm^2 at 800 °C. Another cell with 7.5 µm-thick YSZ electrolyte, 2 µm-thick SDC buffering

layer and BSCF cathode delivered a MPD of 1040 mW/cm^2 at 750 °C [211]. Esposito *et al*. fabricated a 1.2 µm-thick YSZ electrolyte using inkjet printer and 3.7% vol.% YSZ colloidal water-based ink. The SOFC with configuration of Ni-YSZ/YSZ/YSZ-LSM produced an OCV of 1.15 V and a MPD of 1.5 W/cm^2 at 800°C [212]. Wang *et al*. optimized the inkjet printing parameters for CGO electrolyte fabrication using a custom-built drop visualization system. It was found that 50:50 vol.% mixing ratio of terpineol and methanol could meet the 3d printing criteria, i.e. ink stability, printability and drop integrity. The printing pressure and nozzle opening time for stable printing were in the range of 400-800 mbar and 550-600 µs respectively [213]. These researchers then deposited the CGO electrolyte on the porous NiO-YSZ anode composite via inkjet printing and achieved a thin electrolyte layer with thickness of less than 10 µm [214]. El-Toni *et al*. used inkjet printing to produce a dense GDC electrolyte layer and a honeycomb porous cathode of LSM. The thickness of the 10-layer electrolyte was about 6 µm and the channel density of LSM honeycomb monolith was 700 channels per square inch with channel size of 800 µm [215]. Han *et al*. fabricated the LSCF cathode layer using modified inkjet printer and adjusted the porosity and thickness by grayscale in the printing image. The anode support SOFC exhibited a MPD of 377 mW/cm^2 at 600 °C [216]. Li *et al*. also used the inkjet printer to fabricate the porous cathode layer of SDC/SSC composite. To improve the performance, 10 wt.% pore former was added into the ink and an optimized powder synthesis method was applied to the preparation. The SOFC showed excellent electrochemical characteristics, with a MPD of 940 mW/cm^2 at 750 °C [217]. Yashiro *et al*. fabricated the LSCF-GDC cathode of SOFC via inkjet printing. A painted cathode layer with large particles was then deposited on the inkjet-print layer to improve the gas permeation. An excellent cell performance was demonstrated with an OCV of 0.94 V and a MPD of 0.71 W/cm^2 at 600 °C [218].

Fused deposition modeling (FDM) is another 3D printing technique to fabricate objects layer by layer. Typically, the filaments of thermoplastic materials are heated to the glass transit state and then extruded through a stainless or brass nozzle to print onto the platform. The nozzle movement is controlled by a XYZ stage that is programmed by the computer. Common thermoplastic filaments include ABS, PLA, and PVA etc. Wei *et al*. prepared the 3D printable graphene/ABS composite filament with graphene weight ratio of 3.8 wt. %. The composites were extruded at 210 °C into a 1.75 mm-diameter filament to fit the commercialized 3D printer [219]. Leon *et al*. used FDM to design and construct an undivided electrochemical flow cell. The mass transport characteristics were evaluated using the reduction of ferricyanide, hexacyanoferrate (III) ions at a nickel surface. The results showed that the performance of 3D printed flow cell is comparable to that of traditional cells [220]. Due to the excellent conductivity of graphene, the graphene/ABS composite filament can be potentially used in the electrical circuit design. Similar synthesis process is applicable to the PLA thermoplastic which is more environmentally friendly than ABS [221]. Besides, FDM can be used to design and fabricate porous 3D scaffolds. The pore volume, structure, and the porosity are controlled by the CAD parameters. The printed scaffolds exhibit excellent mechanical properties and biocompatibility. Therefore, 3D printing via FDM has a huge potential to be applied to tissue engineering [222-226]. To our best knowledge, the research that focuses on fuel cell fabrication via FDM is limited. Dudek synthesized the PA12-HAP composites and extruded the mixture into filaments at 185 °C. The filaments were used to produce structural components for low-temperature proton exchange membrane fuel stacks [227]. However, this study focuses on designing the structural components instead of electrolyte or electrodes. In order to fabricate the electrodes, the fuel cell materials have to be mixed into the thermoplastics to make the composite filaments. Compared to inkjet

printing, the FDM is a more convenient and cost-effective method. More importantly, it can produce the porous structure after sintering which is a perfect solution to increase the porosity of fuel cell electrodes.

In this chapter, the FDM is applied to fabricate the cathode on a half SOFC button cell. Details of the processes including mixing, extruding, printing, sintering, assembling, and characterization are discussed. Traditional dip-coating is also applied for performance comparison. The experimental results show that FDM is a promising technique for the SOFC/SOPC manufacturing.

3.2 Experimental

3.2.1 3D printer and extruder

The 3D printer used in the experiment is a common desktop 3D printer purchased from Monoprice, as shown in Figure 36a. The build area is 200×200×180 mm^3 with the minimum resolution as low as 0.1 mm. The maximum extrusion temperature is 260 °C and the printer head can move as fast as 150 mm/s. The 3D printer requires standard 1.75 mm filaments made of thermoplastic materials, including ABS, PLA, PVA, TPU, PETG, etc. The 3D printer is operated via G-code files that can be created from Ultimaker Cura. Generally, the 3D model is built in a CAD software (e.g. Autodesk Fusion 360) and then transferred to Cura to set up various printing parameters, such as lay height, extruding temperature, internal pattern, etc. The printing process of FDM is shown as Figure 37. The motor is responsible for feeding the filament to the nozzle by friction. When the nozzle temperature reaches above the melting point, the filament changes to a glass transit state. The melted plastic is then extruded through the nozzle and printed on the platform. Cooling happens immediately after the extrusion, enabling solidification in a short time.

The objects will be created layer by layer with the nozzle movement in x-z plane and platform movement in y direction.

Figure 36. FDM devices: a. 3D printer; b. extruder.

The filament extruder was purchased from Filastruder, in order to fabricate composite filament in house. The typical extrusion rate ranges from 10 in/min to 36 in/min depending on materials and temperature. The cylinder heater is located closely to the nozzle as shown in Figure 38a. The extruder can be operated from room temperature to 260 °C. The working temperature is limited by the heater power to prevent thermal deposition of thermoplastic polymers. When the materials, normally powder or pellets, are fed into the extruder, the rotating drill will transport the raw materials to the nozzle. Due to the high temperature that is above the melting point, the thermoplastics are melted into glass transit state around the cylinder heater and then squeezed into filaments through the nozzle. However, it becomes more difficult for the extrusion process if the raw materials are composites, i.e. mixture of thermoplastics and ceramic or metal powders because the material fluidity is strongly dependent on the concentrations and viscosity of

thermoplastic polymers. Increasing the extrusion temperature is another effective method of improving the material fluidity, but this can potentially lead to the thermal decomposition of the polymers. To solve this problem, we have redesigned the heating system of the extruder. Specifically, the heating cord (HTC-030, OMEGALUX, US) was applied to wrap around the drill tube as shown in Figure 38b. The extended heating area was aimed to preheat the raw materials before reaching the nozzle part. This preheating design can effectively improve the material fluidity and decrease the squeezing resistance. The heating cord was connected to the temperature controller (689-0000, Barnant Company, US) that can supply much more power and control the temperature more precisely.

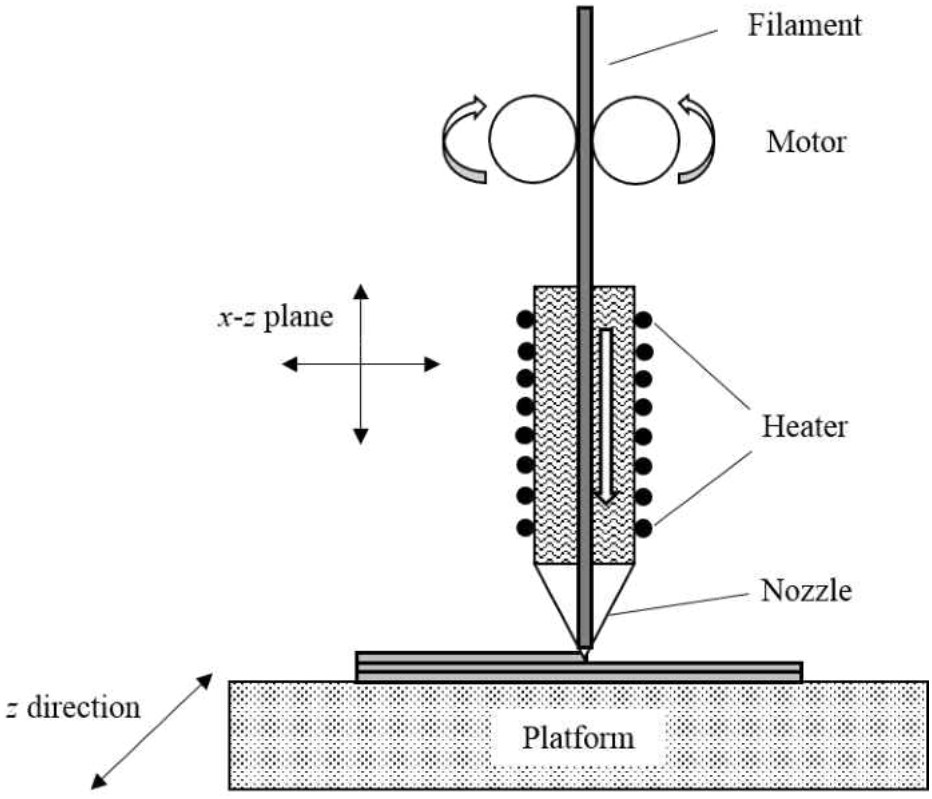

Figure 37. Schematic diagram of FDM process.

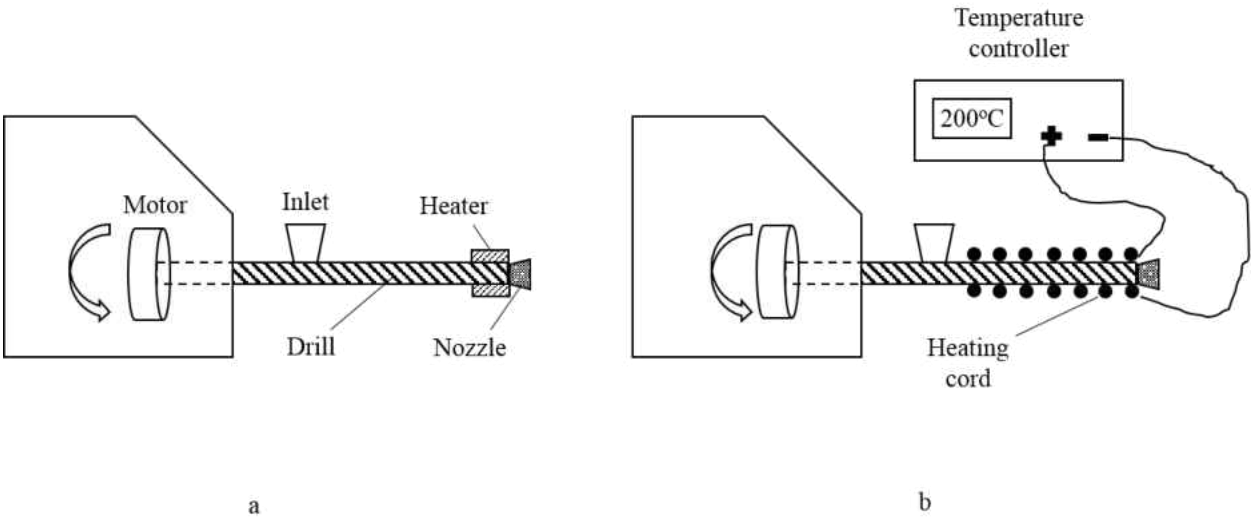

Figure 38. Heating system design of filament extruder: a. before design, b. after design.

3.2.2 Searching for appropriate thermoplastics

We identified the criteria for selecting the appropriate thermoplastic polymers for mixing with ceramic powders. First, the thermoplastic particles should not differ too much with ceramic particles in size. If the particle size of thermoplastic is much larger, the ceramic powders will be attached on the spherical surface during the mixing process. Such non-uniform distribution can significantly affect the filament homogeneity during extrusion. Vice versa, if the particle size of ceramic is too large. Second, the thermoplastic polymers should be liquid soluble if they cannot meet the first criteria. The polymers can be dissolved in the liquid where the ceramics are added before mixing by the blender. After liquid evaporation, the composites are able to be extruded into filaments. Third, the melting point (glass transit temperature) of thermoplastics should be lower than working temperature of the extruder and printer. As mentioned above, the maximum operation temperature of the extruder and printer are both 260 °C. Thus, the thermoplastic

melting point should fall below this upper limit so that the polymer is suitable for extrusion and printing processes. Fourth, the boiling point or decomposition temperature of the thermoplastics should be higher than the working temperature of extruder and 3D printer. Otherwise, the polymers would be vaporized during extrusion, resulting in gas bubbles.

The physical and chemical properties of common thermoplastic materials for 3D printing have been summarized in Table 3. In this study, ABS, Aquazol 50, PVA and Nylon 12 (PA12) are applied to be mixed with ceramics for filament extrusion. Specifically, ABS based mixture is obtained after it's dissolved by the acetone while the others are made through ball milling without liquid. Even though other polymers, i.e. PLA, TPU and PETG etc., are widely used as commercial filaments for 3D printer, it is difficult to find commercially available bulk with small particles.

Table 3. Physical and chemical properties of common thermoplastic materials for 3D printing [228, 229].

Thermoplastics	Particle size	Liquid soluble	Melting point/°C	Boiling point/°C	Density g/cm^3
ABS	N/A	acetone	105*	N/A	0.9-1.53
Aquazol 50	~ 0.8 mm	water	110-120	N/A	1.14
PVA	~ 1 mm	water	200	228	1.19
Nylon 12	45 µm	N/A	178-180	314-315	1.01
PLA	N/A	N/A	150-160	N/A	1.25
TPU	N/A	N/A	50-145	N/A	1.06-1.21
PETG	N/A	N/A	240-260**	N/A	1.27

* glass transit temperature, ** suggested working temperature of 3D printer

The ceramic materials we have used in this study include alumina (Al_2O_3, ~1 μm, 2.7 g/cm^3), YSZ (0.5-0.7 μm, 6.1 g/cm^3), LSM (0.48 μm, 6.5 g/cm^3) and LSCF (0.39 μm, 1.203-2.8 g/cm^3). The alumina was applied to fabricate the composite filaments for preliminary test. YSZ is the electrolyte material that is usually mixed with cathode materials, LSM and LSCF, to make the oxygen electrode. Compared with LSM cathode, YSZ-LSM electrode exhibits similar thermal expansion coefficient with YSZ electrode. Thus, the delamination issue during the SOFC/EC operation could be avoided.

3.2.3 Mixing

The porosity of the 3D-printed objects can be calculated by the volume percentage of the thermoplastic materials, since only the polymers are vaporized or decomposed after sintering. It is mathematically expressed as the equation 39.

$$\phi = \frac{V_p}{V_p + V_c} = \frac{W_p/\rho_p}{W_p/\rho_p + W_c/\rho_c} \tag{39}$$

$$\frac{W_p}{W_c} = \frac{\phi\rho_p}{(1-\phi)\rho_c} \tag{40}$$

where, V, W and ρ denote the material volume, weight and density respectively. The index of p and c denote the thermoplastic polymers and ceramics respectively. For the mixture that contains multiple ceramics, the symbols represent the average value of volume, weight and density. The typical porosity of fuel cell electrodes ranges from 40% to 60%. The weight ratio of polymer and ceramic can be then calculated by equation 40. Note that, ϕ represents the initial porosity before sintering. The practical porosity is even lower with consideration of ceramic shrinkage at high temperature.

The ingredients of polymer-ceramic composite for filament fabrication in this study have been summarized in Table 4. For ABS-Al_2O_3 composite, the ABS polymer was dissolved in the acetone before adding the alumina. The solution was blended uniformly and then air-dried in the fume hood as the preparation for extrusion. For other composites, after the polymer-ceramic powders were prepared, they were mixed thoroughly by the ball miller (Jar Mill, US Stoneware, USA) for 24 hours. All the materials were measured by the balance (HR-100A, Hogentogler & CO, USA) with resolution of 0.1 mg. Note that compared to PA12, PVA has bigger particle size as shown in Table 3. The incompatible particle size will lead to inhomogeneous mixture despite of long-term ball milling. Therefore, the vol. % of PVA (porosity) has to be increase for successful extrusion. On the other hand, the vol. % of PA12 is allowed to be much lower due to its smaller particle sizes. Lower porosity can also be obtained in the Aquazol 50 based composite due to its low melting point and high fluidity. The ceramic structure will be unstable after sintering if the vol. % of polymer (porosity) is too high. The composite mixtures are shown in Figure 39 as the preparation for filament extrusion.

Table 4. Ingredients of polymer-ceramic composite for filament fabrication.

Composites	Ratio	Porosity	Mixing method
ABS-Al_2O_3	1:1 wt.%	69.23%	acetone & blender
Aquazol-Al_2O_3	1:1 wt.%	77.6%	ball miller
PVA- Al_2O_3	3:1 wt.%	87.19%	ball miller
PVA-LSM	3:1 wt.%	94.25%	ball miller
PA12-LSM	1:1 wt.%	86.55%	ball miller
PA12-LSM-YSZ	LSM-YSZ, 1:1 wt.% PA12-[LSM-YSZ], 3:2 vol.%	60%	ball miller

PA12-LSCF-YSZ	LSCF-YSZ, 1:1 wt.% PA12-[LSCF-YSZ], 3:2 vol.%	60%	ball miller

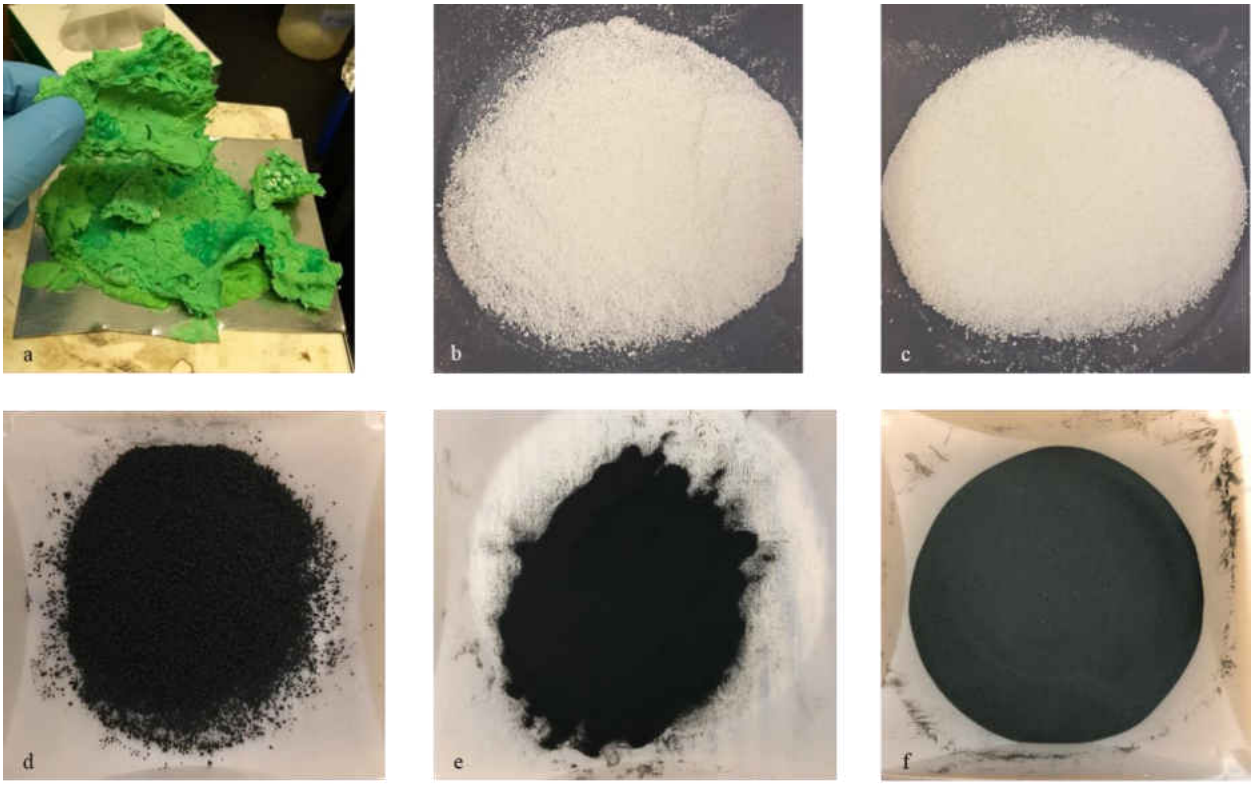

Figure 39. Thermoplastic-ceramic composite mixing: a. ABS-Al_2O_3; b. Aquazol-Al_2O_3; c. PVA-Al_2O_3; d. PVA-LSM; e. PA12-LSM; f. PA12-LSM-YSZ.

3.2.4 Extrusion

The extruder with improved preheating system was used for fabrication of composite filaments. For ABS-Al_2O_3 composite as shown in Figure 39a, it needs to be shaped into small pellets before extrusion. The extruding temperature is strongly dependent on the thermoplastic melting point and vol. %. Higher extruding temperature can potentially cause the vaporization or

decomposition of the thermoplastic materials, leading to the non-uniform filaments. On the other hand, lower extruding temperature would decrease the composite fluidity, making it more difficult for the extrusion process. In this study, successful extrusion can be achieved at ~150 °C for ABS and Aquazol 50 based composites. The PA12 based composites have to be extruded at approximately 200°C due to its high melting point and low concentration as shown in table 3 and table 4.

The extruded composite filaments are shown in Figure 40. Even though ABS filaments are widely used, the extruded ABS-Al_2O_3 composite filaments are too brittle and unable to be 3D printed directly. This is because when the ABS pellets were dissolved in the acetone during mixing, the molecular structure of the ABS would be changed from long-chain forms to short-chain forms, thus affecting the physical properties, such as brittleness. Similar brittleness was observed from Aquazol-Al_2O_3 despite of mixing by ball milling. However, the Aquazol based filament can be softened by moisture absorption due to its water solubility. The balance between brittleness and softness has be adjusted well before printing, which could limit the application of such composite filament. The PVA based filaments, including PVA-Al_2O_3 and PVA-LSM, were extruded with rough surface due to incompatible polymer and ceramic particles. It is necessary for these filaments to be polished by sand paper before printing. PA12 based composites, including PA12-LSM, PA12-LSM-YSZ and PA12-LSCF-YSZ, are the best filaments we have extruded so far. Compared to the other composite, the PA12 based filaments exhibited excellent flexibility as shown in Figure 40e. More importantly, lower porosity (60%) can be achieved to maintain structural stability after sintering. These advantages are attributed to the compatible particle sizes of PA12 (45 μm) with the ceramic powders.

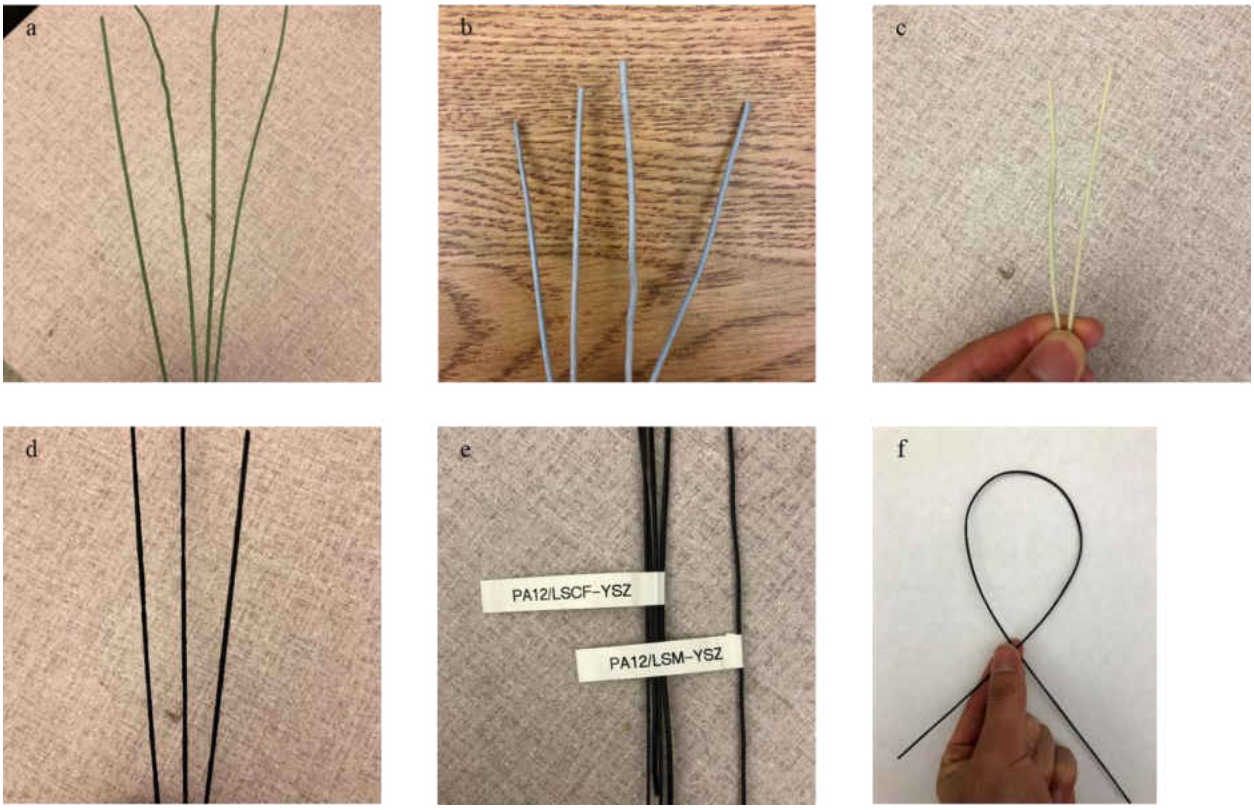

Figure 40. Extruded thermoplastic-ceramic filaments based on the ingredients in table 4. a. ABS-Al_2O_3; b. Aquazol-Al_2O_3; c. PVA- Al_2O_3; d. PVA-LSM; e. PA12 based composites including PA12-LSM-YSZ and PA12-LSCF-YSZ; f. flexibility of PA12 based composite filaments.

3.2.5 Printing

The default printing temperature of ABS is 230 °C and the same working temperature is applicable for Aquazol based filaments due to the similar melting point as shown in table 3. For PVA and PA12 based filaments with higher melting point, a higher printing temperature of 250°C is suggested. The 3D printed objects were either in a square shape with 20×20 mm^2 or a circle shape with a diameter of 30 mm. The thickness of unit layer was set as 0.25 mm and the 0.4 mm-nozzle device was programmed to print 4 layers for each sample with total thickness of

1mm. Particularly, the PA12-LSM-YSZ and PA12-LSCF-YSZ based filaments were used to fabricate the porous SOFC cathodes. They had a higher vol. % of ceramic materials and thus a lower fluidity. Therefore, a larger nozzle diameter of 1 mm is necessary to avoid a choked nozzle. The SOFC cathodes are 3D printed with a diameter of 15 mm and a thickness of 1mm.

The 3D printed objects are shown in Figure 41. Similar with the composite filaments, Aquazol-Al_2O_3 object was too brittle to be removed from the platform (Figure 41a). It can be concluded that Aquazol 50 is not suitable as the polymer to 3D print SOFC cathodes. The PVA based filaments, either PVA-Al_2O_3 or PVA-LSM, can be used to print the composite samples (Figure 41b and 41c). However, these samples showed a rough surface due to the non-uniform material distribution in the filaments and discontinuous printing. On the other hand, the 3D printed samples based on PA12 composites exhibited excellent uniformity at various material combination and porosity (Figure 41d and 41e).

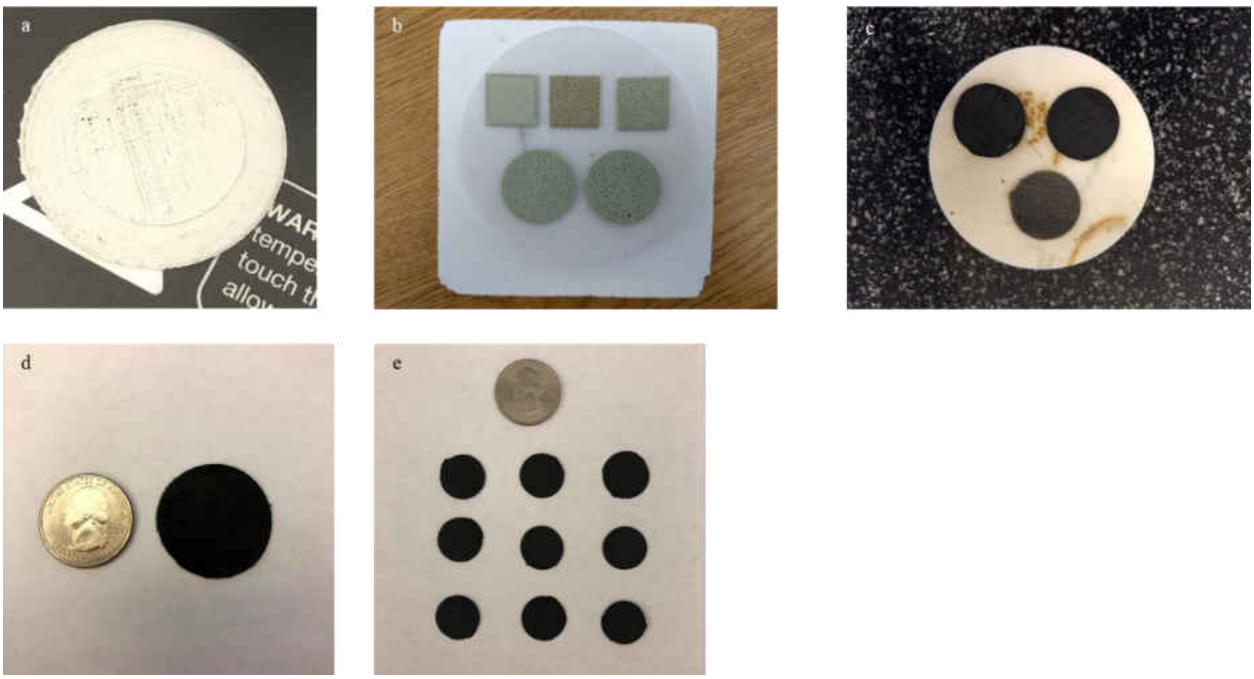

Figure 41. 3D printing objects using the composite filaments: a. Aquazol-Al_2O_3; b. PVA- Al_2O_3; c. PVA-LSM; d. PA12-LSM; e. SOFC cathodes including PA12-LSM-YSZ and PA12-LSCF-YSZ.

3.2.6 Sintering

Sintering is the process of compacting and forming a solid mass of material by heat. During sintering, the thermoplastic polymers in the composite are vaporized or decomposed leaving the porous ceramic structure. The atoms in the ceramics diffuse across the boundaries of the particles, fusing the particles together and creating a solid structure. The furnace (KSL-1700X, MTI Corporation, USA) with maximum temperature of 1700 °C was used for sintering process. PVA-Al_2O_3 based samples were sintered at 1400 °C for 4 hours with increasing and decreasing rate of 2 °C/min. The sintering temperature of PVA-LSM and PA12-LSM were 1100 °C and 900 °C, respectively. Other conditions were the same with PVA-Al_2O_3 based samples.

The 3D printed composite samples after sintering are shown in Figure 42. A sintering shrinkage of over 50% was observed from the PVA-Al_2O_3 based samples. The large thermal shrinkage results from the high sintering temperature and long heat duration. PVA-LSM samples showed an incomplete structure after sintering due to extremely high porosity. However, the porosity cannot be decreased during the mixing because the incompatible particle sizes of PVA and LSM. Thus, PVA may not be a suitable polymer to fabricate composite filaments. The PA12-LSM based samples exhibited excellent porous structure with neglectable shrinkage after sintering. Nevertheless, the delamination between the 3D printed cathodes and electrolyte was observed even though the polymer glue is applied initially at the interface. Further improvements to strengthen the bonding at cathode/electrolyte interface are necessary for the 3D printing technique.

Figure 42. The 3D printed composite samples after sintering: a. PVA-Al_2O_3; b. PVA-LSM; c. PA12-LSM.

3.2.7 SOFC button cell preparation

To avoid delamination at the cathode/electrode interface, pre-melting of the 3D printed cathode was applied before sintering. Specifically, the cathode and electrode was heated on the hotplate (Isotemp, Fisher Scientific, USA). When the temperature is above the thermoplastic melting point, the 3D printed cathode is in the glass-transit state and there is more contact surface area between the cathode and electrolyte. A stronger bonding was achieved after the thermoplastic solidification as shown in Figure 43b. However, the cracks would be observed at the cathode after sintering (Figure 43c). This is because when the furnace temperature is above the boiling point of the polymers, the internal pressure is generated and accumulated between the layers of 3D printed cathode as shown in Figure 43d. The cathode surface would be cracked if the pressure is high enough. Therefore, the pressing is necessary to prevent the internal pressure accumulation.

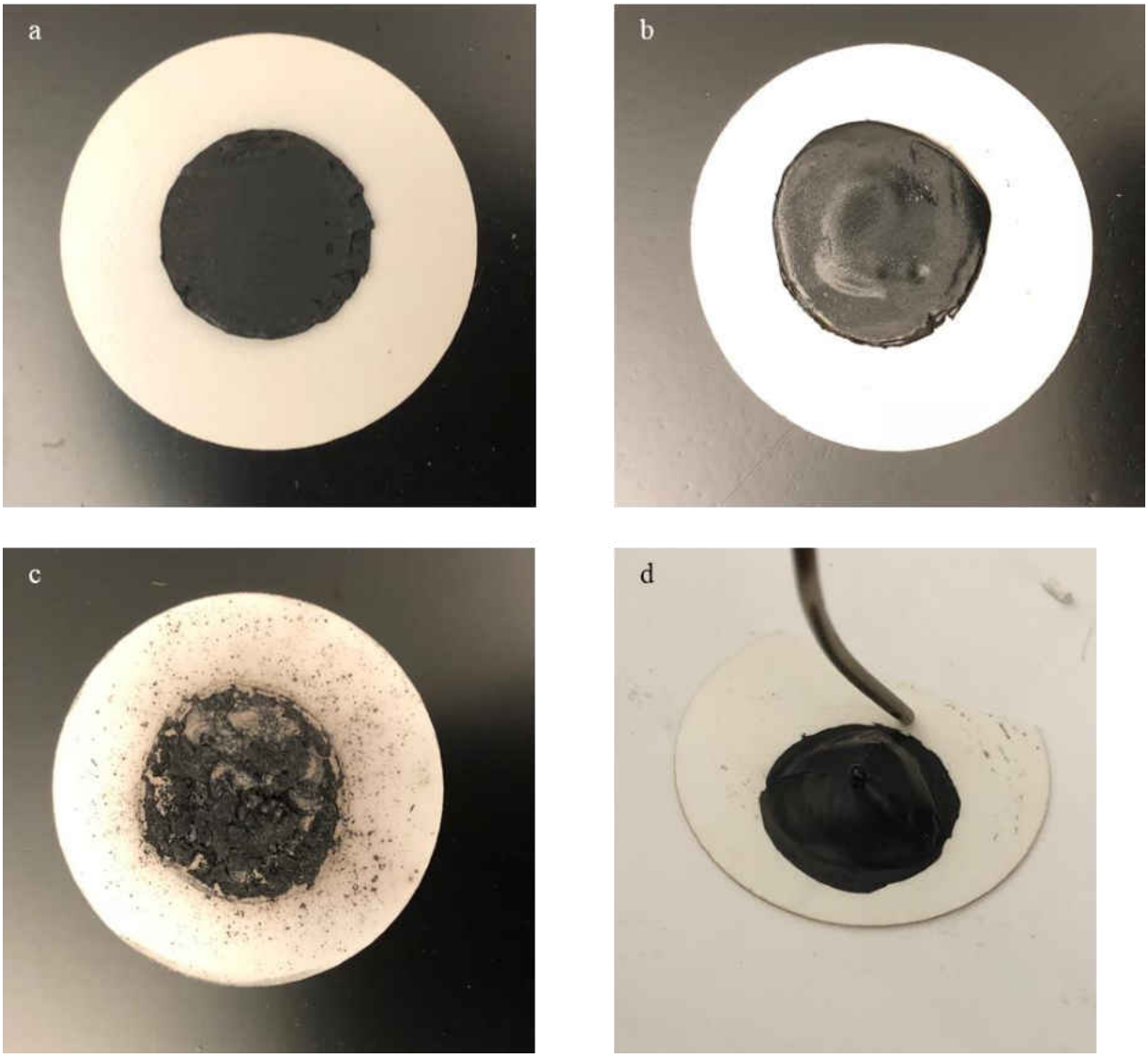

Figure 43. Bonding 3D printed cathode on the electrode: a. before melting; b. after melting; c. after sintering; d. during sintering.

It is difficult to directly apply pressing in the furnace due to the limited space of the furnace. Thus, the pressing was conducted on the hotplate after pre-melting when the temperature is above the boiling point of thermoplastic polymers. The whole process was operated in the fume hood. The sample was then sintered in the furnace to achieve the porous

structure as shown in Figure 44a. To act as the reference, the traditional dip-coating of cathode was applied as shown in Figure 44b. To prepare the composite cathode, LSM (or LSCF) powders and YSZ powders were mixed by ball milling with a weight ratio of 1:1. The mixed powder was stirred with the terpineol-cellulose vehicle to get the stable composite cathode paste. The terpineol-cellulose vehicle was prepared by dissolving 6 wt. % cellulose into 94 wt. % terpineol. The cellulose acted as the pore former and it would be decomposed at temperature of 260-270 °C. After the composite paste was brushed on the electrolyte, the sample was sintered in the furnace at 1000 °C for 2 hours.

Afterwards, the silver mesh was attached on the electrodes by silver ink for current collection (Figure 44c and 44d). The silver wire was placed next to the mesh with ink adhesion. This would allow for 4 point conductivity testing and a lead for measuring voltage, while the other drew the current. The silver ink needs to be dried at 100 °C before firing the sample at 800 °C for an hour with increasing and decreasing rate of 1 °C per minute. The active area of button cell was dependent on the shape of silver mesh or silver ink. In this study, two kinds of silver mesh were used with a circular area of 0.5 cm^2 and a square area of 1 cm^2.

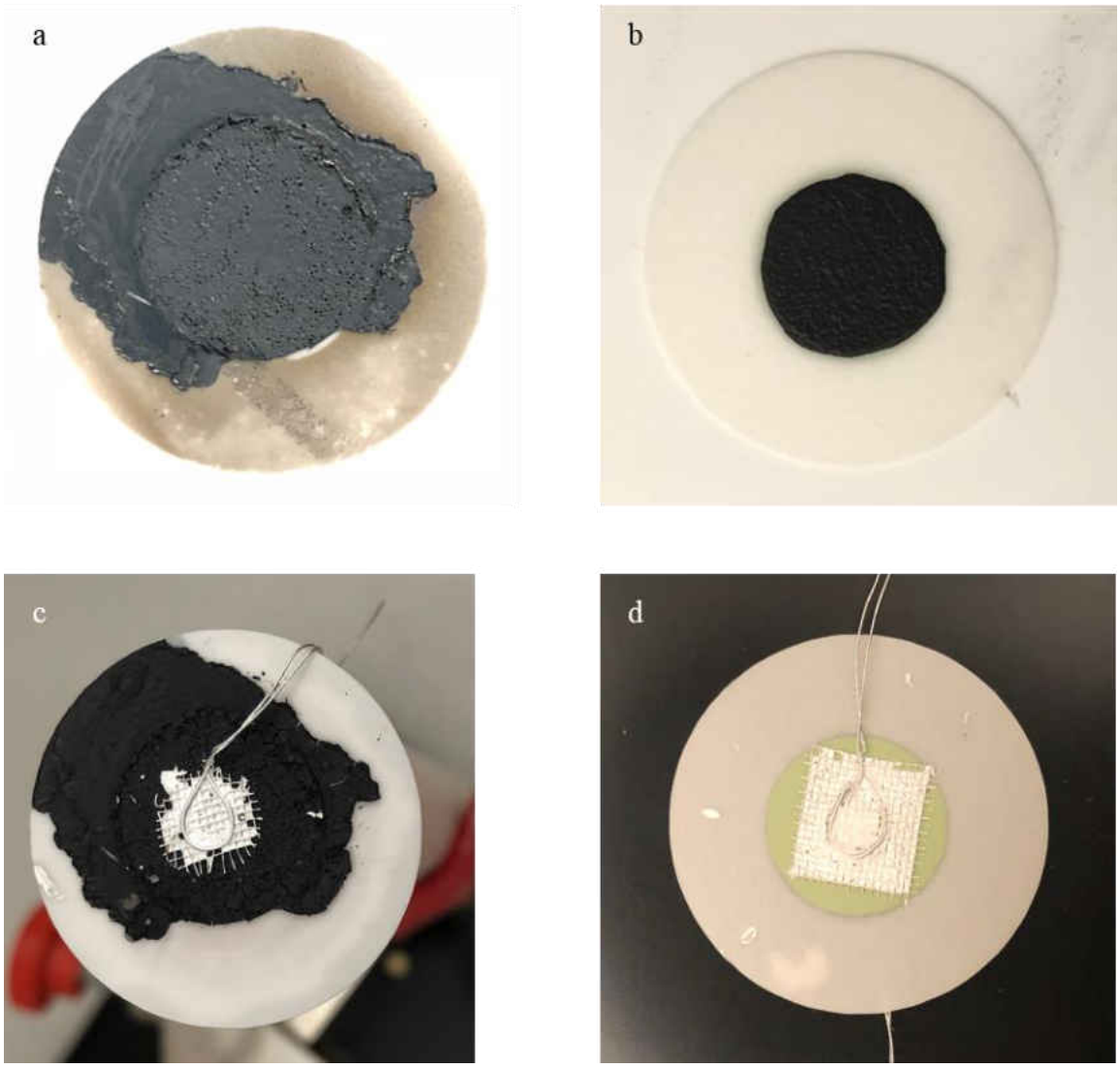

Figure 44. SOFC button cell preparation: a. pressing and sintering; b. dip-coating; c. electrical collector on the cathode; d. electrical collector on the anode.

3.2.8 Experimental setup for SOFC characterization

The button cell was finally assembled on the ceramic tube with cathode side exposed to the ambient as shown in Figure 45a. The ceramic paste (Ceramabond 552, Aremco, USA) was used for sealing between the anode side and the ceramic tube. Note that, the inner diameter of the tube should be larger than the anode diameter to cover all the effective area. To achieve the

strong ceramic bonding, the paste was dried at room temperature for 1-4 hours followed by the step cure at 90 °C and 260 °C for 2 hours at each temperature. The four attached silver wires were extended to the other end of the ceramic tube as shown in Figure 45b. Two wires were connected to the voltage detector while the other two were connected to the load for current detection. Besides, the hydrogen was pumped into the ceramic tube though the stainless pipe that was close to the cell anode. The outlet was connected to the exhausted system for safety. Both hydrogen inlet and outlet pipes were fixed by silicon rubber at the end of ceramic tube. The prepared SOFC button cell was then placed horizontally inside the middle part of tubular furnace (GSL-1100X, MTI Corporation, USA) as shown in Figure 45c. The air was pumped to the cathode from the other side of the furnace. Either thermal blocker or asbestos was used for thermal insulation on two sides of the furnace. The fuel cell test station (855 SOFC, Scribner, USA) was used to characterize the cell performance as shown in Figure 45d. The hydrogen flow rate was controlled as 50, 100 and 200 sccm while the air flow rate was set at 250 sccm. The test station can detect, control and record the voltage and current of the SOFC at various conditions. The cell operation temperature was controlled by the furnace ranging from 700 °C to 800°C.

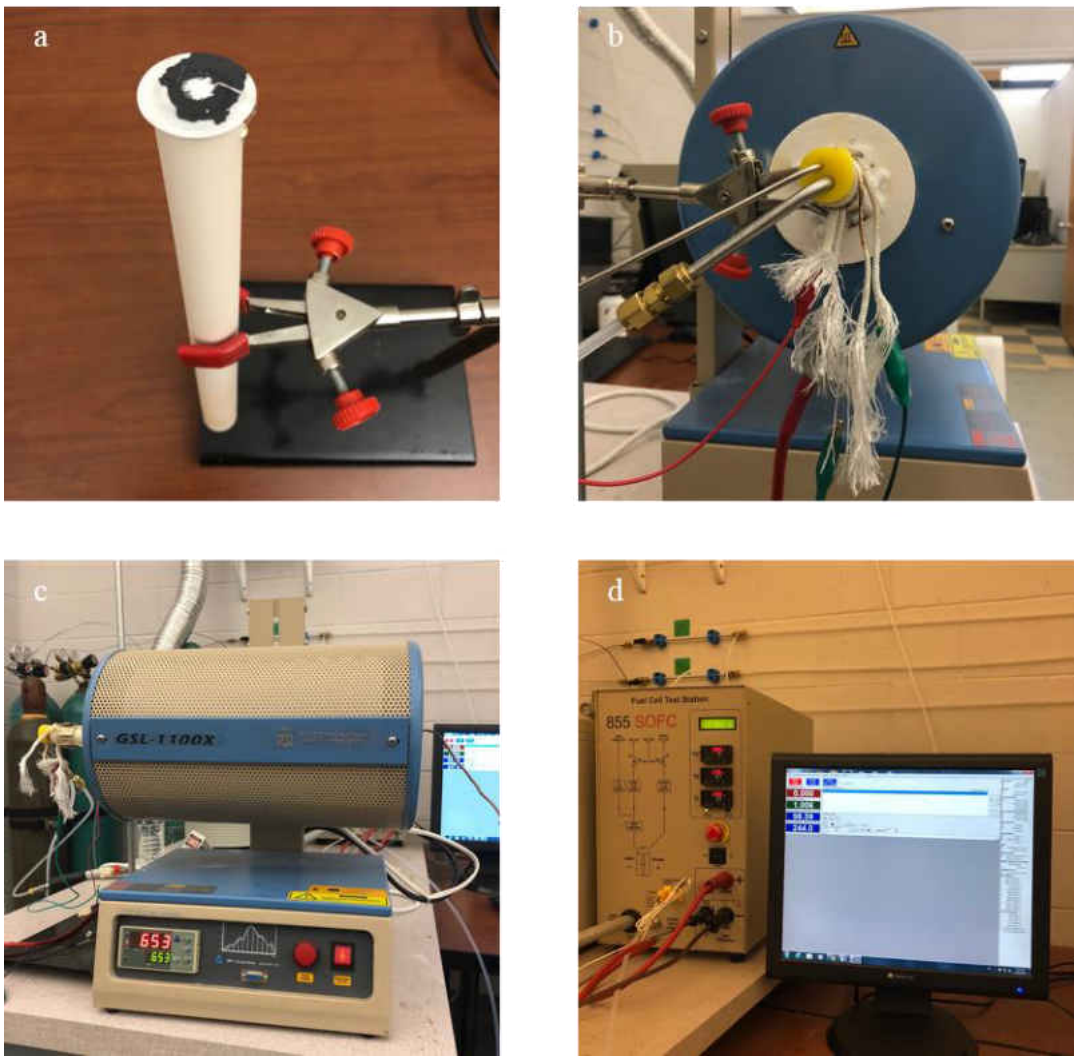

Figure 45. Experimental setup for SOFC characterization: a. ceramic tube assembly; b. hydrogen inlet/outlet and voltage/current detection; c. temperature control by furnace; d. gas control and data acquisition.

3.2.9 SEM inspection

After characterization, the samples were disassembled from the experimental setup and their surface structures were then inspected by SEM to identify the cathode porosity. Due to the nonconductivity of cathodes, it is necessary to coat a thin conductive layer on the sample surface

before SEM inspection. The deposition process was conducted using Au target in the sputter coater (Hummer 6.2, Anatech, USA) as shown in Figure 46a and 46b. During sputtering, the air was first exhausted by inert argon gas and the chamber was then vacuumed to 4.4×10^3 Pa for higher deposition rate. The applied current was 15 mA with deposition duration of 2 minutes. Afterwards, the samples were loaded in the SEM (Phenom ProX, Micromeritics, USA) for surface inspection as shown in Figure 46c. The acceleration voltage was 10 kV with magnification range of 560-74000x. Besides, the 3D surface structure of the cathodes was characterized by the digital-video microscopy system (HK-7700, HIROX, USA) as shown in Figure 46d.

Figure 46. Inspection equipment: a. sputter coater; b. sputtering process; c. SEM; d. optical microscope.

3.3 Results and discussion

3.3.1 Dip-coating LSM cathode

The SOFC button cell with dip-coating cathode was first tested as the reference. The active area was 0.5 cm^2. The cell was preheated to 400 °C and the hydrogen was then pumped through ceramic tube to the anode with a flow rate of 100 sccm while the cathode was exposed to the ambient in the furnace. The data (voltage and current density) had been recorded with the frequency of 1/30 s^{-1} since the temperature increased from 400 °C to 750 °C with a rate of 1 °C/min. The cell anode is made of NiO and it can be reduced to Ni at hydrogen atmosphere. As

shown in Figure 47, it took approximately 2 hours to fully reduce the anode with the maximum OCV of 1.09 V at 525 °C. Voltage fluctuation happened at 510 °C due to reconnecting the detectors. The cell OCV then maintained for 1.5 hours and started decreasing since the operation temperature continued to increase. This trend could be explained by the thermodynamics in section 1.3.3. At 750 °C, the button cell showed an OCV of 1.03 V which is lower than the theoretical value due to humidified hydrogen according to equation 18. Afterwards, the load was applied by the test station at voltage control mode. However, only a neglectable current density of 0.021 A/cm^2 at 0.12 V was detected that indicated the serious degradation issues. As the temperature decreased with 1 °C/min, the cell OCV showed an increase first and then a decrease. The increase can be explained by the thermodynamics as well and the decreasing OCV resulted from declining ion conductivity of YSZ electrolyte. The post-inspection of the SOFC button cell indicated a serious cracking and leaking problems of electrolyte as shown in Figure 48a. This was attributed to the significant thermal gradient during cell operation. To solve such problems, either thermal block or asbestos at two sides of tubular furnace is necessary to avoid thermal gradient. Besides, ceramic paste can be brushed on the electrolyte surface to strengthen the mechanical properties as shown in Figure 48b.

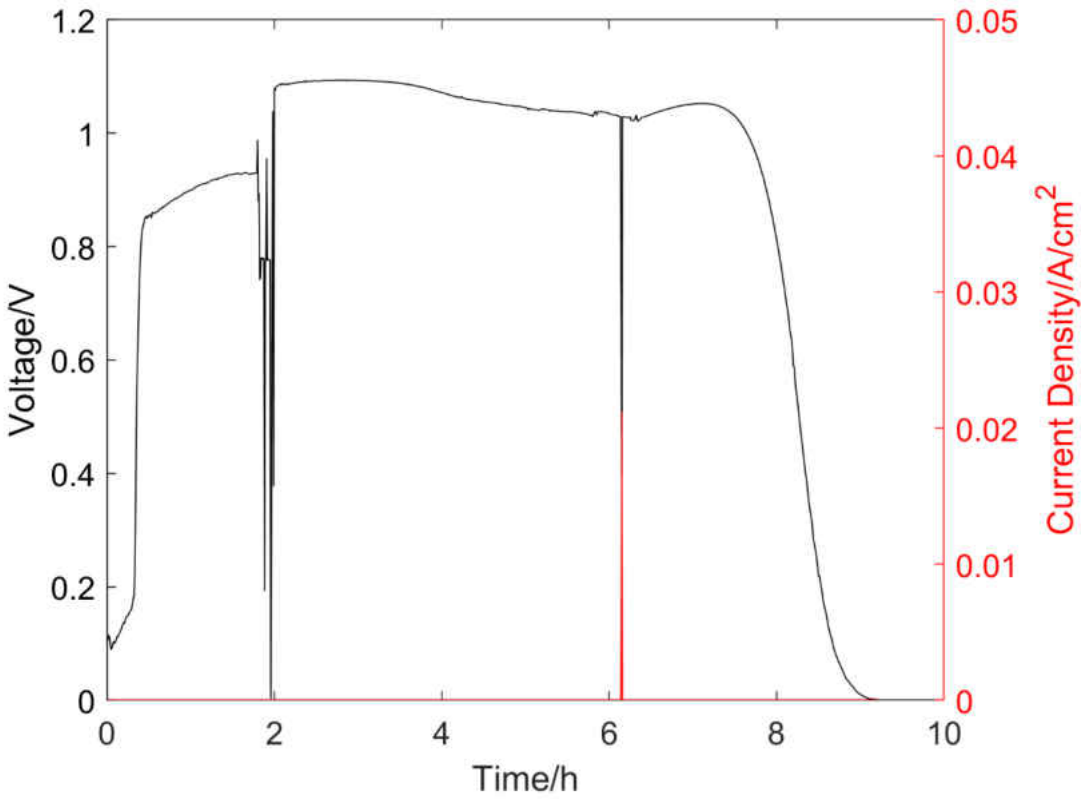

Figure 47. Characterization of SOFC button cell #1 with dip-coating LSM cathode (0.5 cm^2 active area).

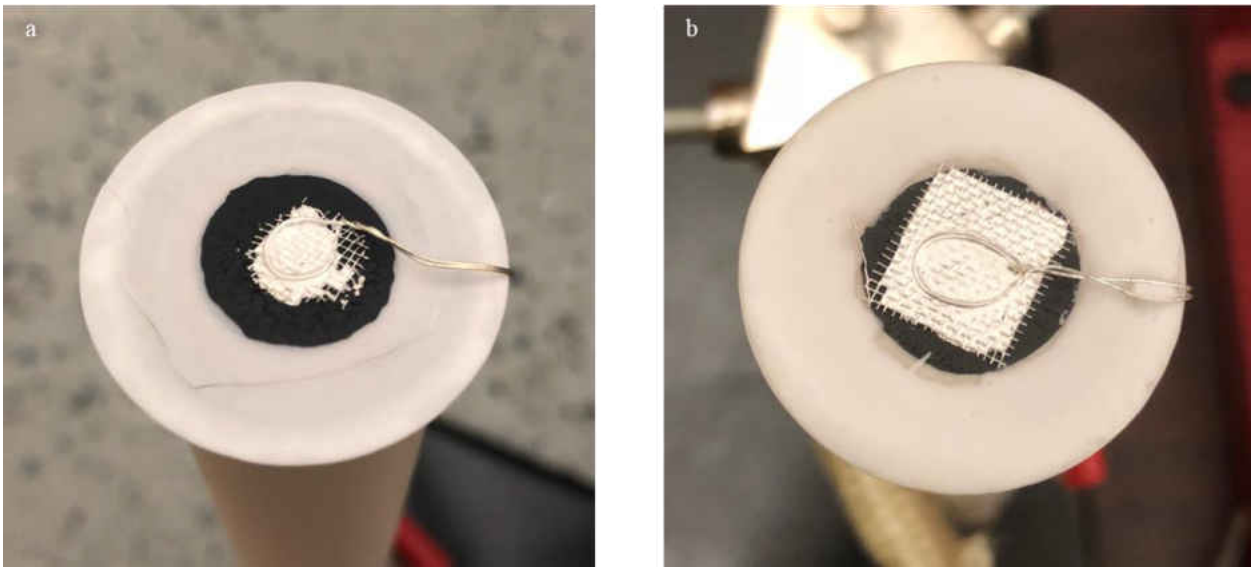

Figure 48. Post-inspection of SOFC button cells: a. cracking problems; b. applying ceramic paste to avoid cracking.

The second SOFC button cell with dip-coating cathode (0.5 cm^2 active area) was tested with the same operation conditions to those of button cell #1. As shown in Figure 49, a slightly unstable OCV of 0.938 V was observed at 750 °C. It is lower than the OCV (1.03 V) of cell #1 at the same conditions. This could be explained by the insufficient time for anode reduction. The hydrogen was pumped to the anode at 750 °C rather than 400 °C and the anode-reduction duration decreased from 6 hours to 2.5 hours before applying the load. Therefore, the NiO anode was not fully reduced to Ni. After running for 10 hours, the cell reached an OCV of 1.00 V that was much closer to the OCV of cell #1.

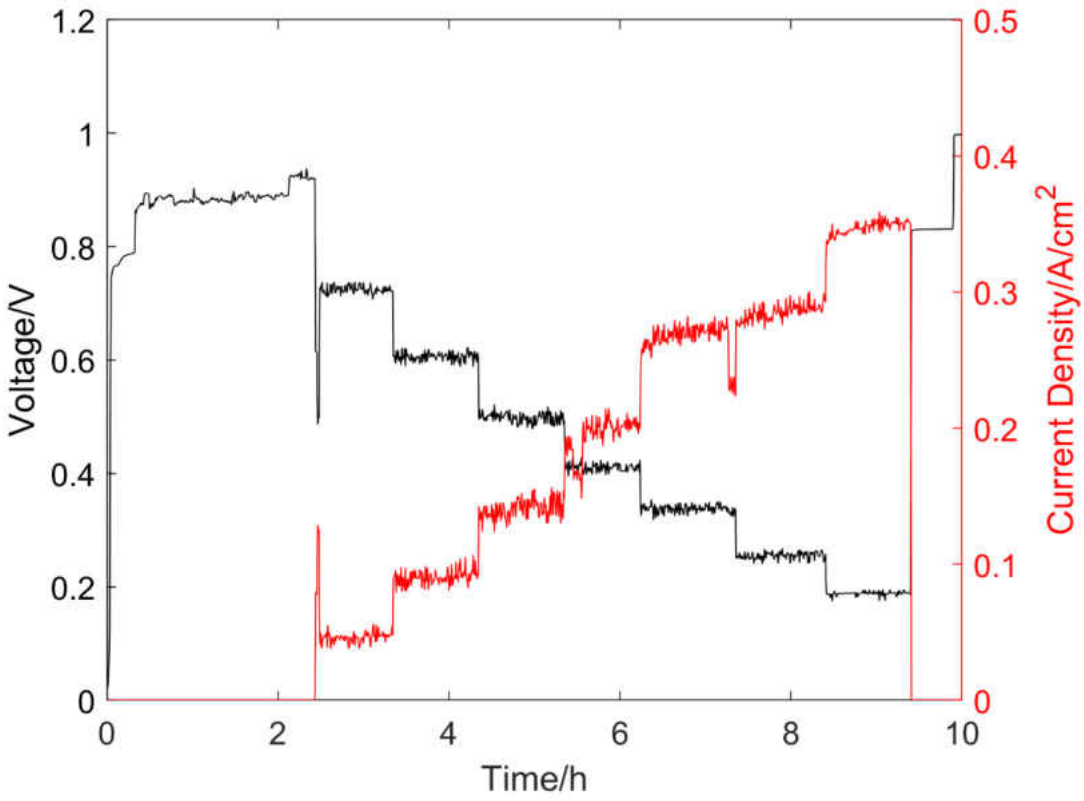

Figure 49. Characterization of SOFC button cell #2 with dip-coating LSM cathode (0.5 cm^2 active area).

The voltage-current relation was characterized by applying various external load to control the voltage. The applied voltage was set from 0.9 V to 0.3 V with the step of 0.1 V. Each step lasted for 30 minutes to achieve a relatively stable state. However, the practical voltage was lower than the setting values due to voltage loss on the connections. The resistance of the 0.3 mm-diameter silver wire was measured as 1 Ω/m. Moreover, the resistance could potentially increase with increasing usage frequency. The V-I characterization was plotted with error bar as shown in Figure 50. Approximately linear relation was observed from the experimental data. Specifically, the area specific resistance (ASR) was calculated as 1.728 $\Omega \cdot cm^2$ at 750 °C based

on the curve slope. Based on the linearly curve fitting, the maximum power output was 0.086 W/cm^2 when the applied voltage was 0.385 V. The test results of SOFC button cells with dip-coating cathode have successfully validated the feasibility of the experimental setup for cell characterization.

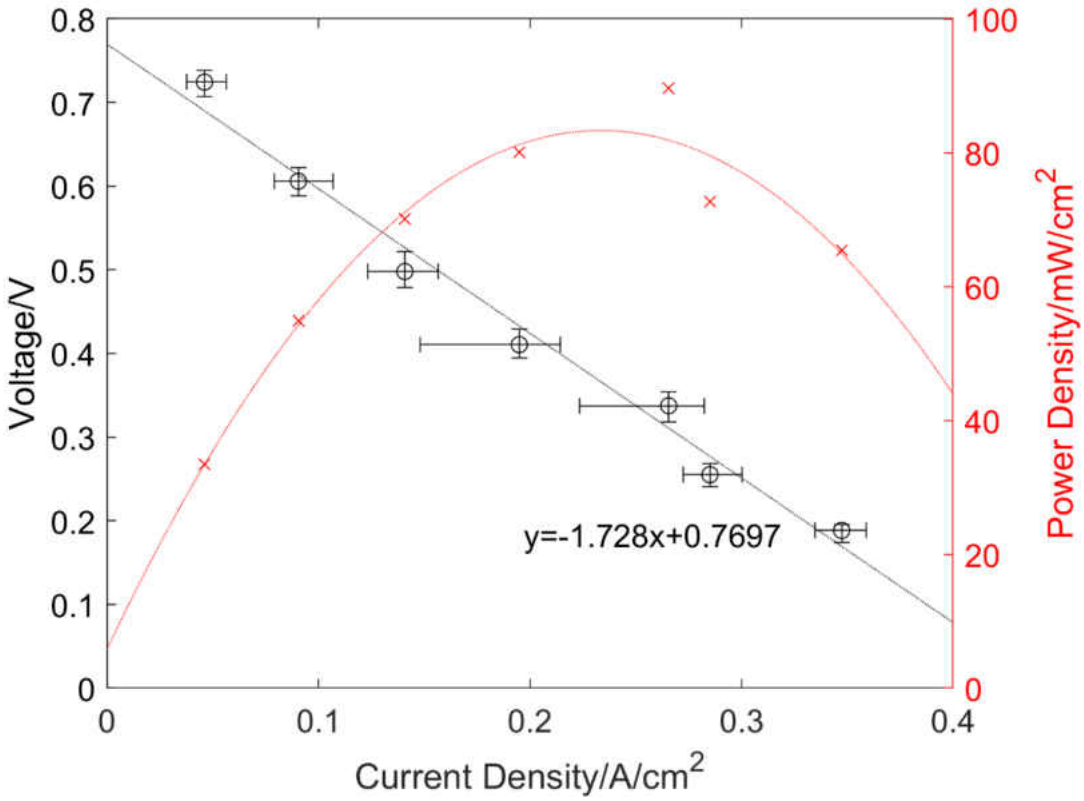

Figure 50. Voltage scan of SOFC button cell #2 with dip-coating LSM cathode (0.5 cm^2 active area) at 750 °C.

3.3.2 SOFC button cell with 3D printed LSM cathode

The SOFC button cell #3 with 3D printed LSM cathode was tested using the same experimental setup. The voltage and current were recorded over the operation time as shown in

Figure 51. With the hydrogen flow rate of 100 sccm, the maximum OCV of 1.122 V was observed when the anode was fully reduced at 500 °C. After that, the OCV decreased with an increase temperature that was consistent with the thermodynamics. The cell showed a stable OCV of 1.03 V at 750 °C that was the same with dip-coating-cathode cells. However, current density of 0.0204 and 0.0321 A/cm^2 were detected when the applied voltage were 0.698 and 0.567 V, respectively. Similar to the first SOFC button cell with dip-coating cathode, it may result from the electrolyte cracking and hydrogen leaking and the post-inspection had confirmed that. Despite of that, the cell could still maintain an OCV of 1.03 V at 750 °C after two hours of operation.

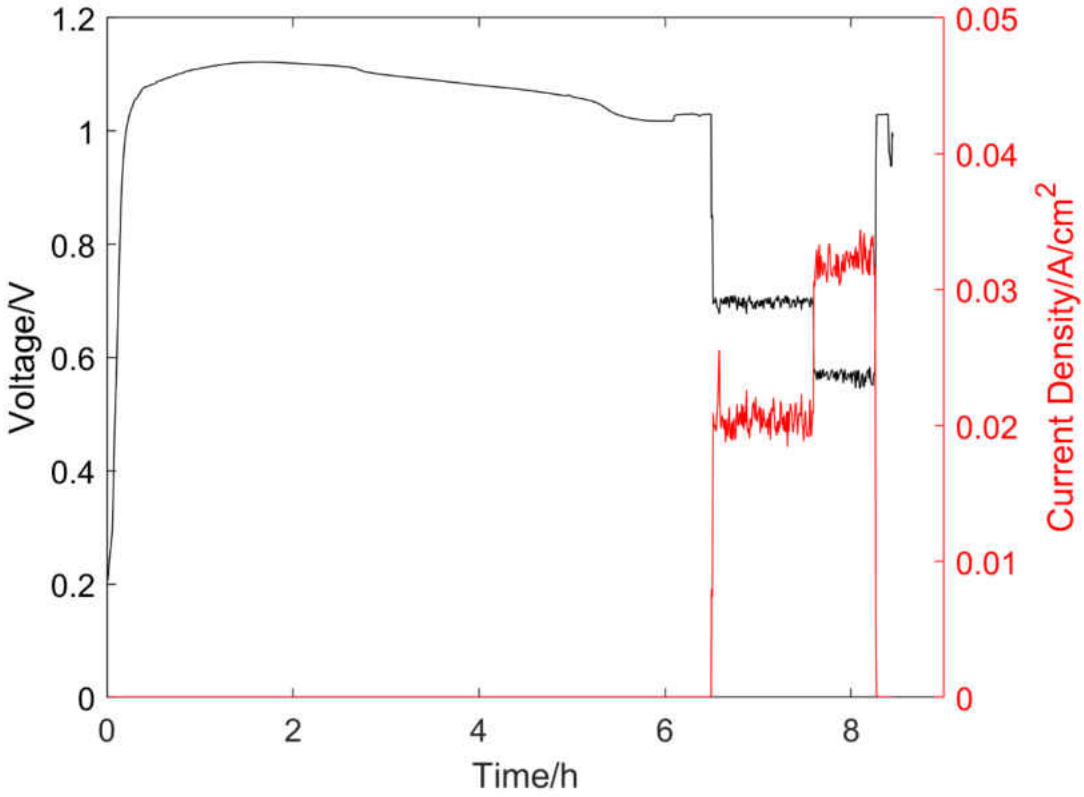

Figure 51. Characterization of SOFC button cell #3 with 3D printed LSM cathode (0.5 cm^2 active area).

The SOFC button cell #4 with 1 cm^2 active area was tested under the same conditions as cell #3. During the anode reduction with increasing temperature from 400 °C, the cell exhibited the maximum OCV of 1.135 V at 530 °C and a stable OCV of 1.068 V at 750 °C. Step voltage was then applied and the current density was recorded when the temperature was maintained at 750 °C. After that, the cell voltage was detected without applying current when the temperature decreased from 750 °C. The whole characterization process was conducted at the hydrogen flow rate of 100 sccm.

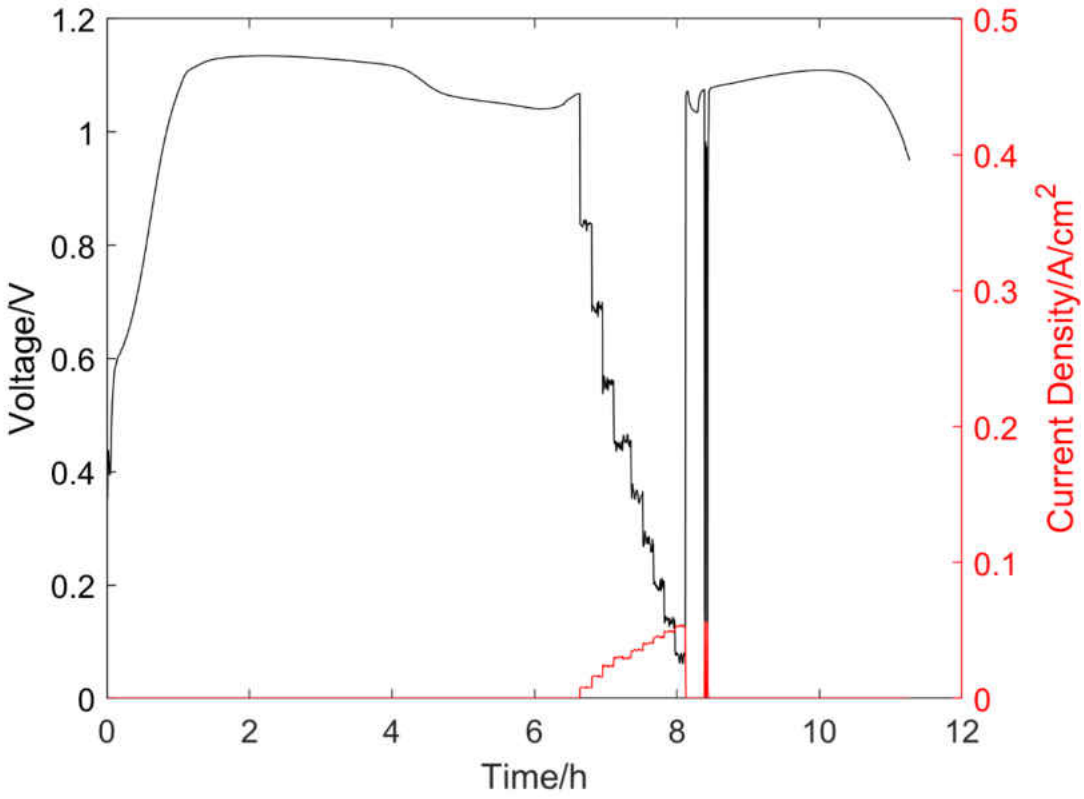

Figure 52. Characterization of SOFC button cell #4 with 3D printed LSM cathode (1 cm^2 active area) at H_2 flow rate of 100 sccm.

Compared to cell #2 with dip-coating cathode, cell #4 showed much lower current density despite of larger active area at similar applied voltage. The post inspection confirmed the

leaking issues between the button cell and ceramic tube. Through linearly fitting the voltage-current data as shown in Figure 53, the cell resistance was estimated to be 17.27 $\Omega \cdot cm^2$, which is an order of magnitude larger than the reference. The maximum power output of cell #4 was only 13.2 mW/cm^2 when the applied voltage was 0.478 V.

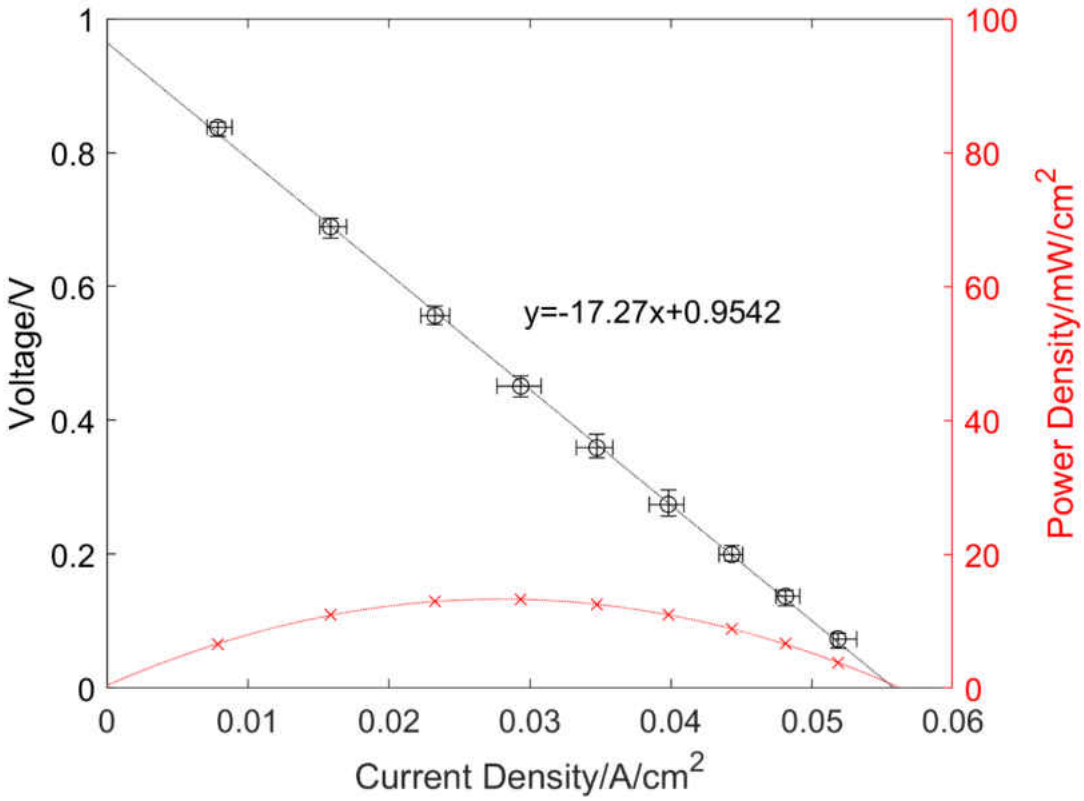

Figure 53. Voltage scan of SOFC button cell #4 with 3D printed LSM cathode (1 cm^2 active area).

The SOFC button cell #5 with 3D printed cathode was characterized under the same conditions with last one. The anode was reduced by hydrogen very quickly within 45 minutes when the maximum OCV was 1.051 V at 450 °C. When the temperature was maintained 750 °C,

the cell showed a stable OCV of 0.978 V that was lower than those of cell #1 and cell #3 (1.03 V). This may be attributed to the insufficient reduction of anode by hydrogen. Two cycles of V-I characterization were then conducted on the cell by controlling the applied voltage. It was kept for 15 minutes for each step to achieve the stable current and voltage. After the first cycle, the anode was fully reduced and the button cell was recovered to an OCV of 1.037 V. The final OCV was 1.03 V after two cycles of characterization.

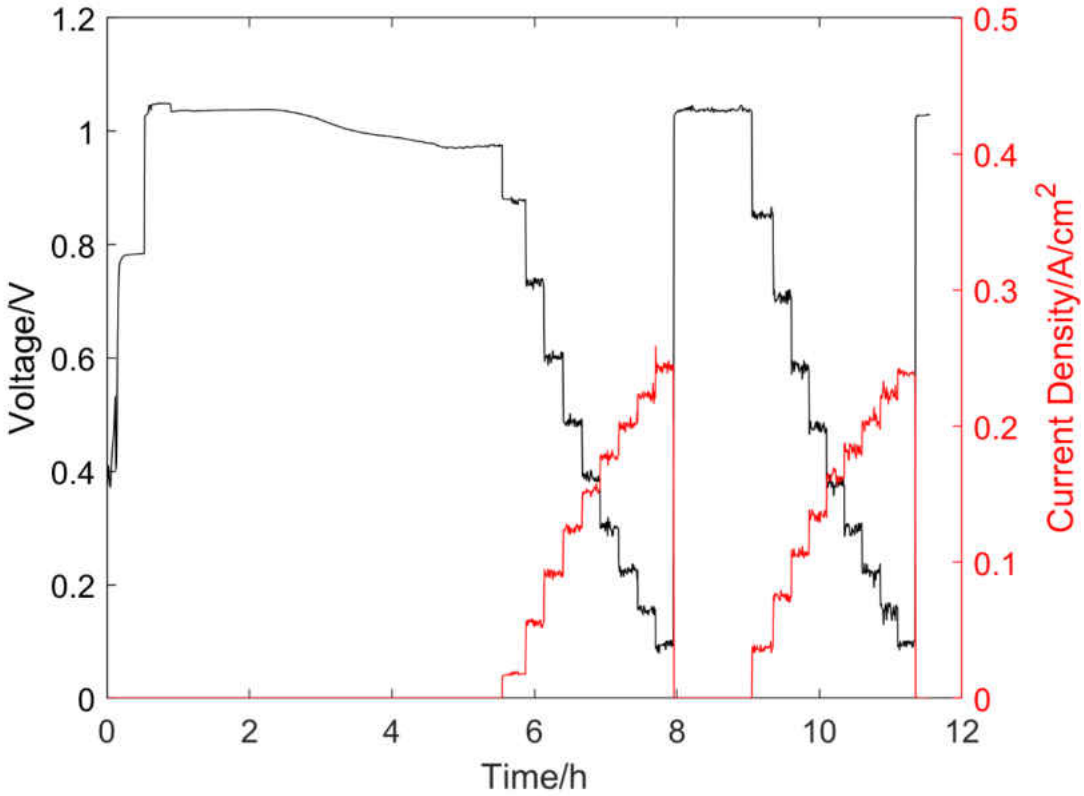

Figure 54. Characterization of SOFC button cell #5 with 3D printed LSM cathode (0.5 cm^2 active area).

The V-I characterizations of two cycles at 750 °C and the hydrogen flow rate of 100 sccm were plotted in Figure 55. The relation of current and voltage was linear for each cycle when the applied voltage increased from 0.1 V to 0.9 V. The cell resistance was estimated by the curve slopes as 3.484 $\Omega \cdot cm^2$ and 3.730 $\Omega \cdot cm^2$ for the first and second cycle respectively. The slightly increased resistance may be attributed to the cell degradation and further cell inspection was necessary to confirm this hypothesis. Compared to the cell #2 with the resistance of 1.728 $\Omega \cdot cm^2$, the cell #5 showed nearly twice larger resistance at the same condition. This may explained by the thicker cathode layer of 3D printing than that of dip coating. The maximum power output was calculated as 61.7 mW/cm^2 when the applied voltage was 0.464 V. Further performance improvements can be conducted by decreasing unit-layer thickness of the 3D printing and adjusting the pressing force during cell preparation, and increasing the active area.

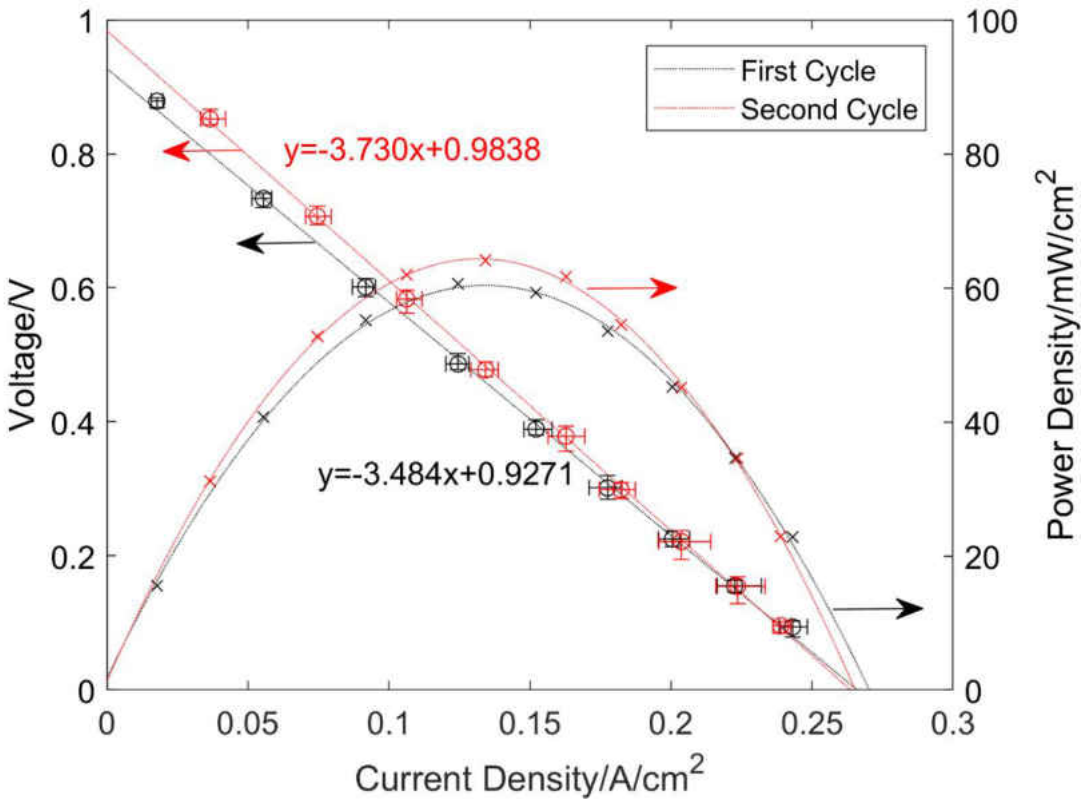

Figure 55. V-I characterization of SOFC button cell #5 for two cycles at 750 °C and 100 sccm of H_2.

Besides manually controlling the applied voltage, the fuel cell test station has the scan-voltage mode in which the cell voltage can be accurately managed in either single scan or double scan. Following the second cycle of V-I characterization, the voltage scans at the hydrogen flow rate of 50, 100 and 200 sccm were conducted on button cell #5 as shown in Figure 56. Double scan was applied for each condition at 750 °C when the applied voltage increased from 0.1 V to 1 V and then decreased back to 0.1 V with a step of 0.05 V. At the hydrogen flow rate of 100 sccm, the cell resistance was calculated as 3.749 $\Omega \cdot cm^2$; that is consistent with test result of the second cycle of V-I characterization. The button cell resistance would decrease from 3.84 $\Omega \cdot cm^2$

to 3.646 $\Omega \cdot cm^2$ with an increase of hydrogen flow rate from 50 sccm to 200 sccm. This is because more hydrogen can participated in the electrochemical reaction and higher H_2 concentration and pressure would improve the cell potential according to equation 18. The maximum power output were 59.2, 64.1, 69.7 mW/cm^2 at the hydrogen flow rate of 50, 100, 200 sccm respectively. It is not recommended to increase the hydrogen flow rate too much since the performance improvement is limited and it would lower the hydrogen utilization efficiency.

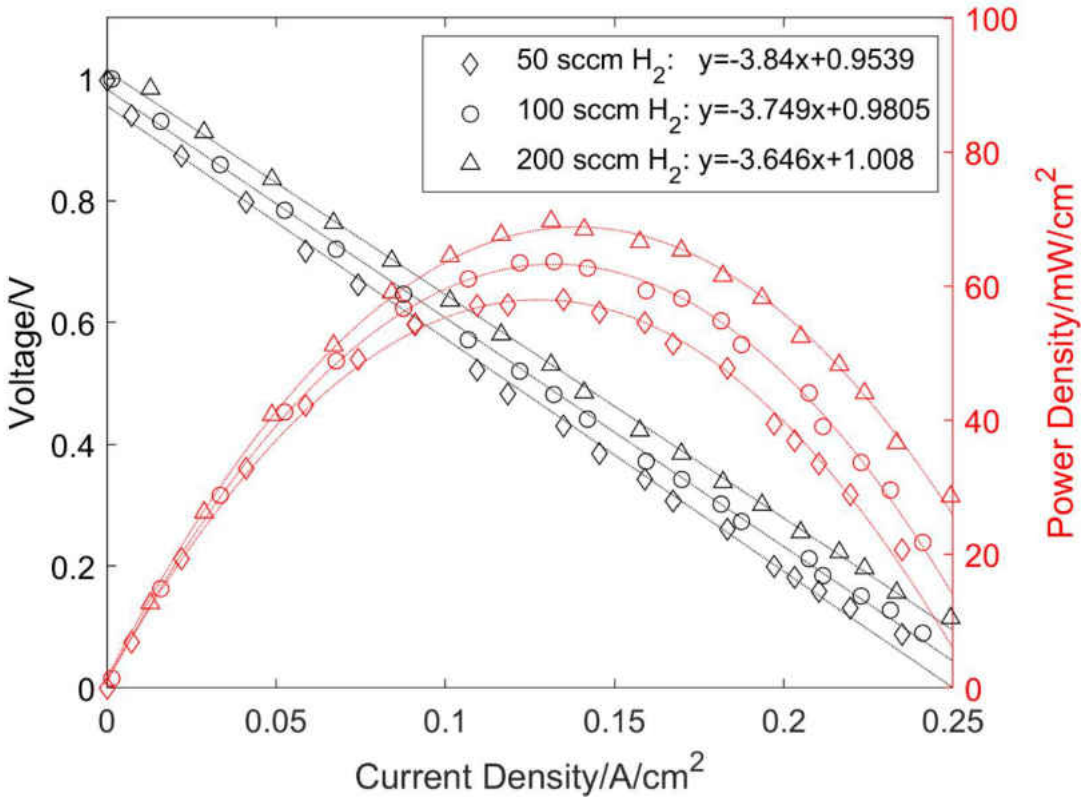

Figure 56. Voltage scan of SOFC button cell #5 with 3D printed cathode (0.5 cm^2 active area) at 750 °C and the hydrogen flow rate of 50, 100, 200 sccm respectively.

The SOFC button cell #6 with 3D printed LSM cathode was characterized as shown in Figure 57. During initial anode reduction with hydrogen flow rate of 100 sccm, the cell exhibited the maximum OCV of 1.127 V at 490 °C. When the temperature reached 750 °C, a stable OCV of 1.063 V was observed. Afterwards, the step voltage was applied from 0.9 V to 0.1 V and the corresponding current density was recorded with a frequency of 1/30 s^{-1}. Three groups of voltage scan were then conducted on the cell #6 at operation temperature of 750 °C, 800 °C and 700 °C respectively. For each group experiment at constant temperature, the cell was tested at the hydrogen flow rate of 50 sccm, 100 sccm and 200 sccm respectively. The air was pumped into the cathode side with a constant flow rate of 250 sccm during the whole characterization process. Finally, the SOFC button cell showed a stable OCV of 1.071 V at 700 °C and H_2 flow rate of 100 sccm.

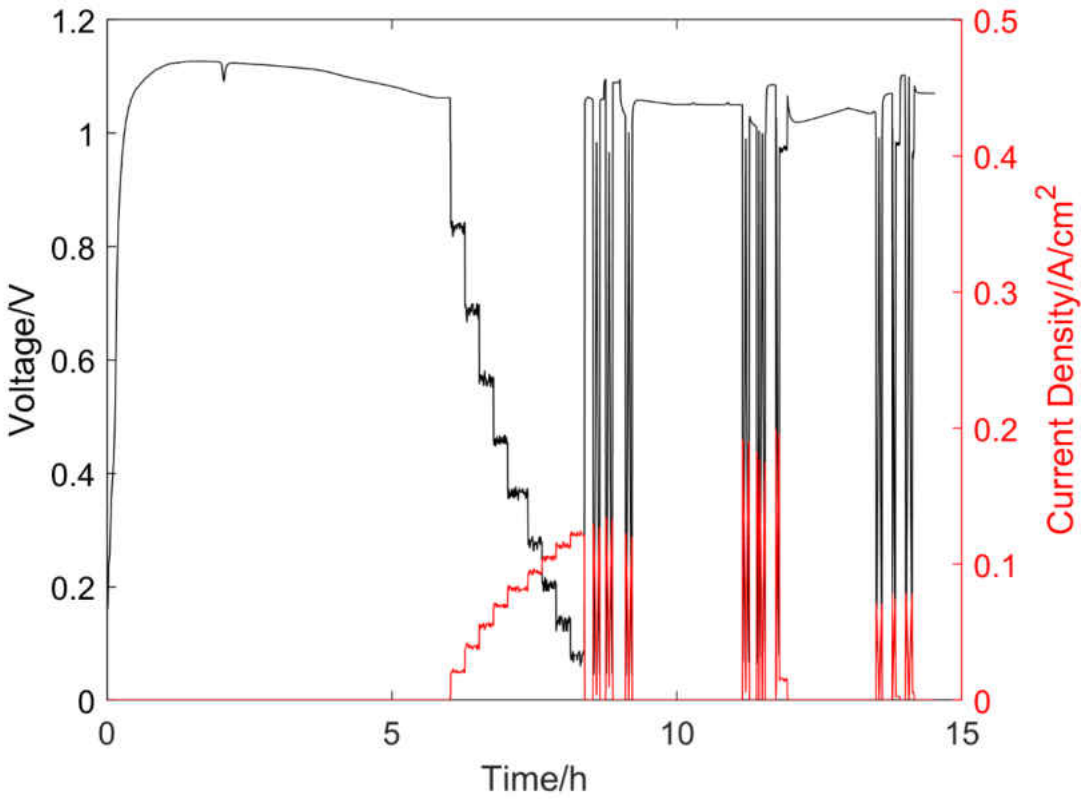

Figure 57. Characterization of SOFC button cell #6 with 3D printed LSM cathode (0.5 cm^2 active area).

The first group of voltage scan was conducted at 750 °C with hydrogen flow rate of 50 sccm, 100 sccm and 200 sccm, respectively. As shown in Figure 58, the experimental data of applied voltage and current density followed linear relation at different H_2 flow rate. The cell resistance was calculated by the slope of linearly fitting curves. It decreased from 7.65 $\Omega \cdot cm^2$ to 7.29 $\Omega \cdot cm^2$ with an increase of gas flow rate. This could be explained by the increasing H_2 pressure or concentration at anode. Compared to the cell #2 with the reference resistance of 1.728 $\Omega \cdot cm^2$, the cell #6 is not competent despite of higher hydrogen flow rate. The maximum power output were 30.1 mW/cm^2, 32.8 mW/cm^2 and 35.3 mW/cm^2 at H_2 flow rate of 50 sccm, 100 sccm and 200 sccm respectively.

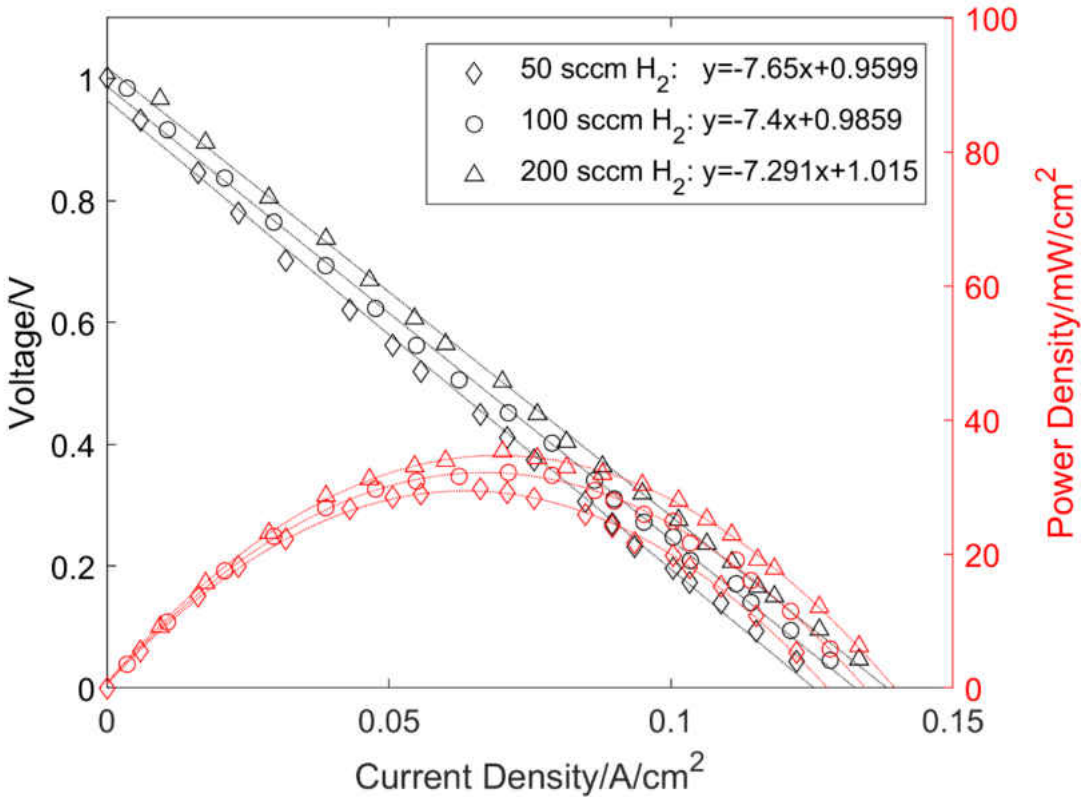

Figure 58. Voltage scan of SOFC button cell #6 with 3D printed LSM cathode (0.5 cm^2 active area) at 750 °C and H_2 flow rate of 50 sccm, 100 sccm and 200 sccm respectively.

The second group of voltage scans was conducted at 800 °C and the other testing conditions were the same with those of the first group. As shown in Figure 59, V-I curves were also approximately linear at different H_2 flow rates. The cell decreased from 5.097 $\Omega \cdot cm^2$ to 4.912 $\Omega \cdot cm^2$ with an increase of gas flow rate. Compared to the first group of voltage scans, the second group test exhibited a much lower resistance. This is because the YSZ electrolyte is more ion conductive at higher temperature. The maximum power outputs were 46.0 mW/cm^2, 50.5 mW/cm^2 and 54.6 mW/cm^2 at H_2 flow rate of 50 sccm, 100 sccm and 200 sccm respectively.

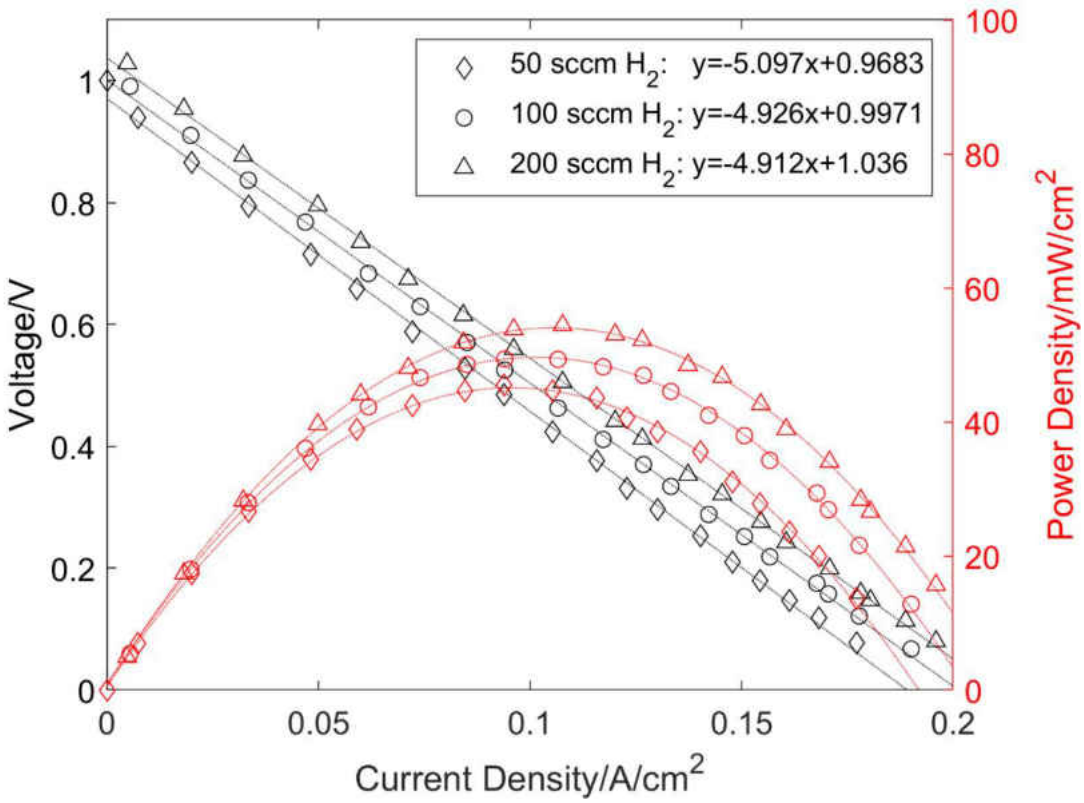

Figure 59. Voltage scan of SOFC button cell #6 with 3D printed LSM cathode (0.5 cm^2 active area) at 800 °C and H_2 flow rate of 50 sccm, 100 sccm and 200 sccm respectively.

The third group of voltage scans was conducted at 700 °C and the other testing conditions were the same with those of the first group. As shown in Figure 60, V-I curves were approximately linear at different conditions. The cell decreased from 12.72 $\Omega \cdot cm^2$ to 12.38 $\Omega \cdot cm^2$ with an increase of gas flow rate. Compared to the resistance of the first group test, the resistance of the third group test was much higher due to the lower ion conductivity of YSZ electrolyte at lower temperature. The maximum power output were 17.8 mW/cm^2, 19.8 mW/cm^2 and 21.1 mW/cm^2 at H_2 flow rate of 50 sccm, 100 sccm and 200 sccm respectively.

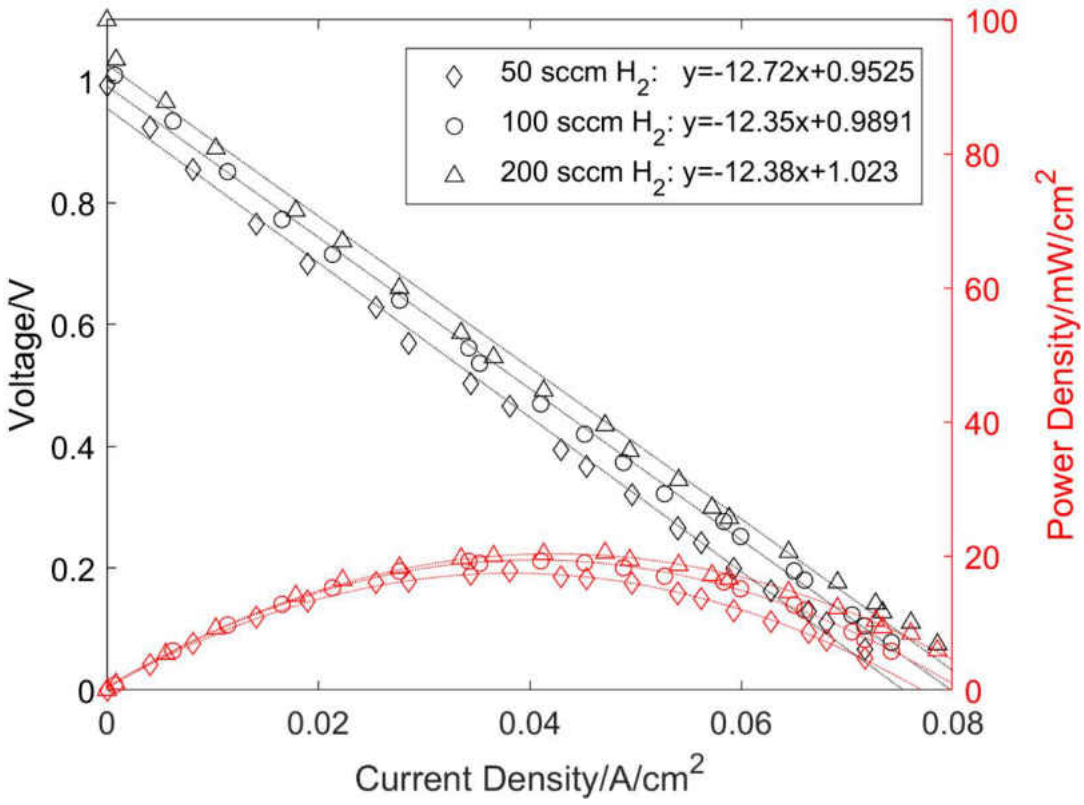

Figure 60. Voltage scan of SOFC button cell #6 with 3D printed LSM cathode (0.5 cm^2 active area) at 700 °C and H_2 flow rate of 50 sccm, 100 sccm and 200 sccm respectively.

The voltage scans of cell #6 with constant H_2 flow rate of 100 sccm at different temperature were shown in Figure 61. Generally, the temperature can affect the SOFC performance in two ways. First, the Nernst potential decreases with increasing temperature due to the decreasing Gibb free energy according to equation 16. Second, the ion conductivity of YSZ electrolyte increases with an increase of temperature. It can be concluded that the first factor is negligible according to the significant decrease of resistance with increasing temperature. When the temperature increased from 700 °C to 800 °C, the maximum power outputs increased remarkably from 19.8 mW/cm^2 to 50.5 $m{\cdot}cm^2$.

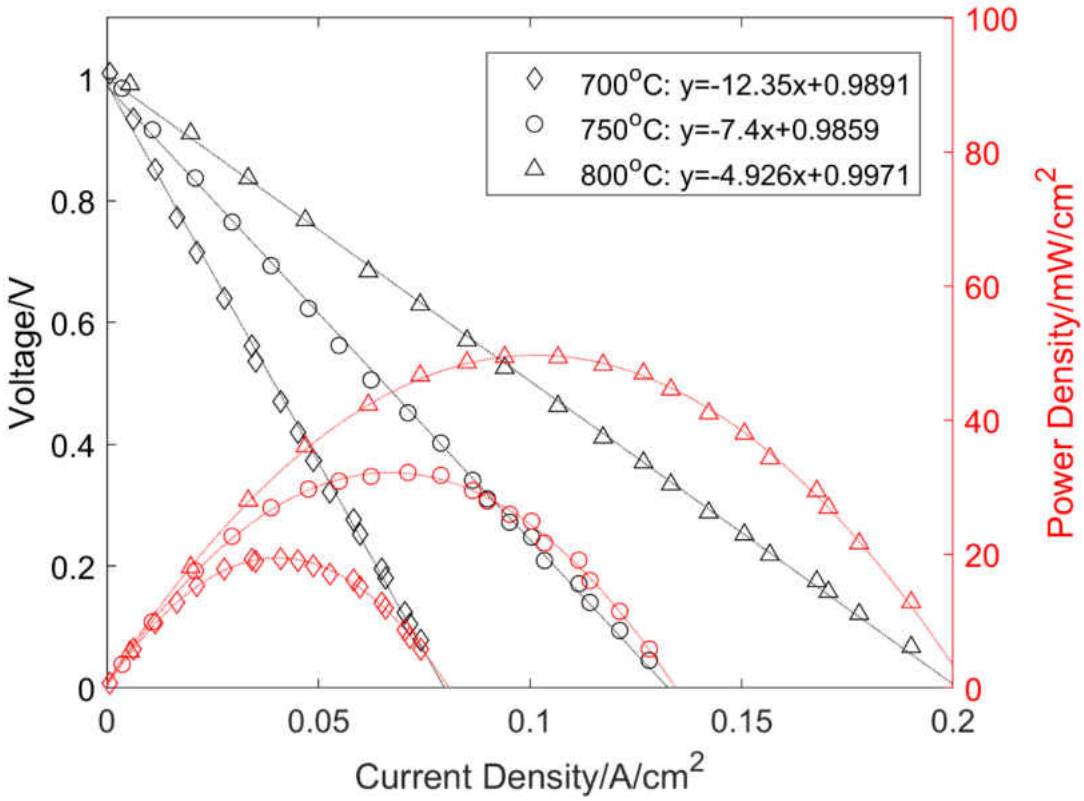

Figure 61. Voltage scan of SOFC button cell #6 with 3D printed LSM cathode (0.5 cm^2 active area) at 100 sccm of H_2 and temperature of 700 °C, 750 °C and 800 °C respectively.

The SOFC button cell #7 with 3D printed LSM cathode (1 cm^2 active area) was tested as shown in Figure 62. With H_2 flow rate of 100 sccm at the anode, the furnace increased from 400 °C (preheat) to 750 °C with increasing rate of 1 °C/min. The cell showed the maximum OCV of 1.128 V at 470 °C and a stable OCV of 1.033 V at 750 °C. Afterwards, the step voltage was applied from 0.9 V to 0.2 V at a constant temperature of 750 °C and a constant H_2 flow rate of 100 sccm. Similar to the testing conditions of cell #6, three groups of voltage scans were then conducted on the cell #7 at operation temperature of 750 °C, 800 °C and 700 °C respectively. For each group experiment at constant temperature, a voltage scan was applied to estimate the cell resistance at the hydrogen flow rate of 50 sccm, 100 sccm and 200 sccm respectively. During the

whole characterization process, the air flow rate was maintained as 250 sccm. Finally, the SOFC button cell showed a stable OCV of 1.041 V at 700 °C and H_2 flow rate of 100 sccm.

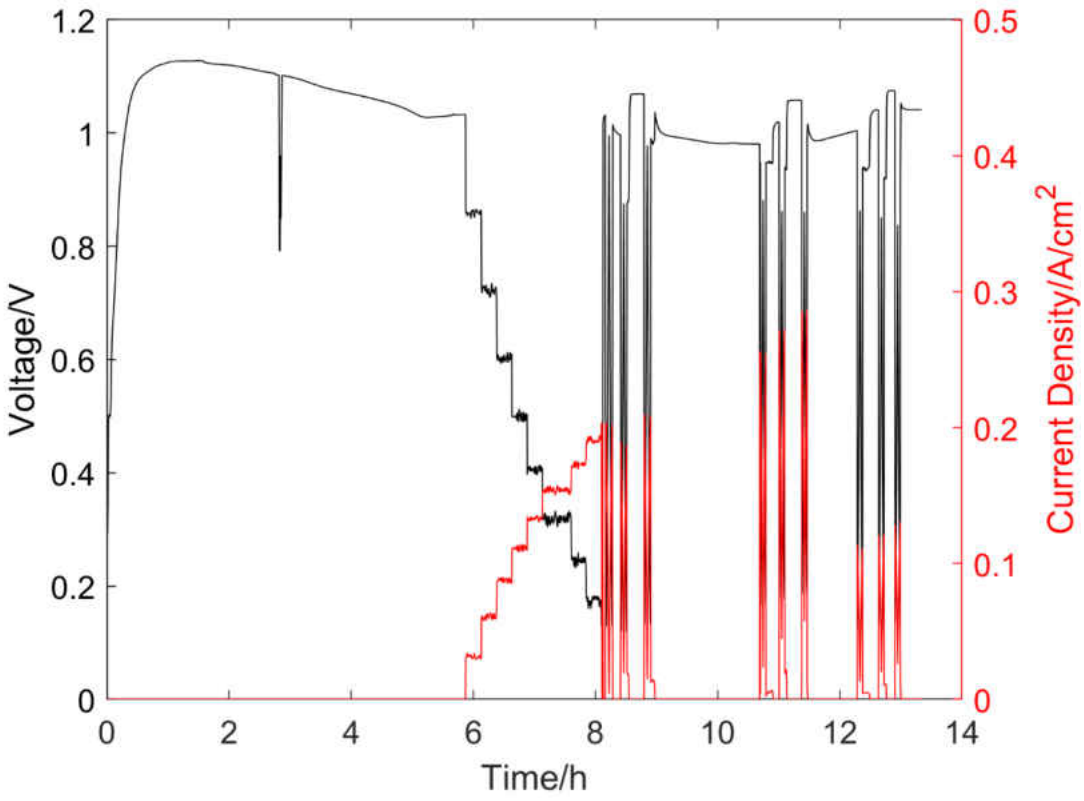

Figure 62. Characterization of SOFC button cell #7 with 3D printed LSM cathode (1 cm^2 active area).

The first group of voltage scans of cell #7 was conducted at 750 °C with hydrogen flow rate of 50 sccm, 100 sccm and 200 sccm respectively. As shown in Figure 63, the relation of applied voltage and current density was approximately linear at different H_2 flow rates. The cell resistance decreased from 4.45 $\Omega \cdot cm^2$ to 4.295 $\Omega \cdot cm^2$ with an increase of H_2 flow rate. It could be explained by the increasing H_2 pressure or concentration at anode. Compared to the cell #6,

the cell #7 showed a lower resistance at the same conditions. This is because the larger active area could reduce the transverse resistance of chargers that were collected by the silver mesh. The maximum power outputs were 50.6 mW/cm^2, 57.2 mW/cm^2 and 60.9 mW/cm^2 at H_2 flow rate of 50 sccm, 100 sccm and 200 sccm respectively.

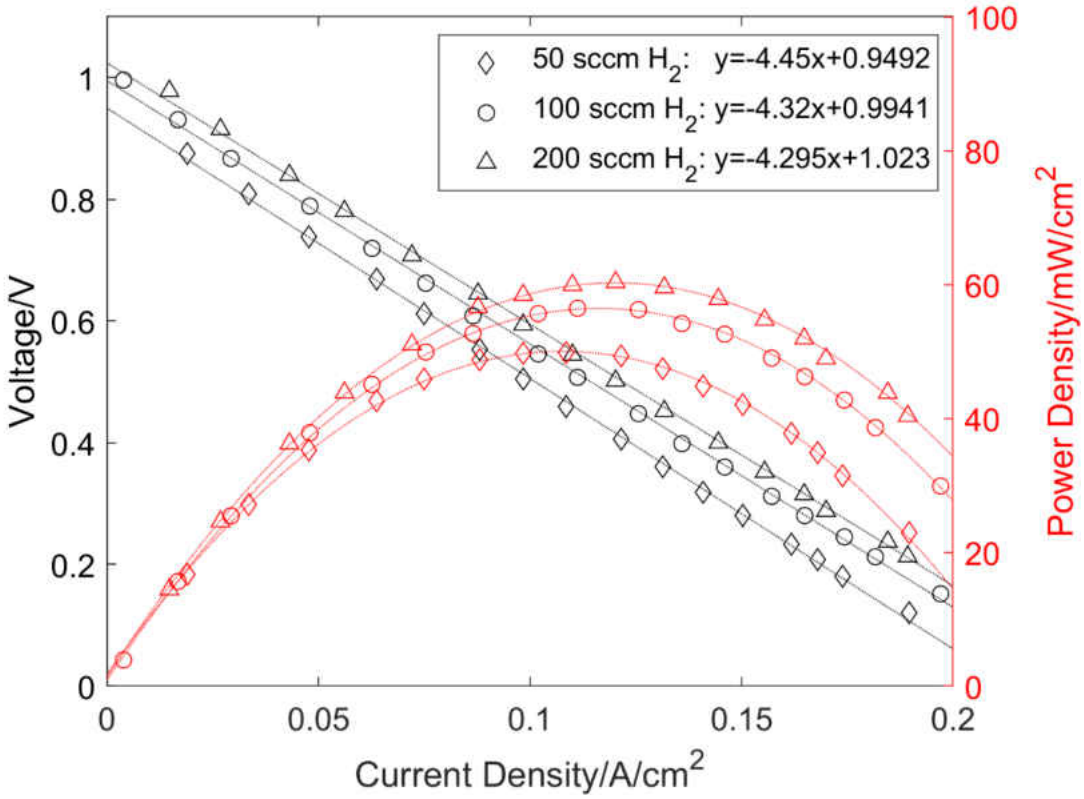

Figure 63. Voltage scan of SOFC button cell #7 with 3D printed LSM cathode (1 cm^2 active area) at 750 °C and H_2 flow rate of 50 sccm, 100 sccm and 200 sccm respectively.

The second group of voltage scans was conducted at 800 °C and the other testing conditions were the same with those of the first group. As shown in Figure 64, V-I curves were also approximately linear at different H_2 flow rates. The cell decreased from 3.076 Ω·cm^2 to

2.934 Ω·cm^2 with an increase of gas flow rate. Compared to the first group of voltage scans, the second group test exhibited a much lower resistance due to more ion conductive of YSZ electrolyte at higher temperature. The maximum power outputs were 72.4 mW/cm^2, 81.0 mW/cm^2 and 88.7 mW/cm^2 at H_2 flow rate of 50 sccm, 100 sccm and 200 sccm respectively.

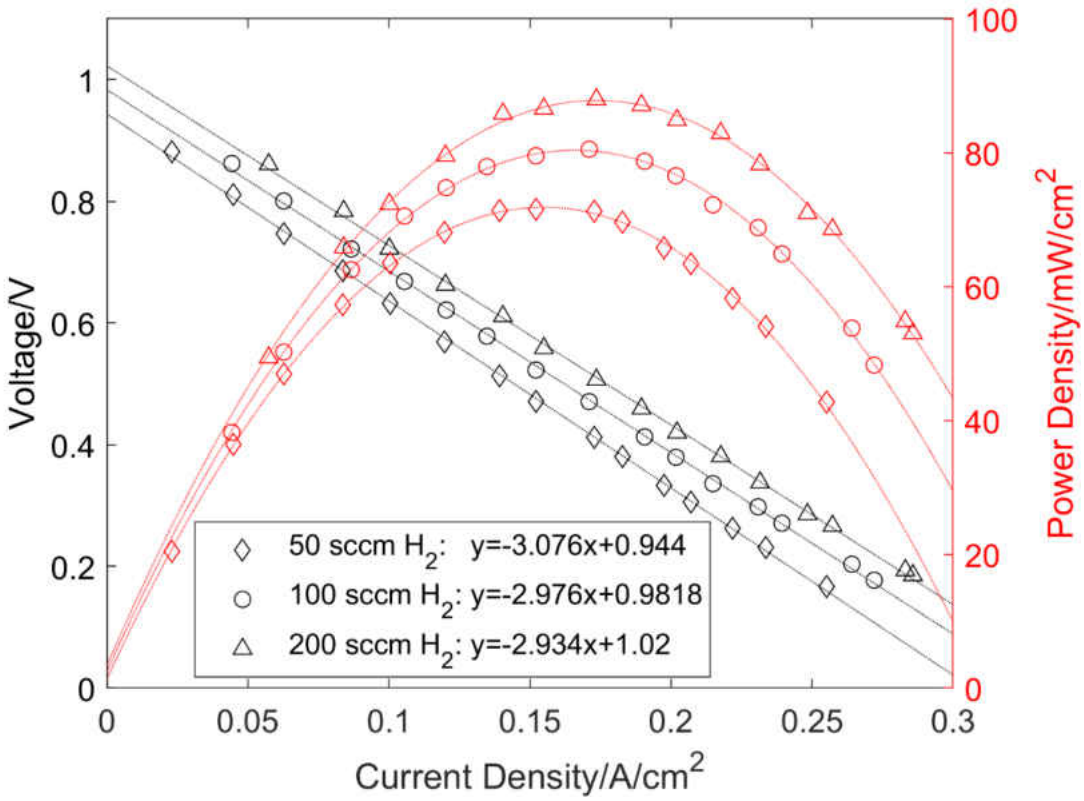

Figure 64. Voltage scan of SOFC button cell #7 with 3D printed LSM cathode (1 cm^2 active area) at 800 °C and H_2 flow rate of 50 sccm, 100 sccm and 200 sccm respectively

The third group of voltage scans was conducted at 700 °C and the other testing conditions were the same with those of the first group. As shown in Figure 65, V-I curves were approximately linear at different conditions as well. The cell decreased from 7.337 Ω·cm^2 to 6.859 Ω·cm^2 with an increase of gas flow rate. Compared to the resistance of the first group test,

the resistance of the third group test was much higher due to the lower ion conductivity of YSZ electrolyte at lower temperature. The maximum power outputs were 30.1 mW/cm^2, 33.7 mW/cm^2 and 36.7 mW/cm^2 at H_2 flow rate of 50 sccm, 100 sccm and 200 sccm respectively.

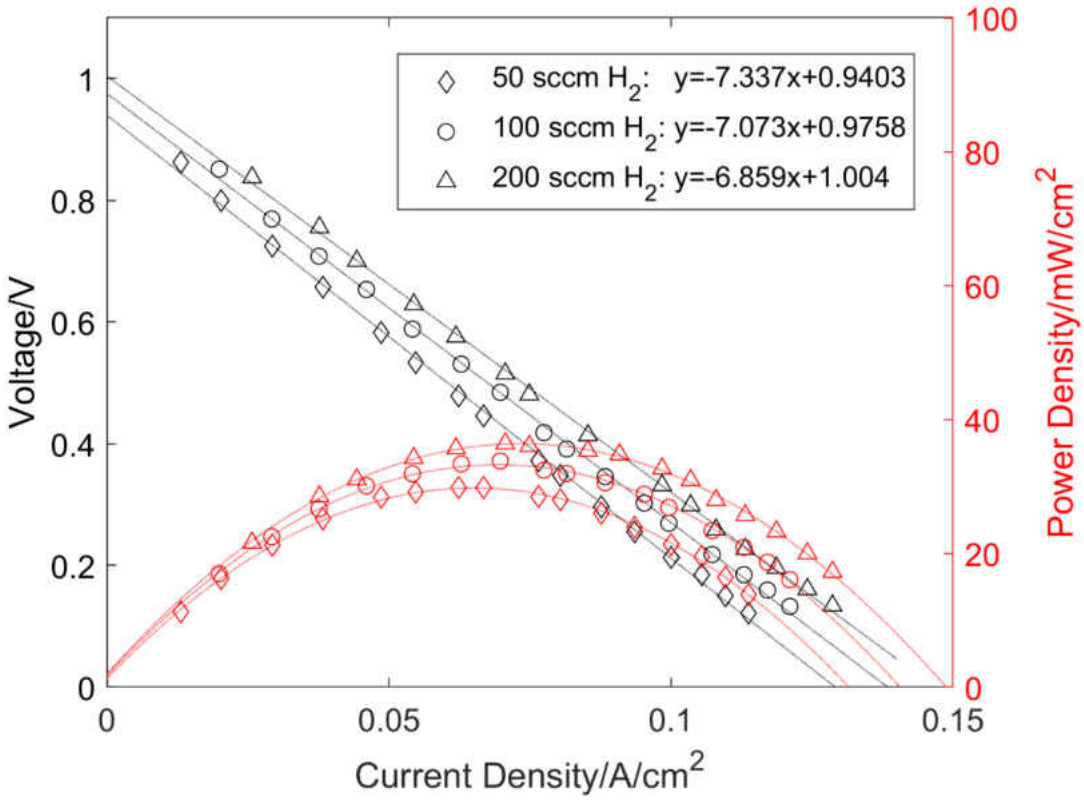

Figure 65. Voltage scan of SOFC button cell #7 with 3D printed LSM cathode (1 cm^2 active area) at 700 °C and H_2 flow rate of 50 sccm, 100 sccm and 200 sccm respectively.

The voltage scans of cell #7 with constant H_2 flow rate of 100 sccm at different temperature were shown in Figure 66. Again, the temperature had a significant effect on the cell performance due to improved ion conductivity of YSZ electrolyte. When the temperature increased from 700 °C to 800 °C, the maximum power outputs increased remarkably from 33.7

mW/cm^2 to 81.0 mW/cm^2. However, the high operation temperature could potentially result in serious degradation issues of the materials especially for the SOFC stacks.

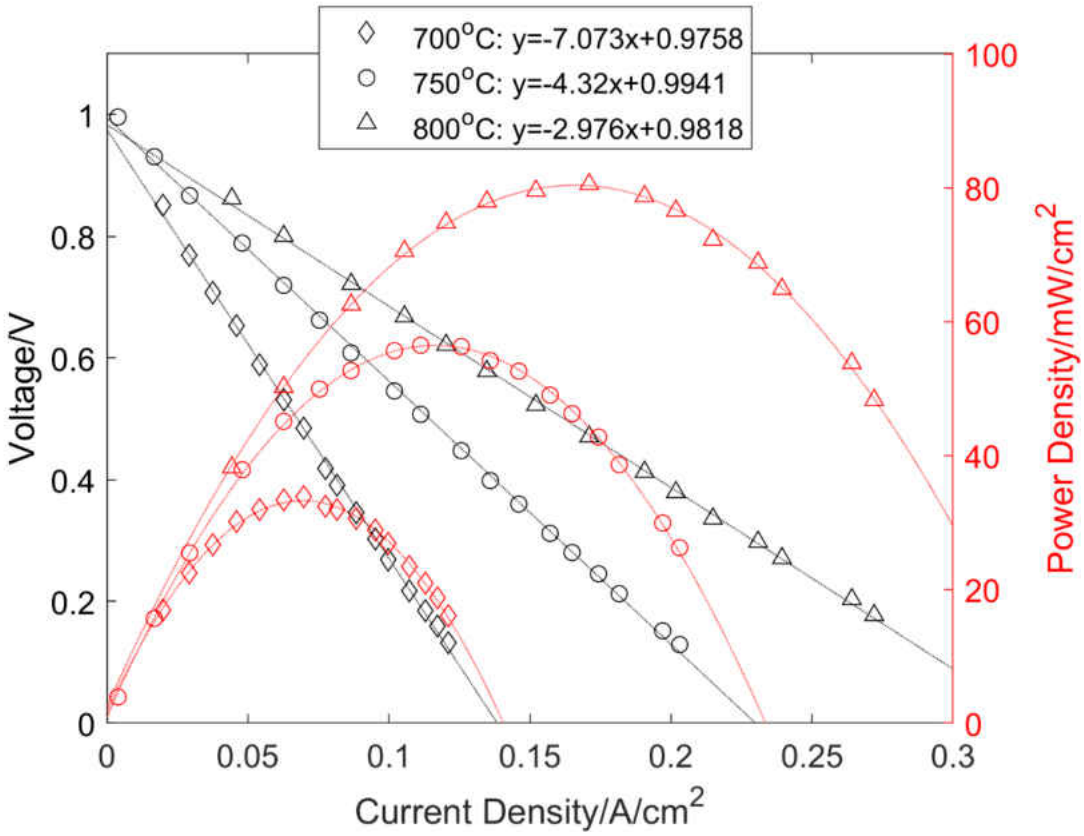

Figure 66. Voltage scan of SOFC button cell #7 with 3D printed LSM cathode (1 cm^2 active area) at 100 sccm of H_2 and temperature of 700 °C, 750 °C and 800 °C respectively.

3.3.3 SOFC button cell with 3D printed LSCF cathode

The SOFC button cell #8 with 3D printed LSCF cathode was characterized as shown in Figure 67. During initial anode reduction with H_2 flow rate of 100 sccm, the cell exhibited the maximum OCV of 1.150 V at 505 °C. When the temperature reached 750 °C, a stable OCV of 1.079 V was observed. Afterwards, the step voltage was applied from 0.9 V to 0.1 V and the

corresponding current density was recorded with a frequency of 1/30 s^{-1}. Three groups of voltage scans were then conducted on the cell #8 at operation temperature of 750 °C, 800 °C and 700 °C respectively. For each group experiment at constant temperature, the cell was tested at the hydrogen flow rate of 50 sccm, 100 sccm and 200 sccm respectively. The air was maintained at a constant flow rate 250 sccm at the cathode side during the whole characterization process. Finally, the SOFC button cell showed a stable OCV of 1.026 V at 700 °C and H_2 flow rate of 100 sccm.

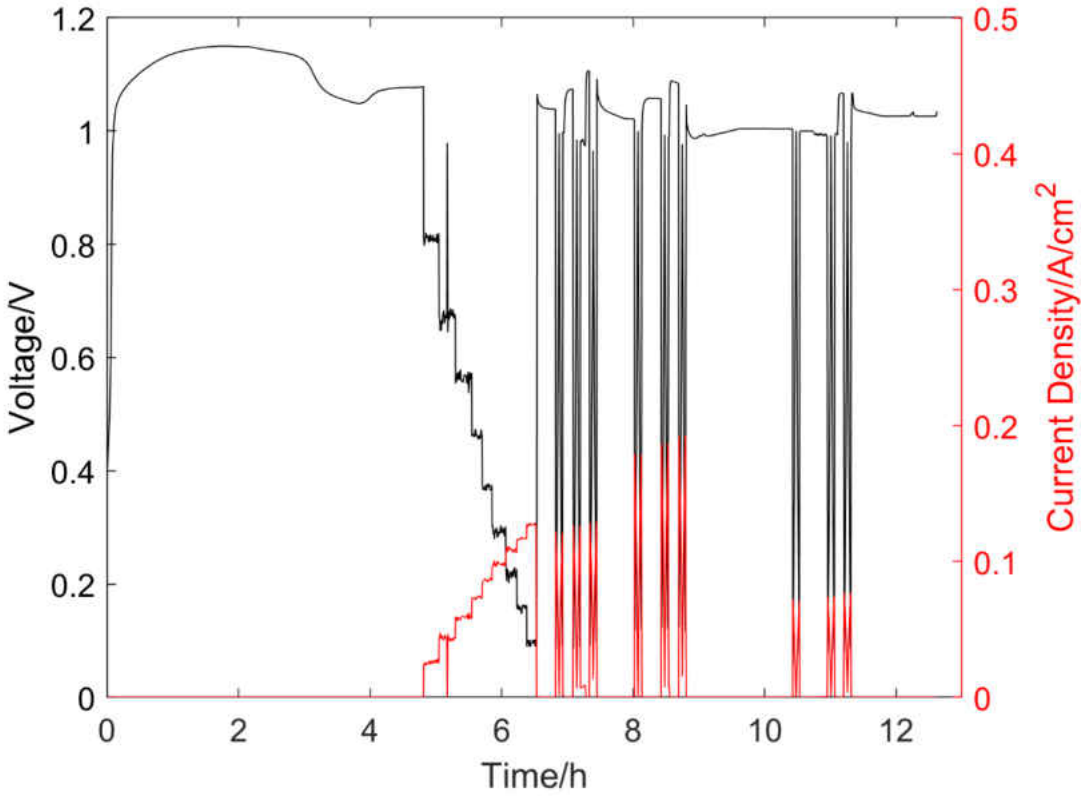

Figure 67. Characterization of SOFC button cell #8 with 3D printed LSCF cathode (1 cm^2 active area).

The first group of voltage scans was conducted at 750 °C with hydrogen flow rate of 50 sccm, 100 sccm and 200 sccm respectively. As shown in Figure 68, the V-I experimental data of LSCF based cell also showed linear relation at different H_2 flow rate. The cell resistance was calculated by the slope of linearly fitting curves. It decreased from 7.536 $\Omega \cdot cm^2$ to 7.498 $\Omega \cdot cm^2$ with an increase of gas flow rate. Compared to the LSM based cells, the cell #8 had similar resistance with cell #6 but higher resistance than cell #5 and cell #7. The maximum power outputs were 32.8 mW/cm^2, 35.1 mW/cm^2 and 37.3 mW/cm^2 at H_2 flow rate of 50 sccm, 100 sccm and 200 sccm respectively.

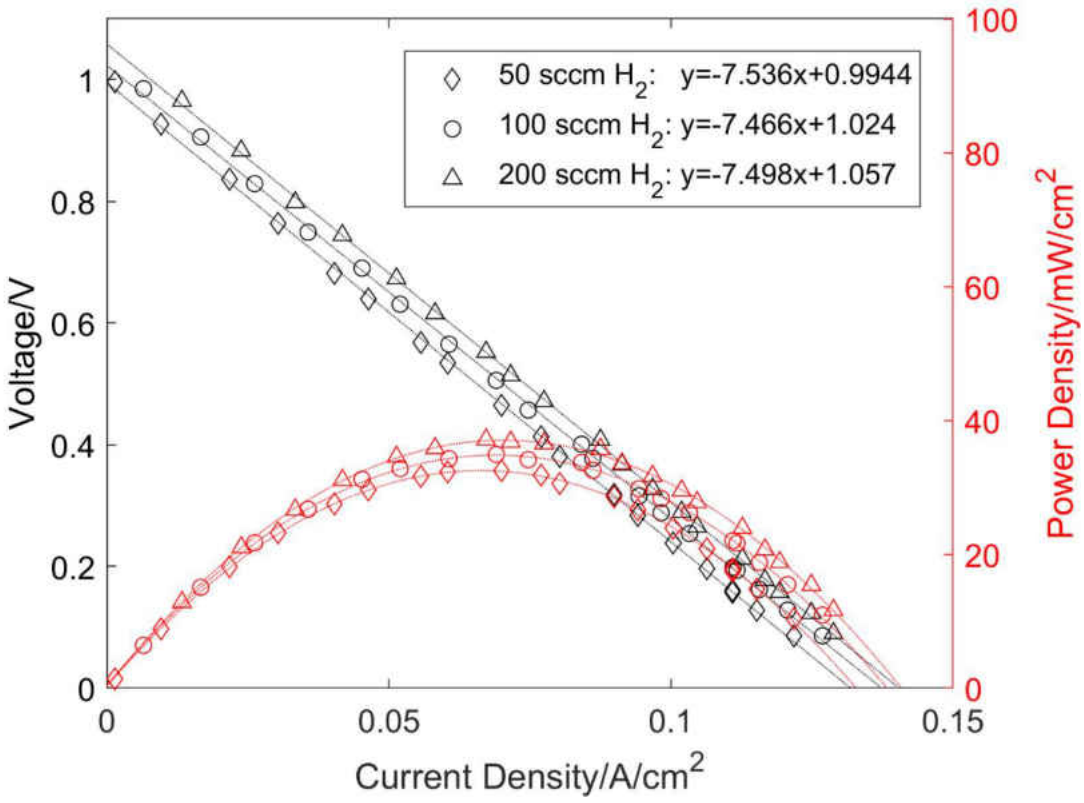

Figure 68. Voltage scan of SOFC button cell #8 with 3D printed LSCF cathode (1 cm^2 active area) at 750 °C and H_2 flow rate of 50 sccm, 100 sccm and 200 sccm respectively.

The second group of voltage scan was conducted at 800 °C and the other testing conditions were the same with those of the first group. As shown in Figure 69, V-I curves were also approximately linear at different H_2 flow rates. The cell decreased from 4.877 $\Omega \cdot cm^2$ to 4.818 $\Omega \cdot cm^2$ with an increase of H_2 flow rate. Compared to the first group of voltage scans, the second group test exhibited a much lower resistance due to higher ion conductivity of YSZ electrolyte at higher temperature. The maximum power outputs were 49.9 mW/cm^2, 54.0 mW/cm^2 and 56.6 mW/cm^2 at H_2 flow rate of 50 sccm, 100 sccm and 200 sccm, respectively.

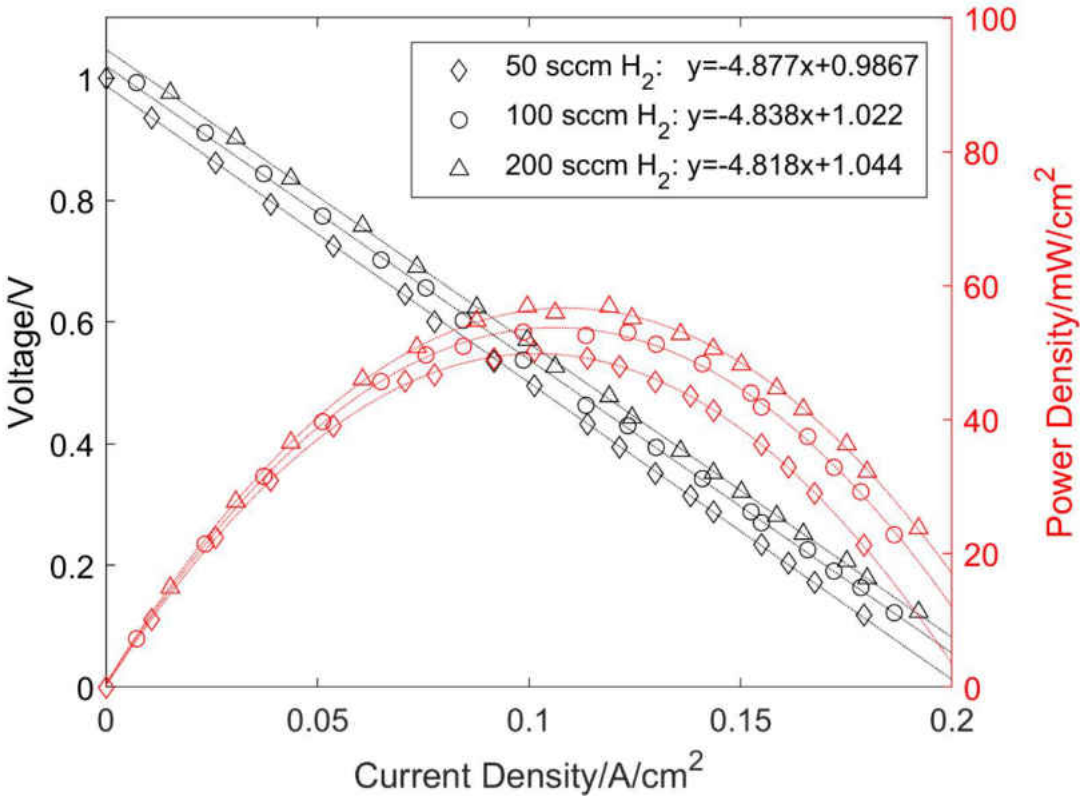

Figure 69. Voltage scan of SOFC button cell #8 with 3D printed LSCF cathode (1 cm^2 active area) at 800 °C and H_2 flow rate of 50 sccm, 100 sccm and 200 sccm respectively

The third group of voltage scans was conducted at 700 °C and the other testing conditions were the same with those of the first group. As shown in Figure 70, V-I curves were approximately linear at different conditions. The cell decreased from 12.52 $\Omega \cdot cm^2$ to 12.07 $\Omega \cdot cm^2$ with an increase of gas flow rate. Compared to the resistance of the first group test, the resistance of the third group test was much higher due to the lower ion conductivity of YSZ electrolyte at lower temperature. The maximum power outputs were 17.8 mW/cm^2, 19.5 mW/cm^2 and 20.8 mW/cm^2 at H_2 flow rate of 50 sccm, 100 sccm and 200 sccm respectively.

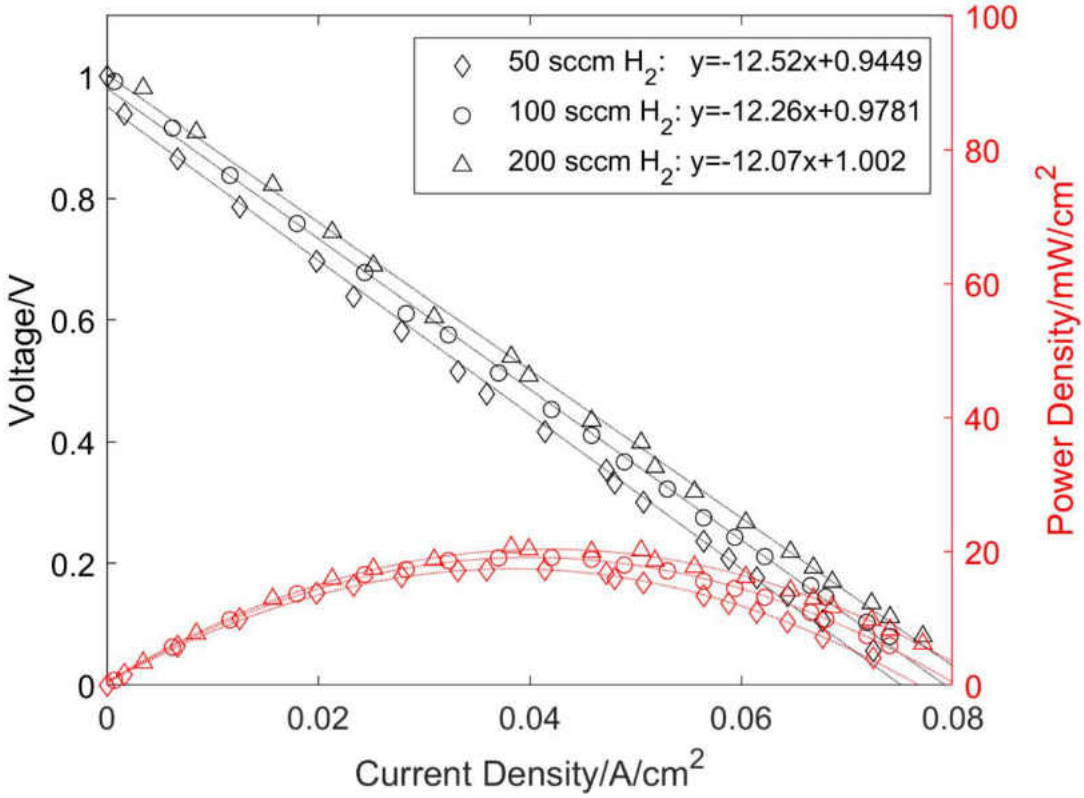

Figure 70. Voltage scan of SOFC button cell #8 with 3D printed LSCF cathode (1 cm^2 active area) at 700 °C and H_2 flow rate of 50 sccm, 100 sccm and 200 sccm respectively.

The voltage scans of cell #8 with constant H_2 flow rate of 100 sccm at different temperature were shown in Figure 71. Similar to LSM based cells, the temperature had a significant effect on the LSCF based cell performance due to improved ion conductivity of YSZ electrolyte. When the temperature increased from 700 °C to 800 °C, the maximum power outputs increased remarkably from 19.5 mW/cm^2 to 54.0 mW/cm^2.

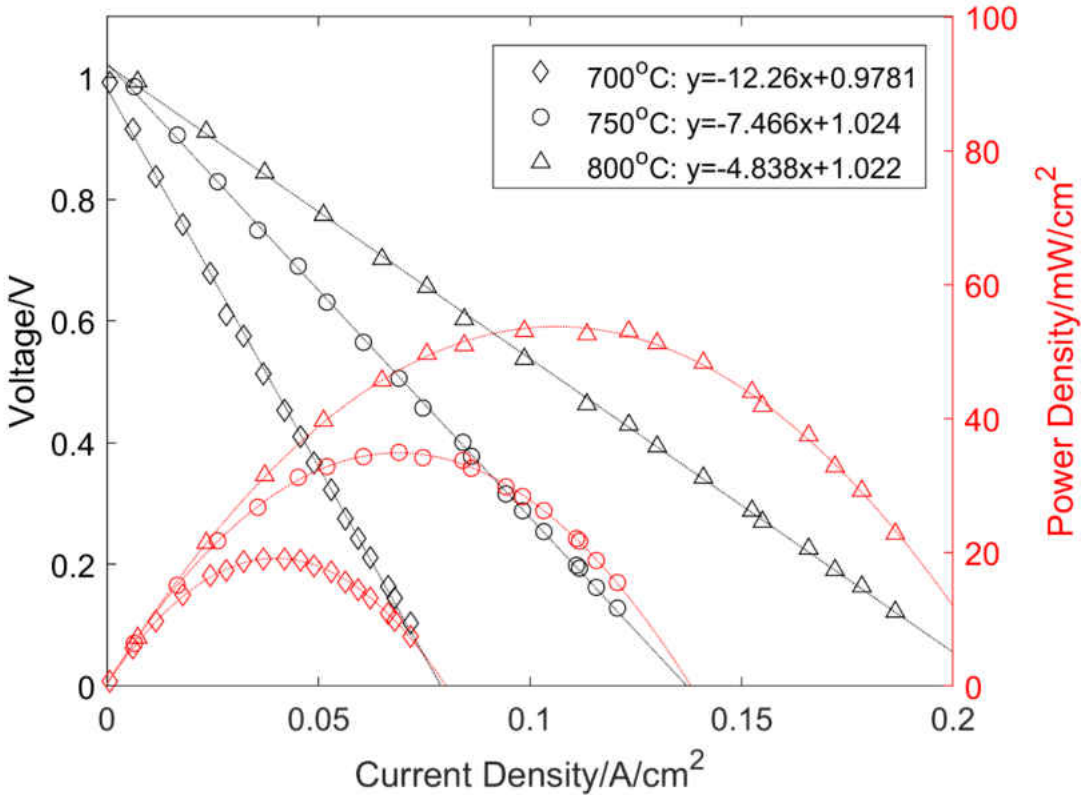

Figure 71. Voltage scan of SOFC button cell #8 with 3D printed LSCF cathode (1 cm^2 active area) at 100 sccm of H_2 and temperature of 700 °C, 750 °C and 800 °C respectively.

The SOFC button cell #9 with 3D printed LSCF cathode was characterized as shown in Figure 72. With H_2 flow rate of 100 sccm at the anode, the cell exhibited the maximum OCV of

1.163 V at 500 °C. A stable OCV of 1.093 V was observed when the temperature reached 750 °C. The step voltage was then applied from 1.0 V to 0.1 V and the corresponding current density was recorded. Afterwards, three groups of voltage scan were conducted on the cell #9 at operation temperature of 750 °C, 800 °C and 700 °C, respectively. For each group experiment maintained at constant temperature, the cell was tested at the hydrogen flow rate of 50 sccm, 100 sccm and 200 sccm respectively. The air was kept at a constant flow rate 250 sccm at the cathode side during the whole characterization process. Finally, the SOFC button cell showed a stable OCV of 1.101 V at 700 °C and H_2 flow rate of 100 sccm.

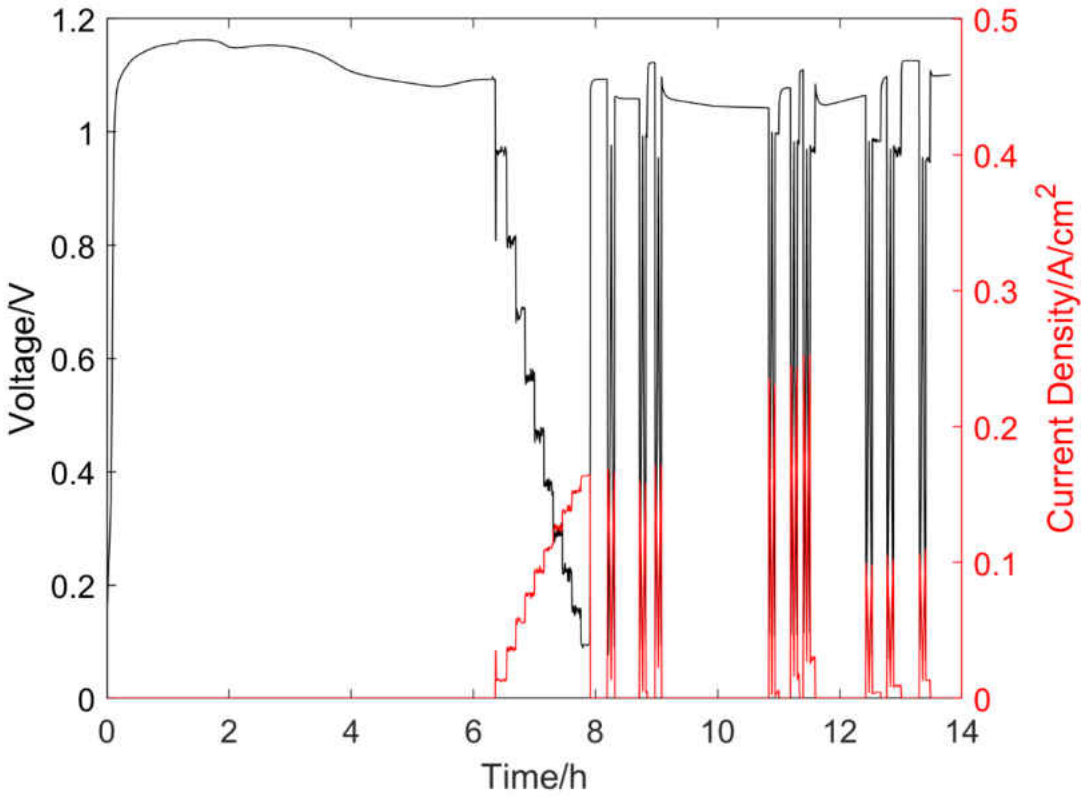

Figure 72. Characterization of SOFC button cell #9 with 3D printed LSCF cathode (1 cm^2 active area).

The first group of voltage scan was conducted at 750 °C with hydrogen flow rate of 50 sccm, 100 sccm and 200 sccm respectively. As shown in Figure 73, the V-I experimental data of LSCF based cell showed linear relation at different H_2 flow rate as well. The cell resistance was calculated by the slope of linearly fitting curves. It ranged from 5.744 $\Omega \cdot cm^2$ to 5.838 $\Omega \cdot cm^2$ with different gas flow rate. Compared to the cell #8 based on LSCF, the cell #9 showed a lower resistance at different conditions. This may be explained by the thinner cathode layer according to the post inspection. The maximum power outputs were 44.0 mW/cm^2, 47.6 mW/cm^2 and 50.3 mW/cm^2 at H_2 flow rate of 50 sccm, 100 sccm and 200 sccm, respectively.

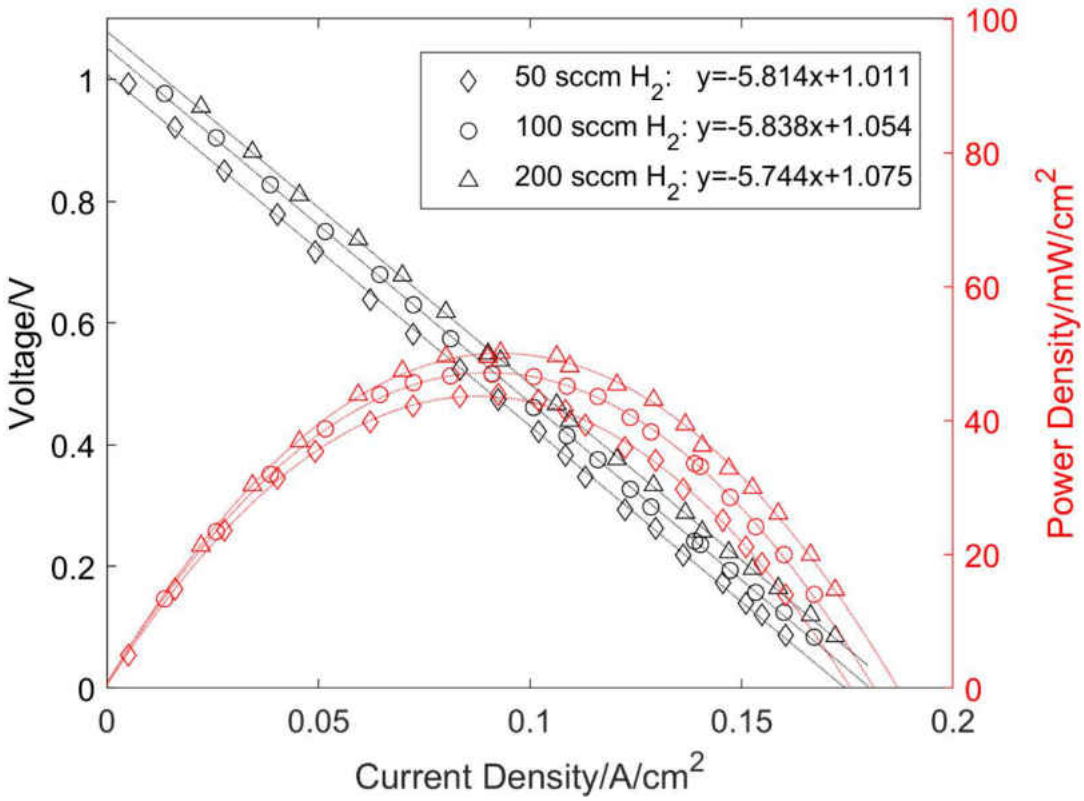

Figure 73. Voltage scan of SOFC button cell #9 with 3D printed LSCF cathode (1 cm^2 active area) at 750 °C and H_2 flow rate of 50 sccm, 100 sccm and 200 sccm respectively.

The second group of voltage scans was conducted at 800 °C and the other testing conditions were the same with those of the first group. As shown in Figure 74, V-I curves were also approximately linear at different H_2 flow rates. The cell decreased from 3.838 $\Omega \cdot cm^2$ to 3.762 $\Omega \cdot cm^2$ with an increase of H_2 flow rate. Compared to the first group of voltage scans, the second group test exhibited a much lower resistance due to higher ion conductivity of YSZ electrolyte at higher temperature. The maximum power outputs were 65.3 mW/cm^2, 70.9 mW/cm^2 and 75.4 mW/cm^2 at H_2 flow rate of 50 sccm, 100 sccm and 200 sccm respectively.

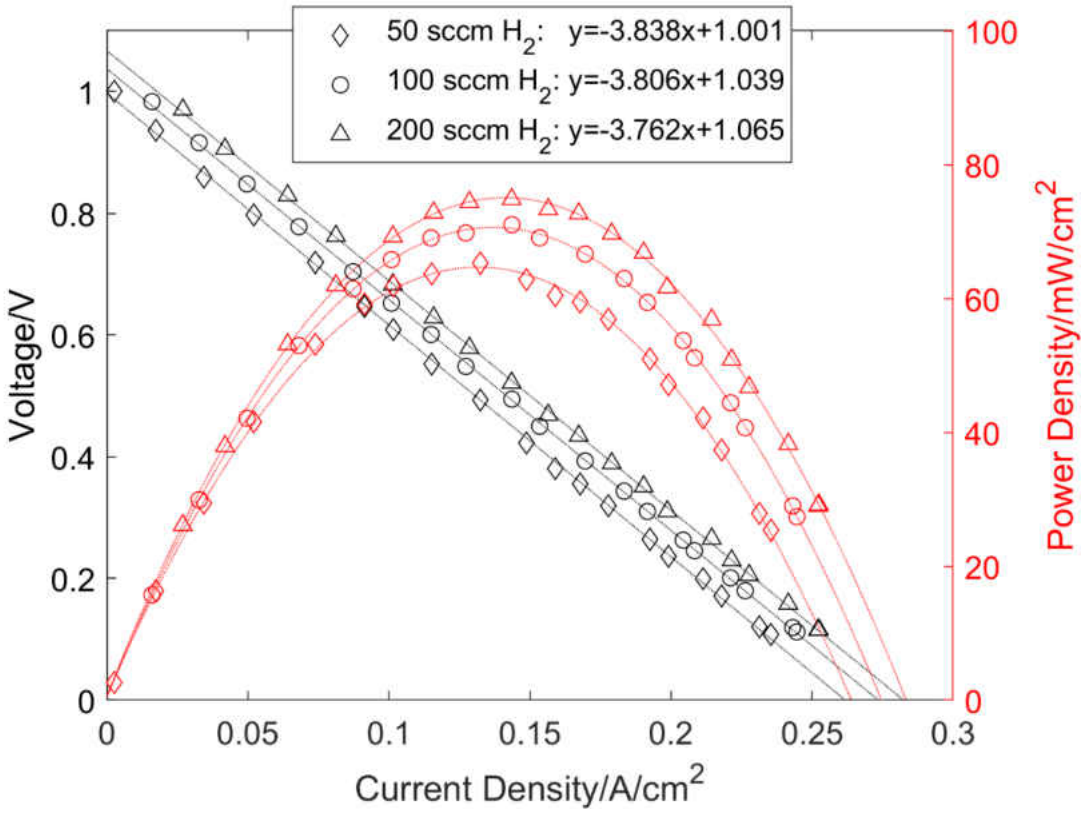

Figure 74. Voltage scan of SOFC button cell #9 with 3D printed LSCF cathode (1 cm^2 active area) at 800 °C and H_2 flow rate of 50 sccm, 100 sccm and 200 sccm respectively.

The third group of voltage scans was conducted at 700 °C and the other testing conditions were the same with those of the first group. As shown in Figure 75, V-I curves were approximately linear at different conditions. The cell decreased from 9.426 $\Omega \cdot cm^2$ to 9.157 $\Omega \cdot cm^2$ with an increase of gas flow rate. Compared to the resistance of the first group test, the resistance of the third group test was much higher due to the lower ion conductivity of YSZ electrolyte at lower temperature. The maximum power outputs were 26.6 mW/cm^2, 28.8 mW/cm^2 and 30.6 mW/cm^2 at H_2 flow rate of 50 sccm, 100 sccm and 200 sccm respectively.

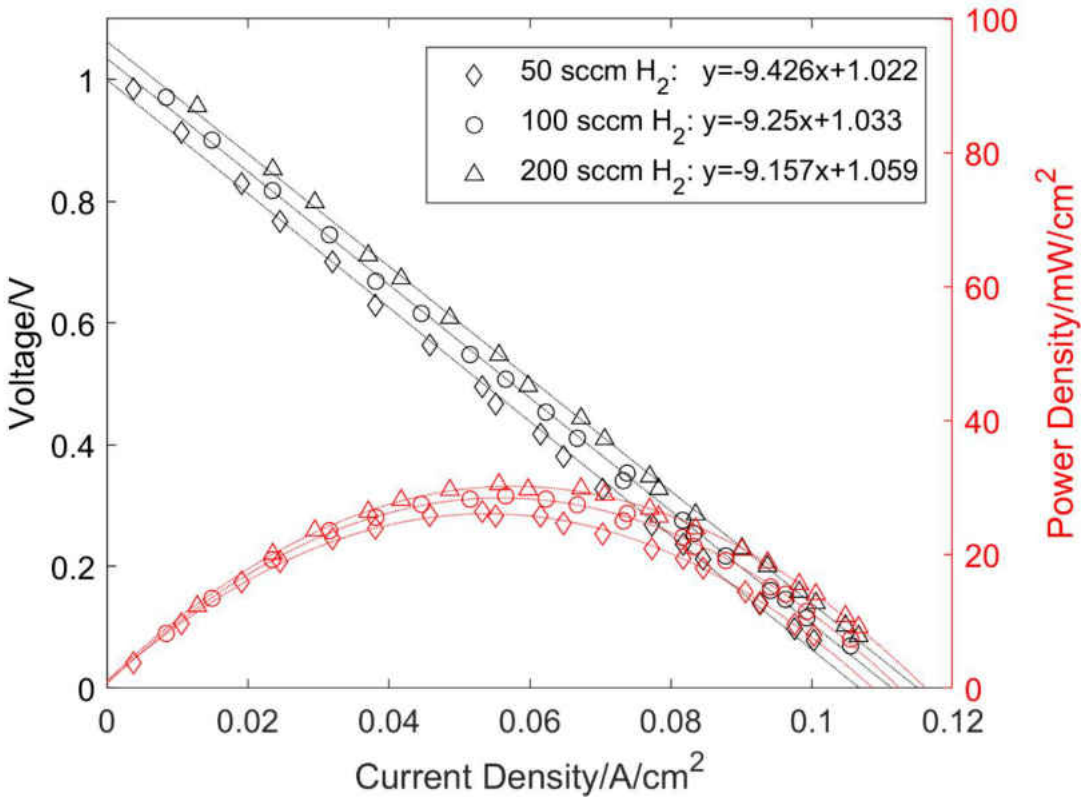

Figure 75. Voltage scan of SOFC button cell #9 with 3D printed LSCF cathode (1 cm^2 active area) at 700 °C and H_2 flow rate of 50 sccm, 100 sccm and 200 sccm respectively.

The voltage scans of cell #9 with constant H_2 flow rate of 100 sccm at different temperature were shown in Figure 76. Similar to all the cells mentioned above, the temperature had a significant effect on the cell #9 performance due to improved ion conductivity of YSZ electrolyte. When the temperature increased from 700 °C to 800 °C with hydrogen flow rate of 100 sccm, the maximum power outputs increased remarkably from 28.8 mW/cm^2 to 70.9 mW/cm^2.

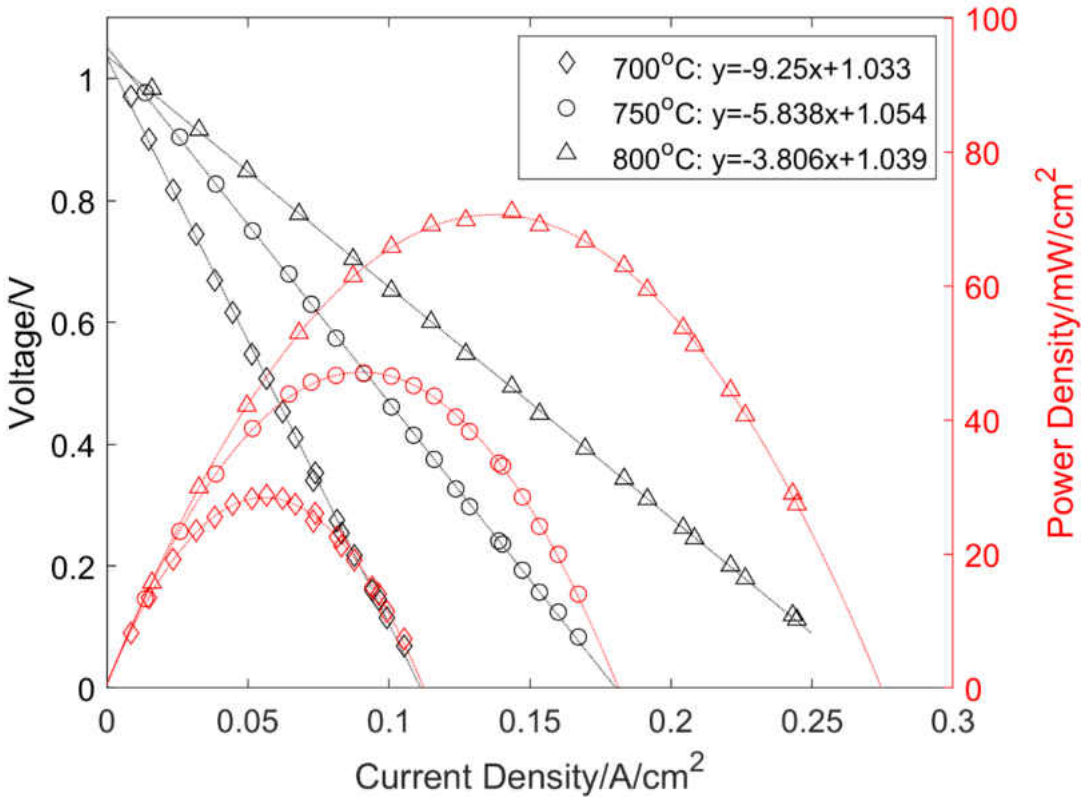

Figure 76. Voltage scan of SOFC button cell #9 with 3D printed LSCF cathode (1 cm^2 active area) at 100 sccm of H_2 and temperature of 700 °C, 750 °C and 800 °C respectively.

3.3.4 Cathode surface characterization

Figure 77 shows the surface characterization of dip-coating LSM cathode. The cracks in Figure 77a resulted from the thermal expansion of LSM layer during sintering. The pores were uniformly distributed with a relatively low density. This is because the concentration of pore former (cellulose) was only 6 wt. % during mixing. The pore sizes exhibited a wide range from 104 nm to 609 nm as shown in Figure 77d.

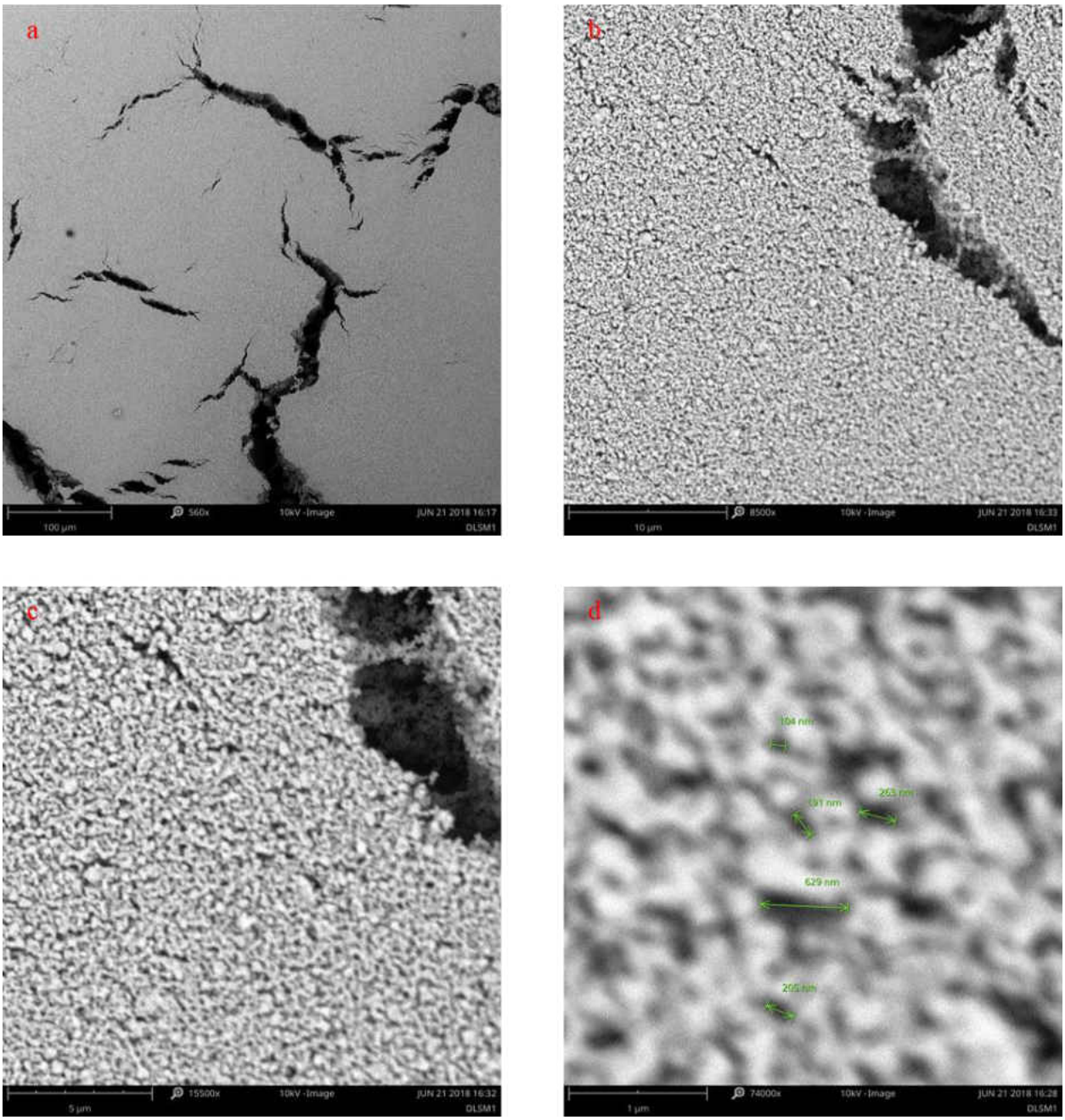

Figure 77. SEM surface characterization of dip-coating LSM cathode with scale bar of a. 100 µm; b. 10 µm; c. 5 µm; d. 1 µm.

Figure 78b, c, and d show the surface characterization of 3D printed LSM cathode. Similar to the dip-coating technique, cracks could not be avoided due to thermal expansion

during sintering as shown in Figure 78b. Compared to the dip-coating cathode, the porosity of 3D printed cathode was higher since the volume ratio of thermoplastic polymers was much higher (60%) during mixing. The porosity was estimated as 35.5% after Matlab image processing based on Figure 78d. However, the performance of 3D printed cell was lower than that of reference cells. This could confirm that the layer thickness of cathodes has a significant influence in the SOFC performance. Further improvement of 3D printed cathodes should focus on reducing the cathode thickness. Note that, the pore size of Ag collector was much bigger as shown in Figure 78a, and the pore dimensions were similar to the reference ranging from 89.5 nm to 835 nm as shown in Figure 78d.

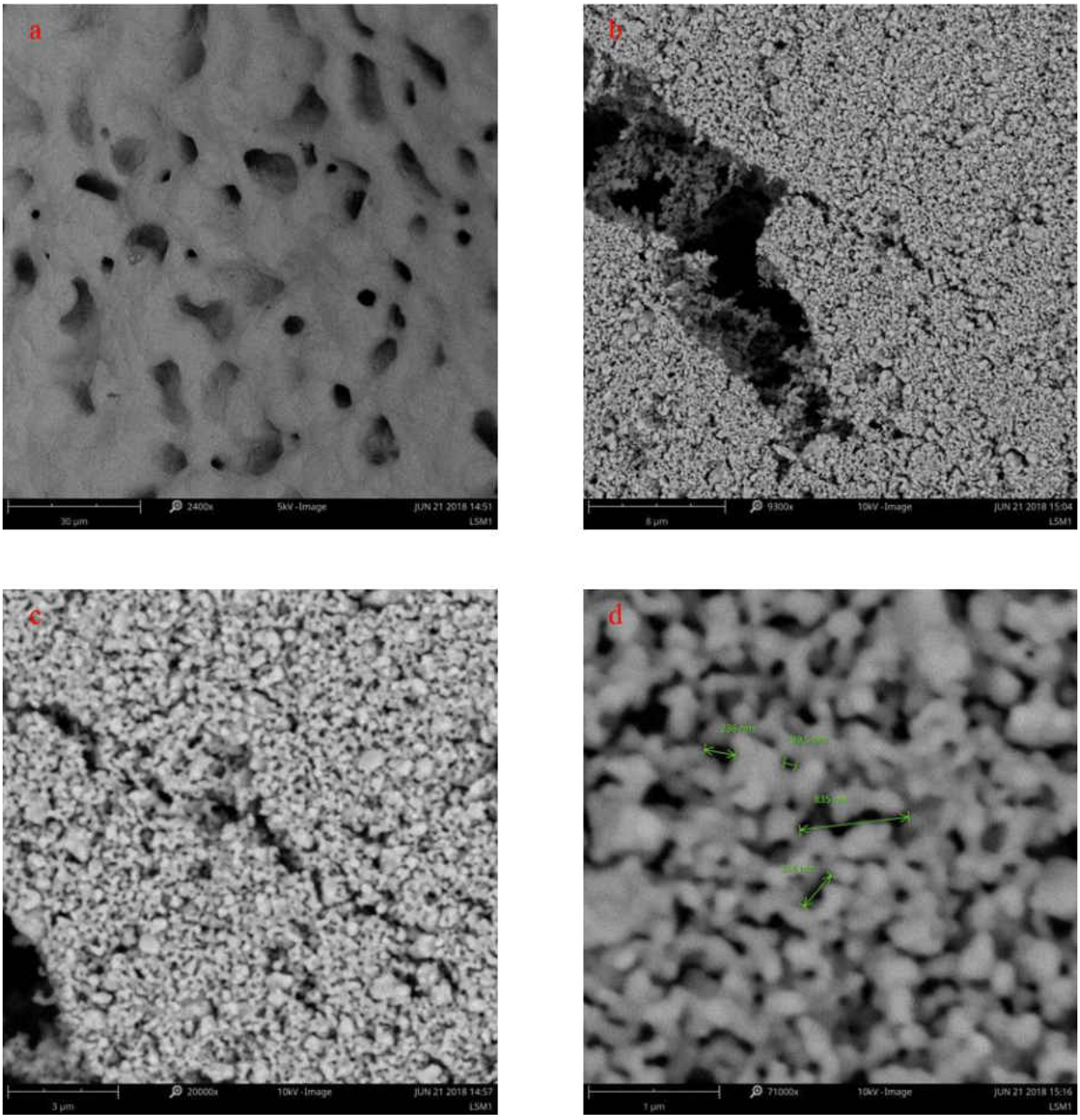

Figure 78. SEM surface characterization of Ag collector (a) and 3D printed LSM cathode with scale bar of b. 8 µm; c. 3 µm and d. 1 µm.

Figure 79 shows the surface characterization of 3D printed LSCF cathodes. Similar to the LSM based cathodes, the LSCF based cathodes had uniformly distributed pores with dimensions

from 152 nm to 887 nm. This is attributed to the same PA 12 volume ratios during mixing. The porosity of LSCF electrode was estimated to be 42.53% via Matlab image processing based on Figure 79d. Therefore, it can be concluded that a better surface structure with higher porosity can be achieved using additive manufacturing technique despite of the layer thickness.

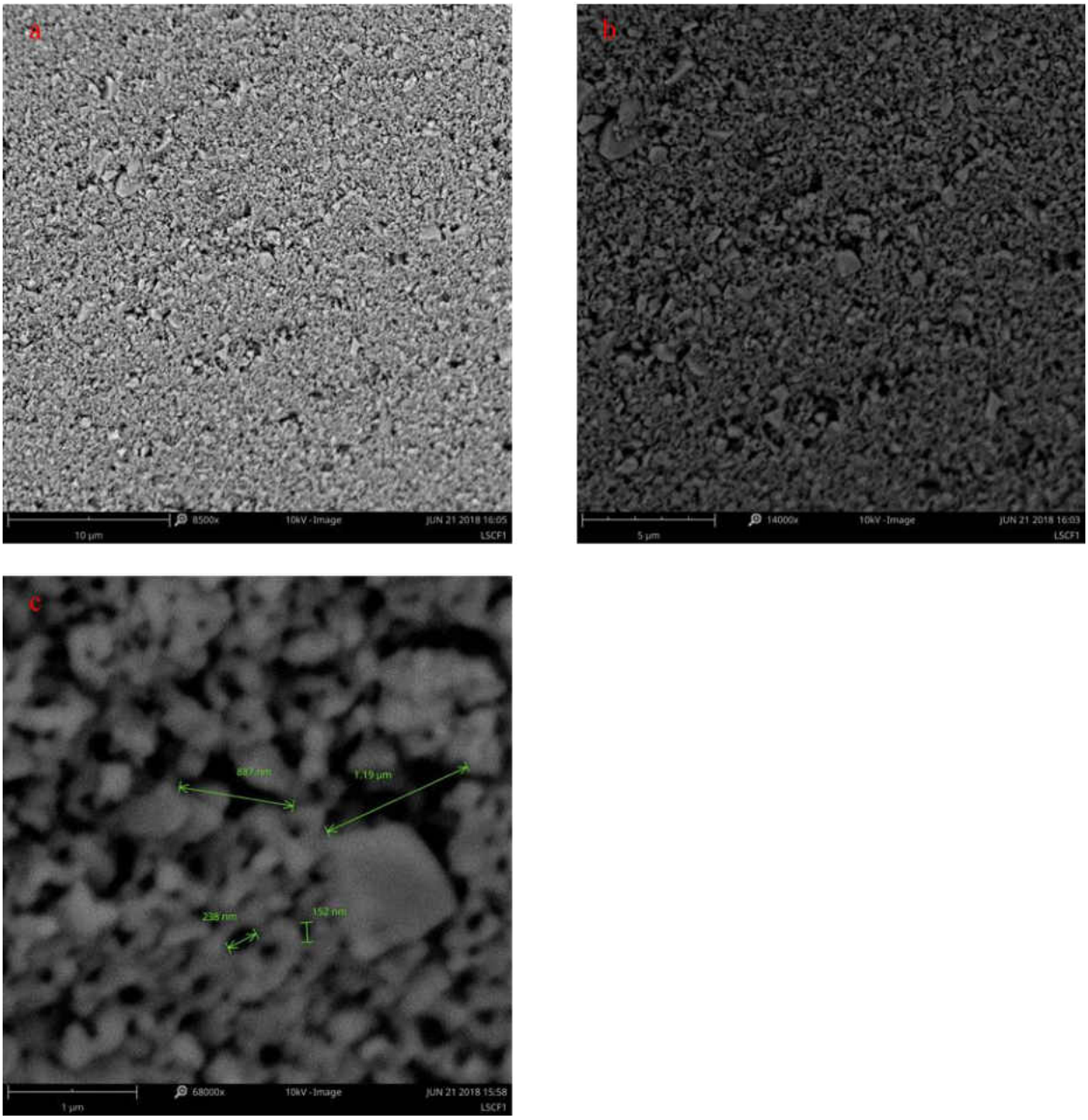

Figure 79. SEM surface characterization of 3D printed LSCF cathode with scale bar of a. 10 µm; b. 5 µm and c. 1 µm.

Finally, the 3D printed LSCF cathode was characterized by optical microscopy to identify the surface smoothness. A local area with dimensions of 2 mm × 1.5 mm was first

targeted in the microscopy as shown in Figure 80a. The 3D image was then generated through horizontal scanning as shown in Figure 80b. A height variance of 70.634 μm was obtained in this local area. Compared to the printing cathode with the thickness of 1 mm, the amplitude was neglectable. Therefore, the delamination issues could be effectively suppressed by preheating & pressing before sintering.

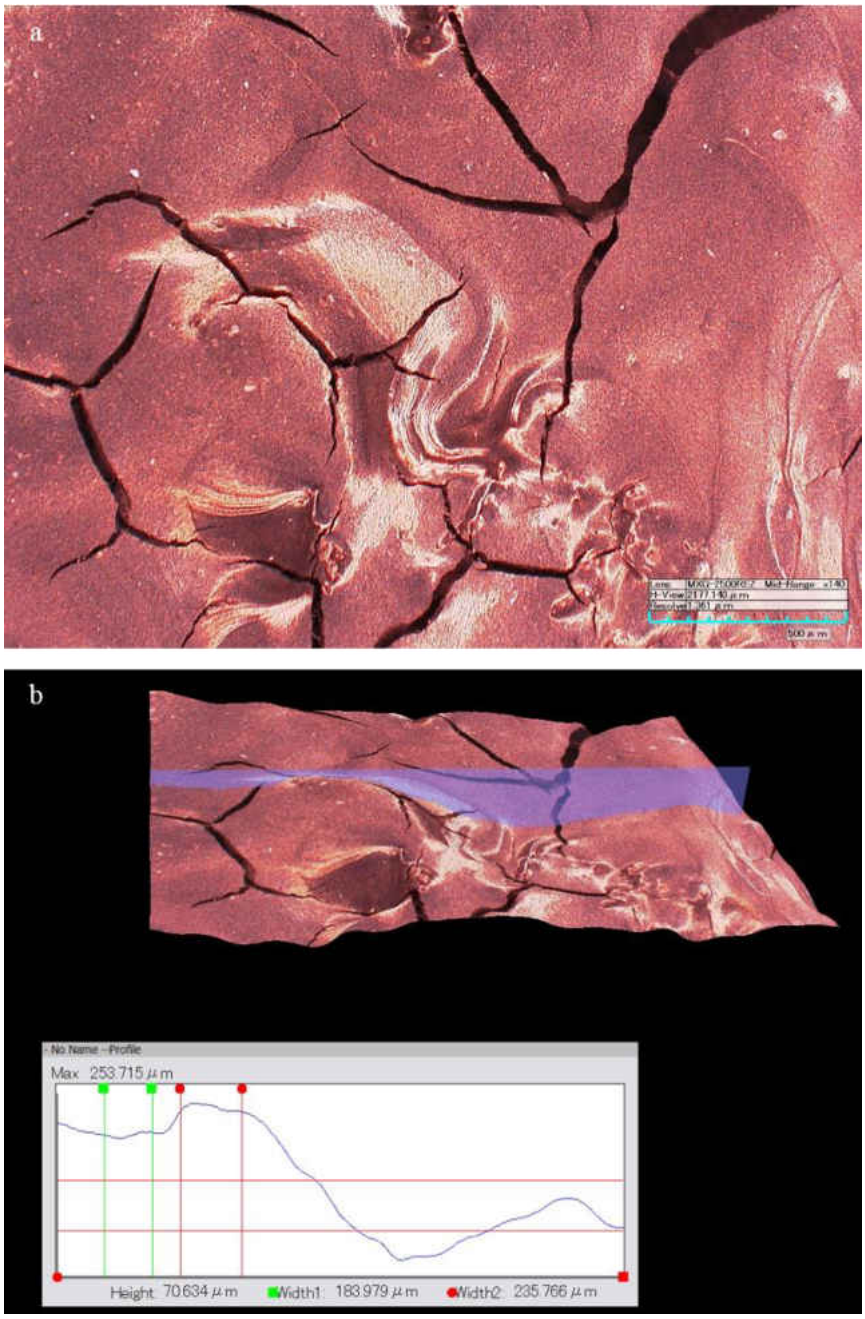

Figure 80. Surface characterization of 3D printed LSCF cathodes using optical microscopy: a. 2D surface and b. 3D surface.

3.4 Summary

In this chapter, FDM 3D printing technique was applied to fabricate the electrodes of SOFC button cells. The new composite filaments were extruded using different thermoplastic polymers and ceramics. Due to compatible particle size and excellent flexibility, PA12 was selected as the matrix of cathode composites. The 3D printed cathodes were then bonded on the half cells through preheating and pressing to avoid delamination issues. After sintering, the SOFC button cells were assembled on ceramic tubes and characterized by the test station. Besides, the button cells with dip-coating cathodes were tested as the reference. The experiments were conducted at operation temperature ranging from 700 °C and 800 °C and H_2 flow rate ranging from 50 sccm to 200 sccm. The parameters and performance of these SOFC button cells were summarized in table 5.

Table 5. Summary of the SOFC button cell characterization.

Cell #	Fabrication	Cathode materials	Active area (cm^2)	OCV* (V)	Resistance* ($\Omega \cdot cm^2$)	Output Power* (mW/cm^2)	Maximum Output Power** (mW/cm^2)
1	Dip coating	LSM	0.5	1.030	---	---	---
2	Dip coating	LSM	0.5	0.938	1.728	85.7	---
3	3D printing	LSM	0.5	1.030	---	---	---
4	3D printing	LSM	1	1.068	17.27	13.2	---
5	3D printing	LSM	0.5	1.037	3.484	61.7	---
6	3D printing	LSM	0.5	1.063	7.4	32.8	54.6
7	3D printing	LSM	1	1.033	4.32	57.2	88.7
8	3D printing	LSCF	1	1.079	7.466	35.1	56.6
9	3D printing	LSCF	1	1.093	5.838	47.6	75.4

*750 °C, 100 sccm H_2; **800 °C, 200 sccm H_2

During characterization, the cell anodes were initially reduced by hydrogen to achieve a stable OCV at 750 °C and 100 sccm H_2. Most cells showed excellent Nernst potential (> 1.03 V) except for cell #2 due to insufficiently reduced anode. Note that, the OCV of LSCF based cells were slightly higher than those of LSM based cells but the reasons still remained unknown. The cell resistance can be estimated by the linear relation of cell voltage and current density. It has a significant effect on the cell performance. The cell #2 with dip-coating cathode was set as the reference and it exhibited the highest power output of 85.7 mW/cm^2 at 750 °C and 100 sccm H_2. This was attributed to the thinnest cathode layer leading to a cell resistance of 1.728 Ω·cm^2. The best performance for LSM based cells and LSCF based cells were 61.7 mW/cm^2 and 47.6 mW/cm^2 respectively. However, these were still lower than the reference cell with traditional dip-coating cathode. Further improvement could focus on reducing the cathode thickness during the 3D printing and pressing process. Besides, increasing the temperature and H_2 flow rate could both increase the cell power output. The former method was more effective due to the significantly enhanced ion conductivity of YSZ electrolyte at high temperature. The latter was not recommended resulting from the unremarkable improvement and excessive waste of H_2. The best performance of 88.7 mW/cm^2 was achieved from the cell with 3D printed LSM cathode at 800 °C and 200 sccm H_2. Therefore, a perspective is provided here on how to apply the addictive manufacturing in the SOFC/SOPC to achieve the competent performance of the cell from traditional fabrication.

CHAPTER 4

CONCLUSIONS AND FUTURE RESEARCH

4.1 Conclusions

As one of the long-term solar-to-hydrogen pathways outlined by DOE, photocatalytic water splitting has received enormous scientific interest in recent decades. In this study, the concept of solid oxide photoelectrochemical cells was proposed in order to harvest more visible sunlight and increase the energy conversion efficiency. Compared to conventional PECs in aqueous environments, the SOPC is operated at higher temperature (> 400 °C) and its theoretical framework was elaborated with highlighted advantages. First, the thermodynamic threshold is significantly reduced from 1.6-1.7 V to 0.85-0.95 V at elevated temperature, thus allowing more choice of semiconductor candidates. Second, the narrowing bandgap at high temperature will enable more visible light absorption. The SOPC integrates a photovoltaic cell and a solid oxide electrolysis cell. The PV cell is responsible for converting solar energy to separated chargers while the SOEC utilizes the chargers to split water for hydrogen generation. The experimental investigation focused on fabrication and characterization of the PV cell and SOEC respectively.

For the PV cell of SOPC, various semiconductor candidates, i.e. n-TiO_2, n-ZnO, n-Fe_2O_3, p-LSM, p-LSC, p-LSCF, p-NiO and Ag, were selected to fabricate either Schottky diodes or p-n diodes. The rectifying properties of these diodes were evaluated from room temperature to 500 °C. The knee voltages were then extracted from the rectifying curves and compared with the Nernst potential for electrolysis in terms of operation temperature. The semiconductor diode is suitable for use in SOPC only if its knee voltages are higher than the electrolysis threshold at specific temperatures. The experimental results showed that only LSM/TiO_2 was potentially applicable in SOPC when the temperature below 450 °C.

For the SOEC/SOFC part, the FDM 3D printing was introduced as a novel manufacturing technique. Different polymeric ceramic composite filaments were fabricated in house. The PA12 based filaments showed the best flexibility and printing quality. The cathodes were printed and bonded on the half cells via preheating and pressing to avoid delamination issues. Porous cathode structure of both LSM and LSCF were achieved. Afterwards, those button cells were evaluated in the fuel cell mode at temperature of 700-800 °C and H_2 flow rate of 50-200 sccm. Compared to the conventional cathode made by dip-coating with power output of 85.7 mW/cm^2 at temperature of 750 °C and 100 sccm H_2, the 3D printed cells showed comparable performance of 61.7 mW/cm^2 and 47.6 mW/cm^2 for LSM cathode and LSCF cathode, respectively. Moreover, increasing temperature could improve significantly the cell performance due to enhanced ion conductivity of YSZ electrolyte. Therefore, it is demonstrated that FDM is viable technology for fabricating porous electrodes for SOFC/SOPCs.

4.2 Future research

We have successfully found the appropriate semiconductor diode for PV part and demonstrated the feasibility of applying FDM 3D printing to SOEC fabrication. Future research should focus on integration and characterization of the proposed SOPC. As shown in Figure 31, GDC is selected as the SOEC electrolyte due to the suggested operation temperature (450 °C) of LSM/TiO_2 diode. The electrolysis cell can be fabricated by 3D printing hydrogen cathode (Ni) and oxygen anode (LSM) on the two sides of electrolyte. The p-LSM and n-TiO_2 are then deposited in sequence on the surface of oxygen anode. Silver mesh is attached on the surface of n-TiO_2 for current collection. Note that, the p-LSM deposition can be omitted due to the same materials as oxygen anode. A thin layer around micro scale of n-TiO_2 is required to allow the

photon absorption by the junction. The characterization of SOPC is conducted step by step as the following procedures.

4.2.1 OCV characterization of SOPC with light irradiation at high temperature

The schematic of experimental setup is shown in Figure 81. The SOPC cell is sandwiched by two ceramic tubes on both sides with ceramic paste for sealing. The cell is then placed at middle of the furnace with PV part irradiated by solar simulator (Newport 500W, Oriel Instruments, USA). Both sides of PV cell are connected and extended by silver wires for OCV detection. When the temperature increases to 450 °C, an OCV that is approximately equal to the diode knee voltage is supposed to be detected with light irradiation. The switch effect of light on the cell voltage should be observed as well.

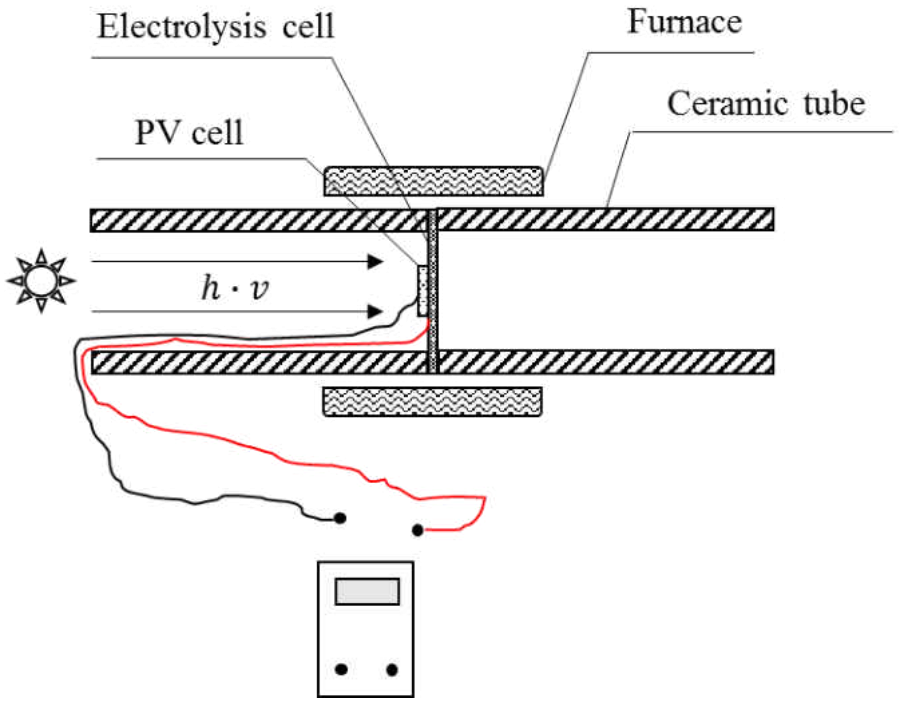

Figure 81. OCV characterization of SOPC with light irradiation at high temperature.

4.2.2 Oxygen pump test of SOPC with light irradiation at high temperature

Before the steam electrolysis test of SOPC, oxygen pump test is necessary due to the possible fact that the OCV obtained from previous test is insufficient for splitting water. During SOPC operation, the electrical potential of PV cell is able to reduce the oxygen molecules into oxygen ions at the cathode of SOEC. The oxygen ions then transfer through the electrolyte under the potential gradient and finally oxidized back into oxygen at the anode side. Basically, this test is aimed to verify the potential of SOPC for radiation energy to chemical energy conversion. Besides the same experimental setup with previous one, the gas inlet and outlet are designed at the ceramic tube of SOEC side. A silver wire is required to connect the PV part and SOEC part for transfer of photogenerated electrons. When the SOPC is operated at 450 °C with light irradiation, the low pressure O_2 is pumped through the inlet of electrolysis cell side and a much lower pressure of O_2 is expected at the outlet due to the operation of SOPC.

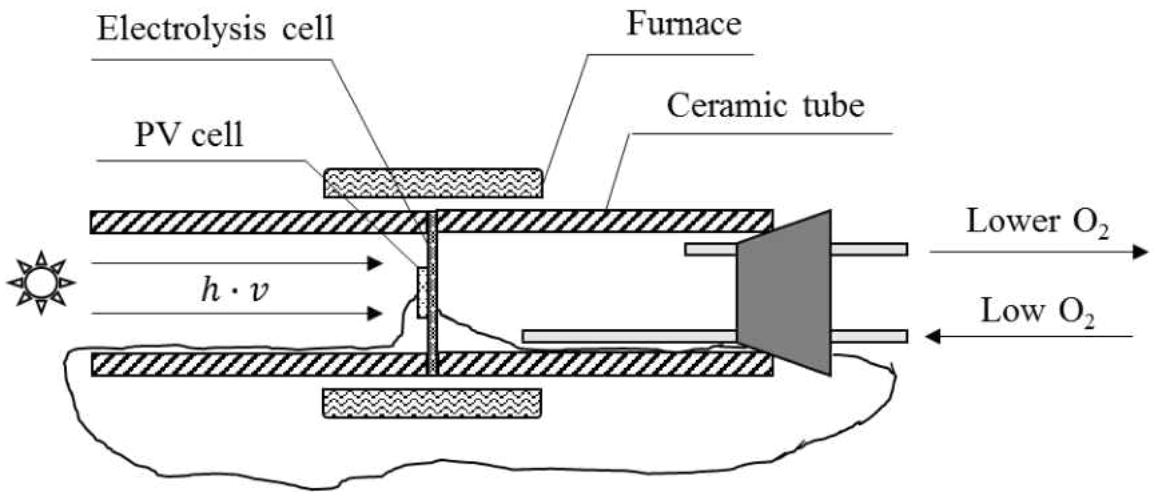

Figure 82. Oxygen pump test of SOPC with light irradiation at high temperature.

4.2.3 Steam electrolysis of SOPC with light irradiation at high temperature

Compared to the oxygen pump test, the inlet of electrolysis cell side is steam while air is used as sweep gas in the PV cell side. If the voltage of PV cell is sufficient for steam electrolysis with light irradiation, the steam can be reduced into hydrogen at the cathode side of electrolysis cell. The oxygen ions can transfer through the GDC electrolyte at 450 °C and then oxidized into oxygen at the anode side. The outlet gas at electrolysis side is collected and analyzed by gas chromatography. The mixture of steam and hydrogen should be detected and this can finally demonstrate the feasibility of our proposed SOPC.

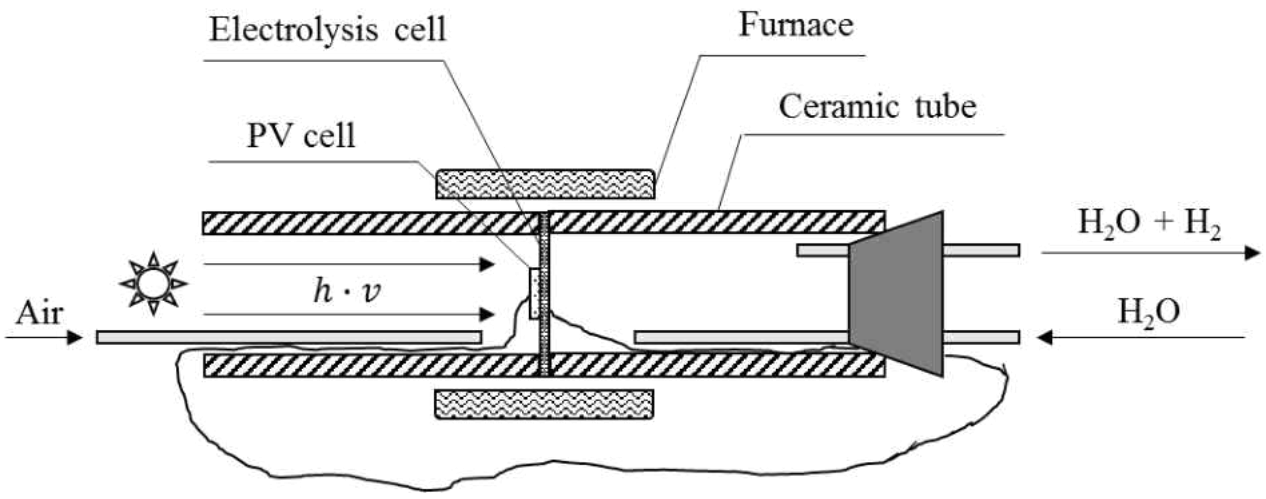

Figure 83. Steam electrolysis of SOPC with light irradiation at high temperature.

REFERENCES

[1] D. Fuel Cell Technologies Office, Hydrogen Production Pathways, https://www.energy.gov/eere/fuelcells/hydrogen-production-pathways.

[2] A. Fujishima, K. Honda, Electrochemical photolysis of water at a semiconductor electrode, Nature 238, (1972) 37-38.

[3] X. Chen, S. Shen, L. Guo, S.S. Mao, Semiconductor-based photocatalytic hydrogen generation, Chemical reviews 110(11) (2010) 6503-6570.

[4] D. Jing, L. Guo, L. Zhao, X. Zhang, H. Liu, M. Li, S. Shen, G. Liu, X. Hu, X. Zhang, Efficient solar hydrogen production by photocatalytic water splitting: from fundamental study to pilot demonstration, International Journal of Hydrogen Energy 35(13) (2010) 7087-7097.

[5] S.S. Mao, X. Chen, Selected nanotechnologies for renewable energy applications, International journal of energy research 31(6-7) (2007) 619-636.

[6] H. Kato, K. Asakura, A. Kudo, Highly efficient water splitting into H2 and O2 over lanthanum-doped NaTaO3 photocatalysts with high crystallinity and surface nanostructure, Journal of the American Chemical Society 125(10) (2003) 3082-3089.

[7] A. Kudo, H. Kato, S. Nakagawa, Water splitting into H2 and O2 on new Sr2M2O7 (M= Nb and Ta) photocatalysts with layered perovskite structures: factors affecting the photocatalytic activity, The Journal of Physical Chemistry B 104(3) (2000) 571-575.

[8] H.G. Kim, D.W. Hwang, S.W. Bae, J.H. Jung, J.S. Lee, Photocatalytic water splitting over La 2 Ti 2 O 7 synthesized by the polymerizable complex method, Catalysis letters 91(3) (2003) 193-198.

[9] S. Ikeda, M. Hara, J.N. Kondo, K. Domen, H. Takahashi, T. Okubo, M. Kakihana, Preparation of K2La2Ti3O10 by polymerized complex method and photocatalytic decomposition of water, Chemistry of Materials 10(1) (1998) 72-77.

[10] K. Maeda, N. Saito, D. Lu, Y. Inoue, K. Domen, Photocatalytic properties of RuO2-loaded β-Ge3N4 for overall water splitting, The Journal of Physical Chemistry C 111(12) (2007) 4749-4755.

[11] R. Abe, Recent Progress on Photocatalytic and Photoelectrochemical Water Splitting Under Visible Light Irradiation, Journal of Photochemistry and Photobiology C: Photochemistry Reviews 11(4) (2010) 179-209.

[12] J. Li, N. Wu, Semiconductor-based photocatalysts and photoelectrochemical cells for solar fuel generation: a review, Catalysis Science & Technology 5(3) (2015) 1360-1384.

[13] Y. Wang, Q. Wang, X. Zhan, F. Wang, M. Safdar, J. He, Visible light driven type II heterostructures and their enhanced photocatalysis properties: a review, Nanoscale 5(18) (2013) 8326-8339.

[14] J. Sun, C. Liu, P. Yang, Surfactant-free, large-scale, solution–liquid–solid growth of gallium phosphide nanowires and their use for visible-light-driven hydrogen production from water reduction, Journal of the American Chemical Society 133(48) (2011) 19306-19309.

[15] R. Abe, K. Sayama, H. Sugihara, Development of new photocatalytic water splitting into H2 and O2 using two different semiconductor photocatalysts and a shuttle redox mediator IO3-/I, The journal of physical chemistry B 109(33) (2005) 16052-16061.

[16] K. Sayama, K. Mukasa, R. Abe, Y. Abe, H. Arakawa, Stoichiometric water splitting into H2 and O2 using a mixture of two different photocatalysts and an IO3−/I− shuttle redox mediator under visible light irradiation, Chemical Communications (23) (2001) 2416-2417.

[17] K. Sayama, K. Mukasa, R. Abe, Y. Abe, H. Arakawa, A new photocatalytic water splitting system under visible light irradiation mimicking a Z-scheme mechanism in photosynthesis, Journal of Photochemistry and Photobiology A: Chemistry 148(1-3) (2002) 71-77.

[18] A.J. Bard, Photoelectrochemistry and heterogeneous photo-catalysis at semiconductors, Journal of Photochemistry 10(1) (1979) 59-75.

[19] K. Sayama, R. Yoshida, H. Kusama, K. Okabe, Y. Abe, H. Arakawa, Photocatalytic decomposition of water into H2 and O2 by a two-step photoexcitation reaction using a WO3 suspension catalyst and an Fe3+/Fe2+ redox system, Chemical Physics Letters 277(4) (1997) 387-391.

[20] G.R. Bamwenda, K. Sayama, H. Arakawa, The effect of selected reaction parameters on the photoproduction of oxygen and hydrogen from a WO3–Fe2+–Fe3+ aqueous suspension, Journal of Photochemistry and Photobiology A: Chemistry 122(3) (1999) 175-183.

[21] K. Tennakone, S. Pushpa, Water photodecomposition with two reversible and separable photosystems, Journal of the Chemical Society, Chemical Communications (20) (1985) 1435-1437.

[22] K. Tennakone, S. Wickramanayake, Water photolysis with copper (I) chloride, Journal of the Chemical Society, Faraday Transactions 2: Molecular and Chemical Physics 82(9) (1986) 1475-1479.

[23] K. Tennakone, R. Tantrigoda, S. Abeysinghe, S. Punchihewa, C. Fernando, Water photolysis via reversible oxidation and reduction between MnO2 and MnO42, Journal of Photochemistry and Photobiology A: Chemistry 52(1) (1990) 43-46.

[24] T. Ohno, S. Saito, K. Fujihara, M. Matsumura, Photocatalyzed production of hydrogen and iodine from aqueous solutions of iodide using platinum-loaded TiO2 powder, Bulletin of the Chemical Society of Japan 69(11) (1996) 3059-3064.

[25] T. Ohno, K. Nakabeya, K. Fujihara, M. Matsumura, Relay of positive holes from photoirradiated Pt-loaded TiO2 particles in an aqueous phase to t-butylhydroquinone in an oil phase, Journal of Photochemistry and Photobiology A: Chemistry 117(2) (1998) 143-147.

[26] K. Fujihara, T. Ohno, M. Matsumura, Splitting of water by electrochemical combination of two photocatalytic reactions on TiO 2 particles, Journal of the Chemical Society, Faraday Transactions 94(24) (1998) 3705-3709.

[27] T. Ohno, D. Haga, K. Fujihara, K. Kaizaki, M. Matsumura, Unique effects of iron (III) ions on photocatalytic and photoelectrochemical properties of titanium dioxide, The Journal of Physical Chemistry B 101(33) (1997) 6415-6419.

[28] T. Ohno, K. Fujihara, K. Sarukawa, F. Tanigawa, M. Matsumura, Splitting of water by combining two photocatalytic reactions through a quinone compound dissolved in an oil phase, Zeitschrift für Physikalische Chemie 213(2) (1999) 165-174.

[29] Y. Bessekhouad, M. Trari, J.-P. Doumerc, CuMnO2, a novel hydrogen photoevolution catalyst, International journal of hydrogen energy 28(1) (2003) 43-48.

[30] S. Saadi, A. Bouguelia, M. Trari, Photocatalytic hydrogen evolution over CuCrO2, Solar Energy 80(3) (2006) 272-280.

[31] R. Brahimi, Y. Bessekhouad, A. Bouguelia, M. Trari, CuAlO2/TiO2 heterojunction applied to visible light H2 production, Journal of Photochemistry and Photobiology A: Chemistry 186(2-3) (2007) 242-247.

[32] A. Derbal, S. Omeiri, A. Bouguelia, M. Trari, Characterization of new heterosystem CuFeO2/SnO2 application to visible-light induced hydrogen evolution, international journal of hydrogen energy 33(16) (2008) 4274-4282.

[33] S. Boumaza, A. Boudjemaa, A. Bouguelia, R. Bouarab, M. Trari, Visible light induced hydrogen evolution on new hetero-system ZnFe2O4/SrTiO3, Applied Energy 87(7) (2010) 2230-2236.

[34] J.S. Jang, D.W. Hwang, J.S. Lee, CdS–AgGaS2 photocatalytic diodes for hydrogen production from aqueous Na2S/Na2SO3 electrolyte solution under visible light ($\lambda \geq$ 420 nm), Catalysis today 120(2) (2007) 174-181.

[35] J.S. Jang, S.J. Hong, J.Y. Kim, J.S. Lee, Heterojunction photocatalyst TiO2/AgGaS2 for hydrogen production from water under visible light, Chemical Physics Letters 475(1-3) (2009) 78-81.

[36] A. Nozik, p-n photoelectrolysis cells, Applied Physics Letters 29(3) (1976) 150-153.

[37] C.-C. Hu, J.-N. Nian, H. Teng, Electrodeposited p-type Cu2O as photocatalyst for H2 evolution from water reduction in the presence of WO3, Solar Energy Materials and Solar Cells 92(9) (2008) 1071-1076.

[38] H.G. Kim, P.H. Borse, J.S. Jang, E.D. Jeong, O.-S. Jung, Y.J. Suh, J.S. Lee, Fabrication of CaFe 2 O 4/MgFe 2 O 4 bulk heterojunction for enhanced visible light photocatalysis, Chemical Communications (39) (2009) 5889-5891.

[39] H.G. Kim, P.H. Borse, W. Choi, J.S. Lee, Photocatalytic nanodiodes for visible-light photocatalysis, Angewandte Chemie 117(29) (2005) 4661-4665.

[40] C. Santato, M. Ulmann, J. Augustynski, Photoelectrochemical properties of nanostructured tungsten trioxide films, The Journal of Physical Chemistry B 105(5) (2001) 936-940.

[41] S.U. Khan, J. Akikusa, Photoelectrochemical splitting of water at nanocrystalline n-Fe2O3 thin-film electrodes, The Journal of Physical Chemistry B 103(34) (1999) 7184-7189.

[42] H. Park, W. Choi, M.R. Hoffmann, Effects of the preparation method of the ternary CdS/TiO 2/Pt hybrid photocatalysts on visible light-induced hydrogen production, Journal of Materials Chemistry 18(20) (2008) 2379-2385.

[43] L.A. Silva, S.Y. Ryu, J. Choi, W. Choi, M.R. Hoffmann, Photocatalytic hydrogen production with visible light over Pt-interlinked hybrid composites of cubic-phase and hexagonal-phase CdS, The Journal of Physical Chemistry C 112(32) (2008) 12069-12073.

[44] H. Tada, T. Mitsui, T. Kiyonaga, T. Akita, K. Tanaka, All-solid-state Z-scheme in CdS–Au–TiO 2 three-component nanojunction system, Nature materials 5(10) (2006) 782.

[45] D. Wang, Z. Zou, J. Ye, A novel Zn-doped Lu2O3/Ga2O3 composite photocatalyst for stoichiometric water splitting under UV light irradiation, Chemical physics letters 384(1-3) (2004) 139-143.

[46] Y. Liu, L. Guo, W. Yan, H. Liu, A composite visible-light photocatalyst for hydrogen production, Journal of Power Sources 159(2) (2006) 1300-1304.

[47] D. Wang, Z. Zou, J. Ye, Photocatalytic water splitting with the Cr-doped Ba2In2O5/In2O3 composite oxide semiconductors, Chemistry of materials 17(12) (2005) 3255-3261.

[48] Y. Ou, J. Lin, S. Fang, D. Liao, MWNT–TiO2: Ni composite catalyst: a new class of catalyst for photocatalytic H2 evolution from water under visible light illumination, Chemical Physics Letters 429(1-3) (2006) 199-203.

[49] X.L. Zheng, J.P. Song, T. Ling, Z.P. Hu, P.F. Yin, K. Davey, X.W. Du, S.Z. Qiao, Strongly Coupled Nafion Molecules and Ordered Porous CdS Networks for Enhanced Visible-Light Photoelectrochemical Hydrogen Evolution, Advanced Materials 28(24) (2016) 4935-4942.

[50] L.W. Qiu Y, Chen W, et al. , Efficient solar-driven water splitting by nanocone BiVO4-perovskite tandem cells, Science Advances 2(6) (2016).

[51] X. Ye, J. Melas-Kyriazi, Z.A. Feng, N.A. Melosh, W.C. Chueh, A semiconductor/mixed ion and electron conductor heterojunction for elevated-temperature water splitting, Physical Chemistry Chemical Physics 15(37) (2013) 15459-15469.

[52] W.C. Chueh, N.A. Melosh, X. Ye, Heterojunction elevated-temperature photoelectrochemical cell, US Patent 20150053568 A1, Feb. 26, 2015.

[53] J. Fleig, G. Walch, G.C. Brunauer, B. Rotter, E. Esmaeli, J. Summhammer, A.K. Opitz, K. Ponweiser, Mixed Conductors under Light: On the Way to Solid Oxide Photo-Electrochemical Cells, ECS Transactions 72(7) (2016) 23-33.

[54] G. Walch, B. Rotter, G.C. Brunauer, E. Esmaeili, A.K. Opitz, M. Kubicek, J. Summhammer, K. Ponweiser, J. Fleig, A solid oxide photoelectrochemical cell with UV light-driven oxygen storage in mixed conducting electrodes, Journal of Materials Chemistry A 5, (2017) 1637-1649.

[55] G.C. Brunauer, B. Rotter, G. Walch, E. Esmaeili, A.K. Opitz, K. Ponweiser, J. Summhammer, J. Fleig, UV-Light-Driven Oxygen Pumping in a High-Temperature Solid Oxide Photoelectrochemical Cell, Advanced Functional Materials 26(1) (2016) 120-128.

[56] K. Xu, A. Chatzitakis, T. Norby, Solid-state photoelectrochemical cell with TiO 2 nanotubes for water splitting, Photochemical & Photobiological Sciences 16(1) (2017) 10-16.

[57] J.E. O'Brien, X. Zhang, Idaho National Laboratory ANNUAL REPORT FY 2013: Direct Solar Hydrogen Production Using High Temperature Solid Oxide Photoelectrochemical Cells, Idaho National Laboratory ANNUAL REPORT FY 2013, 2013, p. 142.

[58] J. Nowotny, M. Radecka, M. Rekas, Semiconducting properties of undoped TiO_2, Journal of Physics and Chemistry of Solids 58(6) (1997) 927-937.

[59] H. Tang, F. Lévy, H. Berger, P.E. Schmid, Urbach tail of anatase TiO_2, Physical Review B 52(11) (1995) 7771-7774.

[60] H. Tang, H. Berger, P.E. Schmid, F. Lévy, Optical properties of anatase (TiO_2), Solid State Communications 92(3) (1994) 267-271.

[61] L. Forss, M. Schubnell, Temperature dependence of the luminescence of TiO_2 powder, Appl. Phys. B 56(6) (1993) 363-366.

[62] T. Kuratomi, K. Yamaguchi, M. Yamawaki, T. Bak, J. Nowotny, M. Rekas, C.C. Sorrell, Semiconducting properties of polycrystalline titanium dioxide, Solid State Ionics 154–155(0) (2002) 223-228.

[63] T.K. Burg, Semiconducting properties of polycrystalline titanium dioxide, The University of New South Wales, 2008.

[64] A. Von Hippel, J. Kalnajs, W.B. Westphal, Protons, dipoles, and charge carriers in rutile in rutile, Journal of Physics and Chemistry of Solids 23(6) (1962) 779-799.

[65] N.R.E. Laboratory, Renewable Hydrogen Production and Electricity/Hydrogen Cogeneration, https://www.nrel.gov/hydrogen/renewable-electrolysis.html.

[66] W. Doenitz, R. Schmidberger, E. Steinheil, R. Streicher, Hydrogen production by high temperature electrolysis of water vapour, International Journal of Hydrogen Energy 5(1) (1980) 55-63.

[67] W. Dönitz, E. Erdle, High-temperature electrolysis of water vapor—status of development and perspectives for application, International Journal of Hydrogen Energy 10(5) (1985) 291-295.

[68] W. Dönitz, G. Dietrich, E. Erdle, R. Streicher, Electrochemical high temperature technology for hydrogen production or direct electricity generation, International journal of hydrogen energy 13(5) (1988) 283-287.

[69] C.M. Stoots, J.E. O'Brien, K.G. Condie, J.J. Hartvigsen, High-temperature electrolysis for large-scale hydrogen production from nuclear energy – Experimental investigations, International Journal of Hydrogen Energy 35(10) (2010) 4861-4870.

[70] A. Brisse, J. Schefold, High Temperature Electrolysis at EIFER, Main Achievements at Cell and Stack Level, Energy Procedia 29(0) (2012) 53-63.

[71] A. Hauch, K. Brodersen, M. Chen, C. Graves, S.H. Jensen, P.S. Jørgensen, P.V. Hendriksen, M.B. Mogensen, S. Ovtar, X. Sun, A Decade of Solid Oxide Electrolysis Improvements at DTU Energy, ECS Transactions 75(42) (2017) 3-14.

[72] A. Odukoya, G. Naterer, M. Roeb, C. Mansilla, J. Mougin, B. Yu, J. Kupecki, I. Iordache, J. Milewski, Progress of the IAHE Nuclear Hydrogen Division on international hydrogen production programs, International Journal of Hydrogen Energy 41(19) (2016) 7878-7891.

[73] T.-L. Liu, C. Wang, S.-J. Hao, Z.-Q. Fu, B.A. Peppley, Z.-M. Mao, J.-L. Wang, Z.-Q. Mao, Evaluation of polarization and hydrogen production efficiency of solid oxide electrolysis stack with La 0.6 Sr 0.4 Co 0.2 Fe 0.8 O 3− δ-Ce 0.9 Gd 0.1 O 1.95 oxygen electrode, International Journal of Hydrogen Energy (2016).

[74] Y. Zheng, T. Chen, Q. Li, W. Wu, H. Miao, C. Xu, W. Wang, Achieving 360 NL h− 1 Hydrogen Production Rate Through 30-Cell Solid Oxide Electrolysis Stack with LSCF–GDC Composite Oxygen Electrode, Fuel Cells 14(6) (2014) 1066-1070.

[75] K.R. Sridhar, C.S. Iacomini, J.E. Finn, Combined H2O/CO2 Solid Oxide Electrolysis for Mars In Situ Resource Utilization, Journal of Propulsion and Power 20(5) (2004) 892-901.

[76] I. Christine, Demonstration of a Stand-alone Solid Oxide Electrolysis Stack with Embedded Sabatier Reactors for 100% Oxygen Regeneration, 41st International Conference on Environmental Systems, American Institute of Aeronautics and Astronautics2011.

[77] T.L. Cable, J.A. Setlock, S.C. Farmer, A.J. Eckel, Regenerative Performance of the NASA Symmetrical Solid Oxide Fuel Cell Design, International Journal of Applied Ceramic Technology 8(1) (2011) 1-12.

[78] G. Cinti, G. Discepoli, G. Bidini, A. Lanzini, M. Santarelli, Co-electrolysis of water and CO2 in a solid oxide electrolyzer (SOE) stack, International Journal of Energy Research (2015).

[79] S. Diethelm, J.V. herle, D. Montinaro, O. Bucheli, Electrolysis and Co-Electrolysis Performance of SOE Short Stacks, Fuel Cells 13(4) (2013) 631-637.

[80] J. Hong, H.-J. Kim, S.-Y. Park, J.-H. Lee, S.-B. Park, J.-H. Lee, B.-K. Kim, H.-J. Je, J.Y. Kim, K.J. Yoon, Electrochemical performance and long-term durability of a 200 W-class solid oxide regenerative fuel cell stack, International Journal of Hydrogen Energy (2014).

[81] S. Fujiwara, S. Kasai, H. Yamauchi, K. Yamada, S. Makino, K. Matsunaga, M. Yoshino, T. Kameda, T. Ogawa, S. Momma, Hydrogen production by high temperature electrolysis with nuclear reactor, Progress in Nuclear Energy 50(2) (2008) 422-426.

[82] Z. Jiang, T. Xiao, V.á. Kuznetsov, P.á. Edwards, Turning carbon dioxide into fuel, Philosophical Transactions of the Royal Society of London A: Mathematical, Physical and Engineering Sciences 368(1923) (2010) 3343-3364.

[83] C. Stoots, J. O'Brien, J. Hartvigsen, Results of recent high temperature coelectrolysis studies at the Idaho National Laboratory, International Journal of Hydrogen Energy 34(9) (2009) 4208-4215.

[84] S.Y. Gómez, D. Hotza, Current developments in reversible solid oxide fuel cells, Renewable and Sustainable Energy Reviews 61 (2016) 155-174.

[85] W. Dönitz, R. Streicher, Hochtemperatur-Elektrolyse von Wasserdampf–Entwicklungsstand einer neuen Technologie zur Wasserstoff-Erzeugung, Chemie Ingenieur Technik 52(5) (1980) 436-438.

[86] X. Zhang, J.E. O'Brien, G. Tao, C. Zhou, G.K. Housley, Experimental design, operation, and results of a 4 kW high temperature steam electrolysis experiment, Journal of Power Sources 297 (2015) 90-97.

[87] M.A. Laguna-Bercero, Recent advances in high temperature electrolysis using solid oxide fuel cells: A review, Journal of Power Sources 203, (2012) 4-16.

[88] G. Hoogers, Fuel cell technology handbook, CRC press2002.

[89] A. Hauch, S.D. Ebbesen, S.H. Jensen, M. Mogensen, Highly efficient high temperature electrolysis, Journal of Materials Chemistry 18(20) (2008) 2331-2340.

[90] A. Brisse, J. Schefold, M. Zahid, High temperature water electrolysis in solid oxide cells, International Journal of Hydrogen Energy 33(20) (2008) 5375-5382.

[91] W. Doenitz, R. Schmidberger, Concepts and design for scaling up high temperature water vapour electrolysis, International Journal of Hydrogen Energy 7(4) (1982) 321-330.

[92] M. Irshad, K. Siraj, R. Raza, A. Ali, P. Tiwari, B. Zhu, A. Rafique, A. Ali, M. Kaleem Ullah, A. Usman, A Brief Description of High Temperature Solid Oxide Fuel Cell's Operation, Materials, Design, Fabrication Technologies and Performance, Applied Sciences 6(3) (2016) 75.

[93] X. Zhang, J.E. O'Brien, R.C. O'Brien, J.J. Hartvigsen, G. Tao, G.K. Housley, Improved durability of SOEC stacks for high temperature electrolysis, International Journal of Hydrogen Energy 38(1) (2013) 20-28.

[94] J. Schefold, A. Brisse, M. Zahid, J.P. Ouweltjes, J.U. Nielsen, Long term testing of short stacks with solid oxide cells for water electrolysis, ECS Transactions 35(1) (2011) 2915-2927.

[95] M.S. Sohal, J.E. O'Brien, C.M. Stoots, V.I. Sharma, B. Yildiz, A. Virkar, Degradation Issues in Solid Oxide Cells During High Temperature Electrolysis, Journal of Fuel Cell Science and Technology 9(1) (2012) 011017.

[96] O.B. JE, Large scale hydrogen production from nuclear energy using high temperature electrolysis, (2010).

[97] C.M. Stoots, J.E. O'Brien, J.S. Herring, J.J. Hartvigsen, Syngas Production via High-Temperature Coelectrolysis of Steam and Carbon Dioxide, Journal of Fuel Cell Science and Technology 6(1) (2009) 011014.

[98] J. Herring, J. Obrien, C. Stoots, G. Hawkes, J. Hartvigsen, M. Shahnam, Progress in high-temperature electrolysis for hydrogen production using planar SOFC technology, International Journal of Hydrogen Energy 32(4) (2007) 440-450.

[99] J.E. O'Brien, C.M. Stoots, J.S. Herring, J. Hartvigsen, Hydrogen Production Performance of a 10-Cell Planar Solid-Oxide Electrolysis Stack, Journal of Fuel Cell Science and Technology 3(2) (2006) 213.

[100] J. Schefold, A. Brisse, M. Zahid, Long term testing of solid oxide fuel cell stacks with yttria stabilized zirconia electrolyte in the H2O electrolysis mode, ECS Transactions 28(11) (2010) 357-367.

[101] J. Mougin, A. Mansuy, A. Chatroux, G. Gousseau, M. Petitjean, M. Reytier, F. Mauvy, Enhanced Performance and Durability of a High Temperature Steam Electrolysis Stack, Fuel Cells 13(4) (2013) 623-630.

[102] M. Reytier, J. Cren, M. Petitjean, A. Chatroux, G. Gousseau, S. Di Iorio, A. Brevet, I. Noirot-Le Borgne, J. Mougin, Development of a cost-efficient and performing high temperature steam electrolysis stack, ECS Transactions 57(1) (2013) 3151-3160.

[103] M. Reytier, S. Di Iorio, A. Chatroux, M. Petitjean, J. Cren, M. de Saint Jean, J. Aicart, J. Mougin, Stack performances in high temperature steam electrolysis and co-electrolysis, International Journal of Hydrogen Energy 40(35) (2015) 11370-11377.

[104] S.-D. Kim, J.-H. Yu, D.-W. Seo, I.-S. Han, S.-K. Woo, Hydrogen production performance of 3-cell flat-tubular solid oxide electrolysis stack, International Journal of Hydrogen Energy 37(1) (2012) 78-83.

[105] F. Alenazey, Y. Alyousef, O. Almisned, G. Almutairi, M. Ghouse, D. Montinaro, F. Ghigliazza, Production of synthesis gas (H 2 and CO) by high-temperature Co-electrolysis of H 2 O and CO 2, International Journal of Hydrogen Energy 40(32) (2015) 10274-10280.

[106] Y. Zheng, Q. Li, W. Guan, C. Xu, W. Wu, W.G. Wang, Investigation of 30-cell solid oxide electrolyzer stack modules for hydrogen production, Ceramics International 40(4) (2014) 5801-5809.

[107] L. Jin, W.B. Guan, X. Ma, C. Xu, W.G. Wang, Achieving Hydrogen Production through Solid Oxide Electrolyzer Stack by High Temperature Electrolysis, (2012) 103-111.

[108] D. Penchini, G. Cinti, G. Discepoli, U. Desideri, Theoretical study and performance evaluation of hydrogen production by 200 W solid oxide electrolyzer stack, International Journal of Hydrogen Energy 39(17) (2014) 9457-9466.

[109] Q. Fu, J. Schefold, A. Brisse, J.U. Nielsen, Durability Testing of a High-Temperature Steam Electrolyzer Stack at 700 °C, Fuel Cells 14(3) (2014) 395-402.

[110] M. Chen, J.V.T. Høgh, J.U. Nielsen, J.J. Bentzen, S.D. Ebbesen, P.V. Hendriksen, High Temperature Co-Electrolysis of Steam and CO2in an SOC Stack: Performance and Durability, Fuel Cells 13(4) (2013) 638-645.

[111] S.D. Ebbesen, J. Høgh, K.A. Nielsen, J.U. Nielsen, M. Mogensen, Durable SOC stacks for production of hydrogen and synthesis gas by high temperature electrolysis, International Journal of Hydrogen Energy 36(13) (2011) 7363-7373.

[112] M. Petitjean, M. Reytier, A. Chatroux, L. Bruguière, A. Mansuy, H. Sassoulas, S. Di Iorio, B. Morel, J. Mougin, Performance and durability of high temperature steam electrolysis: from the single cell to short-stack scale, ECS Transactions 35(1) (2011) 2905-2913.

[113] J. Mougin, A. Chatroux, K. Couturier, M. Petitjean, M. Reytier, G. Gousseau, F. Lefebvre-Joud, High Temperature Steam Electrolysis Stack with Enhanced Performance and Durability, Energy Procedia 29 (2012) 445-454.

[114] H. Spacil, C. Tedmon, Electrochemical dissociation of water vapor in solid oxide electrolyte cells II. Materials, fabrication, and properties, Journal of The Electrochemical Society 116(12) (1969) 1627-1633.

[115] H. Arashi, H. Naito, H. Miura, Hydrogen production from high-temperature steam electrolysis using solar energy, International journal of hydrogen energy 16(9) (1991) 603-608.

[116] R. Hino, K. Haga, H. Aita, K. Sekita, R&D on hydrogen production by high-temperature electrolysis of steam, Nuclear Engineering and Design 233(1-3) (2004) 363-375.

[117] R.D. Green, P.H. Matter, C. Holt, M. Beachy, J. Gaydos, S.C. Farmer, J. Setlock, Development Status for a Combined Solid Oxide Co-Electrolyzer and Carbon Formation Reactor System for Oxygen Regeneration, AIAA SPACE 20162016, p. 5454.

[118] Z.R. Hesabi, M. Mazaheri, T. Ebadzadeh, Enhanced electrical conductivity of ultrafine-grained 8Y2O3 stabilized ZrO2 produced by two-step sintering technique, Journal of Alloys and Compounds 494(1-2) (2010) 362-365.

[119] F. Bidrawn, G. Kim, G. Corre, J. Irvine, J.M. Vohs, R.J. Gorte, Efficient reduction of CO2 in a solid oxide electrolyzer, Electrochemical and Solid-State Letters 11(9) (2008) B167-B170.

[120] W. Wang, Y. Huang, S. Jung, J.M. Vohs, R.J. Gorte, A comparison of LSM, LSF, and LSCo for solid oxide electrolyzer anodes, Journal of The Electrochemical Society 153(11) (2006) A2066-A2070.

[121] W. Wang, R.J. Gorte, J.M. Vohs, Analysis of the performance of the electrodes in a natural gas assisted steam electrolysis cell, Chemical Engineering Science 63(3) (2008) 765-769.

[122] V. Kharton, E. Tsipis, E. Naumovich, A. Thursfield, M. Patrakeev, V. Kolotygin, J. Waerenborgh, I. Metcalfe, Mixed conductivity, oxygen permeability and redox behavior of K2NiF4-type La2Ni0. 9Fe0. 1O4+ δ, Journal of Solid State Chemistry 181(6) (2008) 1425-1433.

[123] G. Schiller, A. Ansar, M. Lang, O. Patz, High temperature water electrolysis using metal supported solid oxide electrolyser cells (SOEC), Journal of Applied Electrochemistry 39(2) (2009) 293-301.

[124] F. Tietz, H.-P. Buchkremer, D. Stöver, Components manufacturing for solid oxide fuel cells, Solid State Ionics 152 (2002) 373-381.

[125] K. Eguchi, T. Hatagishi, H. Arai, Power generation and steam electrolysis characteristics of an electrochemical cell with a zirconia-or ceria-based electrolyte, Solid State Ionics 86 (1996) 1245-1249.

[126] F. He, D. Song, R. Peng, G. Meng, S. Yang, Electrode performance and analysis of reversible solid oxide fuel cells with proton conducting electrolyte of BaCe0. 5Zr0. 3Y0. 2O3− δ, Journal of Power Sources 195(11) (2010) 3359-3364.

[127] B. Zhu, I. Albinsson, C. Andersson, K. Borsand, M. Nilsson, B.-E. Mellander, Electrolysis studies based on ceria-based composites, Electrochemistry communications 8(3) (2006) 495-498.

[128] B. Molero-Sánchez, J. Prado-Gonjal, D. Ávila-Brande, M. Chen, E. Morán, V. Birss, High performance La0. 3Ca0. 7Cr0. 3Fe0. 7O3− δ air electrode for reversible solid oxide fuel cell applications, International Journal of Hydrogen Energy 40(4) (2015) 1902-1910.

[129] S. Lee, J.-M. Kim, H.S. Hong, S.-K. Woo, Fabrication and characterization of Cu/YSZ cermet high temperature electrolysis cathode material prepared by high-energy ball-milling method: II. 700° C-sintered, Journal of Alloys and Compounds 467(1-2) (2009) 614-621.

[130] A. Kaiser, E. Monreal, D. Stolten, Preparation techniques and materials for long term stable SOFC-Single cell membranes, Ionics 3(1-2) (1997) 143-148.

[131] P. Kim-Lohsoontorn, N. Laosiripojana, J. Bae, Performance of solid oxide electrolysis cell having bi-layered electrolyte during steam electrolysis and carbon dioxide electrolysis, Current Applied Physics 11(1) (2011) S223-S228.

[132] M. Liang, B. Yu, M. Wen, J. Chen, J. Xu, Y. Zhai, Preparation of LSM–YSZ composite powder for anode of solid oxide electrolysis cell and its activation mechanism, Journal of Power Sources 190(2) (2009) 341-345.

[133] Q. Ma, F. Tietz, Comparison of Y and La-substituted SrTiO3 as the anode materials for SOFCs, Solid State Ionics 225 (2012) 108-112.

[134] A. Atkinson, S. Barnett, R.J. Gorte, J. Irvine, A.J. McEvoy, M. Mogensen, S.C. Singhal, J. Vohs, Advanced anodes for high-temperature fuel cells, Nature materials 3(1) (2004) 17.

[135] S.K. Pratihar, A.D. Sharma, H.S. Maiti, Electrical behavior of nickel coated YSZ cermet prepared by electroless coating technique, Materials chemistry and physics 96(2-3) (2006) 388-395.

[136] M. Ni, M.K. Leung, D.Y. Leung, Mathematical modeling of the coupled transport and electrochemical reactions in solid oxide steam electrolyzer for hydrogen production, Electrochimica Acta 52(24) (2007) 6707-6718.

[137] H.S. Hong, U.-S. Chae, S.-T. Choo, The effect of ball milling parameters and Ni concentration on a YSZ-coated Ni composite for a high temperature electrolysis cathode, Journal of Alloys and Compounds 449(1-2) (2008) 331-334.

[138] Y. Li, Y. Gan, Y. Wang, K. Xie, Y. Wu, Composite cathode based on Ni-loaded La0. 75Sr0. 25Cr0. 5Mn0. 5O3− δ for direct steam electrolysis in an oxide-ion-conducting solid oxide electrolyzer, International Journal of Hydrogen Energy 38(25) (2013) 10196-10207.

[139] J. Zhang, K. Xie, Y. Gan, G. Wu, B. Ding, Y. Zhang, Y. Wu, Composite titanate cathode enhanced with in situ grown nickel nanocatalyst for direct steam electrolysis, New Journal of Chemistry 38(8) (2014) 3434-3442.

[140] L. Mingyi, Y. Bo, X. Jingming, C. Jing, Influence of pore formers on physical properties and microstructures of supporting cathodes of solid oxide electrolysis cells, international journal of hydrogen energy 35(7) (2010) 2670-2674.

[141] A. Mielewczyk-Gryń, K. Gdula, S. Molin, P. Jasinski, B. Kusz, M. Gazda, Structure and electrical properties of ceramic proton conductors obtained with molten-salt and solid-state synthesis methods, Journal of Non-Crystalline Solids 356(37-40) (2010) 1976-1979.

[142] P. Kim-Lohsoontorn, D. Brett, N. Laosiripojana, Y. Kim, J. Bae, Performance of solid oxide electrolysis cells based on composite La0. 8Sr0. 2MnO3− δ–yttria stabilized zirconia and Ba0. 5Sr0. 5Co0. 8Fe0. 2O3− δ oxygen electrodes, International Journal of hydrogen energy 35(9) (2010) 3958-3966.

[143] Q. Liu, C. Yang, X. Dong, F. Chen, Perovskite Sr2Fe1. 5Mo0. 5O6− δ as electrode materials for symmetrical solid oxide electrolysis cells, international journal of hydrogen energy 35(19) (2010) 10039-10044.

[144] P. Addo, B. Molero-Sanchez, M. Chen, S. Paulson, V. Birss, CO/CO2 Study of High Performance La0. 3Sr0. 7Fe0. 7Cr0. 3O3–δ Reversible SOFC Electrodes, Fuel cells 15(5) (2015) 689-696.

[145] S.H. Jensen, P.H. Larsen, M. Mogensen, Hydrogen and synthetic fuel production from renewable energy sources, International Journal of Hydrogen Energy 32(15) (2007) 3253-3257.

[146] R.M. Clemmer, S.F. Corbin, Influence of porous composite microstructure on the processing and properties of solid oxide fuel cell anodes, Solid State Ionics 166(3-4) (2004) 251-259.

[147] Y. Bo, Z. Wenqiang, X. Jingming, C. Jing, Microstructural characterization and electrochemical properties of Ba0. 5Sr0. 5Co0. 8Fe0. 2O3− δ and its application for anode of SOEC, International journal of hydrogen energy 33(23) (2008) 6873-6877.

[148] Z. Wang, M. Mori, T. Araki, Steam electrolysis performance of intermediate-temperature solid oxide electrolysis cell and efficiency of hydrogen production system at 300 Nm3 h− 1, international journal of hydrogen energy 35(10) (2010) 4451-4458.

[149] F. Chauveau, J. Mougin, J.-M. Bassat, F. Mauvy, J.-C. Grenier, A new anode material for solid oxide electrolyser: The neodymium nickelate Nd2NiO4+ δ, Journal of Power Sources 195(3) (2010) 744-749.

[150] M. Prestat, A. Morandi, A. Heel, L. Holzer, P. Holtappels, T. Graule, Effect of graphite pore former on oxygen electrodes prepared with La0. 6Sr0. 4CoO3− δ nanoparticles, Electrochemistry Communications 12(2) (2010) 292-295.

[151] VPS, Solid oxide based electrolysis and stack technology with ultra-high electrolysis current density and effeciency, (2017).

[152] T.L. Skafte, J. Hjelm, P. Blennow, C. Graves, Quantitative review of degradation and lifetime of solid oxide cells and stacks, Proceedings of 12th European Sofc & Soe Forum 2016, European Fuel Cell Forum, 2016.

[153] Y. Zheng, J. Wang, B. Yu, W. Zhang, J. Chen, J. Qiao, J. Zhang, A review of high temperature co-electrolysis of H 2 O and CO 2 to produce sustainable fuels using solid oxide electrolysis cells (SOECs): advanced materials and technology, Chemical Society Reviews 46(5) (2017) 1427-1463.

[154] K. Chen, S.P. Jiang, Review—materials degradation of solid oxide electrolysis cells, Journal of The Electrochemical Society 163(11) (2016) F3070-F3083.

[155] P.A. Lessing, A review of sealing technologies applicable to solid oxide electrolysis cells, Journal of Materials Science 42(10) (2007) 3465-3476.

[156] G. Corre, A. Brisse, 9000 hours operation of a 25 solid oxide cells stack in steam electrolysis mode, ECS Transactions 68(1) (2015) 3481-3490.

[157] Q. Liu, X. Dong, G. Xiao, F. Zhao, F. Chen, A novel electrode material for symmetrical SOFCs, Advanced Materials 22(48) (2010) 5478-5482.

[158] ENERGY.GOV. https://energy.gov/eere/fuelcells/hydrogen-production-pathways.

[159] F.F. Abdi, L. Han, A.H. Smets, M. Zeman, B. Dam, R. Van De Krol, Efficient solar water splitting by enhanced charge separation in a bismuth vanadate-silicon tandem photoelectrode, Nature Communications 4 (2013).

[160] S. Hu, C. Xiang, S. Haussener, A.D. Berger, N.S. Lewis, An analysis of the optimal band gaps of light absorbers in integrated tandem photoelectrochemical water-splitting systems, Energy & Environmental Science 6(10) (2013) 2984-2993.

[161] H. Takenaka, E. Torikai, Y. Kawami, N. Wakabayashi, Solid polymer electrolyte water electrolysis, International Journal of Hydrogen Energy 7(5) (1982) 397-403.

[162] R. Pässler, Parameter sets due to fittings of the temperature dependencies of fundamental bandgaps in semiconductors, Physica Status Solidi (b) 216(2) (1999) 975-1007.

[163] Y.P. Varshni, Temperature dependence of the energy gap in semiconductors, Physica 34(1) (1967) 149-154.

[164] K.P. O'Donnell, X. Chen, Temperature dependence of semiconductor band gaps, Applied Physics Letters 58(25) (1991) 2924-2926.

[165] M. Cardona, T.A. Meyer, M.L.W. Thewalt, Temperature dependence of the energy gap of semiconductors in the low-temperature limit, Physical Review Letters 92(19) (2004) 196403.

[166] S.M. Sze, Physics of semiconductor devices, 2nd ed., Wiley & Sons, New York, 1981.

[167] T. Kuratomi, K. Yamaguchi, M. Yamawaki, T. Bak, J. Nowotny, M. Rekas, C. Sorrell, Semiconducting properties of polycrystalline titanium dioxide, Solid State Ionics 154, (2002) 223-228.

[168] J. Bardeen, Surface states and rectification at a metal semi-conductor contact, Physical Review 71(10) (1947) 717.

[169] C. Mead, W. Spitzer, Fermi level position at metal-semiconductor interfaces, Physical Review 134(3A) (1964) A713.

[170] S.M. Sze, Semiconductor devices: physics and technology, John Wiley & Sons2008.

[171] A. Saxena, Forward current-voltage characteristics of Schottky barriers on n-type silicon, Surface science 13(1) (1969) 151-171.

[172] M. Atalla, Investigation of Hot Electron Emitter, AIR FORCE CAMBRIDGE RESEARCH LABS HANSCOM AFB MA, 1962.

[173] A p–n junction in thermal equilibrium with zero-bias voltage applied, https://commons.wikimedia.org/wiki/File:Pn-junction-equilibrium-graphs.png.

[174] C.-T. Sah, R.N. Noyce, W. Shockley, Carrier generation and recombination in pn junctions and pn junction characteristics, Proceedings of the IRE 45(9) (1957) 1228-1243.

[175] Y. Xu, M.A. Schoonen, The absolute energy positions of conduction and valence bands of selected semiconducting minerals, American Mineralogist 85(3-4) (2000) 543-556.

[176] K.T. Fountaine, H.J. Lewerenz, H.A. Atwater, Efficiency limits for photoelectrochemical water-splitting, Nature communications 7 (2016) 13706.

[177] S. Haussener, S. Hu, C. Xiang, A.Z. Weber, N.S. Lewis, Simulations of the irradiation and temperature dependence of the efficiency of tandem photoelectrochemical water-splitting systems, Energy & Environmental Science 6(12) (2013) 3605-3618.

[178] I.E. Castelli, T. Olsen, S. Datta, D.D. Landis, S. Dahl, K.S. Thygesen, K.W. Jacobsen, Computational screening of perovskite metal oxides for optimal solar light capture, Energy & Environmental Science 5(2) (2012) 5814-5819.

[179] C. Zhou, J.E. O'Brien, G. Rajan, S. Marsillac, X. Zhang, Water Splitting Using High Temperature Solid Oxide Photoelectrochemical Cell and Visible Sunlight: Searching for the Appropriate Semiconductor Materials, Journal of The Electrochemical Society 164(7) (2017) H497-H502.

[180] Z. Jiang, T. Xiao, V.L. Kuznetsov, P.P. Edwards, Turning carbon dioxide into fuel, Philosophical Transactions of the Royal Society A: Mathematical, Physical and Engineering Sciences 368, (2010) 3343-3364.

[181] J.E. O'Brien, C.M. Stoots, G.L. Hawkes, M.G. McKellar, J.S. Herring, High temperature electrolysis of steam, in: R. Hino, X. Yan (Eds.), The CRC Nuclear Hydrogen Production Handbook, CRC, New York, 2010.

[182] Z. Wang, P.K. Nayak, J.A. Caraveo-Frescas, H.N. Alshareef, Recent Developments in p-Type Oxide Semiconductor Materials and Devices, Advanced Materials 28(20) (2016) 3831-3892.

[183] H. Ohta, K.-i. Kawamura, M. Orita, M. Hirano, N. Sarukura, H. Hosono, Current injection emission from a transparent p–n junction composed of p-SrCu2O2/n-ZnO, Applied Physics Letters 77(4) (2000) 475-477.

[184] H. Ohta, M. Orita, M. Hirano, H. Hosono, Fabrication and characterization of ultraviolet-emitting diodes composed of transparent p-n heterojunction, p-SrCu2O2 and n-ZnO, Journal of Applied Physics 89(10) (2001) 5720-5725.

[185] H. Ohta, H. Mizoguchi, M. Hirano, S. Narushima, T. Kamiya, H. Hosono, Fabrication and characterization of heteroepitaxial p-n junction diode composed of wide-gap oxide semiconductors p-ZnRh2O4/n-ZnO, Applied Physics Letters 82(5) (2003) 823-825.

[186] H. Ohta, M. Hirano, K. Nakahara, H. Maruta, T. Tanabe, M. Kamiya, T. Kamiya, H. Hosono, Fabrication and photoresponse of a pn-heterojunction diode composed of transparent oxide semiconductors, p-NiO and n-ZnO, Applied Physics Letters 83(5) (2003) 1029-1031.

[187] N. Münzenrieder, C. Zysset, L. Petti, T. Kinkeldei, G.A. Salvatore, G. Tröster, Room temperature fabricated flexible NiO/IGZO pn diode under mechanical strain, Solid-State Electronics 87 (2013) 17-20.

[188] S. Kim, J. Cianfrone, P. Sadik, K.-W. Kim, M. Ivill, D. Norton, Room temperature deposited oxide pn junction using p-type zinc-cobalt-oxide, Journal of Applied Physics 107(10) (2010) 1-5.

[189] M.-J. Choi, M.-H. Kim, D.-K. Choi, A transparent diode with high rectifying ratio using amorphous indium-gallium-zinc oxide/SiNx coupled junction, Applied Physics Letters 107(5) (2015) 1-4.

[190] G.C. Brunauer, B. Rotter, G. Walch, E. Esmaeili, A.K. Opitz, K. Ponweiser, J. Summhammer, J. Fleig, UV-Light-Driven Oxygen Pumping in a High-Temperature Solid Oxide Photoelectrochemical Cell, Advanced Functional Materials 26(1) (2016) 120-128.

[191] H. Hosono, Y. Ogo, H. Yanagi, T. Kamiya, Bipolar Conduction in SnO Thin Films, Electrochemical and Solid-State Letters 14(1) (2011) H13-H16.

[192] D. Jing, L. Guo, L. Zhao, X. Zhang, H. Liu, M. Li, S. Shen, G. Liu, X. Hu, X. Zhang, K. Zhang, L. Ma, P. Guo, Efficient solar hydrogen production by photocatalytic water splitting: From fundamental study to pilot demonstration, International Journal of Hydrogen Energy 35(13) (2010) 7087-7097.

[193] U. Pal, S. Gopalan, W. Gong, Materials system for intermediate-temperature SOFC based on doped lanthanum-gallate electrolyte, US Patent 20070009784 A1, Jan 11, 2007.

[194] L.-W. Tai, M. Nasrallah, H. Anderson, D. Sparlin, S. Sehlin, Structure and electrical properties of La 1− x Sr x Co 1− y Fe y O 3. Part 1. The system La 0.8 Sr 0.2 Co 1− y Fe y O 3, Solid State Ionics 76(3) (1995) 259-271.

[195] X. Ge, X. Huang, Y. Zhang, Z. Lu, J. Xu, K. Chen, D. Dong, Z. Liu, J. Miao, W. Su, Screen-printed thin YSZ films used as electrolytes for solid oxide fuel cells, Journal of Power Sources 159(2) (2006) 1048-1050.

[196] H. Gu, R. Ran, W. Zhou, Z. Shao, Anode-supported ScSZ-electrolyte SOFC with whole cell materials from combined EDTA–citrate complexing synthesis process, Journal of Power Sources 172(2) (2007) 704-712.

[197] N. Mahato, A. Banerjee, A. Gupta, S. Omar, K. Balani, Progress in material selection for solid oxide fuel cell technology: A review, Progress in Materials Science 72, (2015) 141-337.

[198] J. Huang, Z. Gao, Z. Mao, Effects of salt composition on the electrical properties of samaria-doped ceria/carbonate composite electrolytes for low-temperature SOFCs, International Journal of Hydrogen Energy 35(9) (2010) 4270-4275.

[199] C. Zuo, S. Zha, M. Liu, M. Hatano, M. Uchiyama, Ba (Zr0. 1Ce0. 7Y0. 2) O3–δ as an Electrolyte for Low-Temperature Solid-Oxide Fuel Cells, Advanced Materials 18(24) (2006) 3318-3320.

[200] StandardTerminology for Additive Manufacturing Technologies, https://compass.astm.org/download/F2792-WITHDRAWN.31373.pdf.

[201] J. Manyika, M. Chui, J. Bughin, R. Dobbs, P. Bisson, A. Marrs, Disruptive technologies: Advances that will transform life, business, and the global economy, McKinsey Global Institute San Francisco, CA2013.

[202] C.W. Tanner, K.Z. Fung, A.V. Virkar, The effect of porous composite electrode structure on solid oxide fuel cell performance I. Theoretical analysis, Journal of The Electrochemical Society 144(1) (1997) 21-30.

[203] M.R. Weimar, L.A. Chick, D.W. Gotthold, G.A. Whyatt, Cost study for manufacturing of solid oxide fuel cell power systems, Pacific Northwest National Laboratory (PNNL), Richland, WA (US), 2013.

[204] M. Singh, H.M. Haverinen, P. Dhagat, G.E. Jabbour, Inkjet printing—process and its applications, Advanced materials 22(6) (2010) 673-685.

[205] D. Young, A. Sukeshini, R. Cummins, H. Xiao, M. Rottmayer, T. Reitz, Ink-jet printing of electrolyte and anode functional layer for solid oxide fuel cells, Journal of Power Sources 184(1) (2008) 191-196.

[206] M. Sukeshini, R. Cummins, T.L. Reitz, R.M. Miller, Ink-Jet Printing: A Versatile Method for Multilayer Solid Oxide Fuel Cells Fabrication, Journal of the American Ceramic Society 92(12) (2009) 2913-2919.

[207] A. Sukeshini, R. Cummins, T. Reitz, R. Miller, Inkjet printing of anode supported SOFC: Comparison of slurry pasted cathode and printed cathode, Electrochemical and Solid-State Letters 12(12) (2009) B176-B179.

[208] A. Sukeshini, P. Gardner, F. Meisenkothen, T. Jenkins, R. Miller, M. Rottmayer, T.L. Reitz, Aerosol jet printing and microstructure of SOFC electrolyte and cathode layers, ECS Transactions 35(1) (2011) 2151-2160.

[209] R. Tomov, M. Krauz, J. Jewulski, S. Hopkins, J. Kluczowski, D. Glowacka, B. Glowacki, Direct ceramic inkjet printing of yttria-stabilized zirconia electrolyte layers for anode-supported solid oxide fuel cells, Journal of Power Sources 195(21) (2010) 7160-7167.

[210] R. Tomov, M. Krauz, A. Tluczek, R. Kluczowski, V.V. Krishnan, K. Balasubramanian, R. Kumar, B. Glowacki, Vacuum-sintered stainless steel porous supports for inkjet printing of functional SOFC coatings, Materials for Renewable and Sustainable Energy 4(3) (2015) 14.

[211] C. Li, H. Shi, R. Ran, C. Su, Z. Shao, Thermal inkjet printing of thin-film electrolytes and buffering layers for solid oxide fuel cells with improved performance, International Journal of Hydrogen Energy 38(22) (2013) 9310-9319.

[212] V. Esposito, C. Gadea, J. Hjelm, D. Marani, Q. Hu, K. Agersted, S. Ramousse, S.H. Jensen, Fabrication of thin yttria-stabilized-zirconia dense electrolyte layers by inkjet printing for high performing solid oxide fuel cells, Journal of Power Sources 273 (2015) 89-95.

[213] C. Wang, S.C. Hopkins, R.I. Tomov, R.V. Kumar, B.A. Glowacki, Optimisation of CGO suspensions for inkjet-printed SOFC electrolytes, Journal of the European Ceramic Society 32(10) (2012) 2317-2324.

[214] C. Wang, R.I. Tomov, R.V. Kumar, B.A. Glowacki, Inkjet printing of gadolinium-doped ceria electrolyte on NiO-YSZ substrates for solid oxide fuel cell applications, Journal of materials science 46(21) (2011) 6889.

[215] A.M. El-Toni, T. Yamaguchi, S. Shimizu, Y. Fujishiro, M. Awano, Development of a Dense Electrolyte Thin Film by the Ink-Jet Printing Technique for a Porous LSM Substrate, Journal of the American Ceramic Society 91(1) (2008) 346-349.

[216] G.D. Han, K.C. Neoh, K. Bae, H.J. Choi, S.W. Park, J.-W. Son, J.H. Shim, Fabrication of lanthanum strontium cobalt ferrite (LSCF) cathodes for high performance solid oxide fuel cells using a low price commercial inkjet printer, Journal of Power Sources 306 (2016) 503-509.

[217] C. Li, H. Chen, H. Shi, M.O. Tade, Z. Shao, Green fabrication of composite cathode with attractive performance for solid oxide fuel cells through facile inkjet printing, Journal of Power Sources 273 (2015) 465-471.

[218] N. Yashiro, T. Usui, K. Kikuta, Application of a thin intermediate cathode layer prepared by inkjet printing for SOFCs, Journal of the European Ceramic Society 30(10) (2010) 2093-2098.

[219] X. Wei, D. Li, W. Jiang, Z. Gu, X. Wang, Z. Zhang, Z. Sun, 3D printable graphene composite, Scientific reports 5 (2015) 11181.

[220] C. Ponce de Leon, W. Hussey, F. Frazao, D. Jones, E. Ruggeri, S. Tzortzatos, R. Mckerracher, R. Wills, S. Yang, F. Walsh, The 3D printing of a polymeric electrochemical cell body and its characterisation, Chemical Engineering Transactions 41 (2014) 1-6.

[221] D. Zhang, B. Chi, B. Li, Z. Gao, Y. Du, J. Guo, J. Wei, Fabrication of highly conductive graphene flexible circuits by 3D printing, Synthetic Metals 217 (2016) 79-86.

[222] D.W. Hutmacher, T. Schantz, I. Zein, K.W. Ng, S.H. Teoh, K.C. Tan, Mechanical properties and cell cultural response of polycaprolactone scaffolds designed and fabricated via fused deposition modeling, Journal of Biomedical Materials Research Part A 55(2) (2001) 203-216.

[223] S.J. Hollister, Porous scaffold design for tissue engineering, Nature materials 4(7) (2005) 518.

[224] D.W. Hutmacher, M. Sittinger, M.V. Risbud, Scaffold-based tissue engineering: rationale for computer-aided design and solid free-form fabrication systems, TRENDS in Biotechnology 22(7) (2004) 354-362.

[225] I. Zein, D.W. Hutmacher, K.C. Tan, S.H. Teoh, Fused deposition modeling of novel scaffold architectures for tissue engineering applications, Biomaterials 23(4) (2002) 1169-1185.

[226] H. Seitz, W. Rieder, S. Irsen, B. Leukers, C. Tille, Three-dimensional printing of porous ceramic scaffolds for bone tissue engineering, Journal of Biomedical Materials Research Part B: Applied Biomaterials 74(2) (2005) 782-788.

[227] P. Dudek, FDM 3D printing technology in manufacturing composite elements, Archives of Metallurgy and Materials 58(4) (2013) 1415-1418.

[228] eSUN, 3D Printing Filaments, https://www.intservo.com/pages/about-us.

[229] S. Dul, L. Fambri, A. Pegoretti, Filaments production and fused deposition modelling of ABS/carbon nanotubes composites, Nanomaterials 8(1) (2018) 49.

[230] E. Tang, T. Wood, S. Benhaddad, C. Brown, H. He, J. Nelson, O. Grande, B. Nuttal, M. Richards, R. Petri, Advanced materials for RSOFC dual operation with low degradation, Report for United States Department of Energy (2012).

[231] H. He, A. Wood, T. Joia, M. Krivy, D. Steedman, Performance Evaluation of Solid Oxide Electrolysis Cells at Versa Power Systems, ECS Transactions 72(8) (2016) 89-96.

[232] Q. Li, Y. Zheng, W. Guan, L. Jin, C. Xu, W.G. Wang, Achieving high-efficiency hydrogen production using planar solid-oxide electrolysis stacks, International Journal of Hydrogen Energy 39(21) (2014) 10833-10842.

[233] J. Mermelstein, O. Posdziech, Development and Demonstration of a Novel Reversible SOFC System for Utility and Micro Grid Energy Storage, Fuel Cells 17(4) (2017) 562-570.

[234] M. Trini, P.S. Jørgensen, A. Hauch, M. Chen, P.V. Hendriksen, Microstructural Characterization of Ni/YSZ Electrodes in a Solid Oxide Electrolysis Stack Tested for 9000 Hours, ECS Transactions 78(1) (2017) 3049-3064.

[235] V.N. Nguyen, Q. Fang, U. Packbier, L. Blum, Long-term tests of a Jülich planar short stack with reversible solid oxide cells in both fuel cell and electrolysis modes, International Journal of Hydrogen Energy 38(11) (2013) 4281-4290.

[236] Q. Fang, L. Blum, N.H. Menzler, Performance and Degradation of Solid Oxide Electrolysis Cells in Stack, Journal of The Electrochemical Society 162(8) (2015) F907-F912.

[237] L. Blum, Q. Fang, L. de Haart, J. Malzbender, N. Margaritis, N.H. Menzler, R. Peters, SOC Development at Forschungszentrum Jülich, ECS Transactions 78(1) (2017) 1791-1804.

[238] G. Rinaldi, S. Diethelm, E. Oveisi, P. Burdet, D. Montinaro, Q. Fu, A. Brisse, Post-test Analysis on a Solid Oxide Cell Stack Operated for 10,700 Hours in Steam Electrolysis Mode, Fuel Cells 17(4) (2017) 541-549.

[239] O.T. Mikko Kotisaari, Dario Montinaro, Jari Kiviaho, SOE stack performance and durability analysis, NEO-CARBON 6th Researchers' Seminar (2016).

[240] T. Hayashi, H. Nakamura, S. Konishi, Joint operation of the TSTA under the collaboration between JAERI and US-DOE, Japan Atomic Energy Research Inst., 1993.

[241] S. Konishi, H. Ohno, H. Yoshida, H. Katsuta, Y. Naruse, Solid oxide electrolysis cell for decomposition of tritiated water, International journal of hydrogen energy 11(8) (1986) 507-512.

APPENDICES

Table 6. Summary of long-term degradation of SOEC in stack level.

Stack Type	Manufacturer	SOEC Configuration	Interconnect	Number of Cells	Current Density (A/cm^2)	Long-term Test (hrs)	Degradation Rate per 1000 hours	Ref.
Planar	VPS	CSC Ni-YSZ/YSZ/MIEC	Haynes 230 [230]	20	2	1200	0.36%	[151, 231]
	MSRI	CSC Ni-YSZ/YSZ/LSCF	---	80	0.41	820	3.1%	[86]
				5	0.2	1000	8.9%	[93]
				5	0.2	1000	3.2%	[93]
	Ceramatec	ESC Ni-CeO_2/ScSZ/La-Co-Fe oxide based perovskite	Alloy 441 with spinel coating	10	0.25,0.317	1000	5.66%, 4.62%	[93]
				10	0.25	1000	6.87%	[93]
				10	0.25	1700	7.4%	[93]
			Low-chromium ferritic stainless steel	25	0.3	900	>40%	[95]
				10	---	>1000	Significant	[69]
				720	0.06	1080	---	[69]
		ESC Ni/ScSZ/Strontium doped manganite	Ferritic stainless steel	10	0.374	---	---	[98, 99]
				10	0.186	---	---	[83, 97]
	NIMTE, CAS	CSC Ni-YSZ/YSZ/LSM-YSZ	SUS 430 ferritic stainless steel	30	0.057	1000	---	[107]
				2	0.1	700	---	[107]
				30	0.15	1030	11.7%	[106]
				2	0-0.2	175	---	[232]
				30	0.15,0.2	500,20	---	[232]
		CSC Ni-YSZ/YSZ/LSCF-GDC	SUS 430 ferritic stainless steel	30	0.5	527	4.06%	[74]
				30	0.35	---	---	[73]
	Sunfire GmbH	ESC Ni-GDC/ScSZ/LSCF	---	1920	0.38	100	---	[233]

Topsoe Fuel Cell	ESC Ni-CGO/YSZ/LSCF	Coated Crofer	5	0.4	4055	5.6%	[94]
	CSC Ni-YSZ/YSZ/LSC	Coated Crofer	25	0.57, 0.72	2528, 5640	2.3%	[156, 234]
	CSC Ni-YSZ/YSZ/LSM-YSZ or LSCF-CGO	Crofer22APU	10	0.75*	1000	<9.1%	[110, 111]
	CSC Ni-YSZ/YSZ/CGO|LSC-CGO|LSC	---	5	0.6	2133	2%	[109]
	CSC Ni-YSZ/YSZ/LSM	Coated Crofer	5	0.4-0.6	2651	3%	[100]
	CSC Ni-YSZ/YSZ/LSM	Coated Crofer	5	0.8	1250	4%	[70]
DTU-Risoe	CSC Ni-YSZ/YSZ/LSM	---	5	1	2000	5%	[70]
ECN	ESC Ni-CGO/YSZ/LSCF	Coated Crofer	5	0.4	>2000	4.6%	[100]
Forschungszentrum Julich	CSC Ni-YSZ/YSZ/LSCF	Crofer22APU	2	0.875	1000	1.5%	[235]
			2	0.5	2300, 1800	0.7%, 1.9%	[236]
			2	0.5	18000	0.7%	[237]
	CSC Ni-YSZ/YSZ/LSM-YSZ	Crofer22APU	4	0.35	---	---	[108]
			4	0.377-0.493	---	---	[78]
CEA	CSC Ni-YSZ/YSZ/YDC-LSCF	Crofer22APU	5	0.5	2700	7-13%	[112]
			5	0.5	1000	6%**	[113]
			3	0.5	1000	3-4%	[101, 113]
	CSC Ni-YSZ/YSZ/LSC	Crofer22APU	3	1	700	1.9-3.6%	[102]
			10	2	---	---	[102]
		AISI441 ferritic stainless steel	10	1.5	---	---	[103]
			25	1.63	---	---	[103]
HTceramix/SOFCpower	CSC Ni-YSZ/YSZ /LSCF-CGO	Crofer22APU	6	0.26, 0.34	1160, 615	5.1%, 0.9-5.8%	[79]

		CSC Ni-YSZ/YSZ/LSC	Crofer22APU	6	0.6	1324	1.9%	[79]
	SOLIDpower	CSC Ni-YSZ/YSZ/LSC	---	6	0.6,0.5	3250, 7000	8%, 0.5%	[238]
		CSC Ni-YSZ/YSZ/LSCF	Crofer22APU	6	1.25	---	---	[105]
		CSC Ni-YSZ/YSZ/LSCF	Steel coated with $MnCo_2O_4$	6	0.775	1500	0.7%	[239]
	Korea Institute of Energy Research	CSC Ni-YSZ/YSZ/LSM	Ceramic	3	0.1	---	---	[104]
	Korea Institute of Science and Technology	CSC Ni-YSZ/ScSZ/LSC-GDC	Metallic	3	0.31	1000	7.75%	[80]
Tubular	Dornier-system GmbH	Ni-YSZ/YSZ/LSM	---	10	0.37	---	---	[91]
		Ni-YSZ/YSZ/LSM	---	5	---	---	---	[240]
	JAERI	Pt/YSZ/Pt	---	24	0.25 A	---	---	[241]
		Ni-YSZ/YSZ/$LaCoO_3$	---	12	0.15	---	---	[116]
	TOSHIBA	Ni-YSZ/YSZ/LSC	---	15	0.45	---	---	[81]
All Ceramic	NASA GRC	Pt-GDC/YSZ/$LaCrO_3$	Co-doped Lanthanum chromite	3	0.75	---	---	[117]

--- Information are not supplied.

VITA

Can Zhou received both his B.S. degree and M.E. degree in Mechanical Engineering from Nanjing University of Aerospace and Astronautics in 2012 and 2014 respectively. He is currently a Ph.D. candidate in the Department of Mechanical and Aerospace Engineering at Old Dominion University. He has been working on the fundamental theory, fabrication and characterization of SOFC/SOPC since 2014. His research interests are developing electrochemical and photoelectrochemical cells under high temperature for hydrogen production.